N73-12855

R-8766

CASE FILE COPY

BOUNDARY COOLED ROCKET ENGINES FOR SPACE STORABLE PROPELLANTS

FINAL REPORT

19 JUNE 1972

CONTRACT NAS7-767

Rocketdyne
North American Rockwell

6633 Canoga Avenue,
Canoga Park, California 91304

R-8766

BOUNDARY COOLED ROCKET ENGINES FOR SPACE STORABLE PROPELLANTS

FINAL REPORT

19 JUNE 1972

Contract NAS7-767

R. C. Kesselring R. M. Knight
B. L. McFarland R. N. Gurnitz

APPROVED BY

F. E. Campagna
Program Manager, Advanced Technology
Small Engines

Rocketdyne
North American Rockwell

6633 Canoga Avenue,
Canoga Park, California 91304

FOREWORD

This program was sponsored by NASA-JPL under Contract NAS7-767 (Rocketdyne General Order 9264). The research was conducted during the 15-month period beginning 1 April 1970 and ending 1 July 1971. The JPL Technical Manager was W. B. Powell.

The Rocketdyne Program Manager was F. E. Campagna. The Project Engineer was Dr. R. N. Gurnitz. R. M. Knight was involved in the injector design, test efforts, and data evaluation. Dr. R. C. Kesselring and B. L. McFarland conducted the thermal (chamber and injector) analytical efforts, data reduction, and interpretation. Detailed injector and chamber designs were performed by L. D. Hemperly and B. Samuelson, respectively.

This report has been assigned Rocketdyne Report No. R-8766.

ABSTRACT

To advance and extend the technology of boundary film/conduction cooled rocket thrust chambers to the space storable propellant combination OF_2/B_2H_6 (oxygen difluoride/diborane), a detailed evaluation of an existing analytical heat transfer model was made. Critical design parameters were identified and their importance determined. Test data reduction methods were developed to enable data obtained from short duration hot firings with a thin walled (calorimeter) chamber to be used to quantitatively evaluate the heat absorbing capability of the vapor film. Hot firings with $FLOX/B_2H_6$ were made with an existing like-doublet injector and a nickel calorimeter chamber. These firings resulted in injector streaking and subsequent degradation of chamber hardware. However, data obtained during these firings permitted a substantial upgrade of the analytical heat transfer model. As a result of these calorimeter firings, efforts were directed toward design of a modification of the existing like-doublet injector. Following fabrication and short duration hot firing checkouts of the newly designed diffusion-bonded injector, a long duration hot firing with a graphite lined chamber designed on the basis of the upgraded analytical heat transfer model was carried out. During this firing a loss of injector control occurred at 33 seconds into the 150-second run due to failure of an originally substandard diffusion bond. Another diffusion bonded injector (designed for operation at somewhat lower face temperatures) was subsequently fabricated. Calorimeter testing with this injector gave every indication of (1) injector operation resulting in only minimal combustion product deposition on the face, (2) no injector streaking, (3) no thermal spikes, (4) no injector face overheating, (5) symmetric heat transfer to the chamber wall, and (6) analytically predictable heat transfer to the chamber wall.

Long duration verification of this injector design was left unaccomplished after unexpected depletion of the contents of the diborane tank after 7 seconds of a planned 75-second test. Nonetheless, effort on this program has resulted in demonstration of the utility of calorimeter chambers, detailed design of a potentially satisfactory $FLOX/B_2H_6$ injector, and an upgraded $FLOX/B_2H_6$ analytical heat transfer model whose validity was demonstrated and which can be used to design $FLOX/B_2H_6$ thrust chambers for indefinite periods of operation.

CONTENTS

Foreword iii
Abstract v
Introduction 1
Summary 5
Analysis and Experimentation 11
Identification of Critical Design Parameters 11
Hardware Design 18
Test Data Evaluation Methods 19
Calorimeter Hot Firings (Tests 001-002) 33
Hardware Modifications Subsequent to Test 002 63
Facility Modifications Subsequent to Test 002 66
Calorimeter Hot Firings (Tests 003-004) 67
Conclusions From Calorimeter Hot Firings (Tests 001-004) 100
New Injector Design 100
Fabrication Technique 118
New Calorimeter Chamber 122
Calorimeter Chamber Hot Firings (Tests 005-007) 128
Use of Contract Injector on In-House Effort (Test 008) 141
Posttest Synopsis of New Injector Design 169
Injector Heat Transfer Reanalysis 172
Injector Modification Subsequent to Test 008 188
Calorimeter Hot Firings (Tests 009-010) 198
Long Duration Test Using Graphite Lined Thrust Chambers. 208
Summary of Results 227
Conclusions 231
Nomenclature 233
References 235
Appendix A
Least Squares Evaluation of Vapor Film Entrainment Rates in Terms of Differential Equation Models 237

Appendix B

Summary of Diborane Tanking Operations and Test Usage 241

B_2H_6 Tanking 241

Propellant Fill Determination Options 242

Test Usage 243

Possible Causes of Accounting Error 243

Prevention of Propellant Depletion 245

Appendix C

Distribution List 249

ILLUSTRATIONS

1. NAS7-304 Posttest Analysis Temperature Comparisons 12
2. NAS7-304 Posttest Analysis Heat Balance Calculation 13
3. Effect of Percent Film Coolant on Heat Transfer for Core MR 15
4. Effect of Percent Film Coolant on Heat Transfer for Core MR 16
5. Effect of Wall Thickness in FLOX/B_2H_6 Graphite Chamber Design With 4.0 Core MR and 10% BLC 17
6. OF_2/B_2H_6 Calorimeter Thrust Chamber 20
7. FLOX/B_2H_6 Nickel Calorimeter Chamber Design 21
8. Schematic of Verification of Current Analysis Methods 23
9. Heat Transfer Results from DEAP Model for Nickel Calorimeter Design 27
10. Comparison of Data Analysis Methods for T_{aw} 30
11. Comparison of Data Analysis Methods for h_f 31
12. Comparison of Entrainment Constants 32
13. Nickel Calorimeter Chamber Following Test 002 34
14. Nickel Calorimeter Chamber - Unburned Side Following Test 002 36
15. Injector Face Following Test 002 37
16. BLC Ring Mass Distribution 39
17. Core Mass Distribution 40
18. Core Mixture Ratio Distribution 41
19. Core and BLC Mass Distribution 42
20. Core and BLC Mixture Ratio Distribution 43
21. Thrust and Flowrates - Test 001 - Core MR = 3.2, 14% BLC 45
22. Thrust and Flowrates - Test 002 - Core MR = 3.3, 10% BLC 46
23. Comparison of Pretest Prediction With Experimental Results - Test 001 48
24. Comparison of Pretest Prediction With Experimental Results - Test 002 49
25. Core Mixture Ratio vs Time for Tests 001 and 002 50

26. Thermocouple Trace at 7 in. From Injector - Test 001 52
27. Thermocouple Trace from 0.5-Inch Location - Test 001 53
28. Posttest Prediction of Test 001 58
29. Heat Flux vs Axial Position - Test 001 60
30. Nickel Thrust Chamber Modification 64
31. Injector BLC Ring Modification 65
32. BLC Ring Mass Distribution, Pretest Run 003 69
33. Core and BLC Mass Distribution, Pretest Run 003 70
34. Core and BLC Mixture Ratio Distribution, Pretest Run 003 71
35. Thrust and Flowrates - Test 003 - Core MR = 3.11, 11% BLC 73
36. Thrust and Flowrates - Test 004 - Core MR = 3.18, 10.7% BLC . . . 74
37. Test 003 - Outside Wall Temperature at 9-Inch Axial Location as Function of Thermocouple Position 77
38. Thermal Spike on Test 003 at 1/2-Inch Axial Location and 0° Thermocouple Position 78
39. Thermal Spike on Test 003 at 1-Inch Axial Location and 90° Thermocouple Position 79
40. Test 004 - Outside Wall Temperature at 9-Inch Axial Location as Function of Thermocouple Position 80
41. Thermal Spike on Test 004 at 1/2-Inch Axial Location and 0° Thermocouple Position 82
42. Thermal Spike on Test 004 at 1-Inch Axial Position and 0° Thermocouple Position 83
43. Test 004 - Outside Wall Temperatures at 3-Inch Axial Location as Function of Thermocouple Position 84
44. Thermal Spike Analysis of Calorimeter Chamber 85
45. Posttest Prediction of Test 001 90
46. Posttest Prediction of Test 004 91
47. Posttest Prediction of Test 003 93
48. Film Temperature Profile for Test 003 94
49. Ratio of Film to Gas Heat Transfer Coefficients vs Film Temperature 98
50. Entrainment Parameter (Le^*/c_{p_g}) vs Distance for Test 003 99

51. Summary of Chamber Damage Locations 101
52. History of NAS7-304 Boundary Layer Coolant Injector 102
53. Element Layout for New Injector Design 104
54. Cant Angles for New Injector Design 105
55. Effect of Row Impingement Angle on Performance 109
56. Mixture Ratio Distribution Calculated From LISP Program for New and NAS7-304 Injector Designs 112
57. Injector Assembly - OF_2/B_2H_6 113
58. Face - OF_2/B_2H_6 Injector 114
59. Body - OF_2/B_2H_6 Injector 115
60. Details - OF_2/B_2H_6 Injector 116
61. Ring - OF_2/B_2H_6 BLC 117
62. Injector Orifice Face Plate (Chamber Side) 120
63. Injector Manifold Body 121
64. New Injector 123
65. New Injector Showing BLC Holes 124
66. BLC Ring Mass Distribution - Pretest Run 005 125
67. Core Mass Distribution - Pretest Run 005 126
68. Core Mixture Ratio Distribution - Pretest Run 005 127
69. New Nickel Calorimeter Chamber 129
70. Thrust and Flowrates for Test 005 - Core MR = 4.25, 4.2% BLC . . 130
71. Injector Face Posttest 005 132
72. Calorimeter Chamber Posttest 005 (Injector End View) 133
73. Thrust and Flowrates for Test 006, Core MR = 4.8, 5.3% BLC . . . 134
74. Test 006 - Outside Wall Temperature at 0.5-Inch Axial Location as Function of Thermocouple Position 135
75. Test 006 - Outside Wall Temperature at 1-Inch Axial Location as Function of Thermocouple Position 136
76. Test 006 - Outside Wall Temperature at 3-Inch Axial Location as Function of Thermocouple Position 137
77. Test - 006 Outside Wall Temperature at 5-Inch Location as Function of Thermocouple Position 138
78. Test 006 - Outside Wall Temperature at 7-Inch Location as Function of Thermocouple Position 139

79. Test 006 - Outside Wall Temperature at 9-Inch Location as Function of Thermocouple Position 140
80. Thrust and Flowrates for Test 007 - Core MR = 2.23, 12.7% BLC . . 142
81. Injector Face Posttest 007 (Before Cleaning) 143
82. Calorimeter Chamber - Posttest 007 (Nozzle View) 144
83. Calorimeter Chamber - Posttest 007 (Injector End View) 145
84. Injector Face - Posttest 007 (After Cleaning) 146
85. IR&D Chamber - Pretest 008 147
86. Thrust vs Time - Test 008 148
87. Oxidizer Flowrate vs Time - Test 008 149
88. Total Fuel Flowrate vs Time - Test 008 150
89. BLC Flowrate vs Time - Test 008 151
90. IR&D Chamber on Stand - Posttest 008 153
91. Injector Face - Posttest 008 154
92. Injector Face - Posttest 008 155
93. IR&D Chamber - Posttest 008 (Injector End View) 156
94. Manifold Injection Pressures vs Time - Test 008 157
95. Injection Pressures vs Time - Tests 005 Through 007 159
96. New Injector Manifold 160
97. $\dot{w}\sqrt{\Delta P}$ vs Time - Test 008 161
98. Chamber Pressure vs Time - Test 008 163
99. Graphite Outside Wall Temperature at 1-Inch Axial Location as Function of Thermocouple Position - Test 008 164
100. Graphite Outside Wall Temperature at 3.5-Inch Axial Location as Function of Thermocouple Position - Test 008 165
101. Graphite Outside Wall Temperature at 5-Inch Axial Location as Function of Thermocouple Position - Test 008 166
102. Graphite Outside Wall Temperature at 6.75-Inch Axial Location as Function of Thermocouple Position - Test 008 167
103. Comparison Between Old and New Injector Design 170
104. Oxidizer Flowrate - ΔP Characteristics of New Injector 171
105. TAP Model Nodal Network for Diffusion-Bonded Injector 174
106. Predicted Steady-State Temperature Distribution (Without Two-Phase Flow) for Diffusion-Bonded Injector - Test 006 Conditions . . 175
107. Predicted Steady-State Temperature Distribution (Including Two-Phase Flow) for Diffusion-Bonded Injector 177

108. Predicted 10-Second Temperature Distribution (Including Two-Phase Flow) for Diffusion-Bonded Injector-Test 006 Conditions 178
109. Predicted 10-Second Temperature Distribution (Including Two-Phase Flow and Local Gas Side Film Enhancement in the Vicinity of Two-Phase Flowing Orifices) for Diffusion-Bonded Injector 180
110. Effect of Operating Conditions on Predicted Steady-State Temperature Distribution 182
111. TAP Model Nodal Network for NAS7-304 Injector 184
112. Predicted Steady-State Temperature Distribution for NAS7-304 Injector Under Test 006 Conditions 185
113. Effect of Decreased Injector Face Plate Thickness on Steady-State Temperature Distribution for Diffusion-Bonded Injector . . 186
114. Comparison of Heat Flows in Injectors of Different Face Plate Thicknesses 187
115. Injector Assembly - OF_2/B_2H_6 189
116. Body - OF_2/B_2H_6 Injector 190
117. Ring - OF_2/B_2H_6 BLC 191
118. Details - OF_2/B_2H_6 Injector 192
119. Face - OF_2/B_2H_6 Injector 193
120. Injector Orifice Face Plate (Chamber Side) 195
121. Injector Orifice Face Plate (Manifold Side) 196
122. Injector Manifold Assembly 197
123. BLC Ring Mass Distribution - Pretest Run 009 199
124. Combined Core/BLC Mass Distribution - Pretest Run 009 200
125. Combined Core/BLC Mixture Ratio Distribution - Pretest Run 009 . . 201
126. Thrust and Flowrates for Test 009 - Core MR = 4.0, 8.3% BLC, P_c = 85 psia 202
127. Test 009 - Outside Wall Temperature at 1-Inch Axial Location as Function of Thermocouple Position 203
128. Test 009 - Outside Wall Temperature at 3-Inch Axial Location as Function at 3-Inch Axial Location as Function of Thermocouple Position 204
129. Test 009 - Outside Wall Temperature at 3-Inch Axial Location as Function of Thermocouple Position 205

130. Test 009 - Outside Wall Temperature at 9-Inch Axial Location As Function of Thermocouple Position 206
131. Injector Face Posttest 009 207
132. Calorimeter on Stand Pretest 010 209
133. Thrust and Flowrates for Test 010 - Core MR = 3.6, 12.5% BLC . . 210
134. Test 010 - Outside Wall Temperature at 1-Inch and 3-Inch Axial Locations as Function of Thermocouple Position 211
135. Test 010 - Outside Wall Temperature at 5-Inch and 9-Inch Axial Locations as Function of Thermocouple Position 212
136. Injector Face Posttest 010 213
137. Boundary-Cooled Graphite Lined Chamber on Stand Pretest 011 . . 214
138. Thrust Chamber Assembly (OF_2/B_2H_6 IR&D) 215
139. Maximum Chamber Temperature vs Time for Various Nickel Chamber Designs 217
140. Nickel and Graphite Chamber Comparison 218
141. Injector Face Posttest 011 219
142. Boundary Cooled Chamber - Injector End View Posttest 011 . . . 220
143. Boundary Cooled Chamber - Nozzle End View Posttest 011 221
144. Thrust and Flowrates for Test 011 - Core MR = 3.9, 11.2% BLC . . 222
145. Test 011 - Outside Graphite Wall Temperature at 1-Inch and 3.5-Inch Axial Locations as Function of Thermocouple Position . . 223
146. Test 011 - Outside Graphite Wall Temperature at 5-Inch and 6.75-Inch Axial Locations as Function of Thermocouple Position . . 224

TABLES

1. Independent Variables to be Studied in Task I 3
2. Dependent Variables to be Evaluated in Task I 3
3. Evaluation of Proposed Data Reduction Methods 28
4. Summary of Calorimeter Film Thermal Data for Test 001 55
5. Summary of Calorimeter Heat Flux Data for Test 001 56
6. Test 001 Posttest Prediction Using DEAP Model 61
7. Summary of Calorimeter Thermal Data for Test 002 62
8. Thrust Chamber Performance 75
9. Le^*/c_{p_g} vs Distance (From Eq. 10) 89
10. Summary of Thermal Data From Test 003 95
11. Summary of Thermal Data From Test 004 96
12. FLOX/B_2H_6 Performance Analysis - Three Ring Injector 108
B-1. B_2H_6 Usage - NAS7-767 (Original Estimate) 244
B-2. Propellant Availability (Minimum Estimate) 246
B-3. Propellant Usage (Maximum Estimate) 247

INTRODUCTION

The overall objective of this program was to advance and extend the technology of boundary film/conduction cooled (INTEREGEN) rocket thrust chambers to the space storable propellant combination OF_2/B_2H_6. The end objective was to establish a set of broadly applicable criteria for the design of injectors and thrust chambers over a range of operating conditions and physical configurations such that efficient, stable combustion can be sustained for indefinitely long firing durations.

To accomplish these objectives, a program was planned which consisted of a balanced effort between analysis and experimentation to provide understanding in depth of the chemical, physical, thermal, and structural aspects of boundary film conduction cooling of OF_2/B_2H_6 engines. The analytical base was provided by a number of thermal, stress, combustion, and engine stability computer programs developed by Rocketdyne on previous contracts and in-house studies. The experimental efforts provided FLOX/B_2H_6 operational data for confirmation and/or upgrading of the analytical model input data.

During the first phase of this program, the analytical models were to be used to define key independent and dependent variables. These models were also to be used to establish baseline test configurations and operating conditions so that even the initial testing could be accomplished near the established program heat transfer and performance goals.

The pertinent independent variables studied are presented in Table 1. Based on the analytical evaluations, as well as on previous OF_2/B_2H_6 data taken at Rocketdyne and elsewhere, certain of these variables (identified in Table 1 by asterisks) were selected for experimental investigation.

A tabulation of the dependent variables which were studied is presented in Table 2. The experimental evaluation of the independent variables denoted by asterisk was accomplished in terms of these dependent variables. Also presented in Table 2 are the evaluation techniques for the dependent variables.

Hot firings were to be made using both thin walled metal calorimeter chambers and boundary cooled (INTEREGEN) chambers. Baseline conditions, around which excursions were to be made, are: (1) 1000-pound thrust, (2) 100-psia chamber pressure, and (3) core mixture ratio of 3.0. In all hot fire testing, 70/30 FLOX was substituted for OF_2 to minimize costs.

The short duration calorimeter chamber tests were to provide the basic heat transfer and performance data as a function of percent film on the walls and injector core mixture ratio. These data were to be used to upgrade the capability of the analytical heat transfer model. The boundary cooled chambers were to be designed on the basis of analytical investigations using the upgraded heat transfer model as well as on performance data obtained in calorimeter chamber testing.

In addition to providing film-conduction cooling and performance data, the purpose of the relatively long duration boundary cooled chamber firings was to permit realistic experimental evaluations of materials from thermal stress and chemical and physical erosion and corrosion standpoints, and deposition from the standpoints of quantity, composition, and spatial distribution.

TABLE 1. INDEPENDENT VARIABLES TO BE STUDIED IN TASK I

	Independent Variable
Chamber:	Geometry Injector-to-throat length Contraction ratio Stagnation pressure Wall material* Wall temperature
Nozzle:	Contour (cone vs. bell expansion)
Liquid Film:	Mass flowrate* Injection method Initial temperature
Core Region:	Mixture ratio*

* = Experimental Testing

TABLE 2. DEPENDENT VARIABLES TO BE EVALUATED IN TASK I

	Dependent Variable	Means of Evaluation*
Film Coolant:	Liquid length	MM, TM
	Fraction of injected film coolant remaining on wall	MM
	Heat transfer coefficient between liquid film and chamber wall	TM, MM
	Degree of liquid film decomposition	MM
	Heat transfer coefficient between vapor film and chamber wall	TM, MM
	Axial variation of adiabatic wall temperature	TM, MM
Solid Deposits:	Quantity	PTA
	Composition	PTA
	Spatial variation	PTA
Combustion:	Efficiency	TC*
Heat Transfer:	Efficiency	TM

*MM = Data match with analytical heat transfer model
TM = Temperature measurement
PTA = Posttest analysis
TC* = Thrust and c* measurements

SUMMARY

A detailed evaluation of analytical methods for predicting heat transfer capabilities of boundary cooled thrust chamber designs was made and critical design parameters such as core mixture ratio, percent boundary layer cooling (BLC), wall thickness, and wall material were identified and the importance of each was determined.

Detailed heat balances on typical chamber designs indicate that: (1) film cooling with B_2H_6 characteristically exhibits short liquid film length (0.5 to 1.0 inch) and low liquid film heat absorption capability, and (2) the success of B_2H_6 as a film coolant is dependent upon the ability of the vapor film to absorb the energy rejected by the combustion gases.

Consequently, test data reduction methods were developed to enable data obtained from short duration hot firings with thin walled (calorimeter) chambers to be used to evaluate the heat absorption capability of the vapor film.

A nickel calorimeter chamber was designed to permit high temperature operating conditions and fabricated for use with an existing like-doublet injector which employed boundary layer coolant directed tangentially to the periphery of the injector (swirl BLC).* The first test with this hardware (100 psia, 3.2 core mixture ratio, and 14 percent of total propellant fuel BLC) resulted in experimental chamber temperatures significantly lower than those analytically predicted by the existing heat transfer model (DEAP). Test 002 (100 psia, 3.3 core mixture ratio, and 10 percent BLC), made immediately following the first test, resulted in a chamber burnthrough at 8.5 seconds into the 10-second programmed duration run. However, in the 90-degree quadrant where thermocouple instrumentation was provided, experimental chamber temperatures were found, as in Test 001, to be significantly lower than those of pretest predictions. Additionally, the BLC ring was found to be free of deposits, although some light, flaky deposits were found on the injector face. Posttest examination and cold flow of the hardware

* This injector was fabricated under NASA Contract NAS7-304 (see Ref. 1)

identified two problem areas: (1) the existence of weldment cracks, where the injector flange was joined to the chamber plenum, which would allow BLC leakage*, and (2) significant nonuniformity in the BLC ring flow distribution. Hardware modifications were made to remedy these conditions.

Tests 003 and 004 were made using a new nickel calorimeter chamber of design identical to the first. These tests employed a nominal core mixture ratio of 3.2 and 11 percent fuel boundary layer coolant. Posttest examination of the hardware following Test 003 indicated no abnormalities. Hardware examination made after Test 004 revealed some gouging in the throat area, as well as a chamber wall discoloration in the vicinity of the chamber burnthrough area on Test 002. However, with the exception of the approximately 90-degree circumferential quadrant where hardware damage occurred, the chamber appeared in "like new" condition.

Data obtained from Tests 001-004 allowed determination of film heat transfer coefficients, film recovery temperatures, and the core/film interaction. Analytical DEAP heat transfer model posttest predictions were matched with experimental data for Tests 001, 003, and 004. Core/film interaction was found to be much less than expected. The analytical DEAP model was consequently upgraded. The upgraded analytical model indicated that the boundary/conduction cooling concept for OF_2/B_2H_6 propellants appeared even more attractive than originally envisioned at the outset of the program.

The injector employed during the first four calorimeter hot firings exhibited fairly uniform operational and excellent chamber compatibility characteristics over a continuous 225-degree chamber sector, but streaking characteristics persisted in the remaining 135-degree sector. Consequently, a new injector was designed and fabricated which was less dependent on precise doublet stream impingement than was the former.

*Leakage was confirmed by motion pictures taken of the firing. Additionally, the potential for BLC leakage was confirmed by posttest weld pressure checks with a specially designed fixture.

The new injector incorporated the following features: (1) inwardly canted fans (like-on-like) to decrease the injector sensitivity to both chamber fuel fan protection and oxidizer misimpingement, (2) improved boundary layer coolant manifolding for more circumferentially uniform boundary layer coolant flow, (3) larger outer row fuel orifices for decreased injector sensitivity to deposition on the injector face, and (4) contoured orifice entrances for more precise propellant flow control. The injector orifice plate was joined to the manifold assembly by the diffusion bonding technique. Pretest pneumatic leak checks, as well as extensive cold flows, of the new injector were made and indicated no anomalous behavior.

Three calorimeter hot firings, Tests 005-007, were made with the new injector. These hot firings indicated: (1) no injector streaking (as evidenced by the absence of local hot spots and/or gouges in the calorimeter chamber), (2) the absence of "thermal spikes" observed with the old injector, (3) minimal amounts of injector face deposition, and (4) analytically predictable chamber heat transfer results. However, some localized overheating of the injector face was observed after Test 007. This was attributed to two-phase oxidizer flow in the larger oxidizer downcomers and facility modifications were made to eliminate such two-phase conditions on future tests.

An in-house hot firing was made with the new injector and an existing IR&D chamber, to evaluate the suitability of graphite as a boundary cooled chamber material. This firing lasted the programmed duration of 150 seconds with a relatively steady thrust and no outward signs of chamber failure. Posttest hardware inspection, however, revealed severe injector face damage, evidently caused by an intermanifold bond failure. The bond failure is believed due to an originally substandard bond caused by poor thermal control during the manufacturing process. The occurrence of a hard start during the 150-second run apparently triggered the failure.

The measured graphite wall temperatures recorded during the long-duration company-sponsored hot firing (Test 008) were compared with values predicted by the upgraded analytical heat transfer model. The DEAP model predictions for Test 008

were found to be in excellent agreement with the measured temperature traces over the first 33 seconds of the firing. Injector control was lost at this time as a result of face burnthrough of the improperly diffusion bonded injector. The data correlation successes and temperature levels experienced in hot fire engendered optimism regarding a successful OF_2/B_2H_6 hot firing with a graphite lined chamber.

Because of the localized injector overheating observed after Test 007, a detailed heat transfer reanalysis of the diffusion bonded injector design was made to verify the applicability of this configuration. A three-dimensional computerized heat transfer model (TAP) was prepared for a one-quarter section of the injector face plate and manifold. This model allowed both the transient and steady-state heat transfer characteristics of the injector face and its associated fuel and oxidizer feed passages to be determined as a function of various gas-side conditions.

Results obtained from the three-dimensional model indicated that the diffusion bonded injector design functioned at a temperature level about 250 F above the operating temperature of the NAS7-304 injector* used earlier in this program. This increased temperature level is sufficiently high to preclude acceptable injector operation should two-phase flow occur in the oxidizer feed system. Therefore, a two-phasing of the oxidizer must be prevented by use of subcooling techniques. Incorporation into the model of the two-phase oxidizer flow condition, which was known to exist during Test 006, was successful in accounting for the localized overheating of the injector face observed after test series 006-007.

Incorporation of possible oxidizer manifold design changes in the existing injector was predicted to be of little beneficial value from a heat transfer standpoint. However, incorporation of a reduced injector face plate thickness (0.205 inch as compared to the original 0.375 inch) was found to decrease the injector face temperature by 200 F. A revised injector design reflecting the 0.205-inch

*For identical operating conditions and injector face heat flux.

injector face plate thickness was, therefore, completed. This design was believed to allow a significantly greater margin of safety with respect to injector operating temperature.

Fabrication of the modified diffusion bonded injector was completed along with fabrication of an ablatively backed, graphite lined, long duration chamber identical to that used in Test 008.

Two additional calorimeter hot firings were made with the new diffusion bonded injector. The first, a 3-second checkout test, was accomplished successfully with no abnormalities. The second, a programmed 10-second test, was prematurely sequence cut at 7 seconds when a small external diborane fire, occasioned by a fitting leak, caused fusion of the thermocouple leads. With the exception of the burned leads, no other damage was sustained.

A long-duration test (programmed 75 seconds) using the new injector and the new graphite lined chamber was prematurely terminated after unexpected depletion of the contents of the diborane tank at 7 seconds into the run. Before the test was manually cut, engine operation at high mixture ratio and insufficient fuel cooling of the injector resulted in injector damage. All previous hot-fire testing with this design gave evidence of:

1. Injector operation resulting in only minimal combustion product deposition on the face
2. No injector streaking
3. No thermal spikes
4. No injector face overheating
5. Symmetric heat transfer to the chamber wall
6. Analytically predictable heat transfer to the chamber wall

The average value of the uncorrected specific impulse efficiency for the diffusion bonded injector design was 86.5 percent with 10.2 percent film coolant*. This value is 3.1 percent lower than the average η_{I_s} value of 89.6 percent with 10.9 percent film coolant obtained during calorimeter testing with the modified NAS7-304 injector.

The test efforts on this program resulted in:

1. Demonstration of the utility of calorimeter chambers at high temperature conditions
2. Detailed design of a satisfactory FLOX/B_2H_6 injector
3. An upgraded FLOX/B_2H_6 analytical heat transfer model whose validity has been demonstrated numerous times and which can be used to design FLOX/B_2H_6 thrust chambers for indefinite periods of operation.

*Average value for all tests having a test duration in excess of 5 seconds with the diffusion bonded injectors.

ANALYSIS AND EXPERIMENTATION

IDENTIFICATION OF CRITICAL DESIGN PARAMETERS

The analytical heat transfer computer model (DEAP) currently in existence at Rocketdyne (Ref. 2) was used to re-examine the predictions of thermal behavior in the graphite INTEREGEN thrust chamber previously tested with FLOX/B_2H_6 under Contract NAS7-304 (Ref. 1). The data match (shown in Fig. 1) between analysis and experiment was achieved by proper selection of a number of parameters, including a chamber core driving temperature equal to $\eta_{c*}^2 T_{theo}$ and a combustion gas-to-vapor-film mass entrainment factor*, Le^*/c_{p_g}, of 11.8. This value of Le^*/c_{p_g} (assumed constant with axial position) was used to analytically study the effect of design parameters. These results are discussed below.

Absorption Mechanism

A detailed heat balance (for thermal equilibrium in the chamber wall) was made for the NAS7-304 INTEREGEN chamber in an effort to provide insight into the energy absorption mechanism when B_2H_6 is used as a film coolant. As shown in Fig. 2**, the amount of energy internally conducted back and subsequently absorbed by the 0.62-inch-long liquid B_2H_6 film is quite small. The major portion of the energy rejected by the combustion gas is absorbed by the B_2H_6 vapor film. The success of B_2H_6 as a film coolant is thus dependent on the ability of the vapor film (with or without entrained combustion gas) to absorb the energy rejected by the combustion gas and to act as a thermal barrier between the chamber core gases and the chamber wall.

---

* Further discussion of the gas entrainment description in the analytical model (DEAP) is presented later in the discussion.

** The percentages shown superimposed on the chamber geometry in Fig. 2 represent a further (subsequent) breakdown of the total amount of heat transferred from the combustion gas (core MR = 3.41) to the boundary layer film in the chamber, the nozzle contraction, and the nozzle exit sections. The sum of the heat transferred from the combustion gas to the boundary layer film (33% + 49% + 18% = 100%) is equal to the summation of the net heat gain to the film and the internal and external radiation losses.

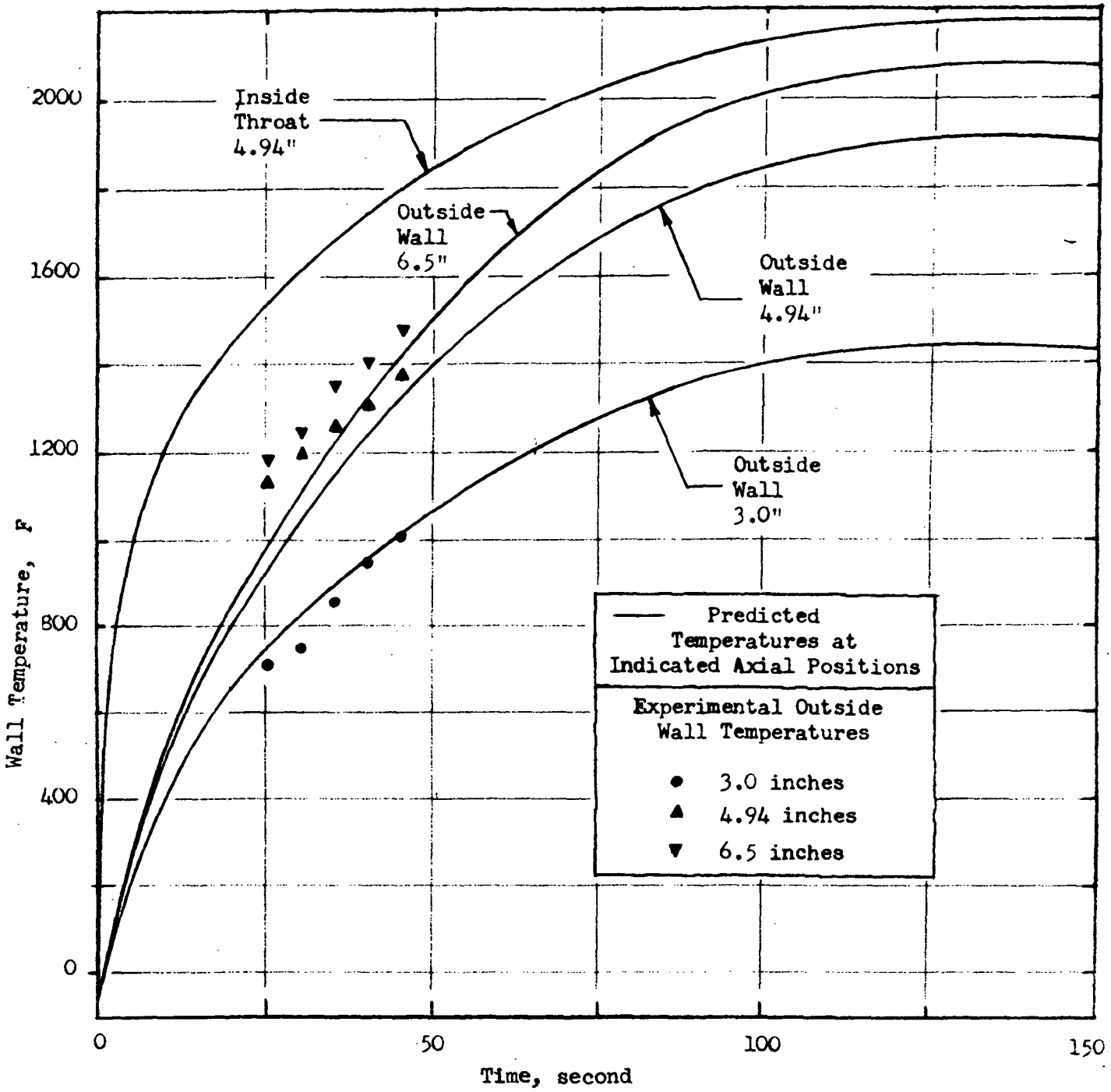

Figure 1. NAS7-304 Posttest Analysis Temperature Comparisons

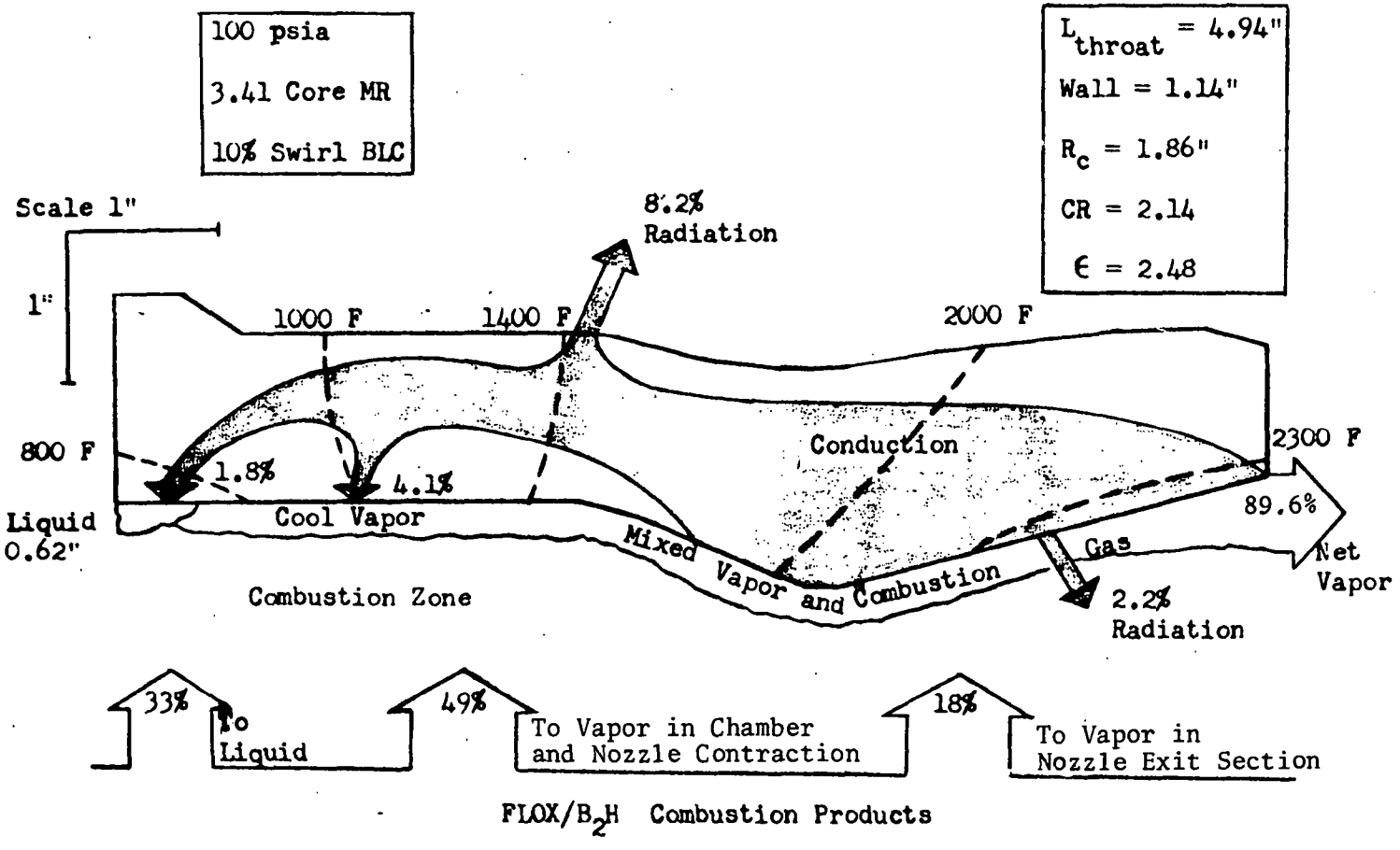

Figure 2. NAS7-304 Posttest Analysis
Heat Balance Calculation

Effects of Core Mixture Ratio and Percent Film Coolant

The effect of core mixture ratio and percent film coolant on INTEREGEN operation was examined through the use of a DEAP model heat balance for a thin wall (0.50-inch) insulated graphite chamber operating at thermal equilibrium. These results are shown graphically in Fig. 3 and 4. The strong influence of percent film coolant on the thermal behavior of the graphite wall is shown through the shift in isotherm location. The lesser effect of varying the core mixture ratio (and thus the combustion gas driving temperature) from 3.0 to 4.0 can also be ascertained by comparing Fig. 3 and 4.

Effects of Wall Thickness

The effect of increasing graphite wall thickness from 0.50 inch to 2.0 inches is shown in Fig. 5. As the wall thickness is increased, axial conduction back toward the injector end is increased and the equilibrium throat temperature and/or maximum temperature in the graphite wall is observed to decrease. The predicted liquid film length remains essentially unchanged. Examination of the heat transfer predictions reveals that vapor binding of the liquid film is predicted to occur for wall thicknesses of 0.75 inch or greater. Vapor binding of the liquid film is defined as the point where an attempt is made to exceed the maximum allowable heat transfer between the wall and the liquid film. Typically, this results in a sudden jump in wall temperature. (This is analogous to increasing boiling heat flux until the peak in the nucleate boiling curve is reached, at which point the surface temperature increases suddenly and transition from nucleate to film boiling occurs.) Vapor binding should occur when the wall temperature in contact with the liquid film exceeds approximately 200 F. The results shown in Fig. 5 indicate that although vapor binding occurs for graphite chamber wall thicknesses of 0.75 inch or greater, the wall temperature does not rise abruptly, but instead appears to reach an equilibrium value (although longer run durations are required to reach thermal equilibrium with the thicker wall chambers). Thus,

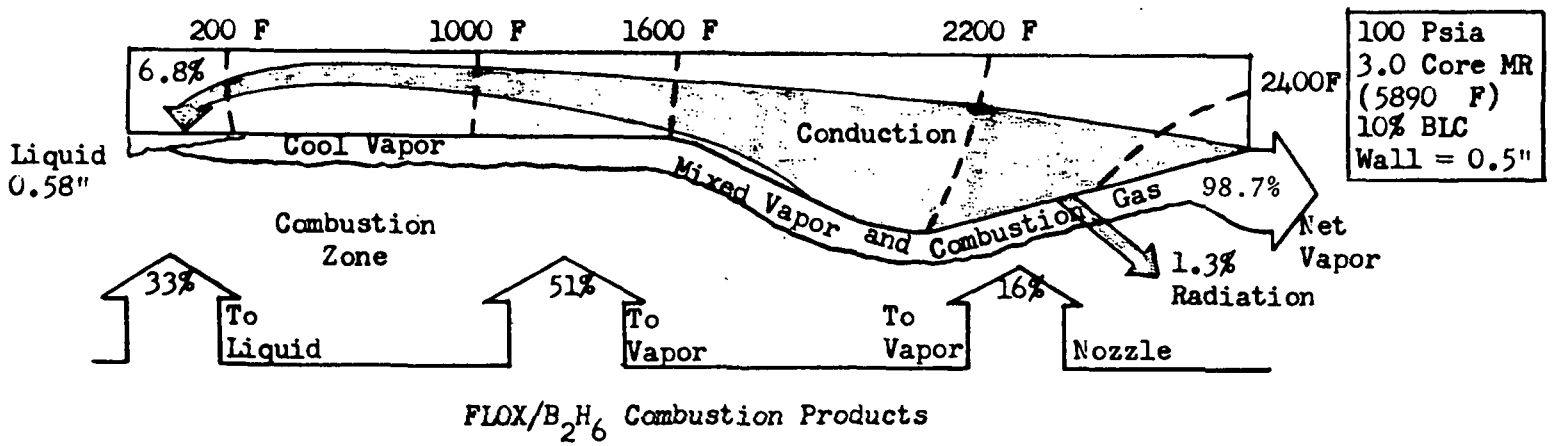

FLOX/B_2H_6 Combustion Products

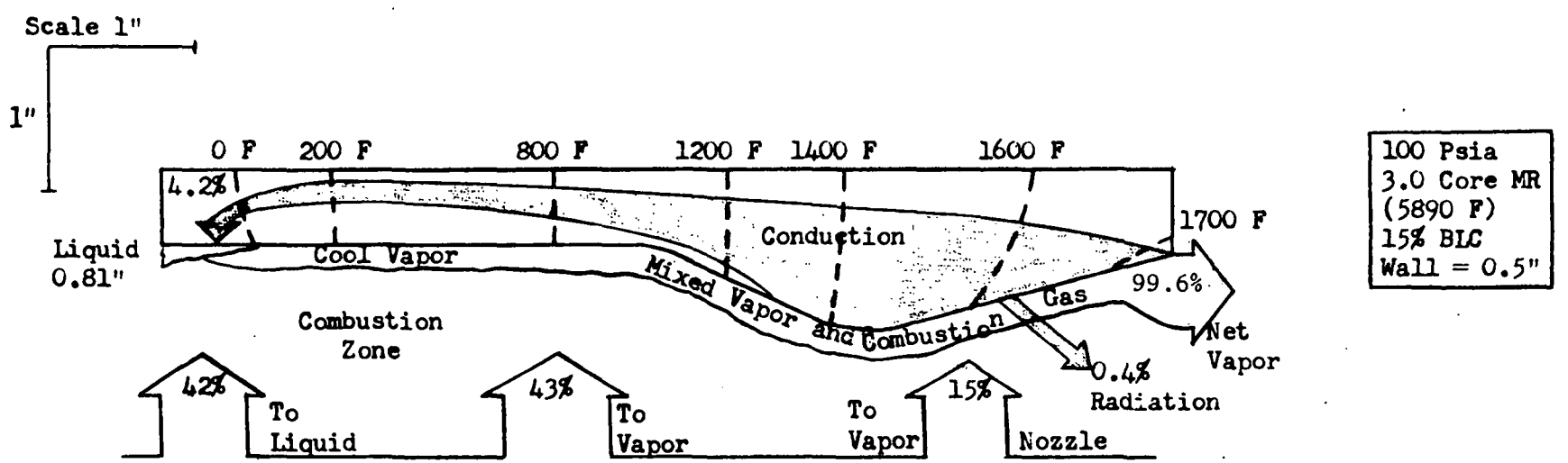

FLOX/B_2H_6 Combustion Products

Figure 3. Effect of Percent Film Coolant on Heat Transfer for 3.0 Core MR

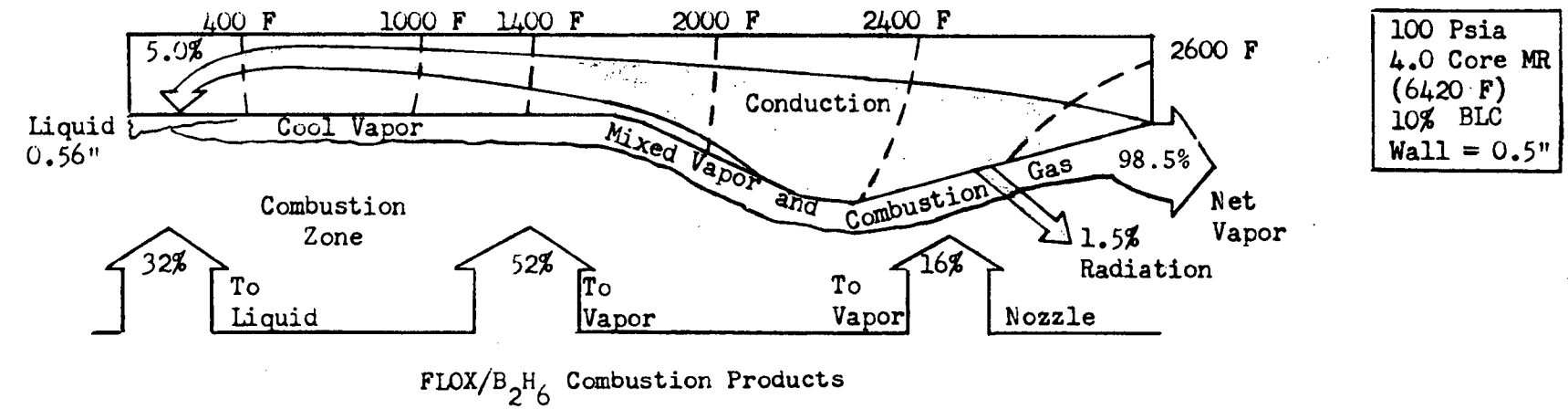

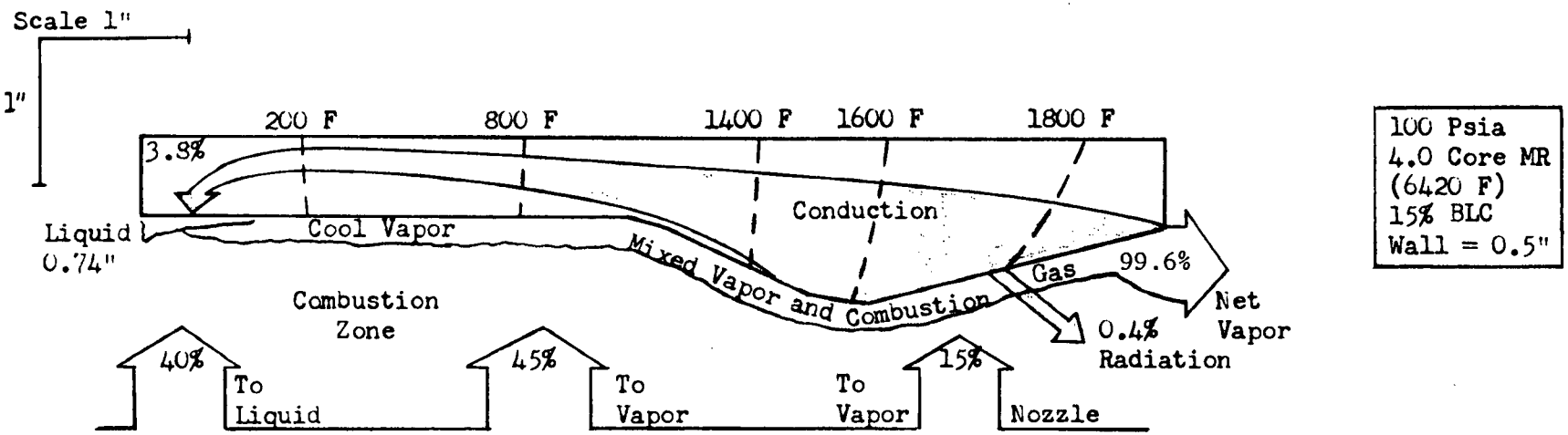

Figure 4. Effect of Percent Film Coolant on Heat Transfer for 4.0 Core MR

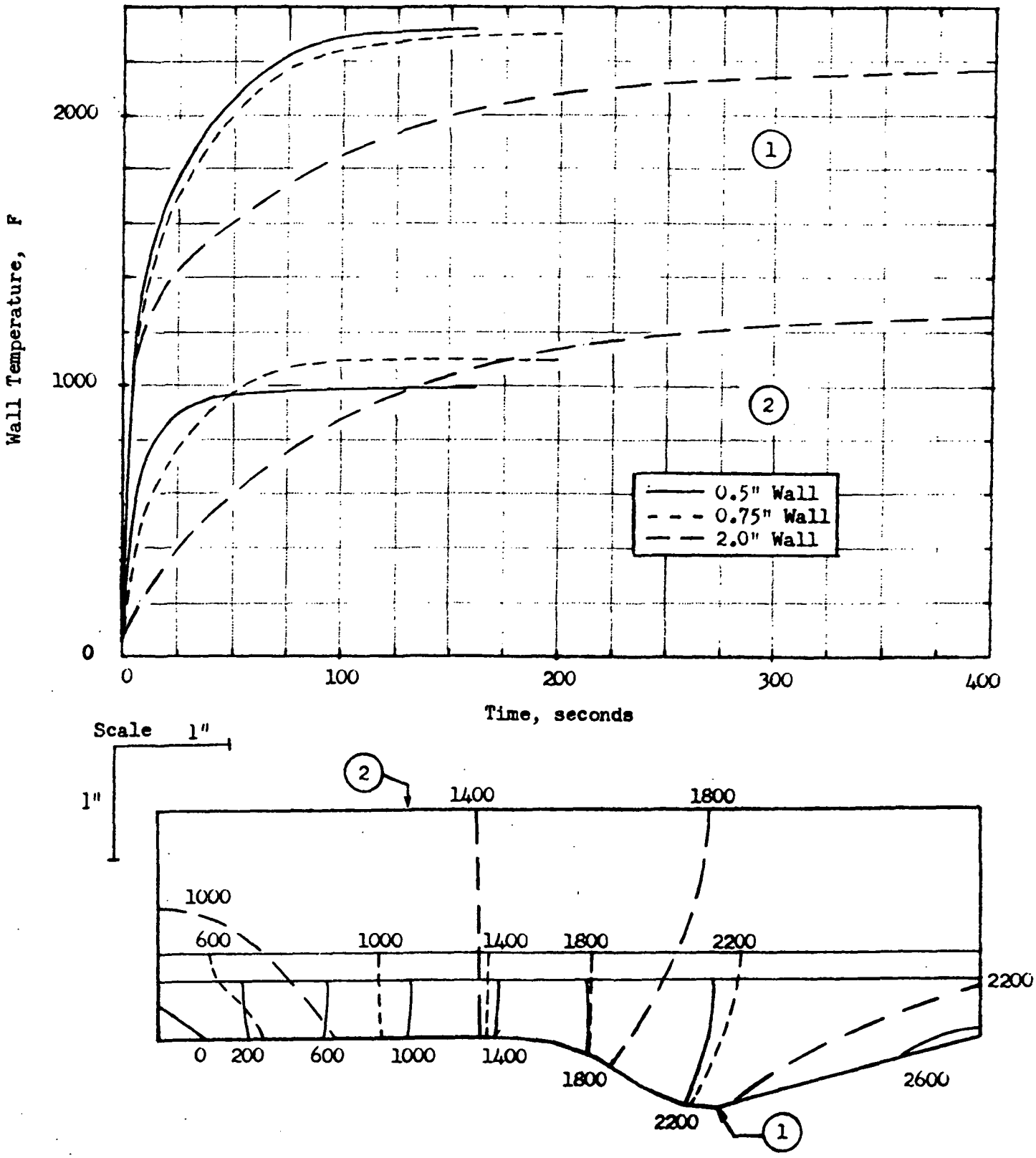

Figure 5. Effect of Wall Thickness in FLOX/B_2H_6 Graphite Chamber Design With 4.0 Core MR and 10% BLC

it is concluded that the B_2H_6 film cooled graphite chamber may be able to operate satisfactorily through its vapor film absorption capability alone. This, however, has never been experimentally demonstrated. One of the objectives of the experimental hot firing portion of the program was, therefore, determination of the vapor film heat transfer characteristics so that the applicability of the DEAP model input could be verified.

Chamber Material - Heat Transfer Interaction

A chamber-material heat-transfer interaction study was carried out. The analytical heat transfer computer model (DEAP) was used to obtain thermal predictions for various chamber materials for a fixed chamber geometry and operating conditions.

Results of this study indicate that columbium and tantalum (with protective coatings), graphite, and zirconium boride are candidate INTEREGEN materials.

Additional results of this study with a further upgrade of the thermal analysis model (following Tests 001-004) also indicate the potential suitability of nickel as an INTEREGEN material.

HARDWARE DESIGN

Calorimeter Chamber Design

As illustrated earlier, the success of B_2H_6 as a film coolant is dependent on the energy absorption capability and thermal barrier properties of the vapor film. Therefore, calorimeter chambers must be designed which will permit determination of heat transfer coefficients between film and wall, film temperatures, and combustion gas entrainment rates in the vapor film. A film temperature of 3100 F was predicted to occur at thermal equilibrium at the end of the expansion section during posttest analysis of the NAS7-304 INTEREGEN chamber. To obtain a film temperature of approximately 3000 F at the end of the expansion

section during short duration calorimeter hot firings, a long nozzle expansion section was employed in the calorimeter design. The wall thickness at the throat must be sufficient to prevent overheating and material failure. A low value of wall thickness near the injector face is desirable to limit axial conduction of heat from the throat region and, thereby, allow data to be obtained in the liquid film region. The value of wall thickness in the expansion section of the nozzle should be as low as required to obtain significant curvature in the temperature-time traces while maintaining sufficient structural integrity. In accord with the above criteria, a five-inch injector-to-throat-length nickel calorimeter chamber was designed using the DEAP model. This chamber has 2.14 contraction and expansion ratios, a five-inch-long nozzle section, and a wall thickness varying from 0.1 inch at the injector face to 0.3 inch at the throat and 0.2 inch at the end of the nozzle. A detail drawing of this chamber is shown in Fig. 6. Thermal predictions for the 5-inch injector-to-throat design are presented in Fig. 7 for the case of 12 percent film coolant.

Injector Design

Modifications of the NAS7-304 swirl boundary layer coolant injector were made to include: (1) a pressure tap through the injector face to permit chamber pressure measurement during long duration tests, (2) incorporation of coolant passages in the oxidizer dome and fuel manifold to permit near ambient temperature engine starts for both the calorimeter and long duration thrust chambers, and (3) enlargement of the injector bolt circle diameter from 6.5 to 8.0 inches to permit attachment to the thrust chambers. The injection orifices and swirl coolant geometry remained unchanged from those used in NAS7-304.

TEST DATA EVALUATION METHODS

Test data from the calorimeter chamber hot firings were used to define the thermal behavior of the B_2H_6 film coolant so that refinements could be made in the INTEREGEN analytical model before designing the long duration INTEREGEN thrust chamber. In past programs (Ref. 3), the interpretation of the transient

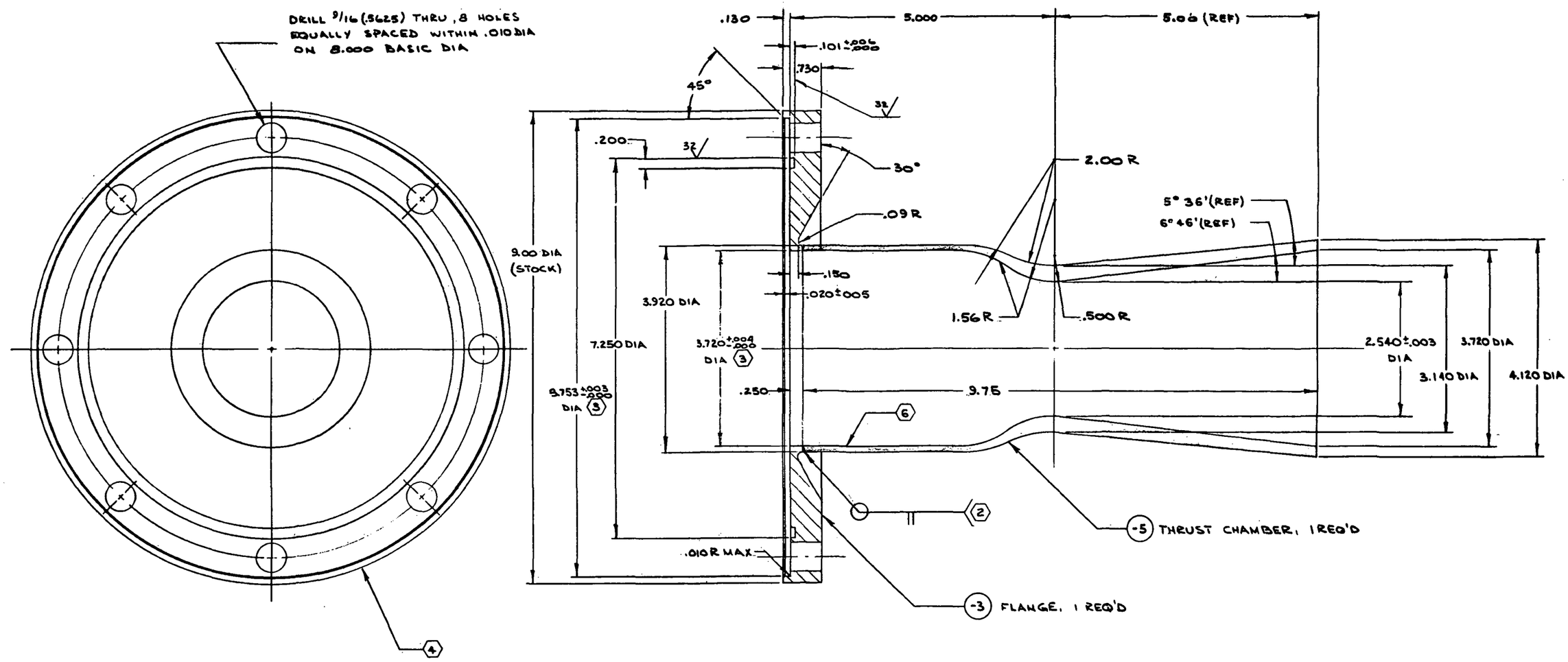

NO	MATERIAL	SIZE	SPECIFICATION
-5	NICKEL 200	4.25 DIA × 10.00	ASTM-B-160
-3	321 OR 347 CRES	9.00 DIA × .75	—

(6) INTERNAL SURFACE 64√

(5) DO NOT CLEAN -5 WITH NITRIC ACID OR OTHER ETCHANT

(4) IDENTIFY PER RAO 104-008

(3) CONCENTRIC WITHIN .003 TIR

(2) WELD PER RAO 107-027, CLASS II

1. MACHINE PER RAO 103-002

NOTE: UNLESS OTHERWISE SPECIFIED

Figure 6. OF_2/B_2H_6 Calorimeter Thrust Chamber

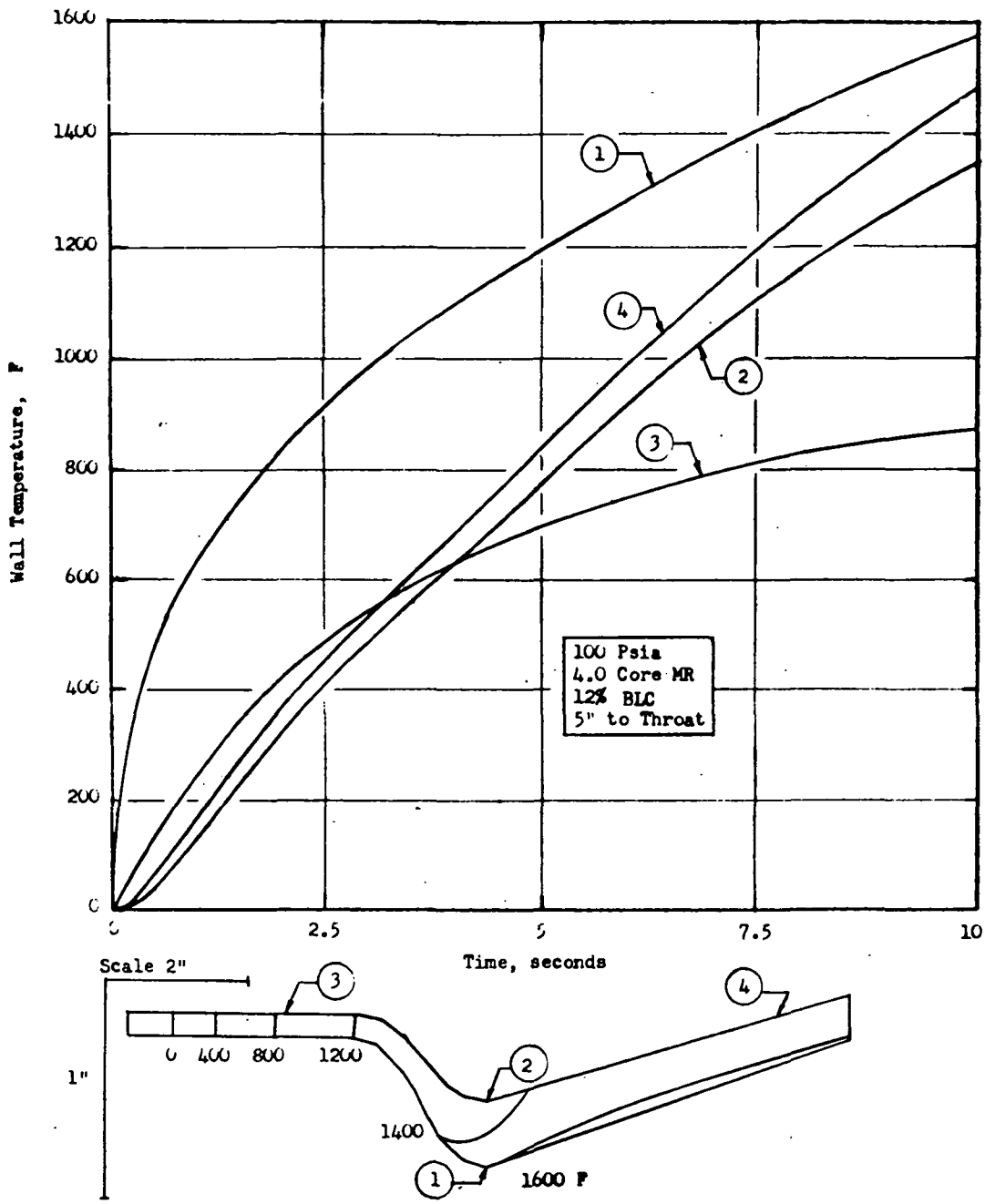

Figure 7. FLOX/B_2H_6 Nickel Calorimeter Chamber Design

thermal data from the thin walled thrust chambers was accomplished with the TRESP computer program, which uses an iterative procedure to obtain film heat transfer coefficients and temperatures based on a constant property solution for the transient heating of an insulated slab (Ref. 4). While accounting for high Biot numbers, this method (TRESP) was not directly applicable to the present program because of the large variation in wall (nickel) thermal properties with temperature and the possibility of slow start transients.

Consequently, new analysis methods were developed which allow for the determination of the adiabatic wall or film recovery temperature (T_{aw}), the film-to-wall heat transfer coefficient (h), and the pseudo-Lewis number (Le*) from measured transient thermal data obtained with the calorimeter chambers. These three quantities are input parameters in the DEAP model. The accuracy of the analytical methods developed was tested in the following manner (see Fig. 8). Known values of the three input parameters (T_{aw}, h, and Le*), based on best current values were fed into the DEAP computer model and the outside calorimeter wall temperature response was calculated. The outside wall temperature response was then used with the integral method of analysis (TEMP) to obtain an inversion prediction of T_{aw} and h which were then compared with the values input to the DEAP model. The T_{aw} prediction from the integral method was also input into the Le* analysis method (FILM) and a prediction for the pseudo-Lewis number was obtained which was compared with the values input into DEAP. The T_{aw} input in DEAP was also input into FILM to check the internal consistency of the DEAP and FILM computer programs.

Integral Method for Determination of Film Temperature and Film Heat Transfer Coefficient

Preliminary analyses of the nickel thrust chambers to be used in the calorimeter hot firings indicated that the large variation in the specific heat of nickel at low temperatures would necessitate the use of a variable property solution to evaluate the test data. Consequently, a computer program (TEMP) was developed based on an integral solution to the conduction equation (Ref. 5) so that test

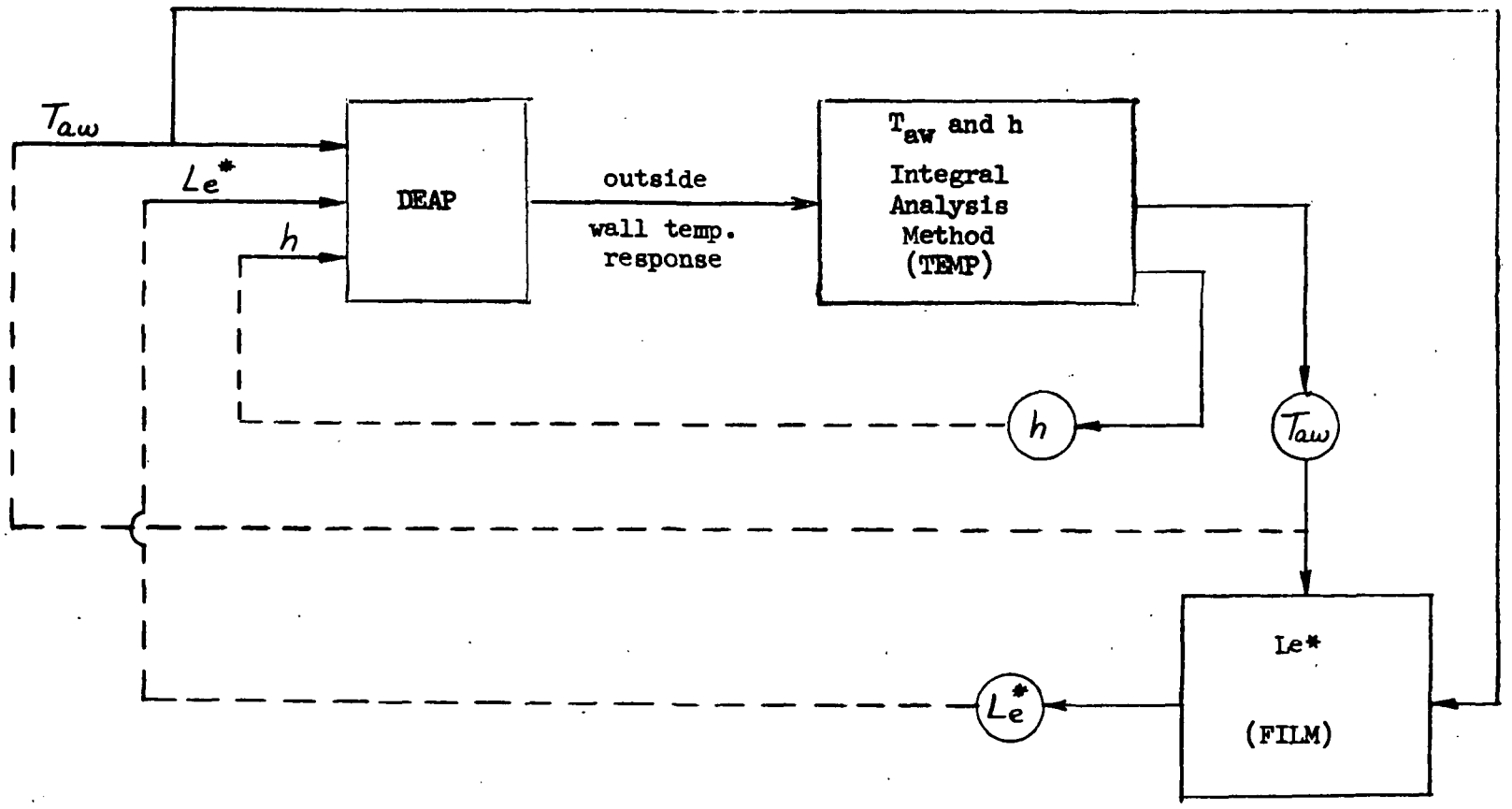

Figure 8. Schematic of Verification of Current Analysis Methods

data from any part of a test where flow conditions remain constant can be analyzed. This allows several independent determinations of film temperature to be made from one set of thermocouple data, and eliminates the necessity of obtaining a step function start transient to apply the analysis method. This approach allows for incorporation of piecewise variation of property values (i.e., properties vary with time, but are assumed constant through the material) into the analysis method and also allows for a correction for axial conduction as indicated in the derivation presented below.

The model is based on an assumed temperature profile through the wall to allow the partial differential equation governing conduction in the wall to be reduced to a total differential equation. The partial differential equation is written as

$$k \frac{\partial^2 T}{\partial x^2} + k \frac{\partial^2 T}{\partial y^2} = \rho c \frac{\partial T}{\partial t} \tag{1}$$

Integration through the wall gives the approximate equation (for an insulated slab)

$$q_s + kL \frac{\partial^2 T}{\partial y^2} = \rho c \frac{\partial}{\partial t} \int_o^L T \, dx \tag{2}$$

When a cubic polynomial is used to represent the temperature profile through the wall, the profile is described by

$$T = T_s - \left(\frac{q_s L}{k}\right) \frac{x}{L} + \left(\frac{q_s L}{k} - \frac{\rho c L^2}{2k} \dot{T}_o\right)\left(\frac{x}{L}\right)^2 + \left(\frac{\rho c L^2}{3k} \dot{T}_o - \frac{q_s L}{3k}\right)\left(\frac{x}{L}\right)^3 \tag{3}$$

Solving Eq. 3 for T_s and substituting into Eq. 2 gives the following equation for the behavior of the wall material

$$hT_{aw} + \left(1 + \frac{hL}{3k}\right) q_c = hT_o + \rho c L \left(1 + \frac{hL}{3k}\right) \dot{T}_o + \frac{(\rho c L)^2 L}{12k} \left(1 + \frac{hL}{6k}\right) \ddot{T}_o \tag{4}$$

If q_c and the derivatives of the back wall temperatures are approximated by their finite difference equivalents, a nonlinear algebraic equation is obtained for each time point (except the first and last) with the form

$$\frac{(\rho cL)^2}{12k\Delta t^2}\left(1 + \frac{hL}{6k}\right)\Delta^2 T_n + \frac{\rho cL}{\Delta t}\left(1 + \frac{hL}{3k}\right)\Delta T_n + hT_n - hT_{aw} -$$

$$q_c\left(1 + \frac{hL}{3k}\right) = \varepsilon_n \tag{5}$$

The TEMP computer program uses a Newton-Raphson iteration procedure to find the best average values of h and T_{aw} by minimizing the sum of ε_n^2. The time period selected for use of this technique must of course be one where an average value can be used to represent h and T_{aw} for the results to have meaning.

Film Method for Determination of Local Entrainment Rate

After obtaining estimates for the film temperature and film-to-wall heat transfer coefficient, it is then necessary to obtain estimates of the entrainment rates of the combustion gas in vapor film.

For this purpose, another data analysis computer program, FILM, was developed. This program employs a least squares technique to determine the local entrainment rates which yield the best agreement between Eq. 6 and 7 (which are used in the DEAP program) and the test data.

$$\dot{w}_f C_{p_f} \frac{\partial T_f}{\partial x} = p\left[(h_g + G_m C_{p_g})(T_g - T_f) - h_f(T_f - T_w)\right] \tag{6}$$

$$\frac{\partial \dot{w}_f}{\partial x} = pG_m \equiv h_g p\left(\frac{Le^*}{C_{p_g}}\right) \tag{7}$$

Development of this approach is presented in Appendix A. This technique requires use of the deduced film temperature at thermal equilibrium ($T_f = T_w = T_{aw}$) as a function of distance, such as obtained using the integral method, rather than the application of the calorimeter data directly. The deduced value of the mass entrainment ratio or pseudo-Lewis number defined by Eq. 7 $Le^* = \frac{GC_{p_g}}{h_g}$ is obtained from the FILM program as a function of axial position rather than assuming a constant value.

Accuracy of the Analytical Methods

As a check case for the integral and FILM methods of analysis, a DEAP case was run for the initial nickel calorimeter design with 4.0 core mixture ratio and 10 percent BLC. An initial wall temperature of zero F was assumed. The inlet coolant temperature was input as a gradually decreasing value (based on the results of Contract NAS7-304)* which reached an equilibrium value at 45 seconds.

The DEAP model thermal predictions for this check case are illustrated in Fig. 9. The DEAP values of T_{aw} and h (at 10 seconds) are found in Table 3. It has been noted that these values vary with time, a sharp discontinuity occurring between 3 and 4 seconds. The value of T_{aw}, for example, at an axial position of 1.3 inches decreased from 805 F at 3 seconds to 404 F at 4 seconds. This variation was discovered to be almost entirely due to the time-variant inlet BLC temperature input to the DEAP model. The time-variant inlet BLC temperature caused the liquid film length to increase from 0.521 inch at one second to 0.553 inch at 10 seconds.

Integral Method. The integral method (TEMP) was used to analyze the simulated data (see Fig. 9) obtained with the DEAP model for the nickel calorimeter design. These results are presented in tabular form in Table 3 and in graphical form

---

* - 70 F at 0 seconds
-115 F at 45 seconds

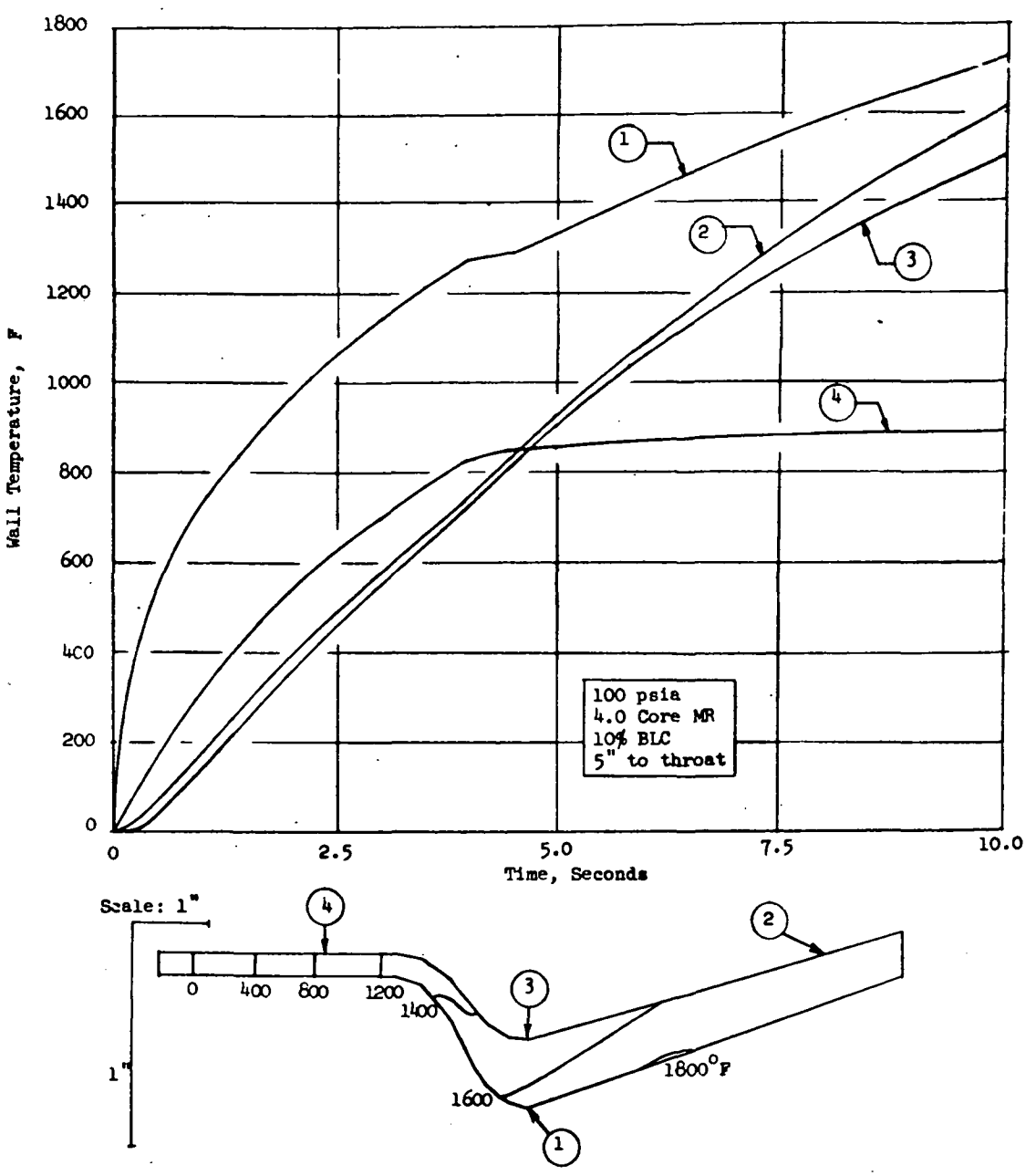

Figure 9. Heat Transfer Results From DEAP Model for Nickel Calorimeter Design

TABLE 3. EVALUATION OF PROPOSED DATA REDUCTION METHODS

(Nickel Calorimeter Check Case D069)

Distance, inches	Wall Thickness, Inch	DEAP Program Values		Integral Method	
		h_f, Btu/in^2 sec F	T_{aw}, F	h_f, Btu/in^2 sec F	T_{aw}, F
0.0	0.100	0.031E-01	-82	0.108E-02	-79
0.371	0.100	0.240E-01	-60	0.243E-03	-80
0.742	0.100	0.129E-02	54	0.821E-03	72
1.30	0.100	0.126E-02	389	0.760E-03	353
1.85	0.100	0.123E-02	655	0.621E-03	661
2.23	0.100	0.120E-02	910	0.185E-02	892
2.78	0.100	0.118E-02	1153	0.139E-02	1144
3.15	0.100	0.116E-02	1341	0.118E-02	1314
3.52	0.117	0.118E-02	1525	0.116E-02	1478
3.89	0.167	0.134E-02	1664	0.128E-02	1649
4.08	0.211	0.150E-02	1761	0.149E-02	1748
4.27	0.250	0.169E-02	1859	0.162E-02	1865
4.45	0.274	0.182E-02	1981	0.164E-02	1984
4.73	0.289	0.190E-02	2121	0.160E-02	2143
5.00	0.300	0.182E-02	2403	0.164E-02	2268
6.00	0.280	0.132E-02	2742	0.127E-02	2628
7.00	0.260	0.103E-02	3007	0.980E-03	2930
8.00	0.240	0.827E-03	3221	0.797E-03	3149
9.00	0.220	0.679E-03	3397	0.648E-03	3375
10.00	0.200	0.571E-03	3475	0.577E-03	3411

in Fig. 10 and 11. In applying the integral method, only the DEAP temperature response predictions between 4 and 10 seconds were used. Thus, only data during a time period where the film temperature was fairly constant were considered. The results shown in Table 3 and Fig. 10 and 11 indicate excellent film temperature agreement over the whole chamber and good film heat transfer coefficient agreement between the DEAP model results and the integral model inversion prediction over a wide range of axial locations (3 inches to 10 inches). The integral method prediction of the heat transfer coefficient becomes less accurate within the first three inches of the chamber. This is because most of the wall temperature change has already occurred within the first 4 seconds at these locations (see Fig. 9). Thus, the total heat flux to the first 3 inches of chamber after this time is quite small and a very small error in film temperature can result in a large error in predicted h. If, for example, $T_{aw} - T_{wall}$ were on the order of 5 degrees, a 5-degree error in the estimation of T_{aw} would result in a 100-percent error in the estimation of h. It should be noted that the good agreement between the DEAP model results and the integral method predictions over a large range of axial positions in the warm vapor film region should allow adequate extrapolation of the film coefficient to the cool vapor film region, in which agreement between the DEAP results and the integral method predictions is poorest. If boundary coolant inlet temperature and thus film temperature conditions were invariant with time and data obtained from zero were used, excellent agreement between DEAP model and integral model would be expected at all axial locations.

Film Method. As a checkout of the data analysis program FILM, the film temperatures predicted by the DEAP model for the calorimeter chamber and the deduced film temperatures from the integral method (see Table 3) were analyzed with the entrainment model. Results are shown in Fig. 12 as the pseudo-Lewis number, Le*, versus axial position, where:

$$Le^* = \frac{G_m \, c_{p_g}}{h_g} \tag{8}$$

The Le* value used for the DEAP calculations was 5.7*.

* Le* = 5.7 corresponds to an entrainment factor, Le^*/c_{p_g}, of 11.8 since $c_{p_g} = 0.482$

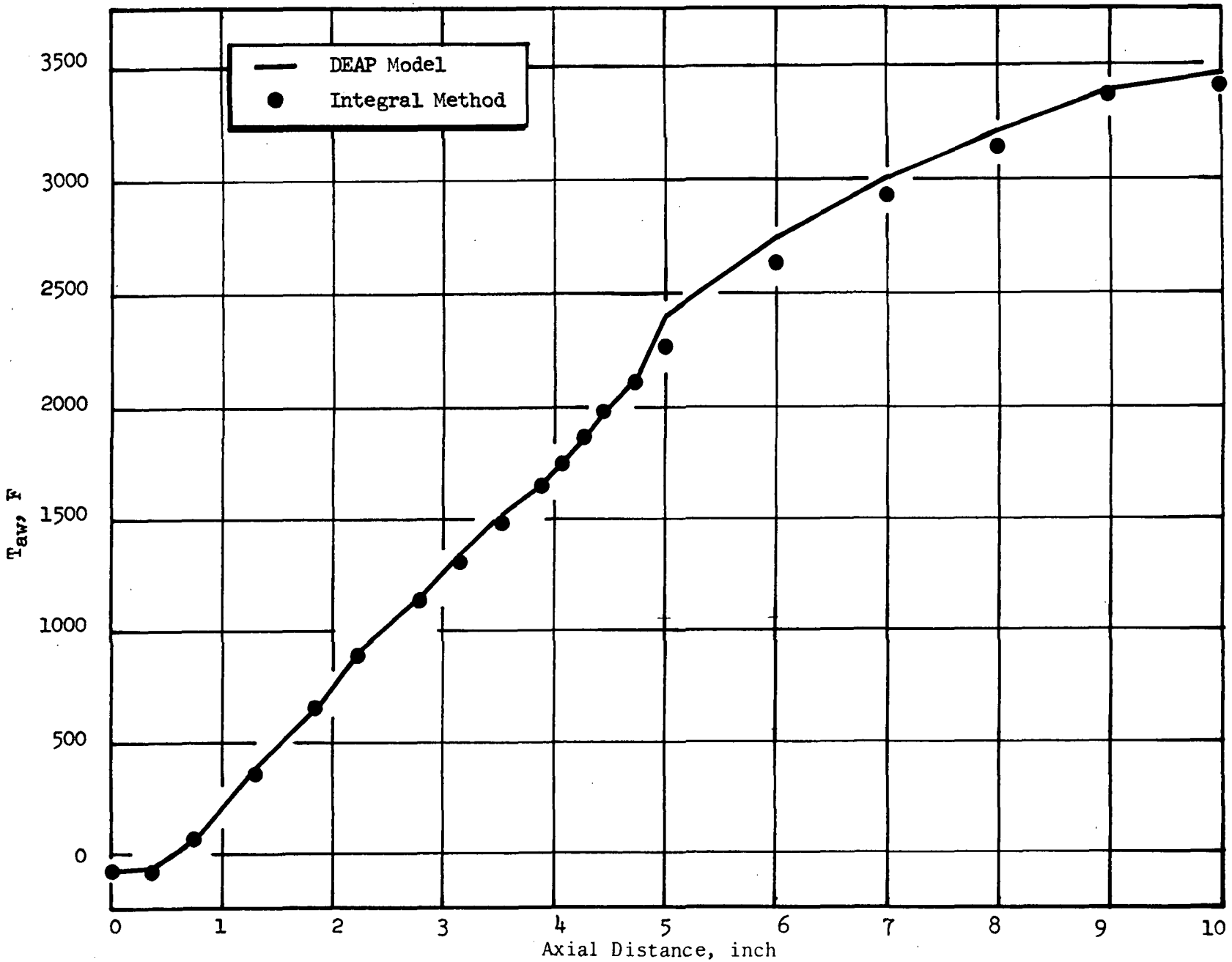

Figure 10. Comparison of Data Analysis Methods for T_{aw}

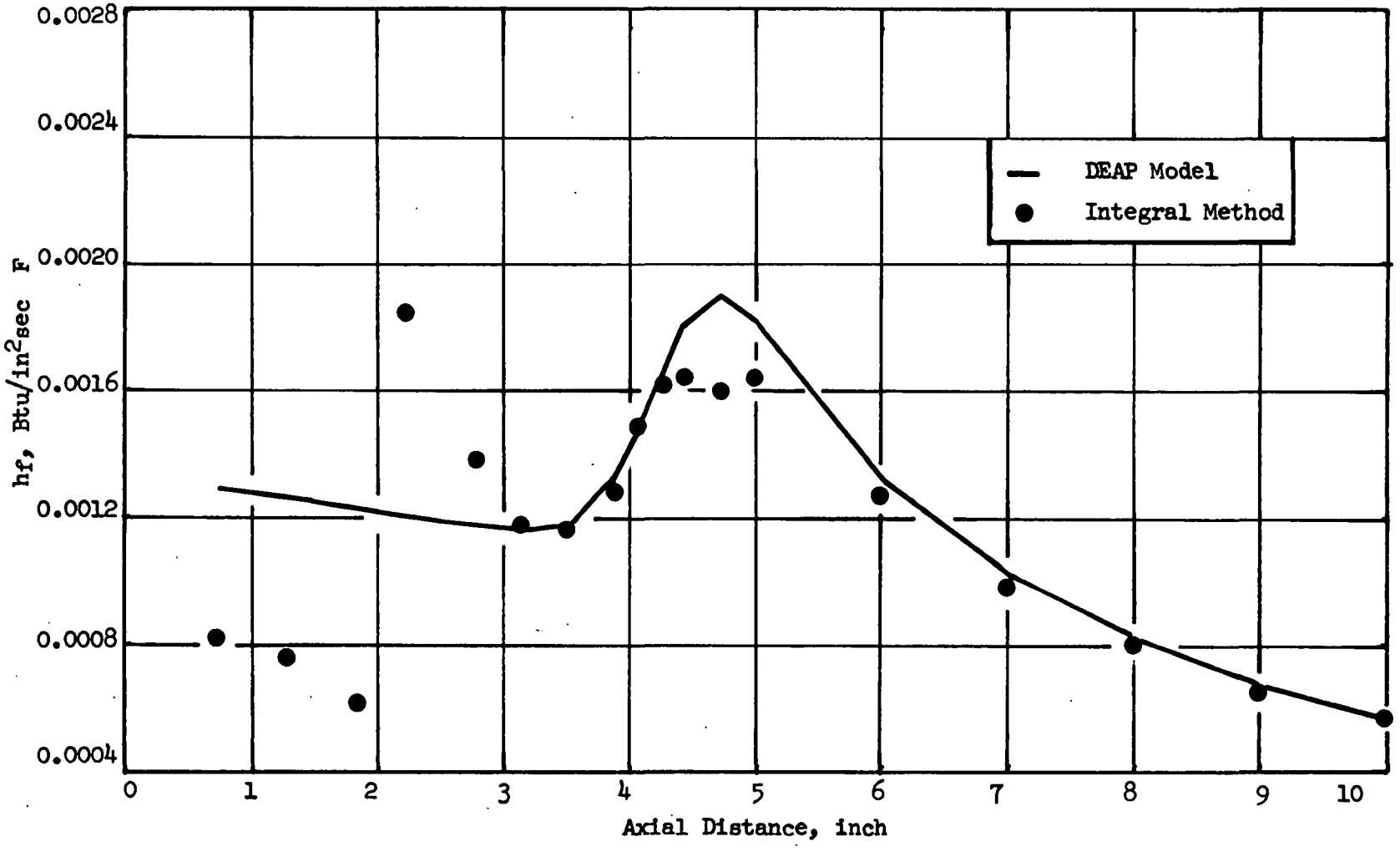

Figure 11. Comparison of Data Analysis Methods for h_f

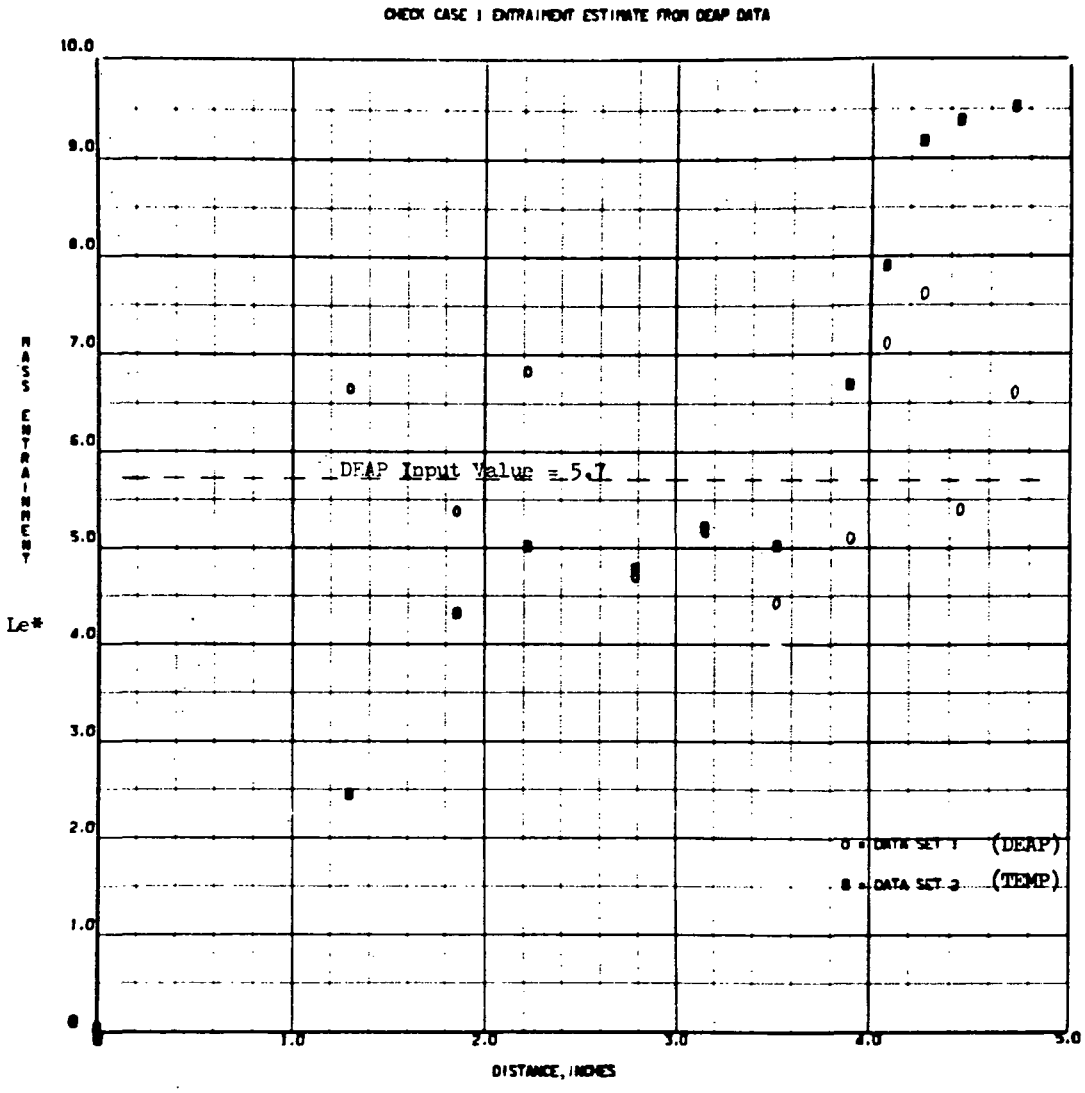

Figure 12. Comparison of Entrainment Constants

It can be seen that the Le* values obtained from the entrainment model vary by ± 20 percent from the correct value (5.7) but with an average value (also obtained from the program) within 1 percent of the correct value.

CALORIMETER HOT FIRINGS (TESTS 001-002)

Initial hot firings were conducted using the NAS7-304 like doublet, swirl BLC injector and the 5-inch-long injector-to-throat nickel calorimeter chamber (Fig. 6). Two tests were made at a nominal chamber pressure of 100 psia and a nominal core mixture ratio of 3.2. On the first test, approximately 14 percent of the total propellant flow was injected as film coolant while on the second test 10 percent BLC was utilized.

The first test had a 10-second programmed duration and exhibited chamber wall temperatures significantly lower than predicted values from the DEAP computer model. (Test results are discussed in more detail in a following section.) Heat transfer asymmetry appeared relatively small and the measured BLC flowrate was steady. Other than some facility feed system induced oxidizer flow variations, no anomalies were noted in Test 001. Motion pictures of the first firing also showed no abnormalities. Upon completion of the first test, the hardware was inspected visually on the stand prior to Test 002. The hardware appeared to be in good condition. There was no evidence of injector misimpingement or uneven coolant flow, either of which would cause severe streaking on the thin walled nickel chamber. The chamber surfaces had an untarnished appearance.

The second test (10 percent BLC) was made immediately following Test 001 hardware inspection. This test, according to motion picture observations, was proceeding normally until about 6.2 seconds after ignition. At this point a leak appeared on the top of the thrust chamber at the weld joining the stainless steel flange and the nickel chamber*. The leak, which appeared as a dark-colored smoke, persisted until a chamber burnthrough (Fig. 13) occurred at

* The leak through the weld was subsequently confirmed with posttest dye penetrant tests and pressure leak tests carried out in the vicinity of the welds with a specially designed leak test fixture.

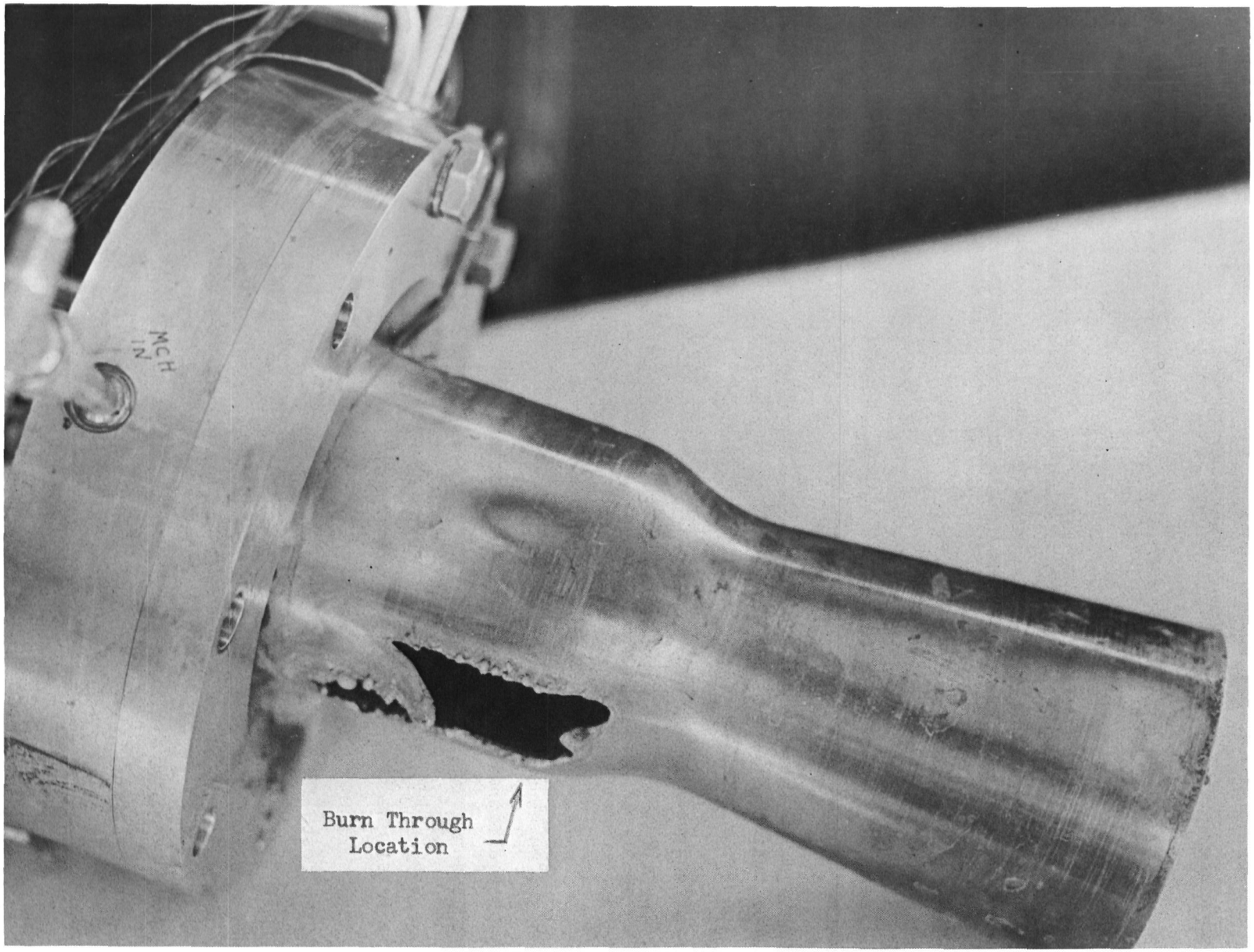

Figure 13. Nickel Calorimeter Chamber Following Test 002

8.5 seconds into the 10-second programmed run. The leak was not visible from the blockhouse due to the brightness of the exhaust flame. Heat transfer asymmetry was relatively large during the test although chamber temperatures as measured by two axial rows of thermocouples 90 degrees apart were significantly less than predicted (DEAP) values. Comparator circuits were used to provide automatic termination should any of five thermocouples on the thrust chamber exceed 1400 F. However, the area of burnout occurred in a 90-degree quadrant sufficiently removed from the two rows of thermocouples (Fig. 14).

Combustion Product Deposition

Posttest observation showed moderate injector face deposition (Fig. 15) which was flaky and non-adherent. No deposits were found in the vicinity of the BLC ring. Chamber deposits were also observed; these were hard and adherent. The flaky deposits on the injector face were not collected prior to posttest cold flow of the injector and were subsequently blown from the injector face upon cold flow initiation. Whether or not such deposits could have actually existed on the injector face during the hot firings in which propellant injection velocities on the order of 100 fps are inexperienced is debatable.

Posttest Injector Cold Flows. Posttest flows were conducted with trichloroethylene and water to determine if injector misimpingement could have caused the failure in Test 002.

The initial step in the posttest analysis consisted of trichloroethylene flows through the fuel and oxidizer orifices to determine the effect of injector face deposition on orifice impingement. Visual observation as well as high speed motion pictures (200 frames/second) of the individual oxidizer and fuel orifice flows showed no degradation of impingement quality. At the conclusion of this experiment, approximately 90 percent of the flaky face deposits had been removed by the force of the impinging jets.

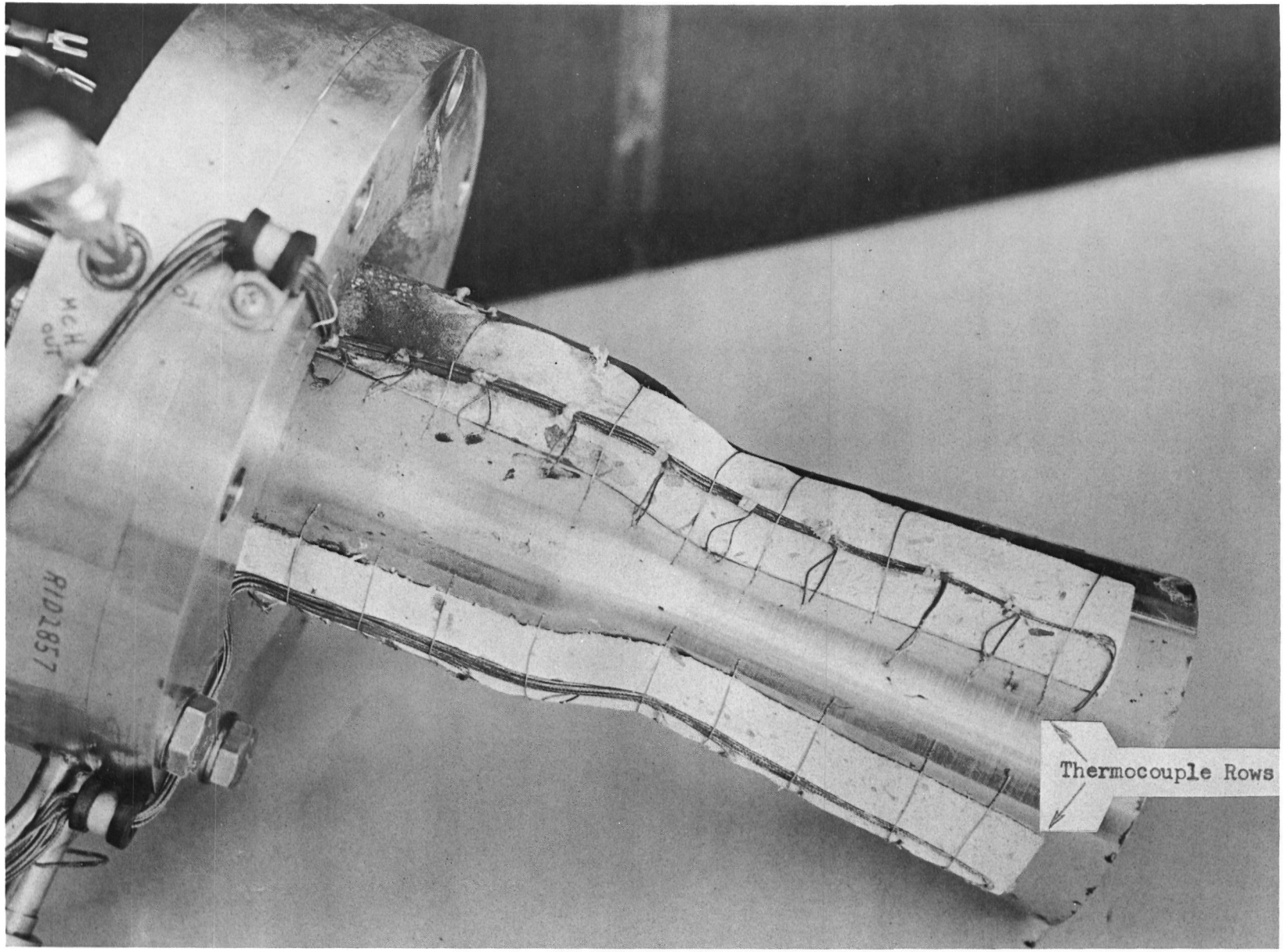

Figure 14. Nickel Calorimeter Chamber, Unburned Side, Following Test 002

Figure 15. Injector Face Following Test 002

The next step in the cold flow analysis consisted of three separate mass-mixture ratio distribution flows utilizing the 29 x 29 collector tube matrix. For these tests, a 3.5-inch-long chamber section was modified and connected to the injector. This assembly was then placed on the top of the tube matrix with careful attention given to the location of the center of the injector.

Three flows were made with trichloroethylene and/or water at flowrates equal to the volumetric flows in Test 002 (3.3 core mixture ratio, 10 percent BLC). The flows consisted of: (1) BLC flow, (2) core flow (fuel plus oxidizer), and (3) BLC plus core flow.

A contour plot of the BLC mass distribution is shown in Fig. 16. Also shown are the geometric center of the injector (+) and the calculated center of the collected mass (0). It is evident that the mass distribution is not circumferentially uniform, particularly in the upper left quadrant of the plot. As a result, the mass center is displaced about 0.6 inch from the geometric center of the injector. The upper left quadrant of Fig. 16 contains 16 percent* of the total flow, whereas the other three quadrants each contain 27 to 30 percent.

The mass distribution and mixture ratio distribution plots for the core flow and the combined core-BLC flow are given in Fig. 17 through 20. The mass distribution plot for the core shows a relatively uniform circumferential distribution with the geometric and mass centers coincident. For the combined flow (Fig. 19), the two centers are not coincident due to the maldistribution of the BLC. The mixture ratio plots (Fig. 16 and 18) show some relatively highly mixture ratios at various locations around the periphery. However, these zones correspond to areas of extremely low mass flux, and are not considered significant. The small amounts of trichloroethylene and water collected in these areas make it difficult to accurately determine local mixture ratio.

---

* 16 percent in a quadrant with 10 percent overall BLC corresponds to an equivalent 6.4 percent BLC in that quadrant.

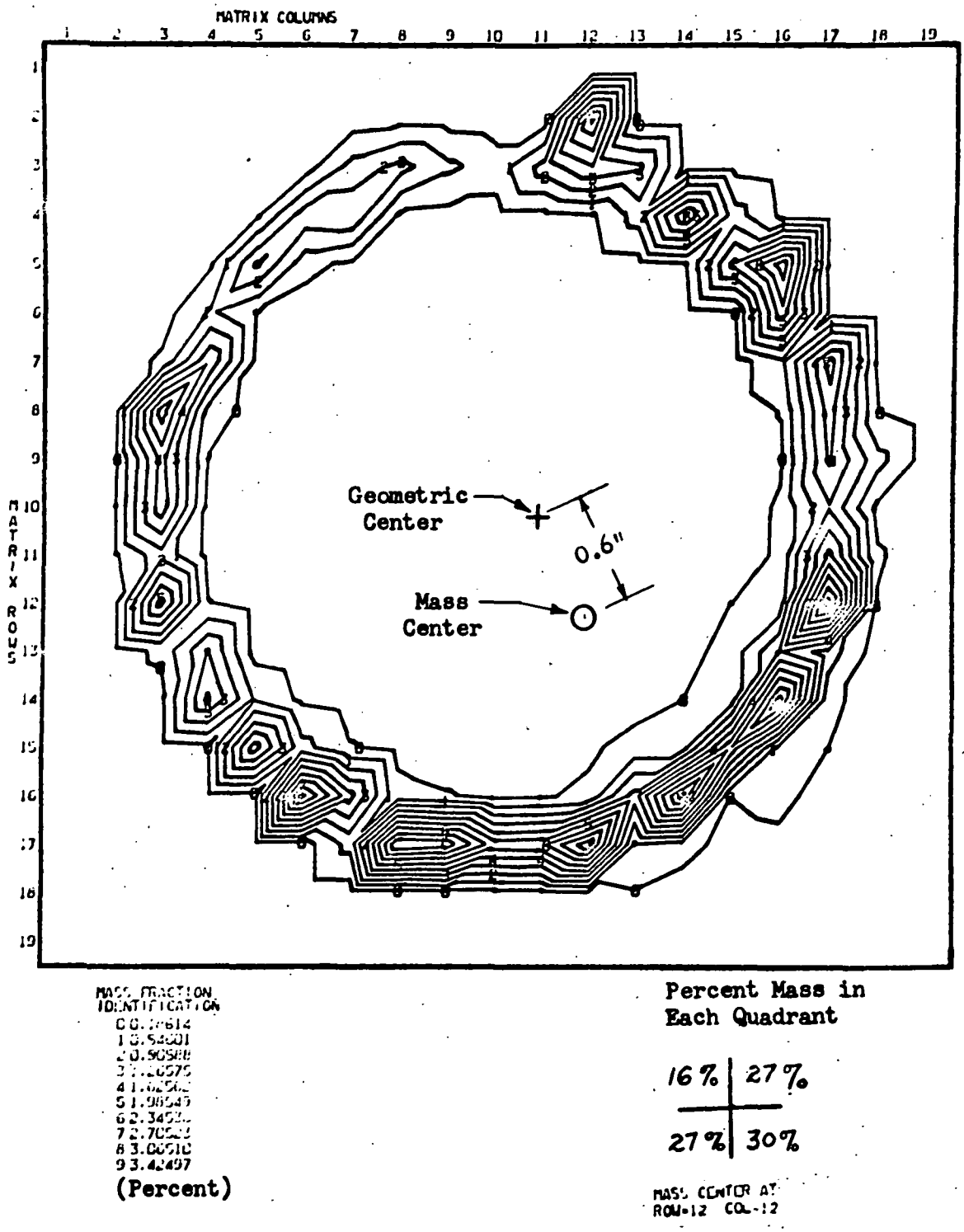

Figure 16. BLC Ring Mass Distribution

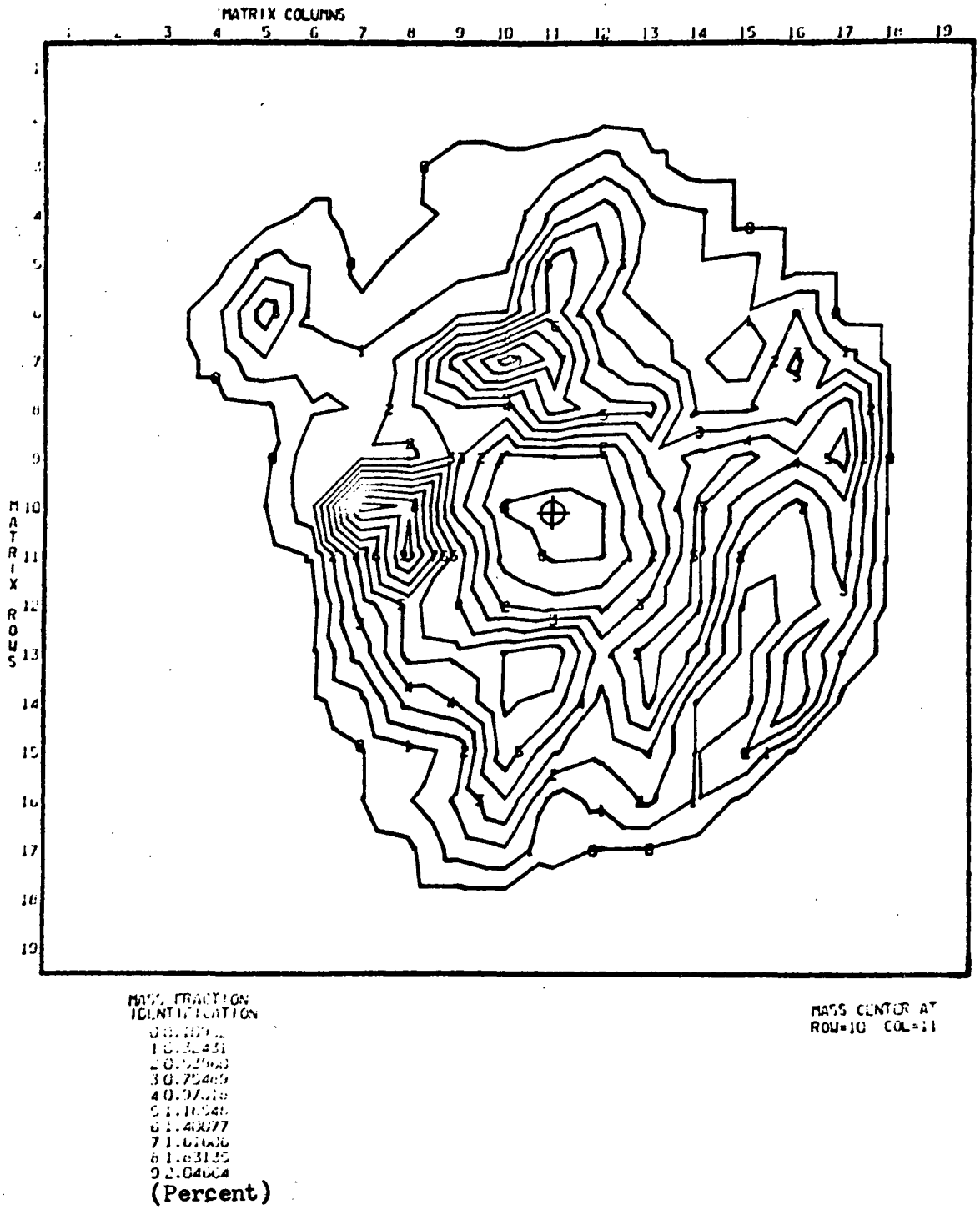

Figure 17. Core Mass Distribution

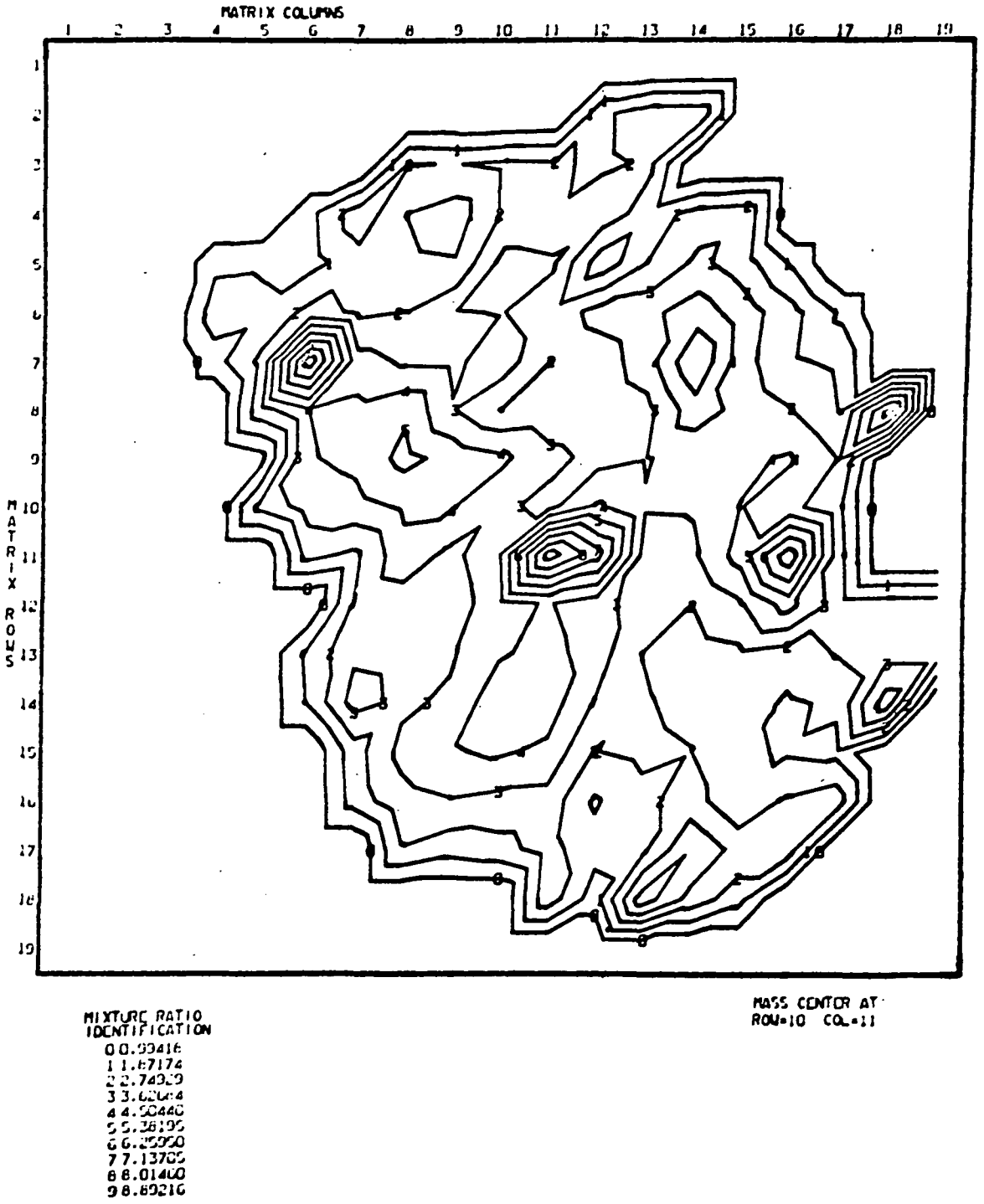

Figure 18. Core Mixture Ratio Distribution

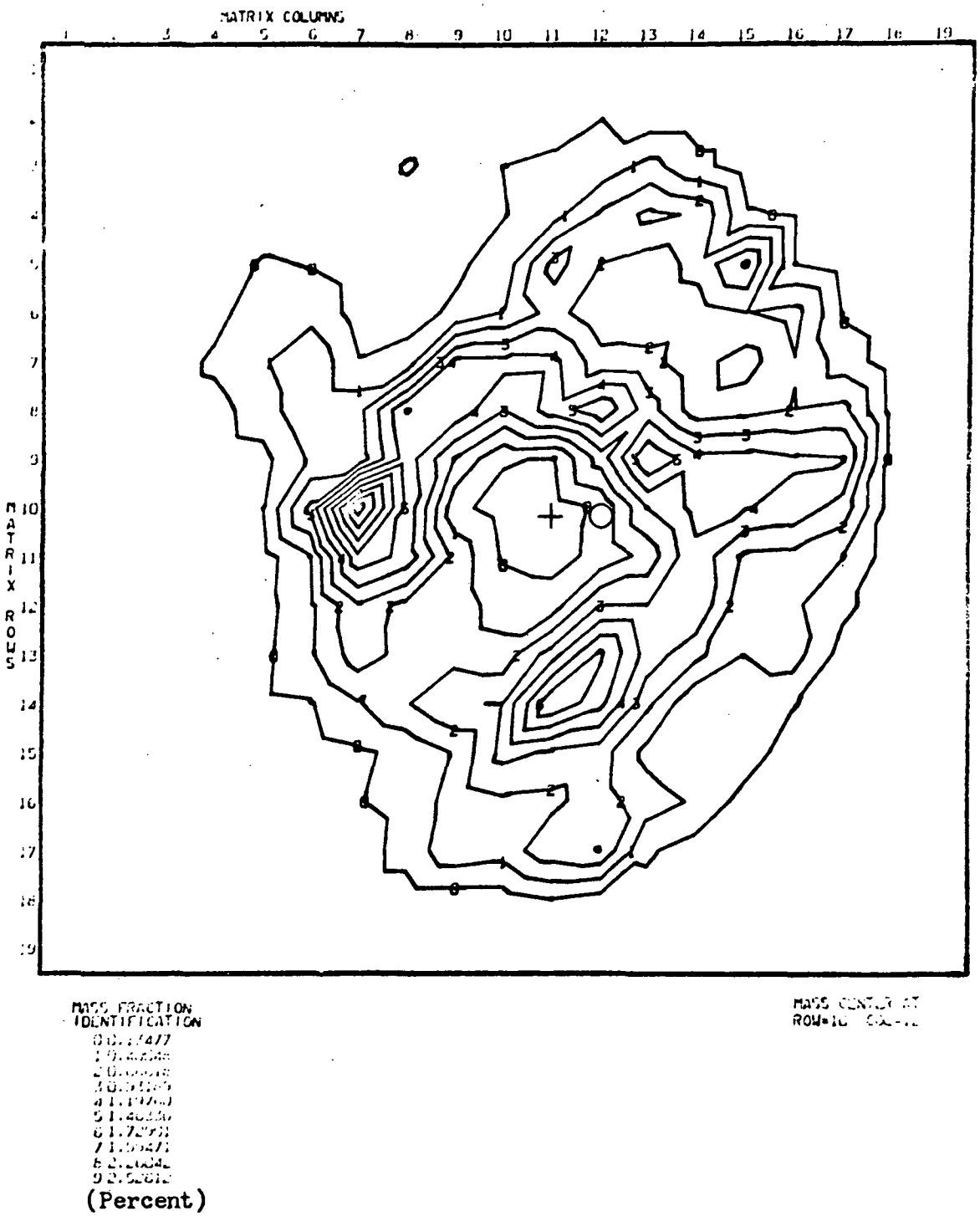

Figure 19. Core and BLC Mass Distribution

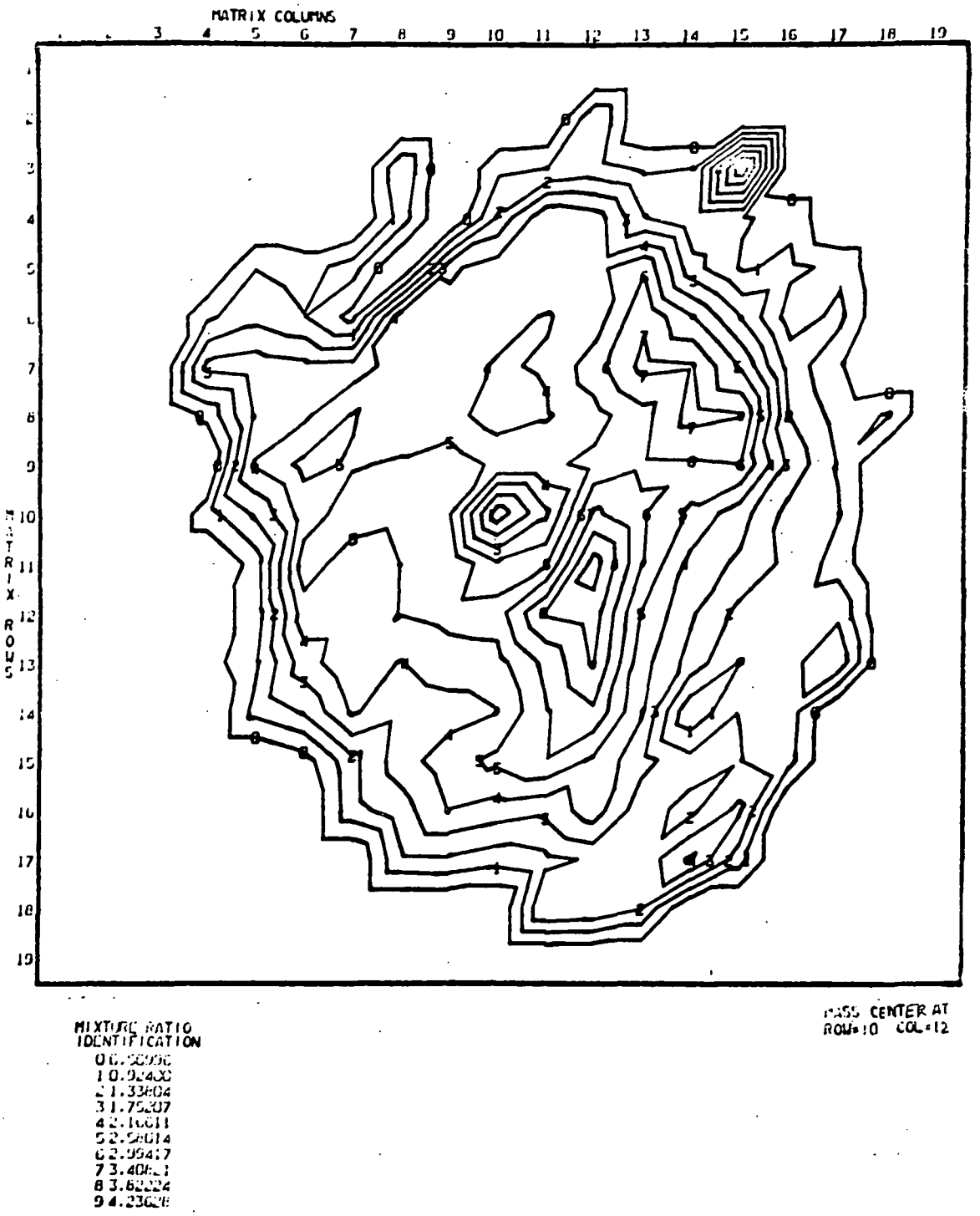

Figure 20. Core and BLC Mixture Ratio Distribution

In summary, the posttest injector cold flow analyses indicate that the Test 003 burnout was probably not attributable to oxidizer or fuel misimpingement or poor core mixture distributions. However, the analyses do indicate an uneven BLC flow distribution. For the overall 10-percent BLC condition, only an equivalent 6.4 percent BLC flowed in one of the 90-degree quadrants. This maldistribution might have contributed to thrust chamber failure, but a more likely failure explanation seems related to the previously discussed leak through the weldment crack. Such a leak would not only have diminished the overall BLC flow but also could have caused a portion of the chamber area to have been completely unprotected by BLC flow. Even though the observed BLC maldistribution may not have been enough to cause a chamber failure with 10 percent overall BLC flow, such a maldistribution could cause a failure when more marginal BLC flow rates are employed. Additionally, of course, an asymmetrical BLC flow creates difficulties in heat transfer analysis.

Performance Results

Precise performance data could not be obtained from Test 001 because of the fluctuations of oxidizer flow (indicated in Fig. 21). Similar oxidizer flow fluctuations, coupled with the chamber leak (Fig. 22), do not permit precise performance determinations for Test 002. As will be discussed subsequently, oxidizer feed system facility modifications were implemented to reduce and quickly stabilize oxidizer flow start transients.

Heat Transfer Results

The heat transfer results described below are based upon data obtained from two axial rows of thermocouples spaced 90 degrees apart around the outside chamber periphery (see Fig. 14). Ten thermocouples were placed in an axial row at locations of 0.5, 1, 2, 3, 4, 5, 6, 7, 8, and 9 inches from the injector face.

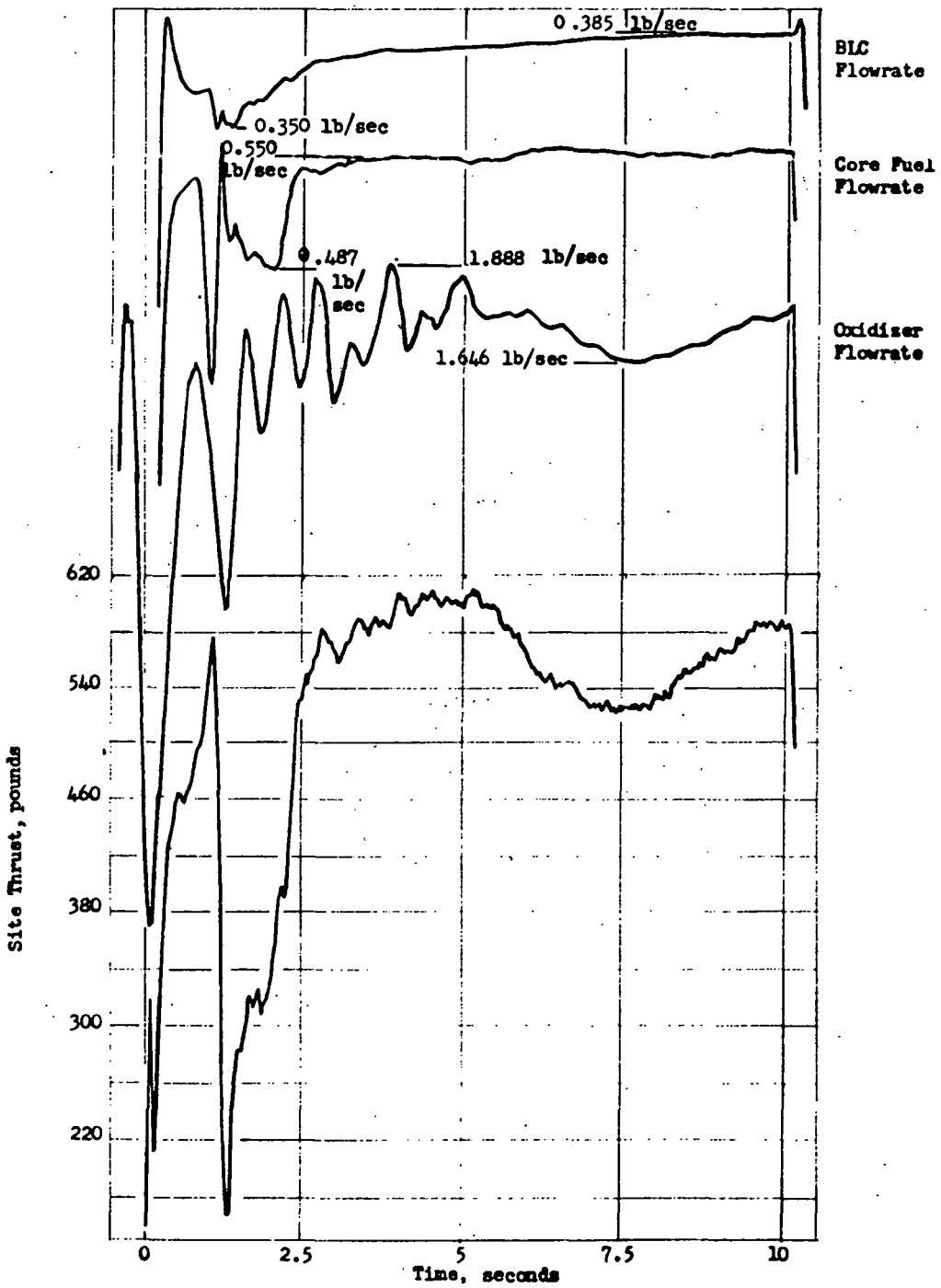

Figure 21. Thrust and Flowrates, Test 001
Core MR = 3.2 14% BLC

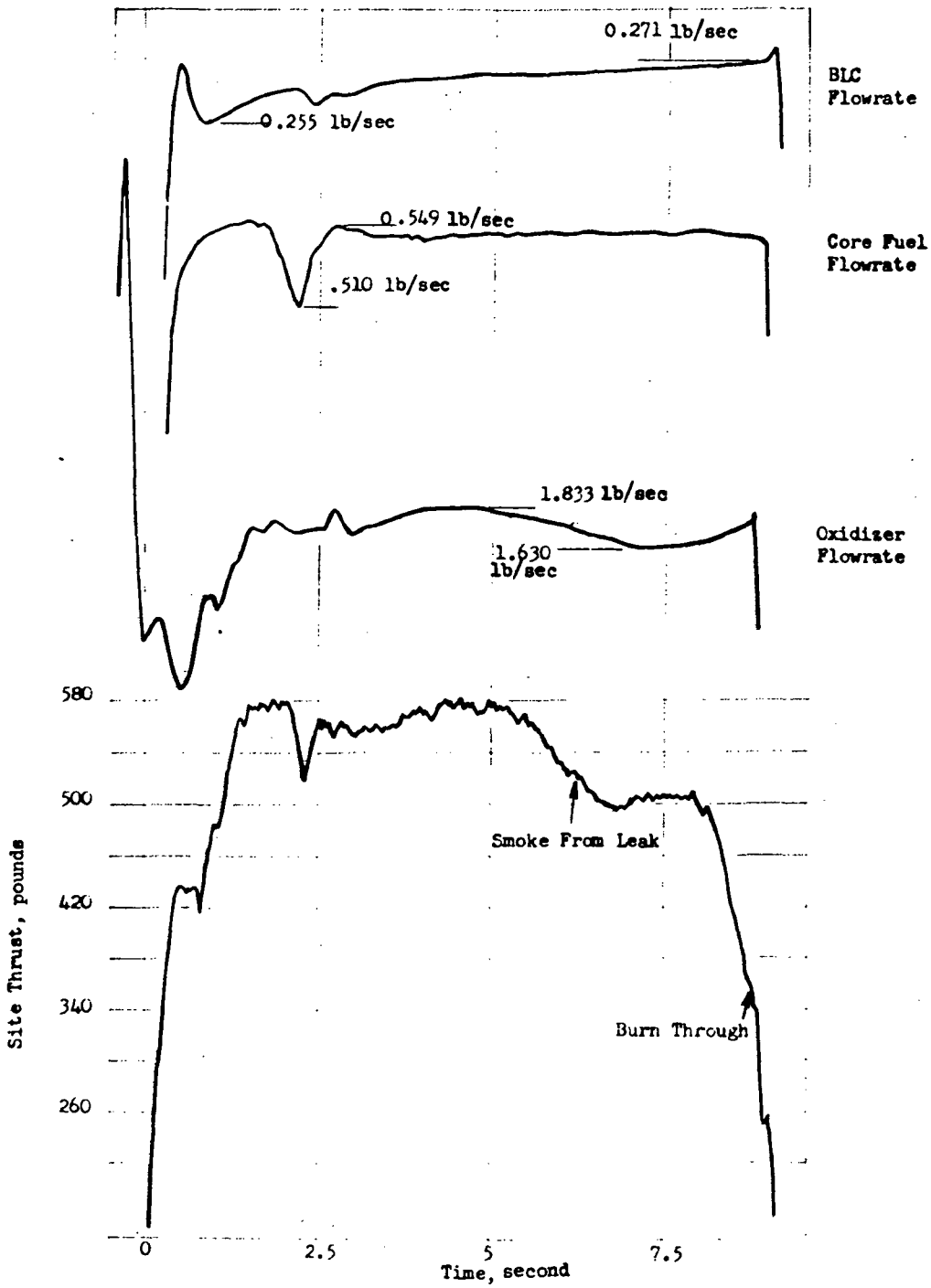

Figure 22. Thrust and Flowrates, Test 002
Core MR = 3.3 10% BLC

Pretest heat transfer predictions based upon the analytical DEAP model were adjusted to account for experimental measured: (1) coolant flowrate, (2) initial chamber wall temperature distribution, (3) coolant inlet temperature, and (4) combustion gas driving temperature. These DEAP model results for Tests 001 and 002 are shown in Fig. 23 and 24, along with experimentally measured chamber wall temperatures. The chamber combustion gas core driving temperature was assumed equal to $\eta_{c*}^2 T_{theo}$ where T_{theo} = 7190 F (mixture ratio = 3.24) and η_{c*} was estimated to be 0.892. A gas-to-vapor film mass entrainment factor, Le^*/c_{p_g}, of 11.8 (based on NAS7-304 posttest analysis) was again employed. It is immediately obvious that measured wall temperatures were considerably below those predicted*. Also, it can be seen from Fig. 23 and 24 that the measured wall temperatures at the two different circumferential locations indicate varying degrees of heat transfer asymmetry in the chamber. The minor asymmetry during Test 001 was caused by uneven BLC flow distribution as evidenced in posttest cold flow studies and discussed earlier in this report. The greater degree of heat transfer asymmetry in Test 002 was caused by a coupling effect of the previously discussed chamber leak and BLC flow asymmetry.

Analysis of the transient thermal data by means of the test data evaluation methods described earlier was complicated by the oxidizer flow fluctuations (Tests 001 and 002) and chamber leak (Test 002). In Test 001, for example, large oxidizer flowrate fluctuations (caused perhaps by gas bubbles in the line) resulted in a core mixture ratio versus time plot as shown in Fig. 25. The combustion gas temperatures corresponding to the various core mixture ratios are indicated also in Fig. 25. It is evident from this plot that relatively steady operating conditions were not achieved until at least 2.5 seconds into the run, and that at 5 seconds into the run a decrease in oxidizer flowrate resulted in a decrease in core mixture ratio to a minimum value at 7.5 seconds, followed by a gradual rise in both core mixture ratio and oxidizer flowrate until programmed test cutoff at 10 seconds. A core mixture ratio versus time

---

* It should be noted that direct comparison of the experimental points and the predicted curves is not entirely correct because of the relatively long start transients experienced during the hot firings. Zero time for the experimental data was assumed to be the time corresponding to the initial rise in thrust.

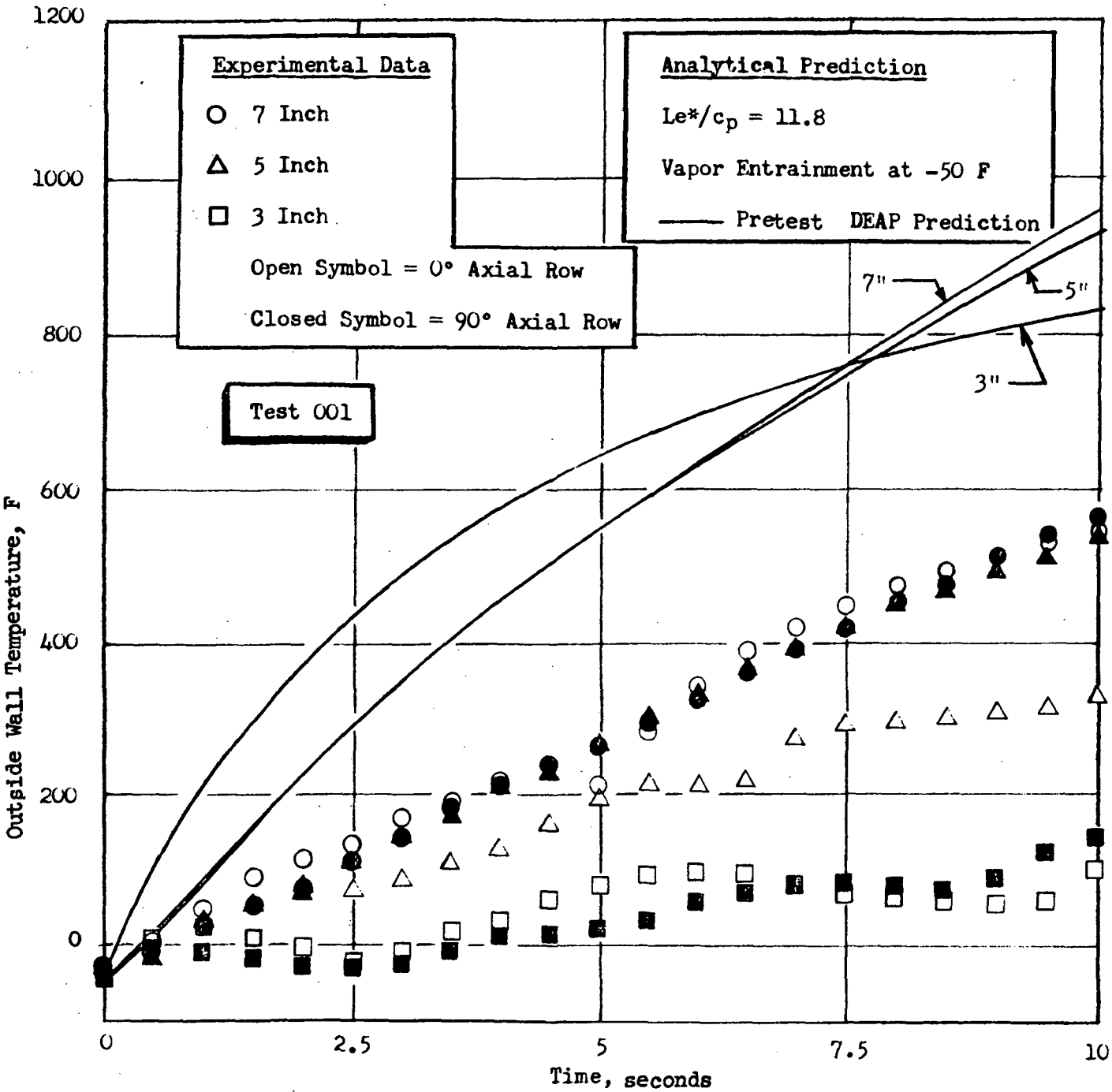

Figure 23. Comparison of Pretest Prediction with Experimental Results, Test 001

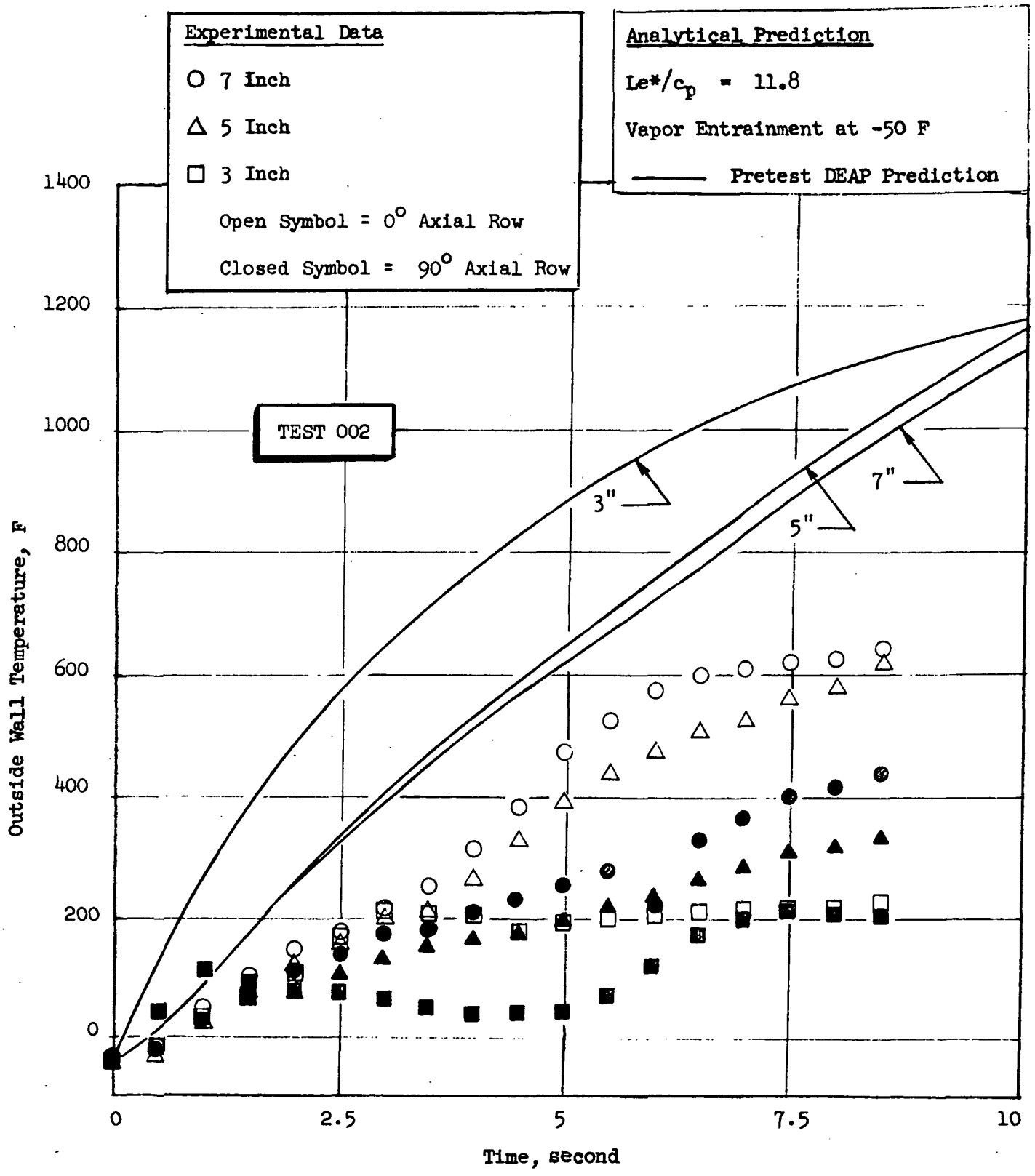

Figure 24. Comparison of Pretest Prediction with Experimental Results, Test 002

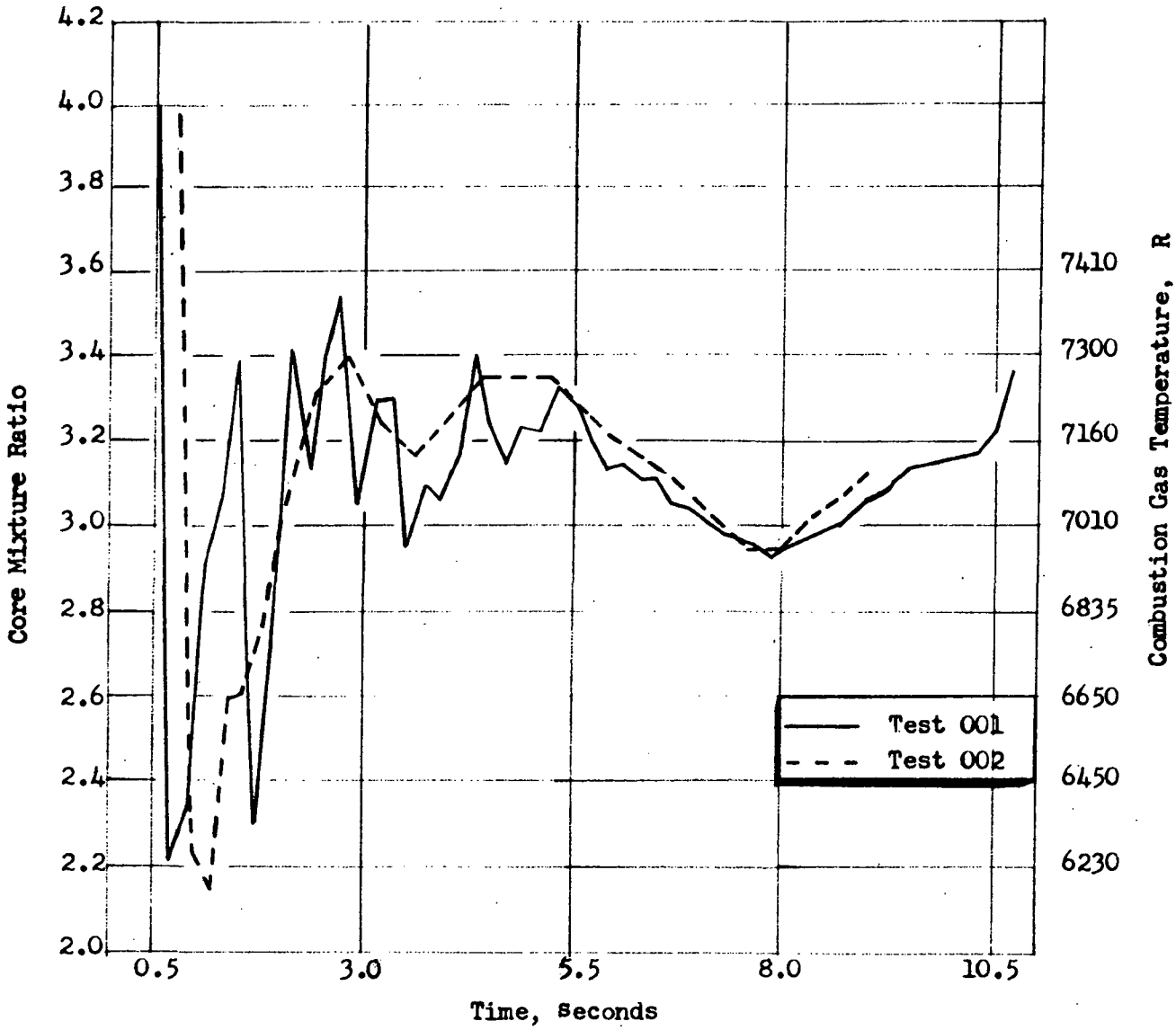

Figure 25. Core Mixture Ratio versus Time for Tests 001 and 002

plot for Test 002 (Fig. 25) showed less fluctuation. However, heat transfer data evaluation for this test was hampered by the chamber leak at approximately 6.5 seconds.

In addition to the fluctuation of operating variables, the much lower than predicted combustion-gas-to-wall heat transfer prevented the measured chamber wall temperatures in the downstream portion of the chamber from even remotely approaching their equilibrium values. This resulted in temperature versus time traces for these thermocouples which were nearly straight lines (for example, Fig. 26). Such a condition strains the application of the TEMP computer model which performs best when a pronounced curvature is present in the temperature versus time trace. Additionally most of the chamber thermocouples exhibited a temperature versus time trace which showed a flat portion near a temperature of 212 F (see Fig. 26)*. This was caused by the formation of frost at the thermocouple location and the subsequent liquefaction and boiling of the frost.

Even with all of the aforementioned problems, a fair amount of heat transfer data could still be extracted from the initial calorimeter firings.

A heat transfer discussion of Test 001 can most appropriately begin with reference to the data from thermocouples near the injector, 0.5-inch from the face, which act as sensitive indicators of the sequence of events (see, for example, Fig. 27). At a -0.4 second, oxidizer flow was initiated and proceeded to cool the chamber wall until BLC fuel injection occurred at zero seconds**. The film cooling flowrate was established (see Fig. 27) at 1.2 seconds, as evidenced by the rapid chilldown from that point in time to -71 F at 2.0 seconds. Wall temperature data at 2.0 seconds indicate that the liquid layer extended past

* As discussed later in this report, facility and hardware modifications were made to prevent the recurrence of frost formation as well as non-uniform propellant flow and/or fluctuating operating conditions.

** The time reference of zero seconds corresponds to the initial rise of measured thrust.

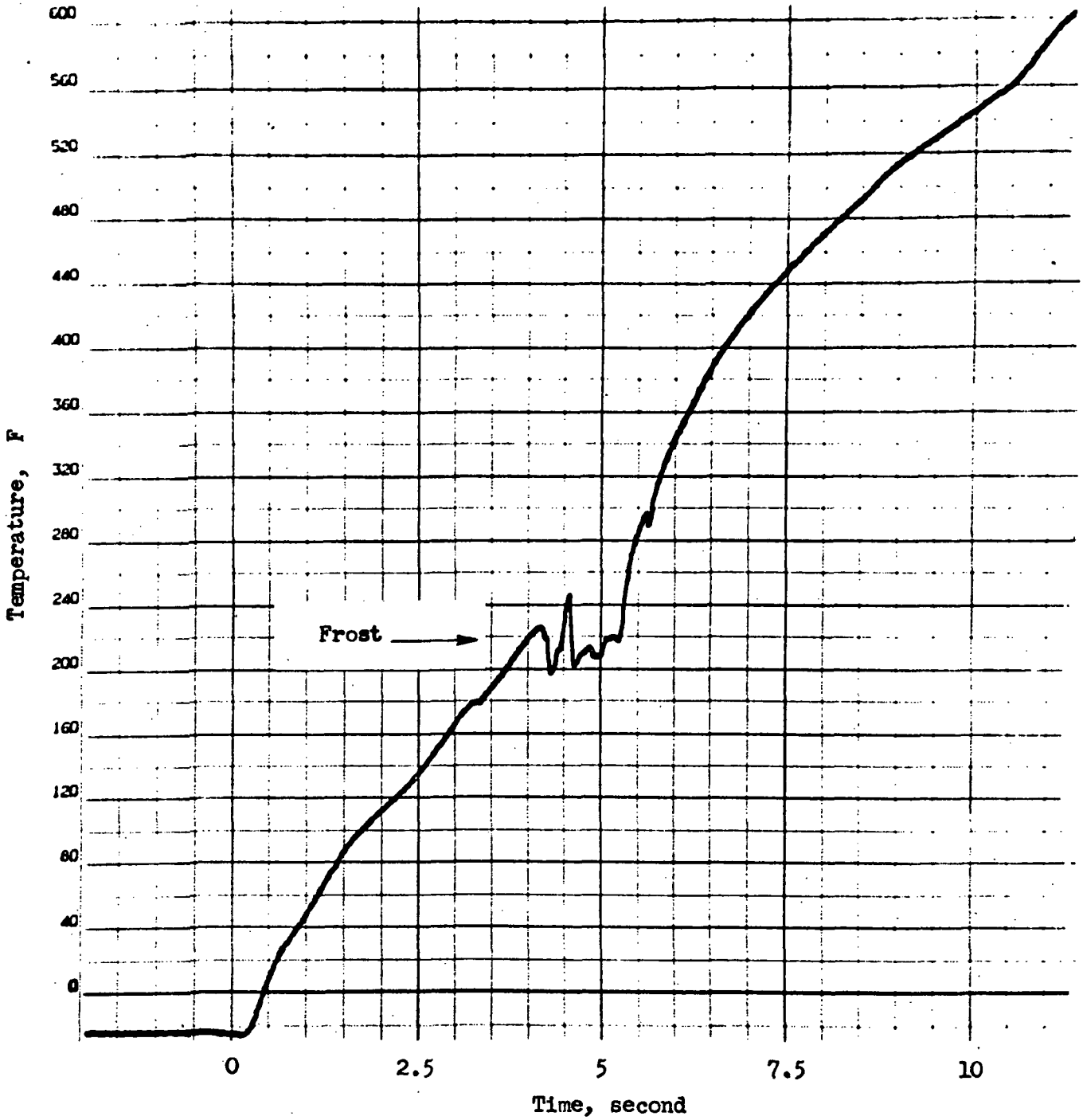

Figure 26. Thermocouple Trace at 7 inches from Injector, Test 001

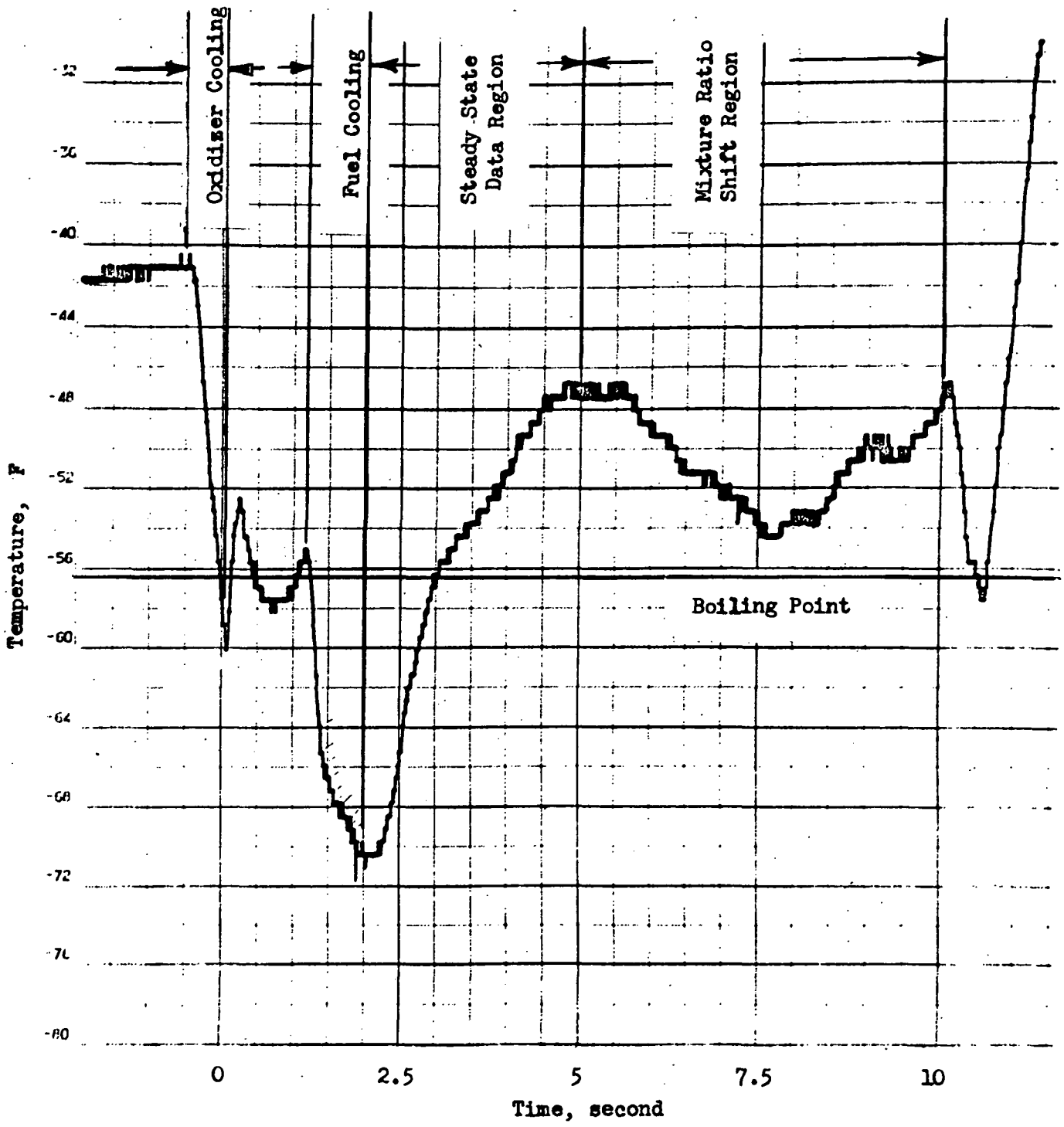

Figure 27. Thermocouple Trace from 0.5-Inch Location, Test 001

the one-half-inch location at that time. This was followed by a rapid recession of the liquid film back past the thermocouple as chamber pressure was established. A mixture ratio shift then occurred, starting at 5.4 seconds, which caused a slight drop in temperature from the peak value.

The data for Test 001 were analyzed using the TEMP program for two time periods: (1) the initial injection period (1 to 2 seconds), and (2) the full chamber pressure period before the mixture ratio shift occurred (2.5 to 5 seconds). For data locations past two inches, with a single exception, application of the TEMP program could not be made due to the difficulties discussed above. However, for those locations, good overall q/A data were obtained.

Table 4 shows the results of the vapor film heat transfer coefficient and recovery film temperature determinations over the first 2 inches of chamber length. Also shown are values for the order of magnitude higher liquid film coefficient. These values were obtained by analysis of the unsteady start transient. Finally, the results of determinations made for h_f and T_f at the 7-inch chamber location are given. The values obtained for the liquid film coefficient are in good agreement with the pretest assumed value of 0.03 Btu/in^2-sec-F. As will be discussed subsequently, the cold vapor film h_f is somewhat lower than originally estimated.

The nearly straight line temperature versus time relationship for the downstream thermocouples (see Fig. 26) permitted calculation of the heat flux to the chamber wall. These q/A values are presented in Table 5. They were obtained primarily during the 2.5- to 5.0-second time interval.

As previously observed from Fig. 23, the experimentally measured wall temperatures during Test 001 were significantly lower than the pretest predicted values. In the 0- to 2-inch chamber section, this was due to lower than estimated film temperatures since the measured film coefficients (h_f) were higher than estimated. In the 2- to 10-inch chamber section, the measured wall

TABLE 4. SUMMARY OF CALORIMETER FILM THERMAL DATA FOR TEST 001

Measurement Location, Distance from Injector Face, inches	Data Slice Time, seconds	h_f^*, Btu/in^2 sec F	T_f^*, F
0.5	1 - 2	0.037/0.022**	-64/-71
	2.5 - 5	0.0024/0.0040	-38/-46
1	2.5 - 5	0.0016/ND	-24/ND
2	2.5 - 5	0.0028/ND	-37/ND
7	2.5 - 5	0.0067/ND	1299/ND

* Results are shown for thermocouples in each of the two axial rows, separated by a slash.

** These values are for the liquid film. The lower values in the time slice 2.5 - 5 seconds are for a vapor film.

ND Not Determined.

TABLE 5. SUMMARY OF CALORIMETER HEAT FLUX DATA FOR TEST 001

Measurement Location, Distance from Injector Face, inches	q/A* Btu/in^{2}sec
1	0.049/0.039
2	0.054/0.079
3	0.09/0.17
4	0.21/0.61
5	0.49/0.78
6	0.76/0.78
7	0.70/0.71
8	0.62/0.59
9	0.50/0.49

* Results are shown for thermocouples in each of the two axial rows, separated by a slash.

temperatures were also lower than predicted. That is also consistent with lower than estimated film temperatures*. Lower than estimated film temperatures could be due to a number of factors, such as lower core driving temperatures or lesser amounts of entrainment (lower Le*).

The effect of varying combustion gas driving temperature between limits felt to be representative of uncertainty in the exact value was investigated. Varying the driving temperature from 5890 F to 4650 F decreased predicted chamber temperatures by only about 100 F. Such a change in predicted chamber temperature was not sufficient to significantly improve the agreement between experimental and predicted results. Therefore, an attempt was next made to vary the combustion gas entrainment in the vapor film. It was found that by varying the entrainment factor, Le^*/c_{p_g}, from 11.8 to 5.0, the experimental nozzle temperatures could be nearly matched. However, the predicted temperatures in the plenum region of the chamber were still significantly higher than the experimental values. The effect of decreasing the entrainment factor was to shift all the predicted wall temperatures downward by approximately equal percentages.

Making the assumption that no entrainment occurred until part way into the convergent section of the chamber** (an axial position of 4.1 inches, which corresponds to a vapor film temperature of 265 F), at which point Le^*/c_{p_g} was maintained at a constant value of 11.8, another DEAP prediction was made. The good agreement between the results of this analytical prediction and the experimental data is shown in Fig. 28***. Partial justification for such an assumption was from monomethylhydrazine film cooling experience where indeed very low entrainment rates between film and core are observed up to the start of chamber convergence.

---

* Although this is also consistent with lower than estimated h_f, the slightly lower than estimated h_f values, such as measured at 7 inches, could not account for the magnitude of the effect noted.

** Previous DEAP runs assumed a constant entrainment factor of 11.8 and gas entrainment in the vapor film beginning when the vapor film reaches -50 F (0.83 inch from the injector face).

*** Incorporated into the posttest analytical prediction shown in Fig. 28 is the experimental chamber pressure variation with time as reflected by the measured thrust shown in Fig. 21.

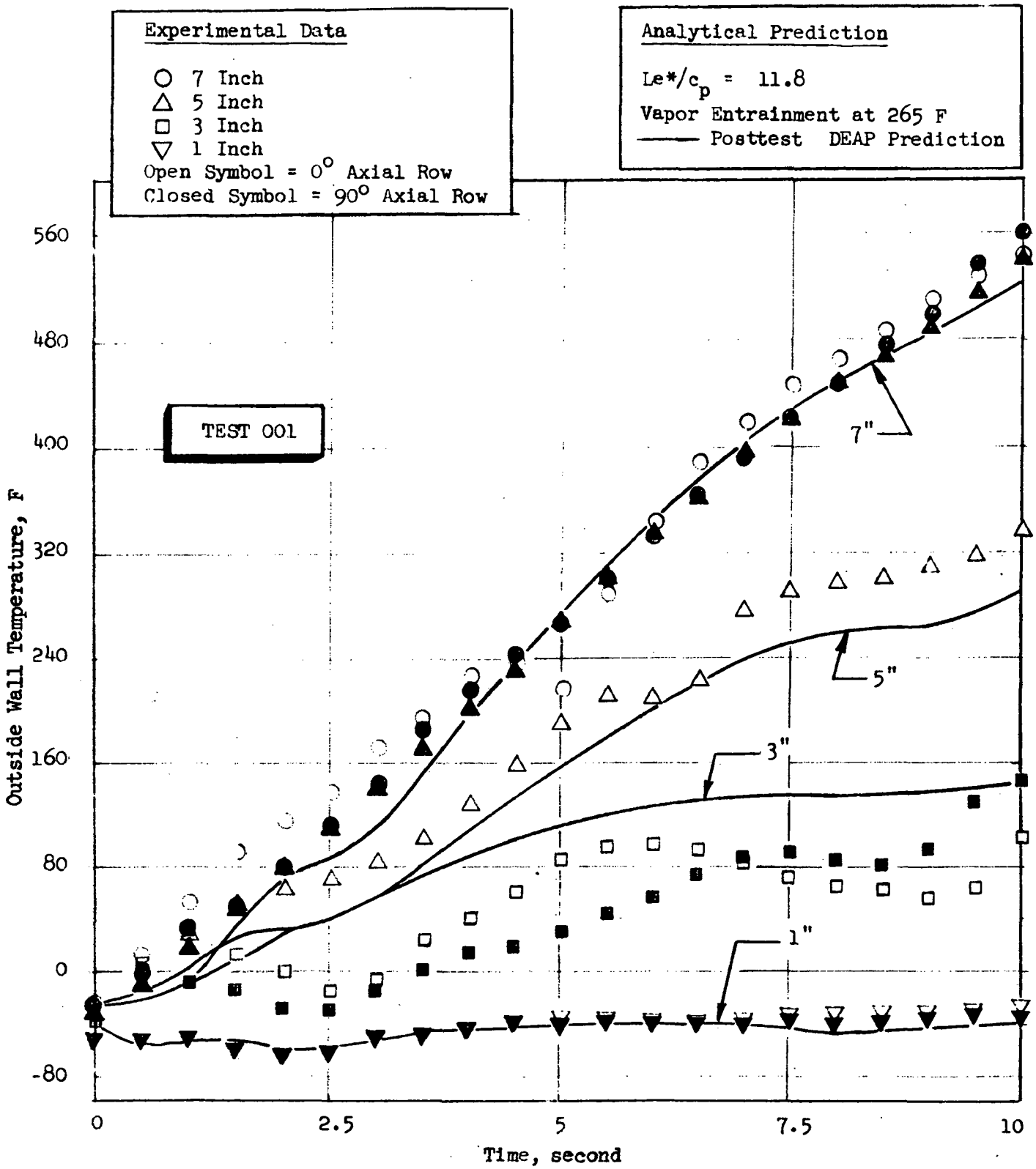

Figure 28. Posttest Prediction of Test 001

In achieving the data match shown in Fig. 28, it should be emphasized that Le^*/c_{p_g} was arbitrarily held constant at 11.8 from the chamber convergent section downstream. Normally, the FILM computer program would be used in conjunction with the recovery film temperature versus axial position values obtained from the TEMP computer program to predict the mass entrainment as a function of axial position. The inability to obtain a complete set of TEMP program predictions from Test 001 for T_{film} versus distance, however, precluded the prediction of Le^*/c_{p_g} versus distance using the FILM program.

The posttest analysis using the DEAP model (see Fig. 28) resulted in heat transfer coefficients, recovery film temperatures, and q/A as a function of axial position as shown in Table 6. The calculated q/A from Table 6 is compared with the Test 001 experimental values in Fig. 29. Also shown in Fig. 29 is the calculated q/A obtained from the DEAP pretest prediction. Good agreement between the experimental results and the posttest prediction is apparent in Fig. 29. It is also apparent that the heat flux to the chamber wall is markedly less than originally predicted.

For the DEAP model calculations, previous h_f correlations were employed. Comparison of Table 4 with Table 6 indicates that in the cool vapor film region a higher h_f is obtained experimentally than that employed in the DEAP model. The overall comparison between the experimental h_f and T_f values (Table 4) and the DEAP prediction values (Table 6) is reasonable, however, in light of the uncertainty in the reduction of the experimental data. The accurate attainment of experimental film coefficients in the remaining calorimeter tests was emphasized to determine whether the h_f correlation in the DEAP model should be changed from that used.

Only a very limited reduction of the data obtained during Test 002 was made. Heat flux was determined at various axial locations for the two rows of thermocouples in Test 002 and these results are presented in Table 7. As the experimental points of Fig. 24 also indicated, the data of Test 002 are quite asymmetric. This, as previously indicated, was due to a coupling effect of BLC flow asymmetry and the chamber leak.

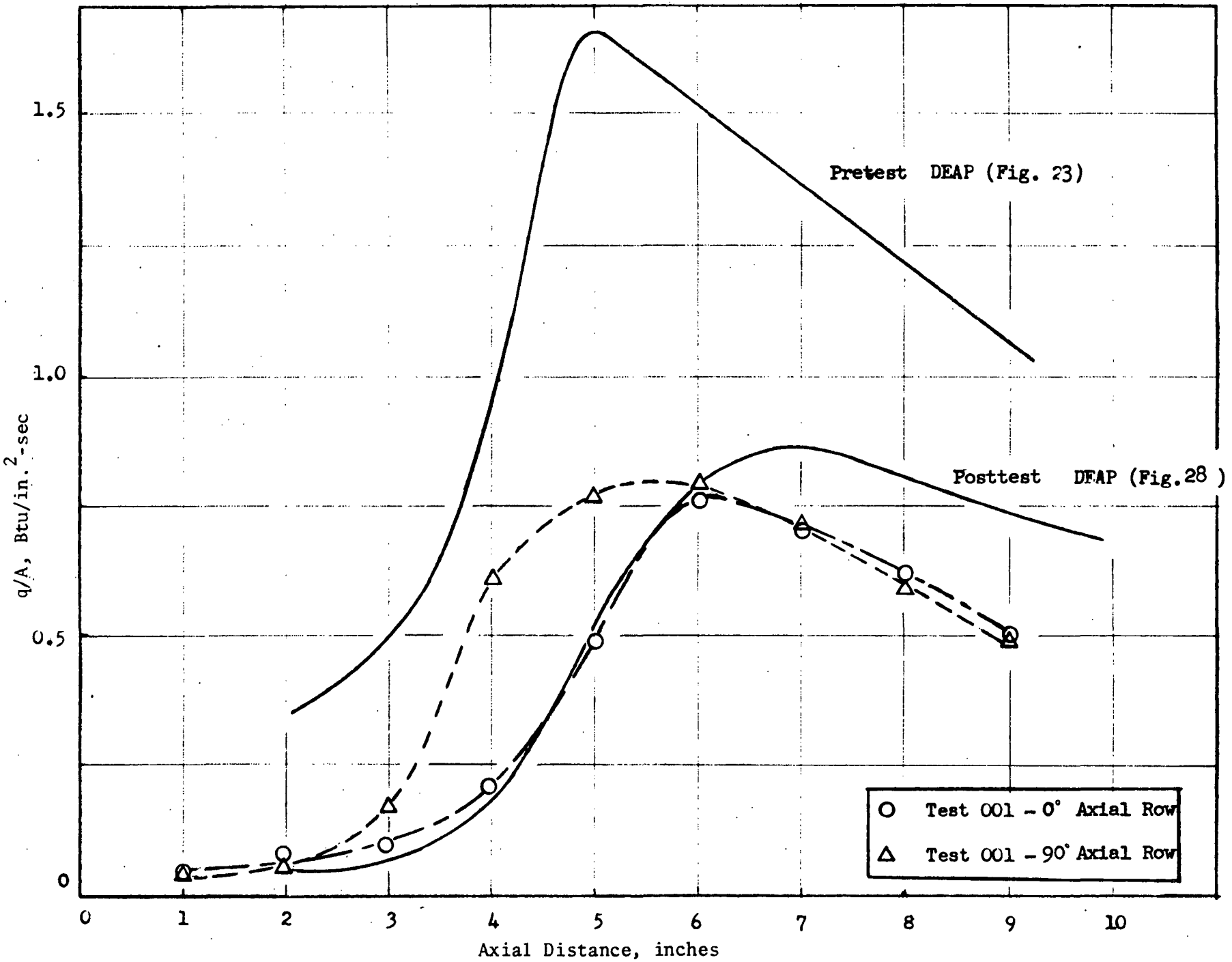

Figure 29. Heat Flux versus Axial Position, Test 001

TABLE 6. TEST 001 POSTTEST PREDICTION USING DEAP MODEL

Distance From Injector Face, inches	h_{vf} Btu/in^2 sec F	T_f, F	q/A Btu/in^2 sec
2	0.00129	86	0.050
3	0.00128	168	0.068
4	0.00163	248	0.177
5	0.00124	705	0.508
6	0.00137	968	0.798
7	0.00105	1168	0.885
8	0.00830	1328	0.755
9	0.00077	1441	0.761
10	0.00066	1492	0.691

TABLE 7. SUMMARY OF CALORIMETER THERMAL DATA FOR TEST 002

Measurement Location Distance From Injector Face, inches	q/A* Btu/in^2 sec
4	1.26/ND
5	1.06/0.50
6	0.94/0.52
7	0.88/0.58
8	0.92/0.62
9	0.77/0.60

* Results are shown for thermocouples in each of the two axial rows, separated by a slash

ND Not Determined

It is concluded from the heat transfer analysis of Test 001 that the relatively low chamber wall temperatures observed were the result of relatively low entrainment rates of combustion gas in the vapor film upstream of the chamber convergent section. Thus there is a strong indication that vapor film cooling is substantially more effective than was originally predicted.

HARDWARE MODIFICATIONS SUBSEQUENT TO TEST 002

Nickel Calorimeter Chamber

The leak that occurred at the flange-chamber wall weldment in Test 002 was postulated as a possible mechanism which caused the burnthrough of the chamber wall in Test 002. Two design modifications were, therefore, incorporated into the design and fabrication of a new calorimeter chamber, as illustrated in Fig. 30. The first change involved relocating the flange-chamber wall weldment as shown in the figure. This also provided a thicker joint at the weldment (0.25-inch vs 0.10-inch). The second change involved the use of nickel 270 for the flange rather than the 321 CRES used in the previous design. Since the calorimeter chamber is also fabricated of nickel 270, the quality of the weld was significantly enhanced.

Injector

The results of the posttest cold flows showed some lack of uniformity of the swirl film coolant on the chamber wall. The coolant ring in the like doublet injector was subsequently removed and replaced by a slightly modified ring. The modifications to the ring were relatively minor and are illustrated in Fig. 31. The wall through which the 16 BLC holes are drilled (i.e., the outer wall of the ring) was increased from 0.030 to 0.045 inch thickness. This was done to produce a longer coolant orifice length and should have the effect of minimizing flow variations from hole to hole in the coolant ring. The second change involved the placement of the BLC orifices closer to the head end of the cavity. This was done to force the coolant to flow a longer path before exiting the lip of the ring. Recent experience at Rocketdyne has shown that this enhances the circumferential distribution of coolant.

Chamber Jacket

To preclude frost formation at or near the thermocouple locations and thus provide a smoother temperature vs time trace for data analysis, the remainder of the calorimeter tests employed a transparent plastic tube placed over the nickel thrust

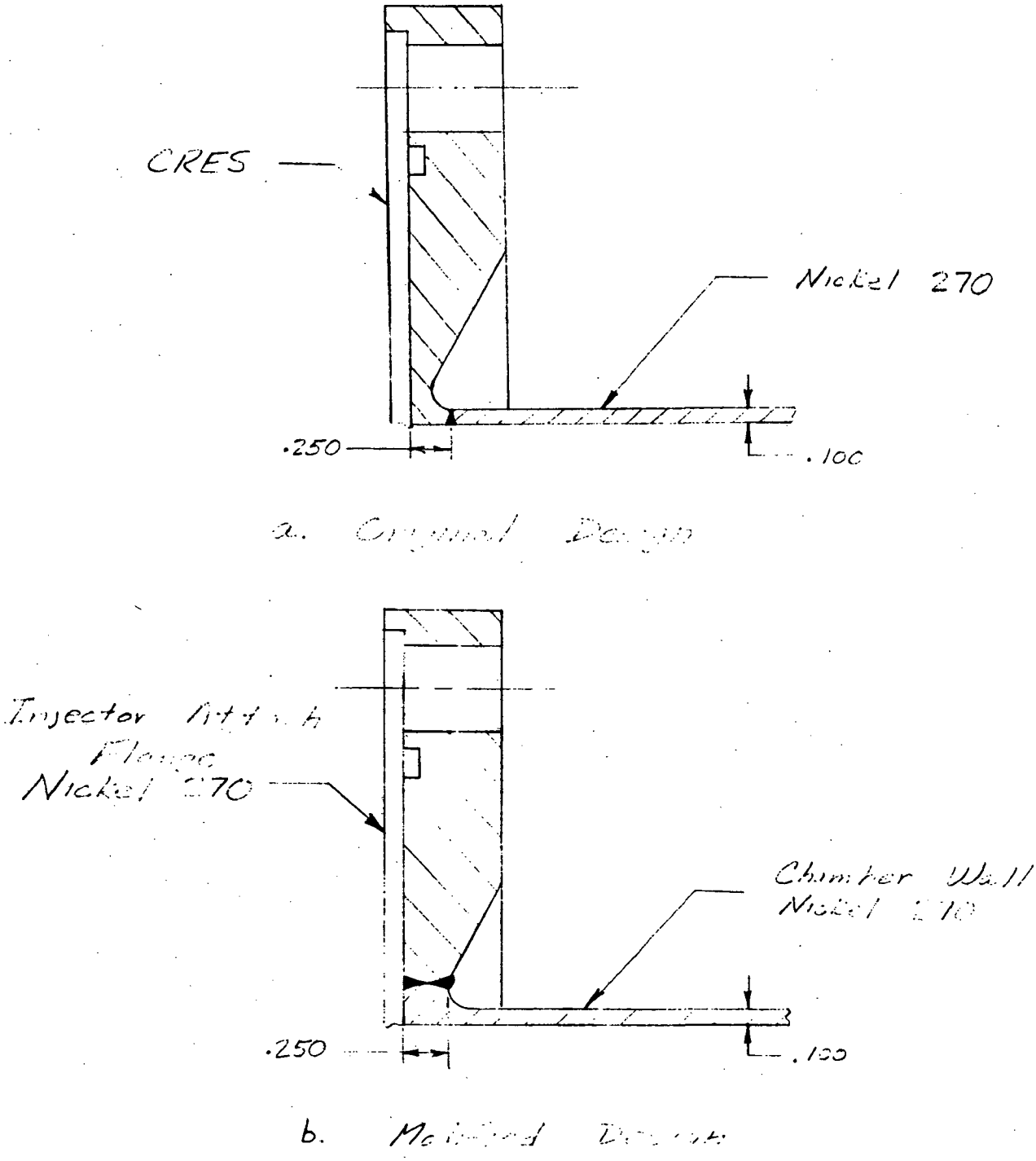

Figure 30. Nickel Thrust Chamber Modification

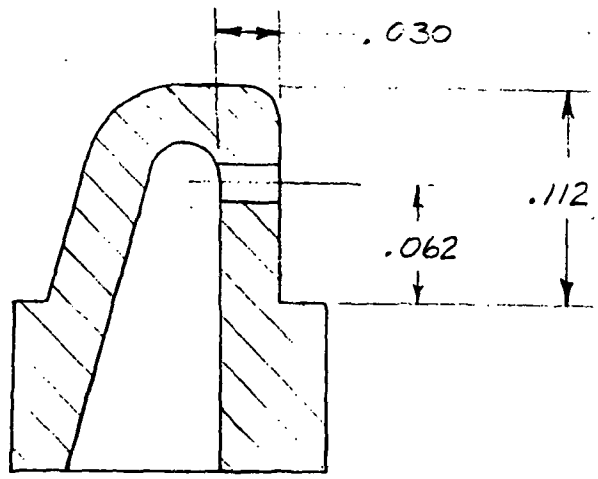

a. Original Design

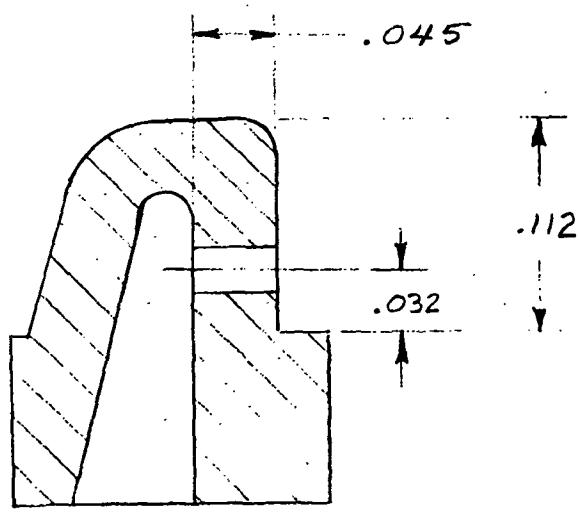

b. Modified Design

Figure 31. Injector BLC Ring Modification

chamber. The annulus between the outer chamber wall and the plastic tube was continually purged with dry GN_2 (-75 degree dew point). The purge gas velocity was maintained at a low level for minimum convective heat transfer. Pretest chamber wall temperatures for the first two tests were in the range of -20 F to -40 F; therefore, the dry GN_2 atmosphere surrounding the chamber can effectively prevent frost formation.

FACILITY MODIFICATIONS SUBSEQUENT TO TEST 002

Two significant difficulties related to the attainment of steady state data were encountered in the initial hot firings. The first involved the plugging of the chamber pressure port on the injector face, which results in a highly erratic pressure measurement. (This was also encountered in previous programs where the pressure ports were located on the chamber wall.) To eliminate plugging, a GN_2 purge was introduced in the line connecting the port and the pressure transducer. Cycling the purge valve during a test expels any deposits and permits an intermittent measurement of chamber pressure.

The second problem area involved unsteady oxidizer flow. This problem was traced to some design shortcomings of the 300-gallon dipleg FLOX tank. The basic problem related to inadequate thermal control of the FLOX as it leaves the unjacketed dipleg. Although restricting orifices were not incorporated into the FLOX feed line, it is not likely that the relatively low tank pressure (~200 psig) contributed to the unsteady flow (low tank pressure was used to minimize the amount of helium pressurant required).

The oxidizer system was modified with the goal of attaining steady flow within a maximum of two seconds after valve opening. Changes included the use of a 43-gallon run tank, restricting orifices and associated higher tank pressures, and the installation of a bleed system between the 300-gallon storage tank and a point just upstream of the main oxidizer valve. Prior to a hot firing test, oxidizer flow is initiated from the run tank to the storage tank. Upon attainment of steady flow (determined by monitoring the temperature and volumetric flowrate recorders) the bleed valve is closed and the main valve opened to initiate the test. These last two functions can be controlled by an electronic sequencer so that the flow through the system is not interrupted.

CALORIMETER HOT FIRINGS (TESTS 003-004)

Following completion of the hardware and facility modifications, two nickel calorimeter firings were made (Test 003 and 004) using a new 5-inch-long (injector-to-throat) chamber identical in geometry to the one employed in Tests 001 and 002.

Tests 003 and 004 were made using Test 002 operating conditions (core mixture ratio of 3.2 and 10 percent boundary layer coolant). A total of 26 thermocouples was placed in four axial rows, 90 degrees apart, to monitor the outside chamber wall temperature. Eleven of these thermocouples were placed on comparator circuits to provide automatic test termination if the measured temperature exceeded a preset value.

Test 003 (101.8 psia* chamber pressure, core mixture ratio of 3.11, and 11.0 percent boundary layer coolant) was terminated after about 8 seconds due to a thermocouple comparator circuit cut when an upstream (3-in.) thermocouple reached a temperature in excess of 600 F. (Thermocouples positioned downstream of 3 inches were set for comparator circuit cut at 1200 F.) Upon completion of Test 003, the hardware was inspected visually on the stand prior to Test 004. This visual inspection revealed no chamber wall discoloration and only a small amount of deposition on the injector face and chamber wall; there were no other irregularities.

Test 004 (103.8 psia chamber pressure, core mixture ratio of 3.18, and 10.7 boundary layer coolant) was then made immediately following the Test 003 posttest inspection. The thermocouple comparator circuit cut temperature was increased to 1000 F for the thermocouples located zero to 3 inches downstream from the injector face and to 1400 F for thermocouples downstream of 3 inches. Test 004 ran for the programmed duration of 10 seconds with no apparent problems. However, posttest examination of the chamber revealed some internal gouging in the nozzle expansion section near the throat as well as chamber wall discoloration in the vicinity of the burnthrough area on Test 002. With the exception of the approximately 90-degree circumferential quadrant where gouging and discoloration occurred, the chamber had an untarnished appearance.

Combustion Product Deposition

Posttest observation showed only moderate deposition on both the injector face and inside chamber wall, similar to that observed upon completion of the first test series.

Samples of both the injector face and chamber wall deposits have been analyzed and found to consist of boric acid (H_3BO_3) and amorphous elemental boron in approximately a 50/50 weight ratio. A trace (0.1-percent) of elemental fluorine was also noted. The boric acid was, most probably, the result of the hydrolysis of the combustion product boron oxide upon exposure to the atmosphere, according to the equation

$$B_2O_3 + 3H_2O \longrightarrow 2H_3BO_3 \tag{9}$$

Cold Flows

Prior to Test 003, the swirl film coolant ring was replaced with a slightly modified configuration. This was done since the cold flow of the previous ring after Test 002 had revealed some nonuniformity of coolant mass distribution around the circumference of the chamber wall.

A mass distribution water flow was performed with the new ring. The resultant distribution, shown in Fig. 32, is significantly more uniform than that determined previously with the original boundary layer coolant ring, with the lowest of four quadrants containing 22 percent of the total collected mass. This compares to the minimum of 16 percent in one quadrant with the previous ring.

After Test 004, the injector was cold flowed to determine if any areas of high mass and mixture ratio could be noted in the region of chamber overheating. The flow was made with trichloroethylene and water, simulating a hot fire core mixture ratio of 3.1, and a film coolant flow of 11 percent. The results shown in Fig. 33 and 34 show no obvious discrepancies in either mass or mixture ratio distribution. The only areas of high mixture ratio near the wall correspond to regions of low

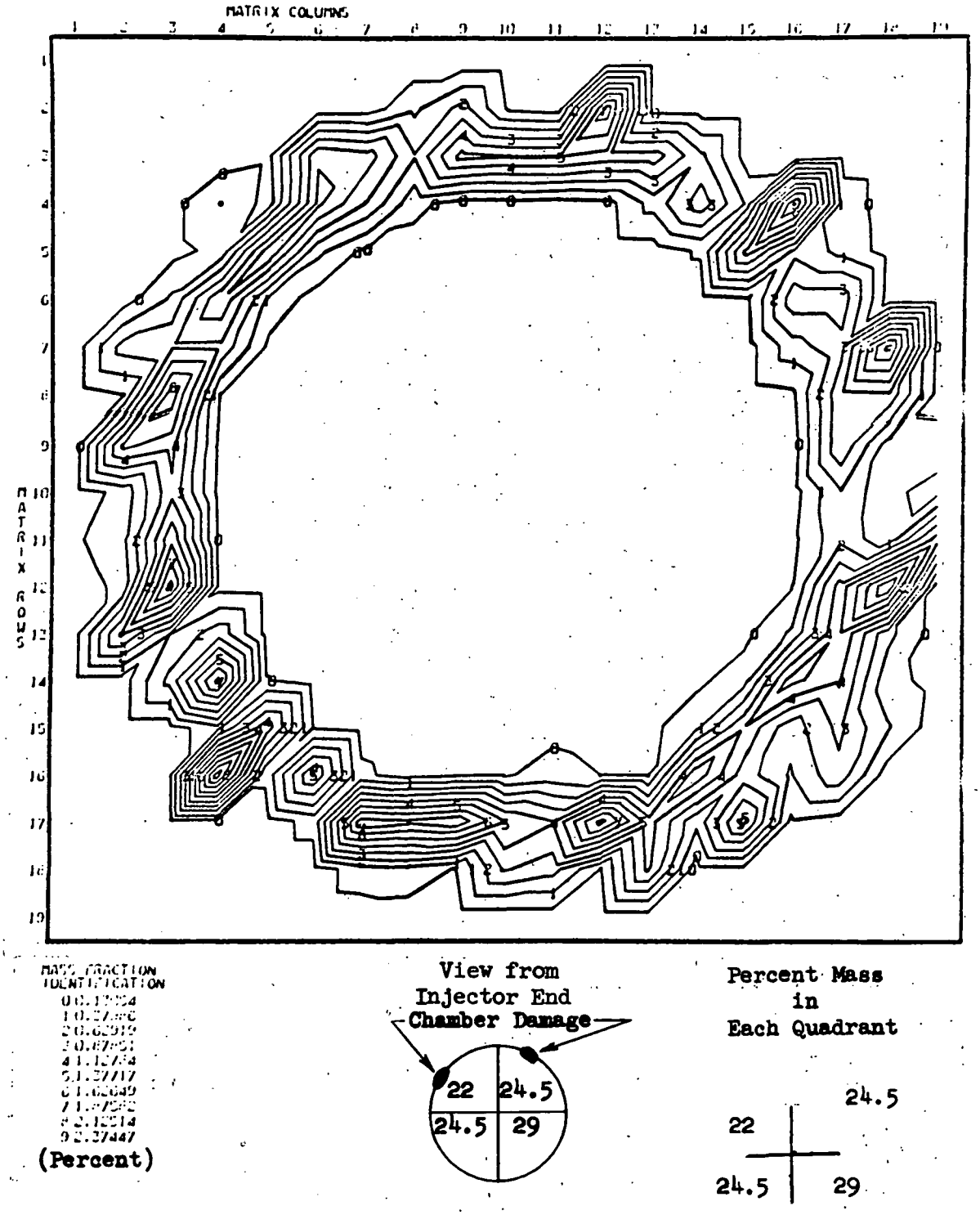

Figure 32. BLC Ring Mass Distribution, Pretest Test 003

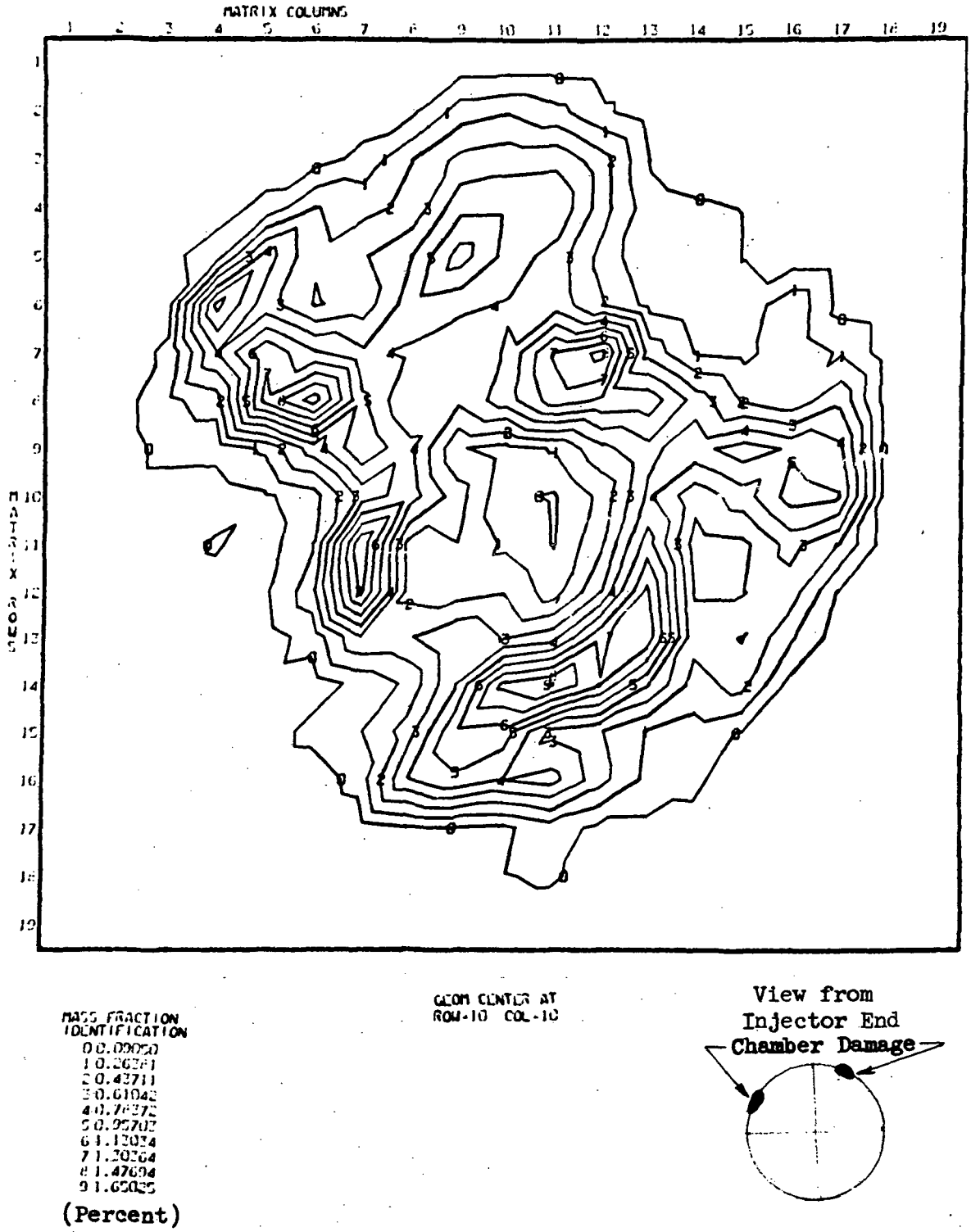

Figure 33. Core and Mass BLC Distribution
Pretest Test 003

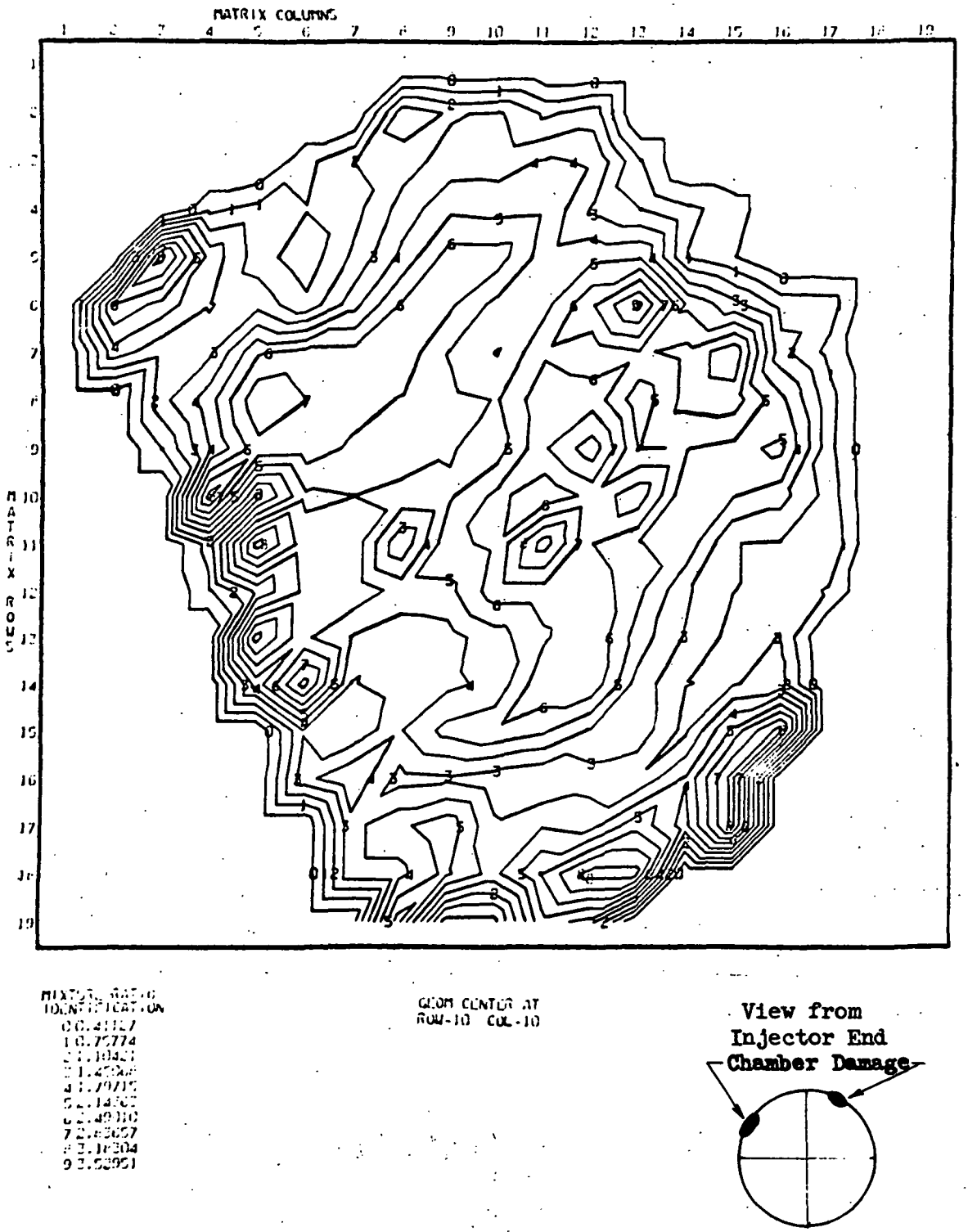

Figure 34. Core and BLC Mixture Ratio Distribution
Pretest Test 003

mass flux, as was the case in the pretest flows. Additionally, there seems to be no correspondence of the cold low mass and mixture ratio distribution anomalies with the areas of chamber overheating experienced in Test 004.

Of course, flow inhomogeneities which could occur during a run as a result of doublet fan disturbances caused by intermittent orifice plugging or face deposition would not be in evidence during the cold flow.

Performance Results

The experimentally measured propellant flowrates for the two tests are shown in Fig. 35 and 36, along with the measured thrust. The thrust chamber performance for Tests 003 and 004 is summarized in Table 8. The average calculated c* efficiency of 88.0 percent obtained in Tests 003 and 004 (conducted under almost identical operating conditions) is 1 percent lower than the value of 89 percent obtained with 11 percent boundary layer coolant in a previous program with the same injector. The average I_{sp} efficiency for Tests 003 and 004 was 89.6 percent.

Heat Transfer Results

The heat transfer results described below are based on data obtained from four axial rows of thermocouples spaced at 90-degree intervals around the outside chamber periphery (see sketch below). The zero-degree and 180-degree rows contained 8 thermocouples each at locations of 0.5, 1, 2, 3, 4, 5, 7 and 9 inches from the injector face. The 90-degree and 270-degree rows contained 5 thermocouples each at 1-, 3-, 5-, 7- and 9-inch positions.

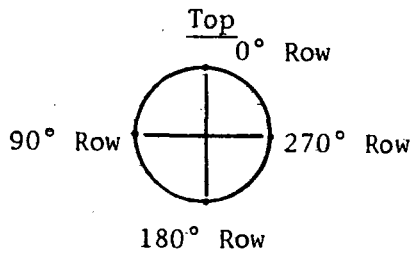

View From Nozzle End

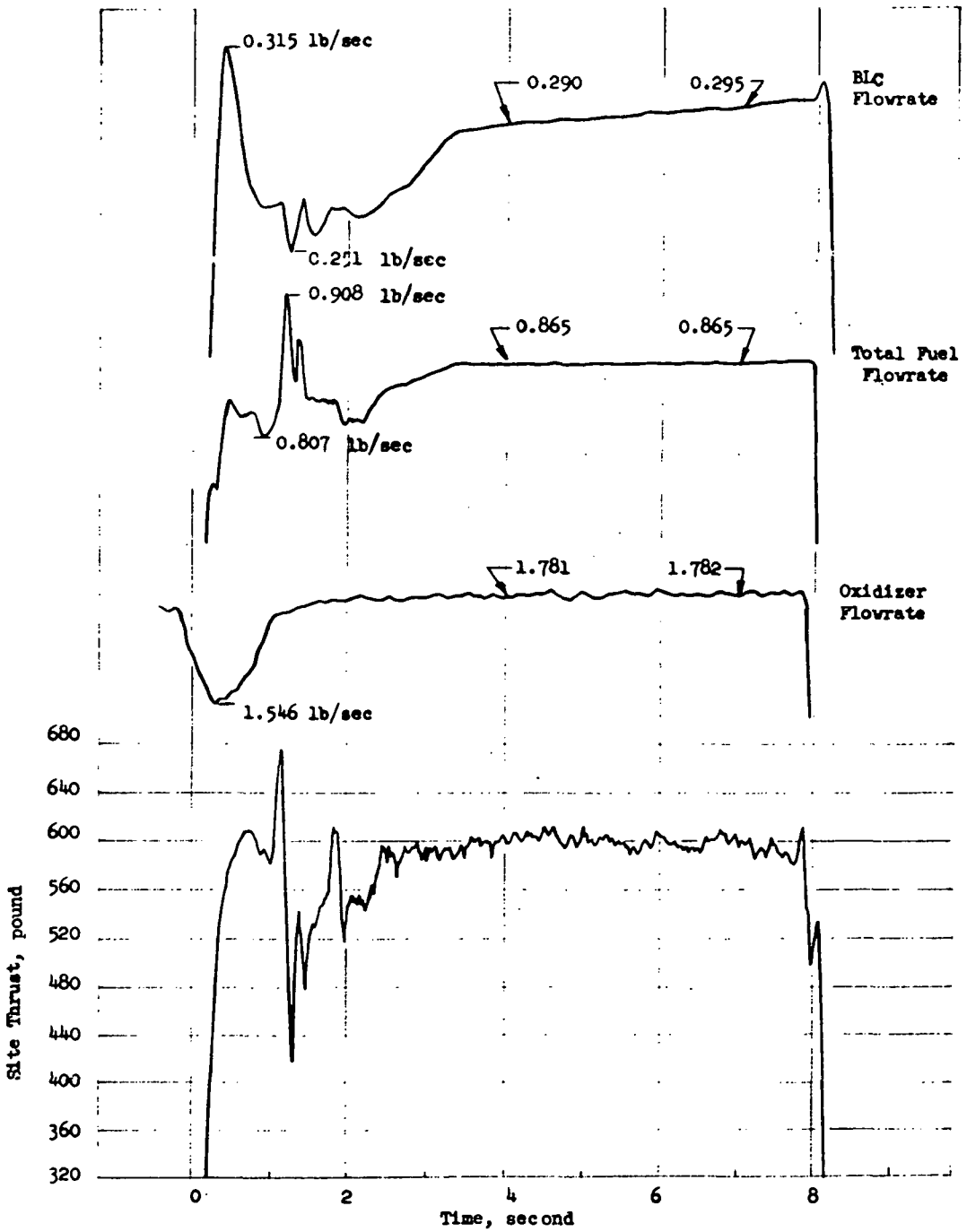

Figure 35. Thrust and Flowrates, Test 003
Core MR = 3.11 11.0% BLC

Figure 35. Thrust and Flowrates, Test 003
Core MR = 3.11 11.0% BLC

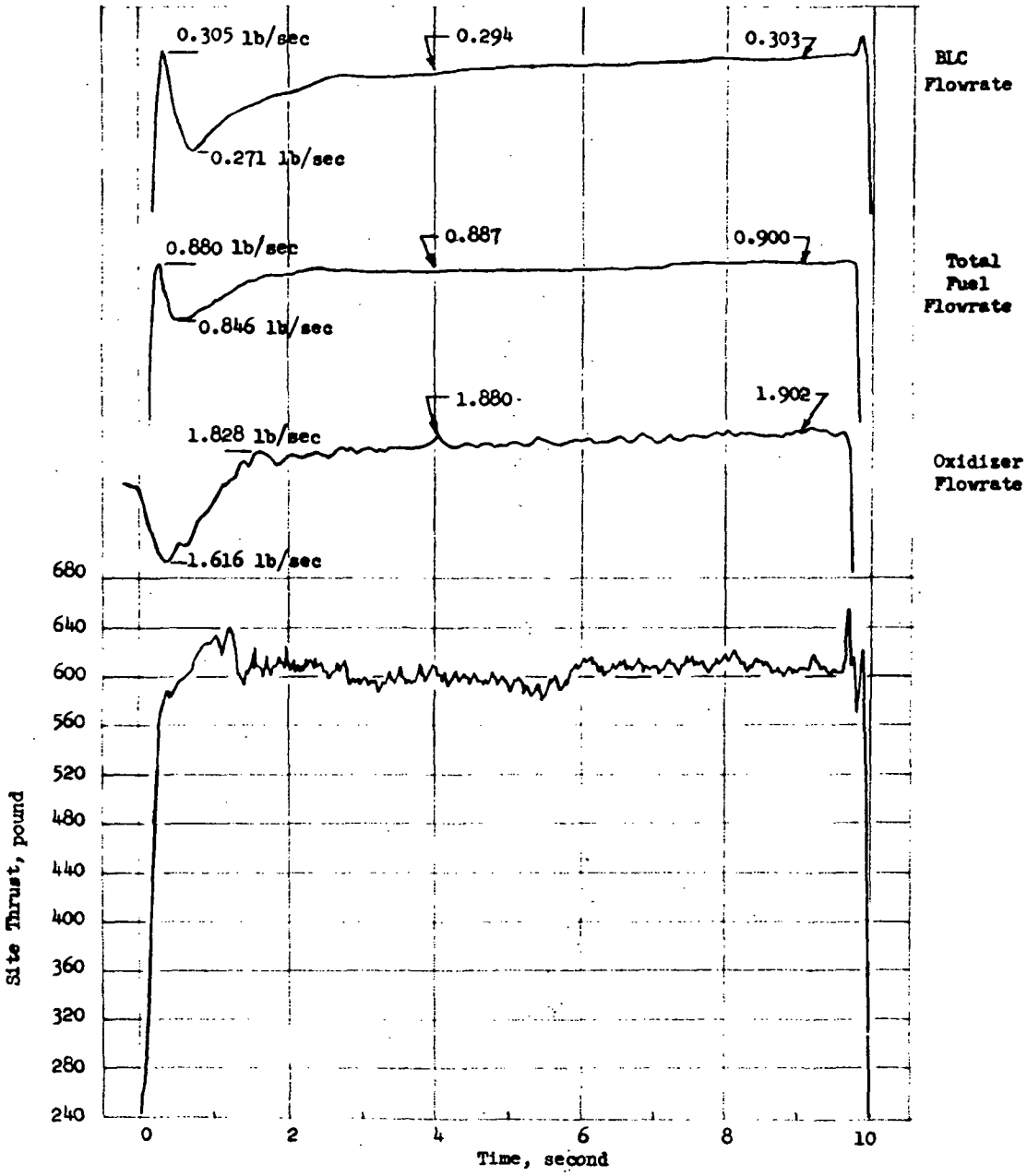

Figure 36. Thrust and Flowrates, Test 004
Core MR = 3.18 10.7% BLC

Figure 36. Thrust and Flowrates, Test 004
Core MR = 3.18 10.7% BLC

TABLE 8. THRUST CHAMBER PERFORMANCE

Test No.	Core Mixture Ratio	Percent BLC	Overall Mixture Ratio	c^*_{exp} (1), ft/sec	$c^*_{ode_{avg}}$, ft/sec	η_{c^*} (2), percent	$I_{s_{exp}}$ (3), seconds	$I_{s_{ode_{avg}}}$, seconds	η_{I_s} (4), percent	Injector(5)	Chamber(6)
003	3.11	11.0	2.06	6050	6755	89.6	283	308.8	91.6	A	A
004	3.18	10.7	2.10	5855	6780	86.4	271	309.5	87.5	A	A
005	4.25	4.2	3.44	--	--	--	307	322.7	(95.0)(7)	B	A
006	4.80	5.3	3.64	--	--	--	277	323.2	85.9	B	A
007	2.23	12.7	1.53	--	--	--	304	294.8	(103.0)(7)	B	A
008	3.44	11.8	2.15	5812	6800	85.5	269	310.5	86.6	B	B
009	4.0	8.3	2.79	--	--	--	269	319.3	(84.3)(7)	C	A
010	3.6	12.5	2.19	--	--	--	270	311.3	86.8	C	A
011	3.9	11.2	2.42	--	--	--	272.5	315.0	86.5	C	B

(1) Calculated from $c^*_{exp} = \frac{P_c A_t g}{\dot{w}_t}$ where $A_t = 5.065$ in.^{2}

$P_o = (P_c \text{ inj tap} + 13.8) \times \begin{matrix} 0.96 \text{ calorimeter chamber} \\ 0.98 \text{ graphite chamber} \end{matrix}$

(2) Calculated from $\eta_{c^*} = \frac{c^*_{exp}}{c^*_{ode_{avg}}} (100)$

(3) Calculated from $I_{s_{exp}} = \frac{F_{site} + 13.8\ (A_{exhaust})}{\dot{w}_t}$ where $A_{exhaust} = 10.87$ in.^{2} for calorimeter chamber; $A_{exhaust} = 12.57$ in.^{2} for graphite chamber

(4) Calculated from $\eta_{I_s} = \frac{I_{sp_{exp}}}{I_{sp_{ode_{avg}}}} (100)$

(5) Injector A - NAS7-304 modified; injector B - see page 102; injector C - see page 189

(6) Chamber A - Calorimeter, $A_e/A_t = 2.14$, $A_{exhaust} = 10.87$ in.^{2}
Chamber B - Graphite, $A_e/A_t = 2.48$, $A_{exhaust} = 12.57$ in.^{2}

(7) Short run, steady-state not obtained

Test 003. As discussed in detail below, the thrust chamber temperatures measured during Test 003 generally were consistent with one another and reflect lower than anticipated values of heat transfer coefficient and low values of core/film interaction, emphasizing the feasibility of the boundary cooled concept for OF_2/B_2H_6 engine application. The only exception is the 180-degree thermocouple row (see Fig. 37). Temperatures recorded by thermocouples in this row rose more sharply initially than temperatures recorded by thermocouples in the other rows, but then decreased their rate of rise abruptly after approximately 3-1/4 seconds into the run, and proceeded to rise at about the same rate as the other thermocouple rows for the remainder of the run. The reason for the high temperatures recorded by the 180-degree thermocouple row (in relation to the temperatures monitored in the other rows) is believed to be found in the boundary layer coolant flow. It can be observed from Fig. 35 that full boundary layer coolant flow was not established in Test 003 until about 3-1/4 seconds into the run, exactly the time at which the 180-degree thermocouple traces abruptly change slope. Also, the 180-degree position is located furthest away from the single boundary layer coolant manifold entrance, thereby achieving full flow conditions last.

The occurrence of a phenomenon that will be referred to as a "thermal spike", was also noted in upstream temperature traces during Test 003. These "thermal spikes" are illustrated in Fig. 38 and 39. The spikes shown in the figures both occurred just prior to, but clearly before, test cutoff. The spike recorded by the 0.5-inch thermocouple at 0-degrees does not appear to be reflected in 0-degree thermocouples located further downstream. However, the spike recorded by the 1-inch thermocouple at 90 degrees is reflected in the next downstream location (3-inch, 90 degrees) before becoming indistinguishable at the 5-inch location).

Test 004. Test 004 temperatures, recorded at any axial location by the various rows of thermocouples, were also found to agree with one another with one exception (see Fig. 40). The row of thermocouples located at the 270-degree circumferential position was observed to record higher temperatures than those of the other rows at all axial locations. This position corresponds to the position at which gouging and severe discoloration were noted. Start transients cannot account for this occurrence. The hotter film temperature at the 270-degree position could be caused

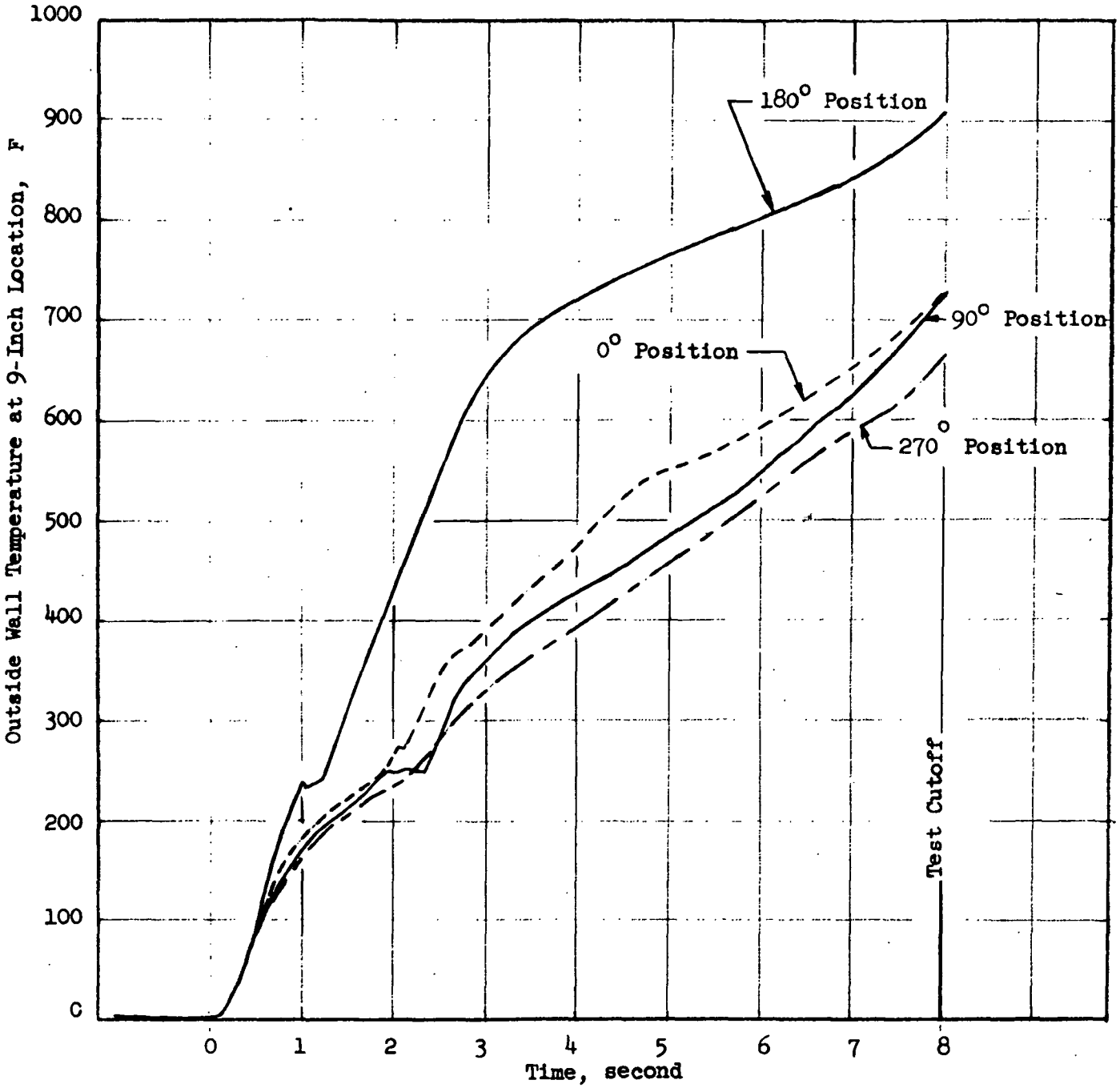

Figure 37. Test 003, Outside Wall Temperature at 9-Inch Axial Location as Function of Thermocouple Position

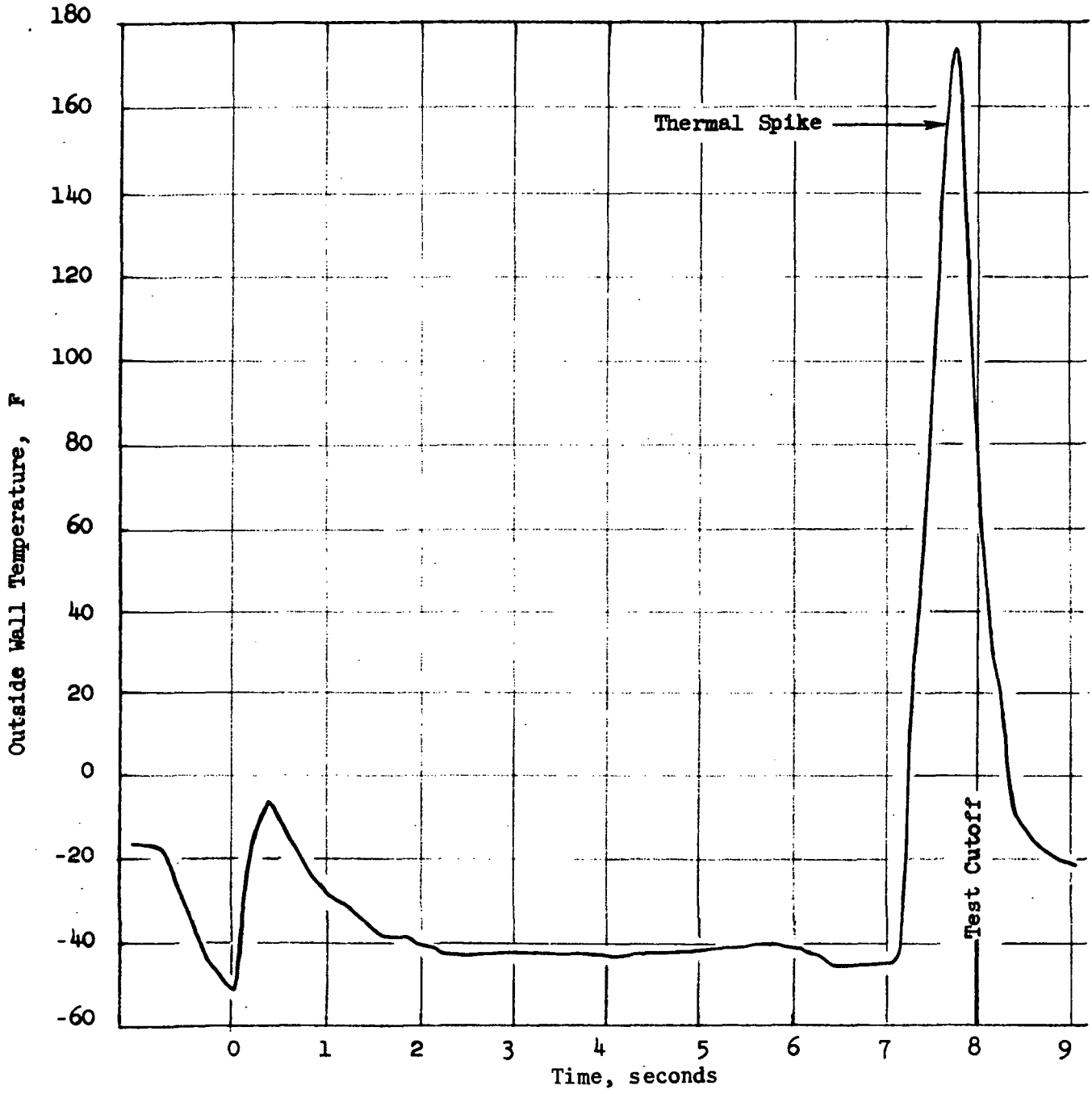

Figure 38. Thermal Spike on Test 003 at 0.5-Inch Axial Location and 0° Thermocouple Position

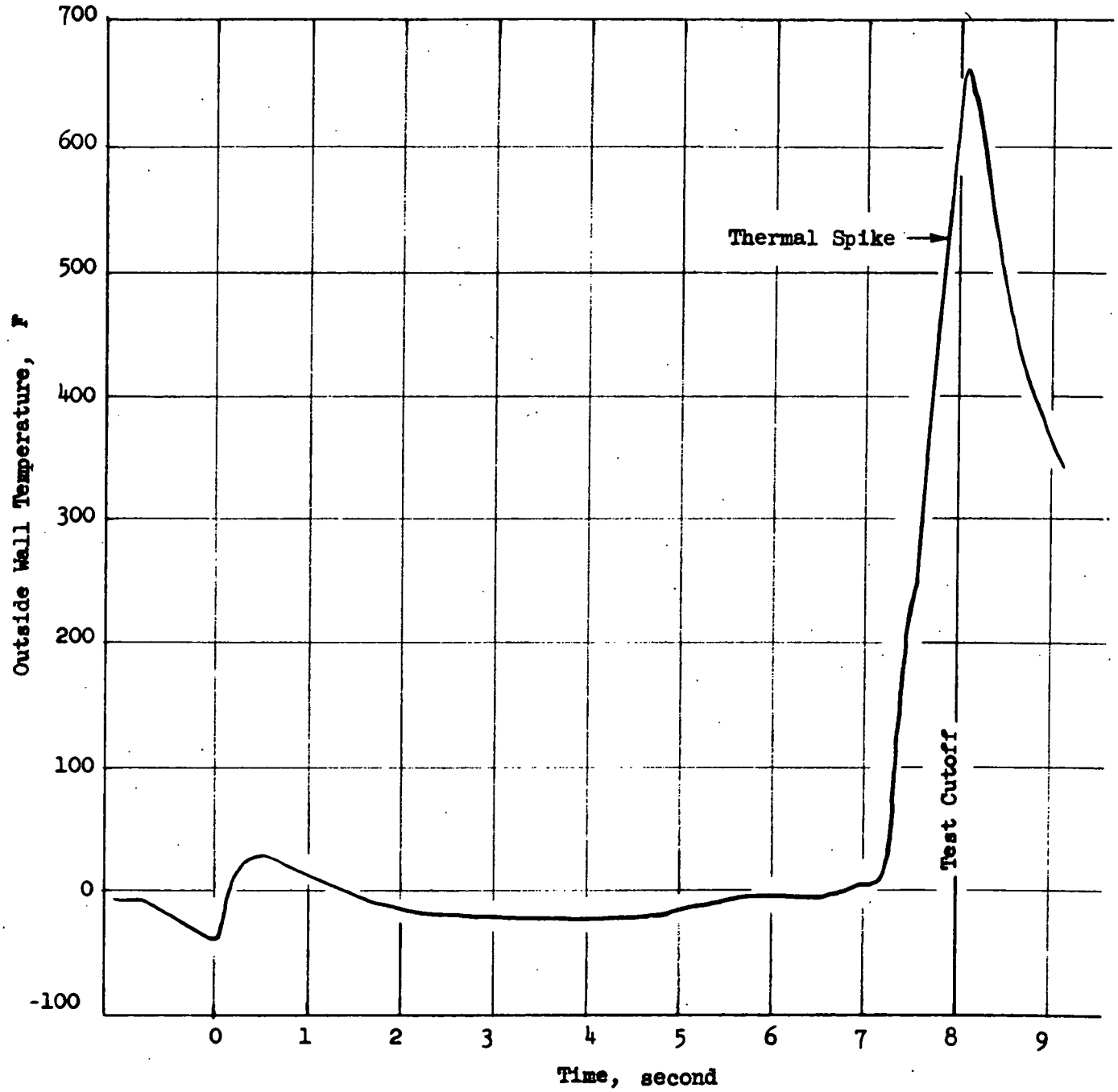

Figure 39. Thermal Spike on Test 003 at 1-Inch Axial Location and 90° Thermocouple Position

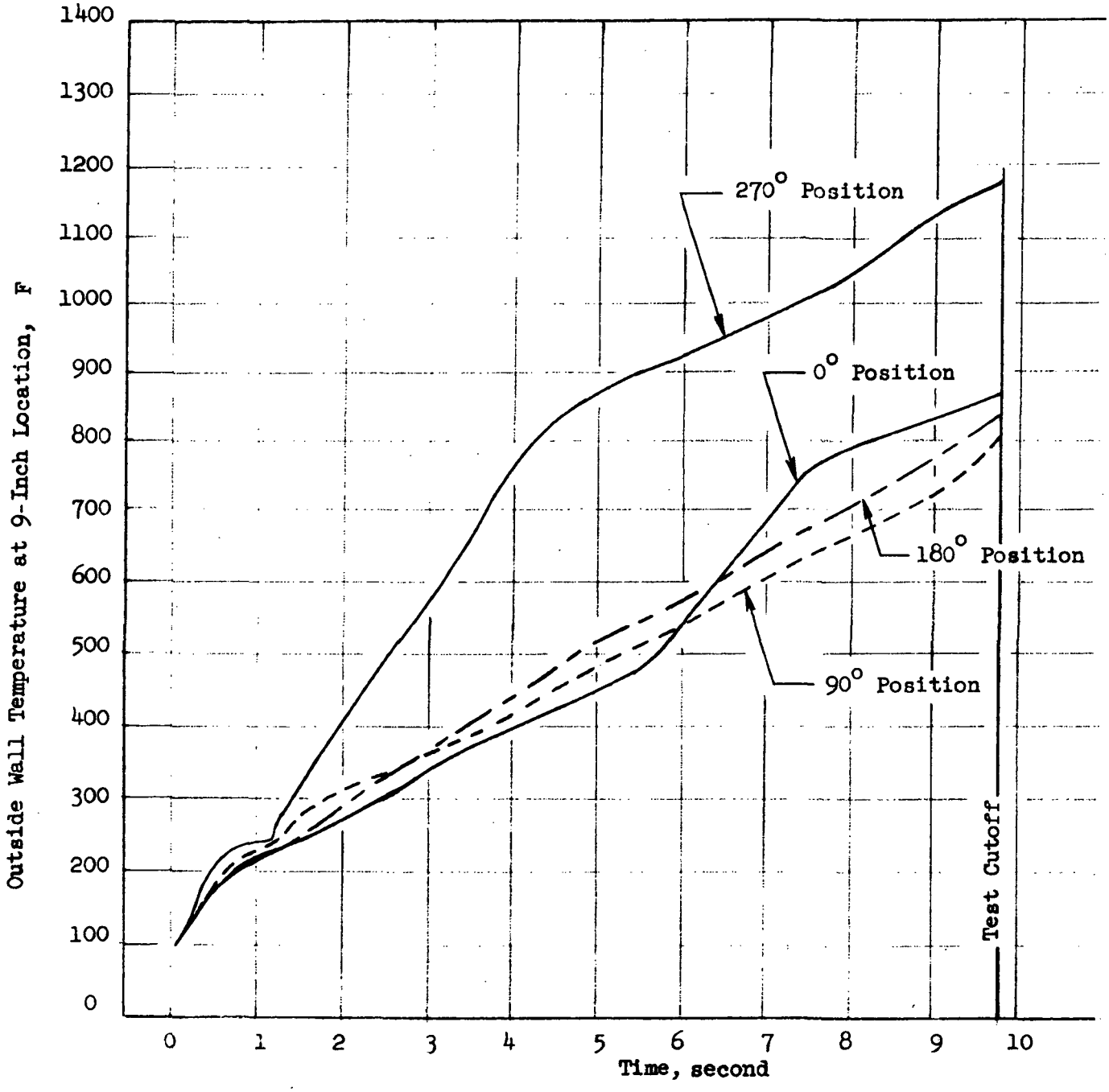

Figure 40. Test 004, Outside Wall Temperature at 9-Inch Axial Location as Function of Thermocouple Position

by either: 1) injector "streaking", resulting in a region of higher-than-average mixture ratio combustion gas at the 270-degree position, or 2) lower than average boundary layer coolant flow at the 270-degree position.

A "thermal spike", similar to those noted in Test 003, was also noted in Test 004. This spike was observed at the 0.5-inch location in the 0-degree thermocouple row (Fig. 41) and was reflected all the way downstream in the 0-degree circumferential position, as evidenced in Fig. 42, 43, and 44.

The occurrence of thermal spikes appears to be random as far as circumferential location is concerned*. The reflection of a spike downstream also appears to occur randomly; however, the occurrence of a spike is consistently identified at one of the 0.5-inch axial locations.

Thermal Spikes. The response of the wall thermocouples to the thermal spikes allowed an estimate to be made of the duration and intensity of the spikes. Figure 44 shows a one-dimensional match of the behavior of the thermocouple shown in Fig. 42, both during spike and following it. The behavior indicates that a step function heat pulse of 0.73-second duration followed by normal cooling by the film adequately represents the measured wall temperature and corresponds to a q/A of 3 to 4 Btu/in.^{2} sec into the wall during the thermal spike.

The cause of these thermal spikes is believed to be the intermittent interference of the fuel fans by deposits on the injector face. The injector face deposits are believed to build up around the fuel orifices (observed in posttest hardware examination) until an outer fuel fan is disrupted, thereby allowing some oxidizer to reach the wall and react with the film coolant. This process would produce random spikes, starting after sufficient injector deposits had formed. The momentum of the fuel jets eventually dislodges the deposit buildup and the thermal spike is ended. During the period of oxidizer impingement, the high heat transfer rate could be accounted for by condensation and freezing of boric oxide from the reaction products onto the wall. Boric oxide freezes at 1077 F, with a latent heat of condensation of 3000 Btu/lb. This large energy release near the wall could easily produce the observed heating rates. The postulated process would be expected

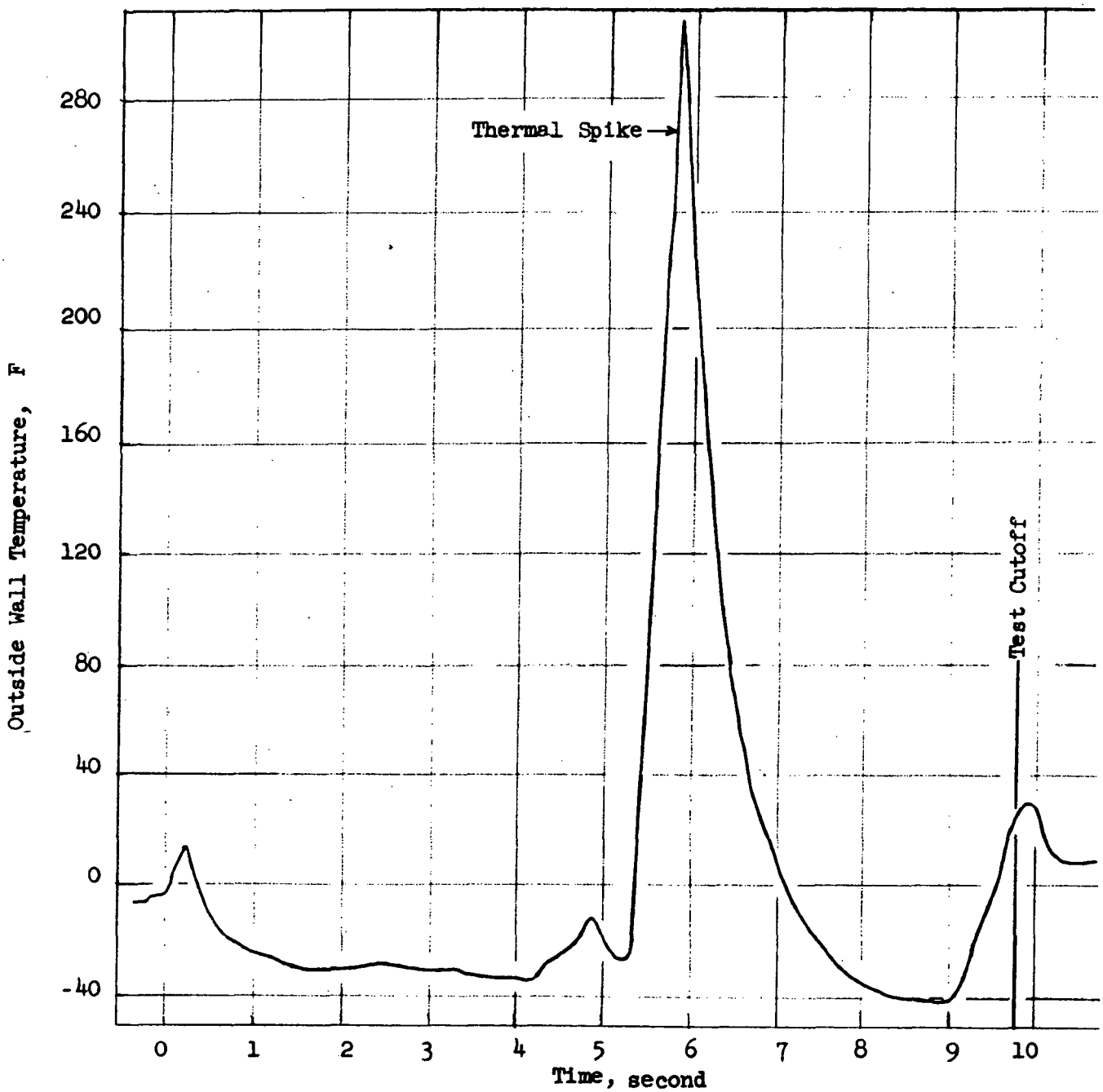

Figure 41. Thermal Spike on Test 004 at 0.5-Inch Axial Location and 0° Thermocouple Position

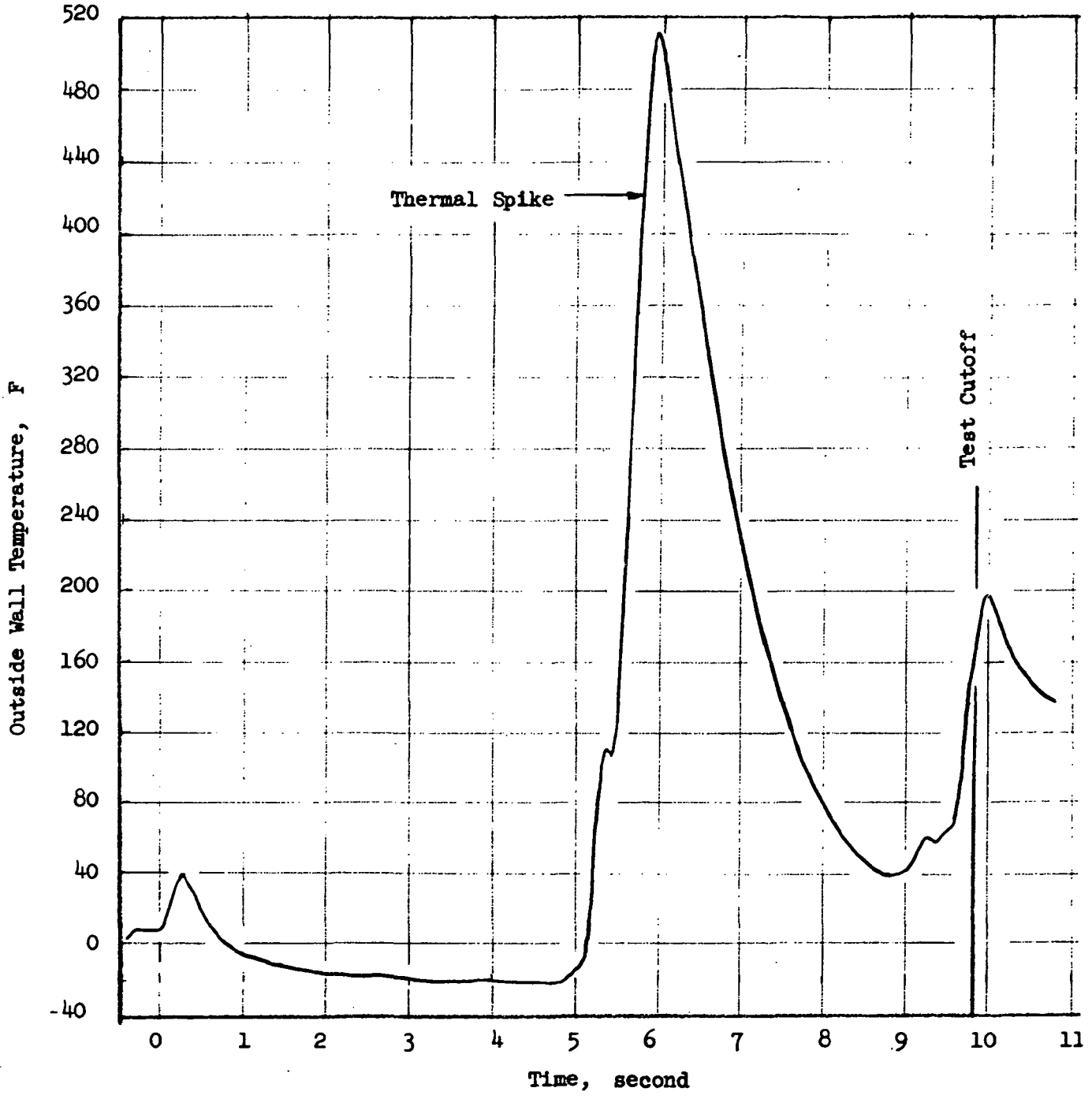

Figure 42. Thermal Spike on Test 004 at 1-Inch Axial Position and 0° Thermocouple Position

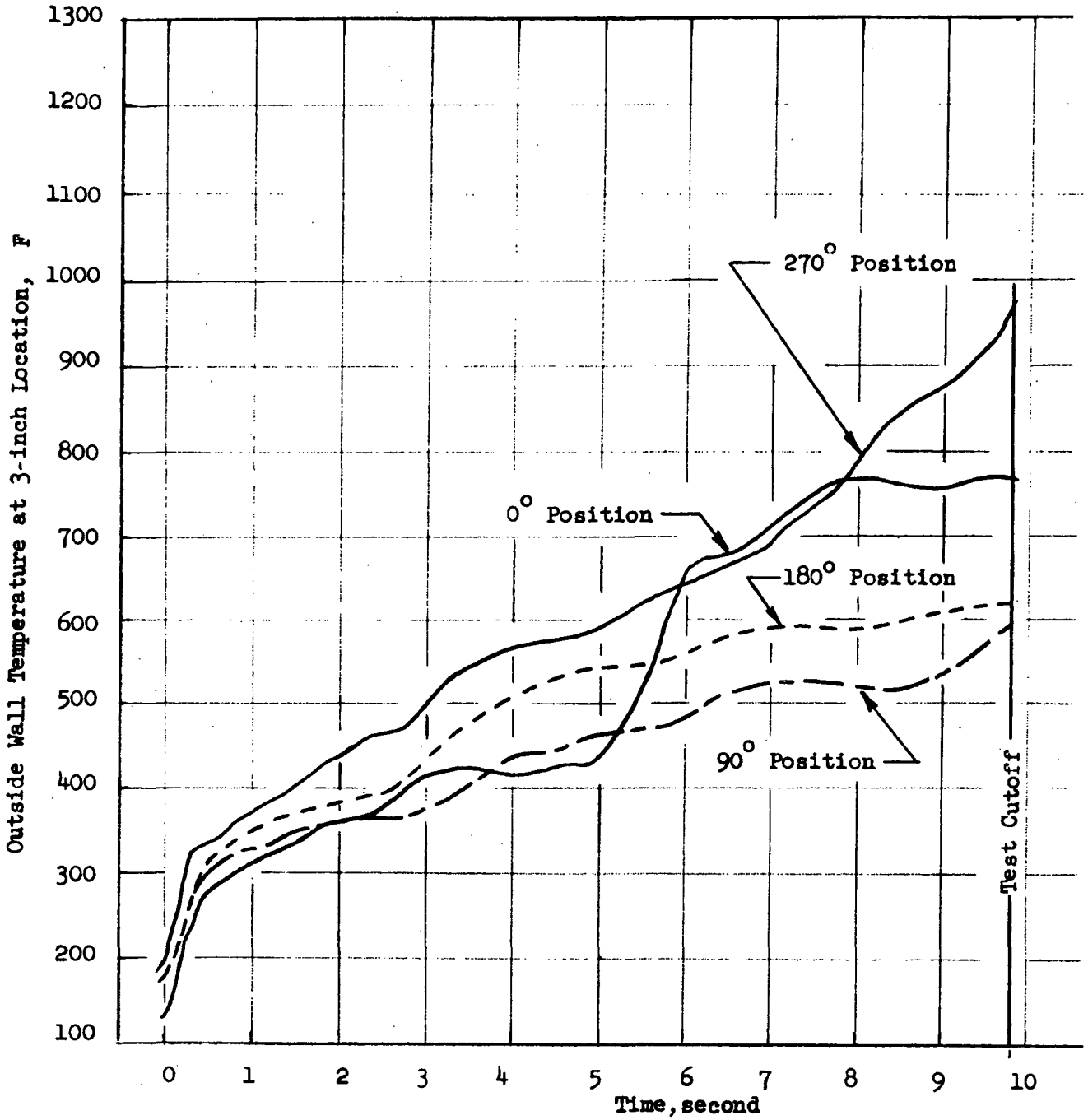

Figure 43. Test 004, Outside Wall Temperature at 3-Inch Axial Location as Function of Thermocouple Position

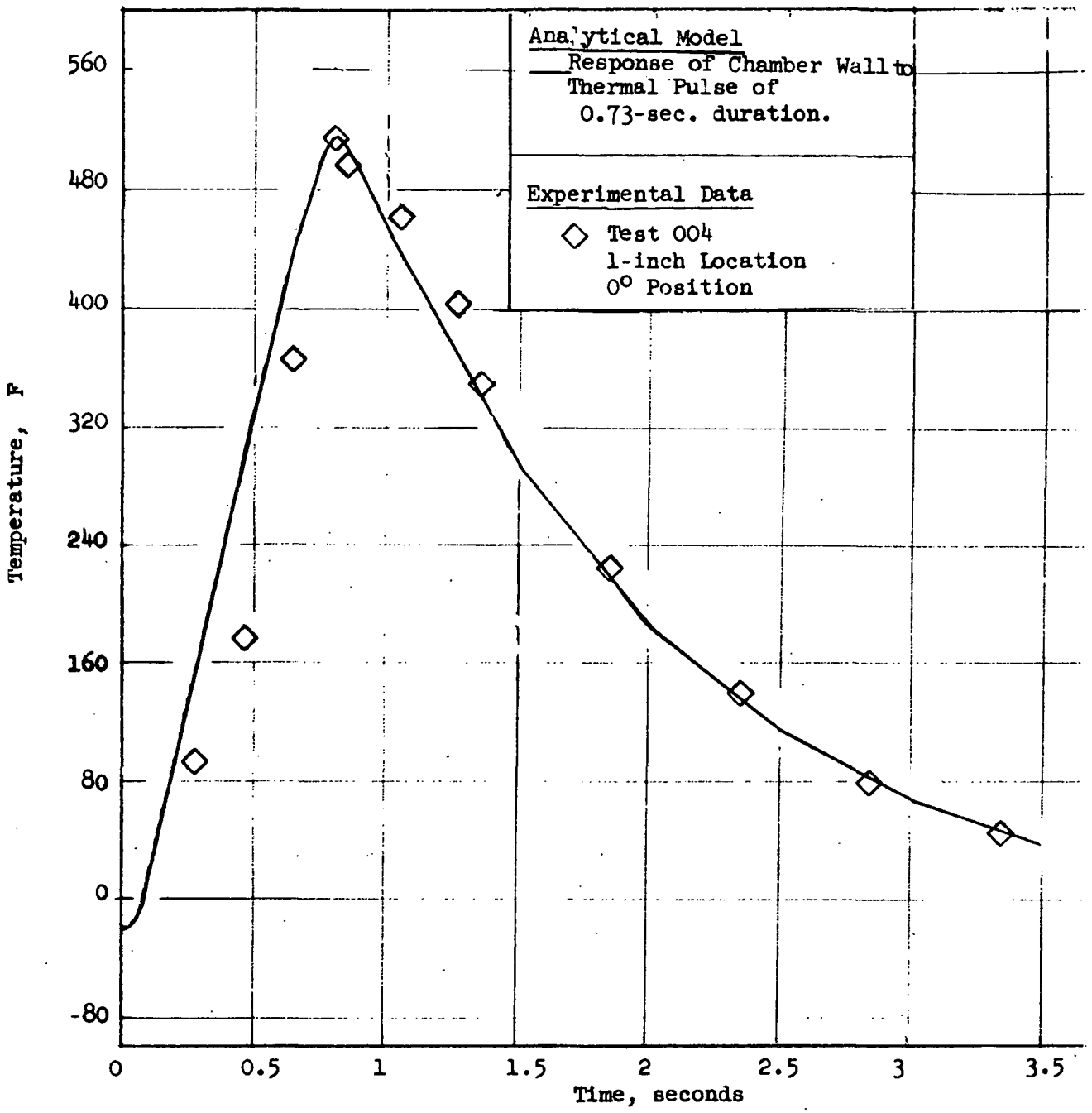

Figure 44. Thermal Spike Analysis of Calorimeter Chamber

to result in deposits of boric oxide on the wall in regions where thermal spikes had occurred. Visual observation of the thrust chamber after Test 004 revealed deposits in these areas starting close to the injector and chemical analysis showed these deposits to consist of approximately 50 weight percent of H_3BO_3, which is most probably obtained by hydrolysis of the combustion product boric oxide, B_2O_3.

DEAP Model Comparisons

Posttest analysis using the analytical DEAP heat transfer model was concentrated on Test 004 because of its longer test duration. Posttest heat transfer predictions based on the DEAP model were adjusted from pretest values to account for experimentally measured: (1) coolant flowrate, (2) initial chamber wall temperature distribution, (3) coolant inlet temperature, (4) chamber pressure lag as reflected by measured thrust, and (5) combustion gas driving temperature. The combustion gas driving temperature was assumed equal to $\eta_{c*}^2 T_{theo}$. Combustion gas entrainment into the vapor film was varied in an effort to match the experimentally measured temperature-time profiles with the analytical profiles. The combustion gas entrainment rate is one of the most important factors influencing the film (and hence the wall) temperature and is also one of the least well known inputs to the analytical DEAP model.

Entrainment is controlled in the DEAP model by two factors: (1) the entrainment rate factor (Le^*/c_{p_g}), and (2) the vapor film temperature, at which entrainment is allowed to begin. Earlier, a fairly good posttest agreement between experiment and model (see Fig. 28) was achieved for Test 001 (14 percent boundary layer coolant) using a mass entrainment rate factor, Le^*/c_{p_g}, of 11.8* and a vapor film entrainment temperature of 265 F, which corresponds to entrainment beginning at an axial position of 4.1 inches. Further posttest analysis of Test 001 data was carried out using an analytical relationship (developed under Contract NAS3-12071) for Le^*/c_{p_g} as a function of Reynolds number (i.e., axial position).

Based on NAS7-304 posttest analysis assuming entrainment when the vapor film reaches -50 F.

Work under NAS3-12071 (Ref. 6) led to a correlation of existing flat plate film cooling data which indicates a strong effect of the free stream flow conditions on entrainment. The resulting equation has the form:

$$Le^* = 1.1 + 0.11 \left(\frac{SU\rho_g}{\mu_g}\right)^{0.4} \tag{10}$$

where:

S = initial gas film thickness (Eq. 11)

U = local combustion gas velocity

ρ_g = combustion gas density

μ_g = stagnation combustion gas viscosity

As developed, Eq. 10 uses the initial gas film thickness, S, to define the Reynolds number. S is the slot thickness for conventional gaseous film cooling, but is indeterminate for liquid film cooling. The approach used here is to define this thickness in terms of the coolant vapor density, ρ_v, at the vaporization temperature and the coolant liquid velocity, V_L, on the wall so that:

$$S = \frac{\dot{w}_{BLC}}{\pi D_c \rho_v V_L} \tag{11}$$

where

$\dot{w}_{BLC}$ = boundary layer coolant mass flowrate

D_c = chamber diameter

ρ_v = vapor density of the boundary layer coolant at the boiling point

V_L = velocity of the boundary layer coolant

This relationship has been used to define the pseudo-Lewis number (Le*) profile along the thrust chamber length.

In conjunction with this entrainment model, an effect observed with earth storable propellants (Ref. 7) must also be considered. This is the low rate of heating of the film for a short distance after it has vaporized, and is similar to the non-mixing effects observed in diffuser tests with gases having widely different properties (Ref. 8). In Ref. 7 it is postulated that when two dissimilar gases mix in a constant area duct, one requirement for mixing theory to apply is that the sonic velocity of the slower moving stream must exceed the actual velocity of the faster stream (i.e., the two streams could reach equal velocities in the constant area duct). When this requirement is not met, mixing does not occur efficiently, and the separate streams persist for a long distance.

In the case of film cooling of the present calorimeter chambers, the combustion gas velocity is approximately 1300 ft/sec in the plenum region of the thrust chamber (assuming 90-percent c* efficiency) so that undecomposed diborane would have to be heated to 200 F before its sonic velocity would equal the combustion gas velocity. Thus, a region of impaired mixing near the end of the liquid film is possible, and the criterion postulated in Ref. 7 is identical to the value empirically required to match the test data obtained with the present calorimeter chamber (as described below).

Application of Eq. 10 was found to yield the values of Le^*/c_{p_g} as a function of distance shown in Table 9. This Le^*/c_{p_g} table was input into the DEAP model and the vapor film entrainment temperature for initiation of core/film interaction was varied until a good data match between Test 001 experimental temperature/time results and analytical posttest predictions was achieved.

The DEAP model used in obtaining the data match shown in Fig. 28 contained an analytical expression in the vicinity of the injector for the gas-to-dry-wall heat transfer coefficient, h_{g_o}, based on the simple Bartz equation, while the Mayer boundary layer expression was used to analytically obtain h_{g_o} downstream. The simple Bartz equation results in a heat transfer coefficient which remains invariant over the chamber length with constant cross-section area. Experimental evidence (Ref. 9, for example) has shown, however, that the axial distribution

TABLE 9. Le^*/c_{p_g} VS DISTANCE (FROM EQ. 10)

Axial Distance, inches	Le^*/c_{p_g}
0	5.94
3	5.94
4	6.41
5	7.35
6	6.98
7	6.69
8	6.40
9	6.17
10	5.94

of heat transfer coefficient in the upstream chamber section of rocket engines more nearly approximates the distribution obtained using the Mayer expression. Therefore, the work reported herein employs the Mayer boundary layer expression in the DEAP model to analytically obtain the gas-to-dry-wall heat transfer coefficient over the entire chamber length. The increased values of h_{g_o} predicted by the Mayer expression upstream necessitated the input of a new combustion driving temperature profile near the injector face to match the experimentally measured temperatures in this area. This new profile assumes a driving temperature equal to 0.5 $\eta_{c^*}{}^2 T_{theo}$ at the injector face, increasing linearly to a value of 0.999 $\eta_{c^*}{}^2 T_{theo}$ at a distance of 2 inches from the injector face. This match, achieved using a vapor film entrainment temperature of 200 F (corresponding to entrainment beginning at 3.1 inches), is shown in Fig. 45. It compares favorably with the data match achieved with a constant Le^*/c_{p_g} of 11.8 and a vapor film entrainment temperature of 265 F, shown in Fig. 28.

Using the Le^*/c_{p_g} table obtained from Eq. 10, the revised combustion driving temperature profile, and a vapor film entrainment temperature of 200 F (corresponding to entrainment beginning at 2.3 inches), the data match for Test 004 shown in Fig. 46 was obtained. This match is better than any match obtained with the constant Le^*/c_{p_g} of 11.8.

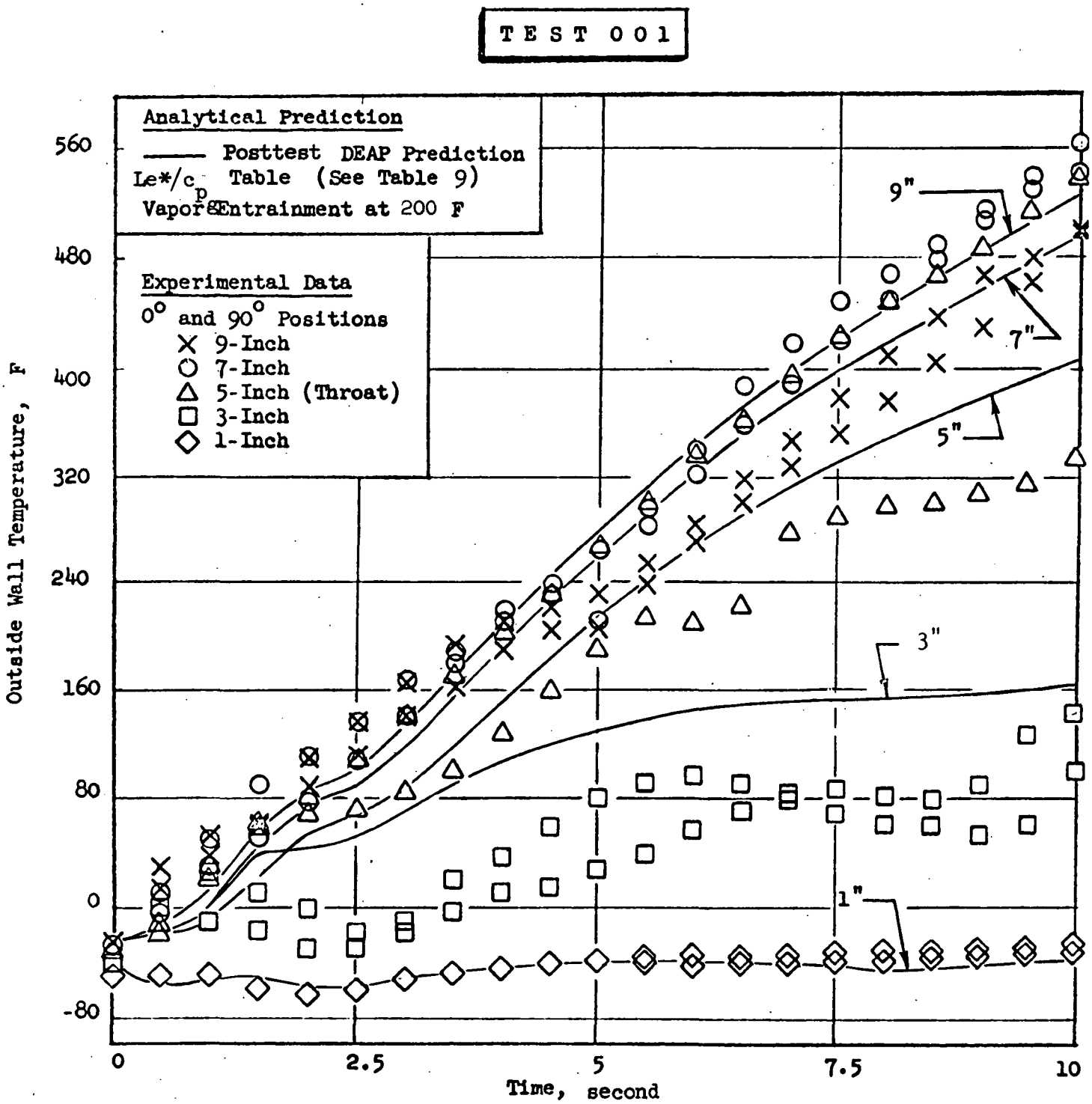

Figure 45. Posttest Prediction of Test 001

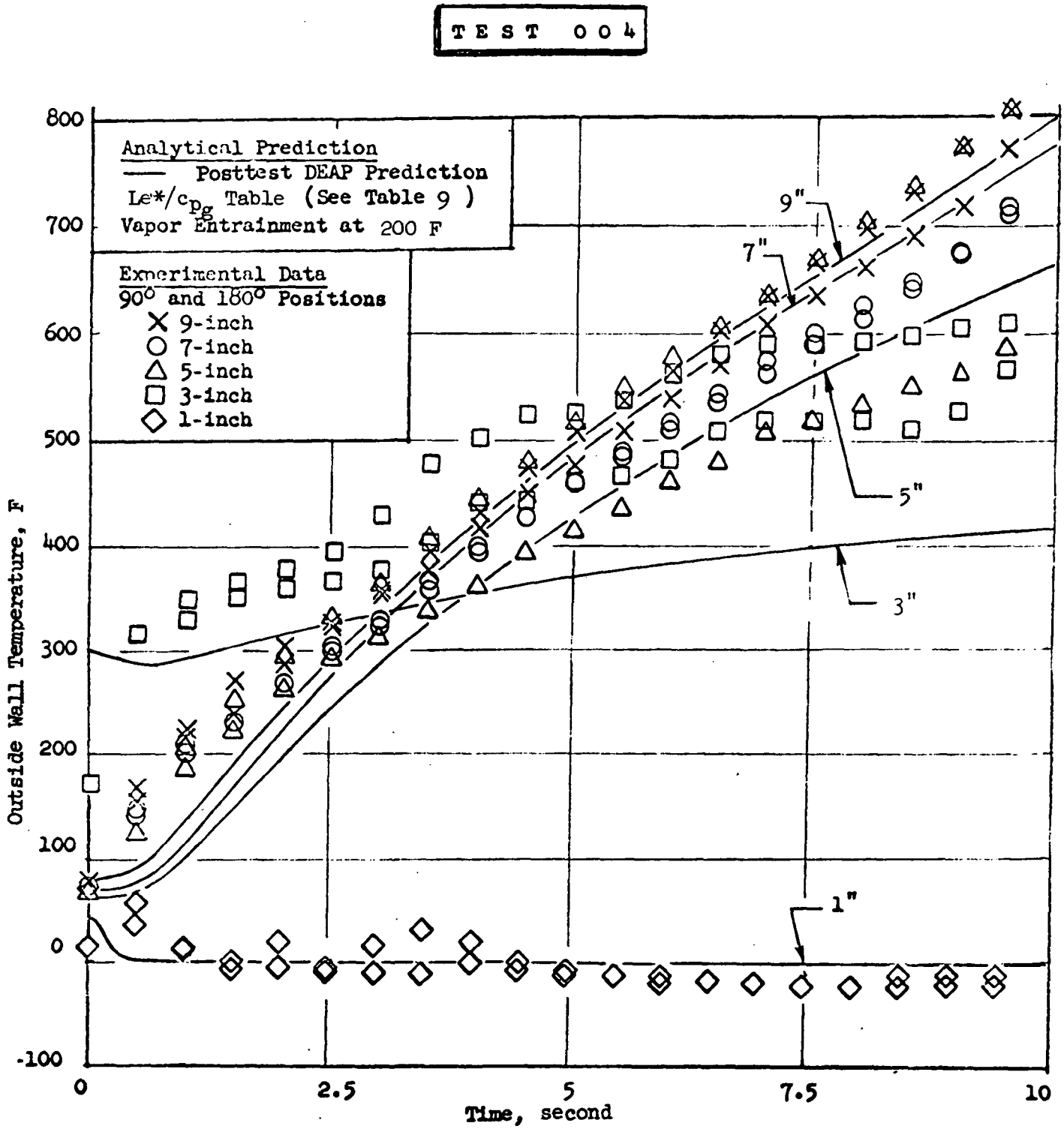

Figure 46. Posttest Prediction of Test 004

The data match obtained between experiment and model for Test 003 using the Le^*/c_{p_g} table, the revised driving temperature profile, and a 200 F-entrainment temperature is shown in Fig. 47.

While the matches shown in Fig. 46 and 47 for Tests 004 and 003 are reasonable on an overall basis, agreement between experiment and analysis at the 3-inch position is poor. The disagreement seems to be associated with the unexplained 150-200 F sudden rise in temperature at start of test. Test 002, run at conditions similar to those used in Test 003 and 004, resulted in nozzle temperatures similar to those experienced in Tests 003 and 004, but did not exhibit the high temperatures at the 3-inch position (see Fig. 24).

Film Temperature and Heat Transfer Coefficient Determinations

The thermocouple data generated during Tests 003 and 004 were more suitable from an analysis standpoint than the data obtained during Tests 001 and 002. Since the test conditions remained approximately constant during Tests 003 and 004, the TEMP program for predicting film recovery temperature could use data generated over nearly the entire test duration, and data on the film heat transfer coefficient and film recovery temperature were obtained at every thermocouple location. The results obtained are tabulated in Tables 10 and 11. Error estimates for the film temperatures are also included.

The film temperatures obtained from the TEMP program for Test 003 are shown in Fig. 48 along with the DEAP model prediction used to match the test data (Fig. 47). The errors in estimating the film temperature in the nozzle are large because the wall temperatures have not yet approached film recovery temperatures.

The film heat transfer coefficients obtained from Tests 001, 003, and 004 are plotted as a ratio of the predicted combustion gas heat transfer coefficient versus film temperature in Fig. 49. DEAP computer model values used to match the test data are also shown. Two conclusions were drawn from the Fig. 49 results: (1) the heat transfer coefficient decreased much more rapidly with increasing film temperature than predicted, and (2) in the cool vapor region, the heat transfer

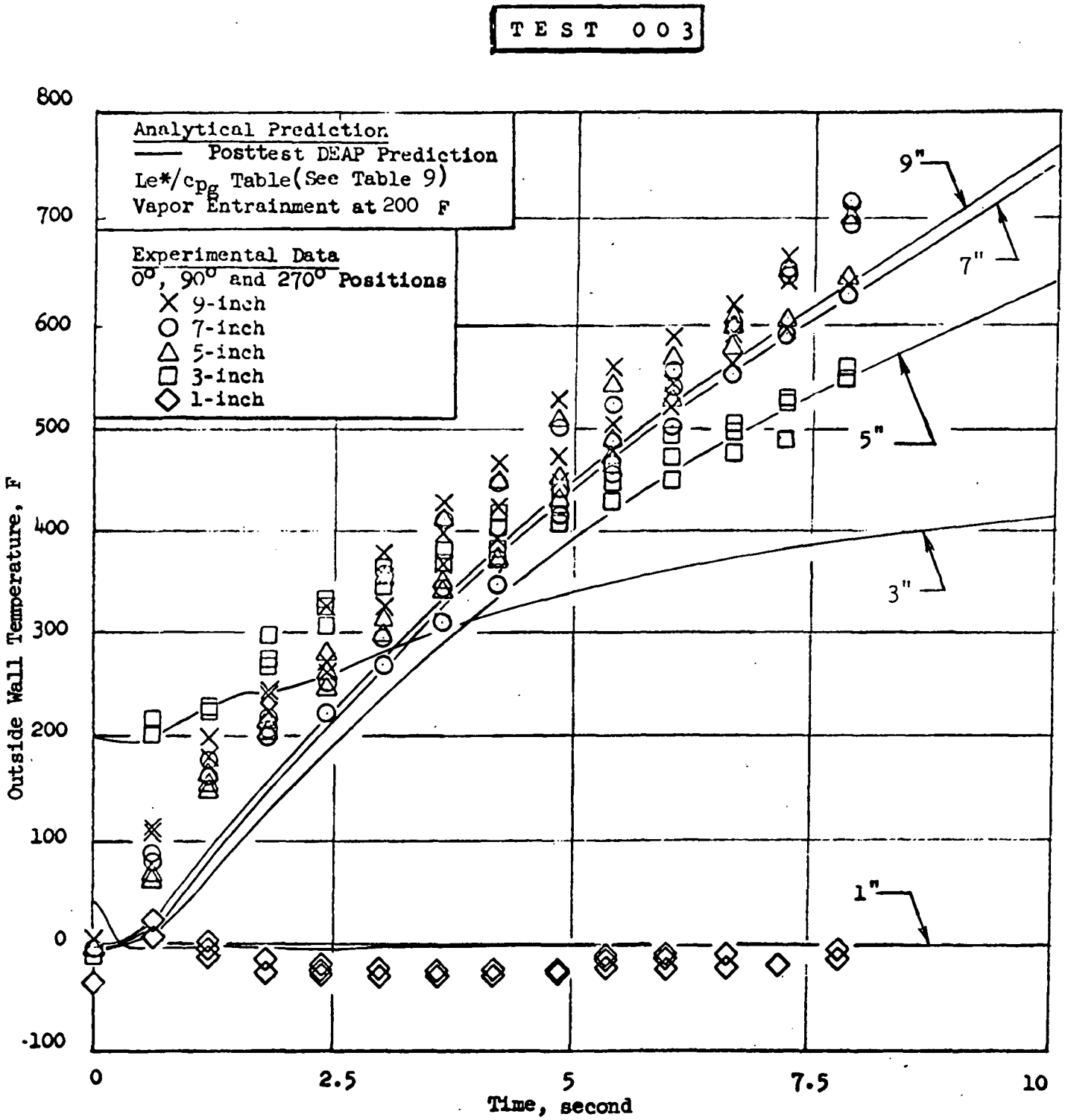

Figure 47. Posttest Prediction of Test 003

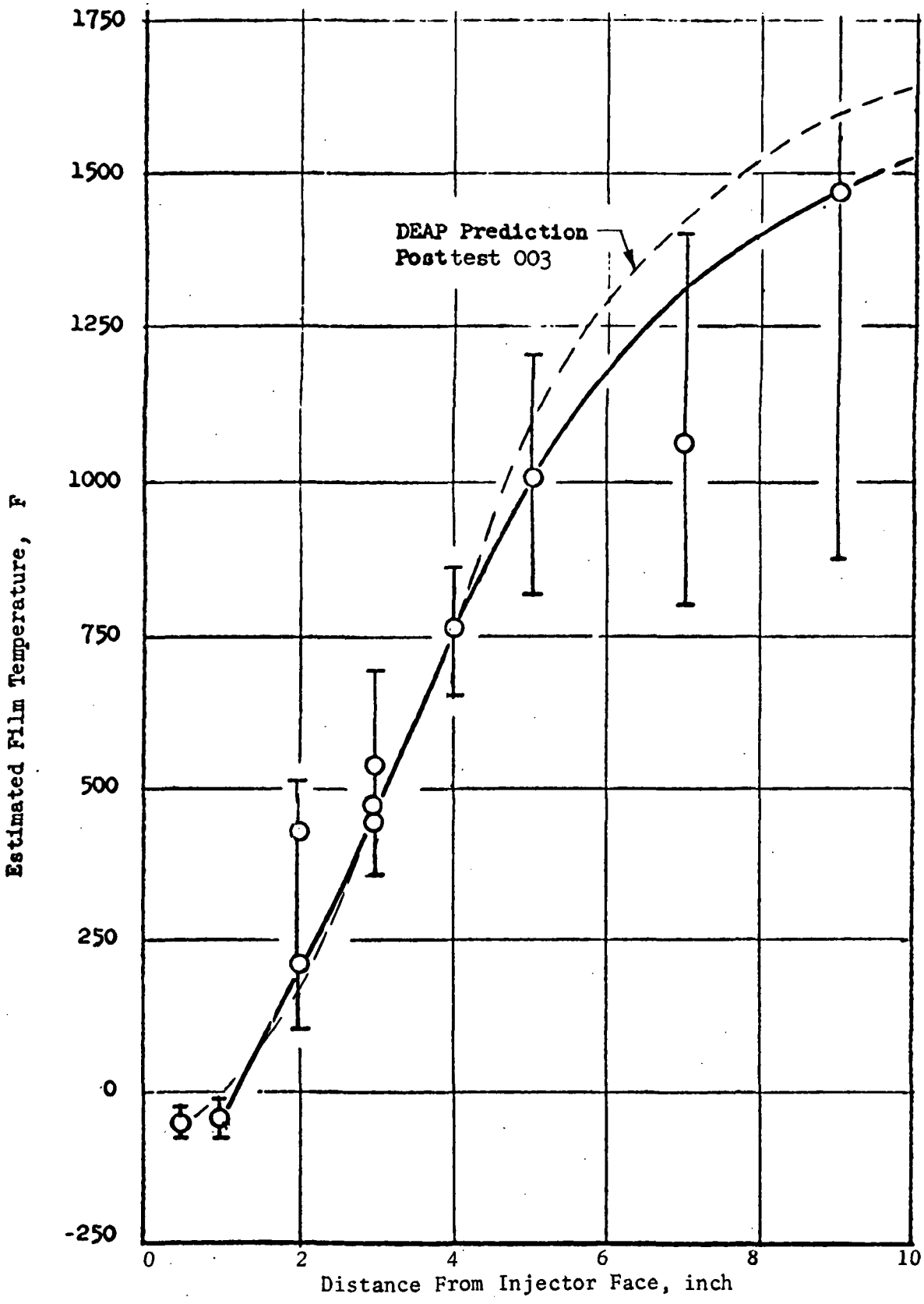

Figure 48. Film Temperature Profile for Test 003

TABLE 10. SUMMARY OF THERMAL DATA FROM TEST 003

Axial Distance, inches	Angular Location, degrees	h_f, Btu/in^{2}sec F	T_f, F	h_f/h_g
0.5	0	0.0040	-45 ±3	7.8
	90	0.0040	-41 ±3	7.8
1	0	0.0045	-28 ±6	9.2
	90	0.0026	-36 ±6	5.3
	270	0.0029	-25 ±20	5.9
2	0	0.0013	211 ±100	3.4
	180	0.0009	437 ±80	2.4
3	0	0.0023	458 ±20	6.6
	90	0.0012	479 ±120	3.5
	180	0.0015	542 ±150	4.3
4	0	0.0050	638 ±600	12.1
	180	0.0034	765 ±100	8.2
5	0, 90	0.0019	1010 ±200	3.5
7	0, 90	0.0013	1066 ±250	3.8
9	0	0.0005	1813 ±600	2.2
	90	0.0006	1475 ±600	2.7
	180	0.0005	1451 ±10	2.2

TABLE 11. SUMMARY OF THERMAL DATA FROM TEST 004

Axial Dist, In.	Angular Location, Degrees	h_f, Btu/in^2 sec F	T_f, F	h_f/h_g
1	0	0.0040	-20 ± 5	8.2
2	180	0.0020	241 ± 3	5.2
3	90	0.0009	574 ± 200	2.6
	180	0.0009	679 ± 200	2.6
4	180	0.0016	813 ± 120	3.9
5	90	0.0012	892 ± 100	2.2
	180	0.0003	3315 ± 750	0.6
7	90	0.0003	2444 ± 300	1.0
	180	0.0004	1777 ± 300	1.2
9	90	0.0001	4571 ± 500	0.6
	180			

coefficient was higher than predicted. Such deviations from the DEAP model would be in the direction of improved INTEREGEN operation, and would indicate a greater thermal design margin than originally predicted.

It should be noted, however, that the limits of error are not shown in Fig. 49 and may be large in some cases (see Tables 10 and 11). In addition, since during the measurement period the outside wall temperatures of the calorimeter chamber had not yet approached the film recovery temperature but were rising at a nearly steady rate with time, the estimate of the film temperature given in Tables 10 and 11 may be on the high side, with the h_f estimate correspondingly on the low side. This would result in the type of comparison with the DEAP model at high film temperatures as shown in Fig. 49. If the heat transfer coefficient ratio h_f/h_g were to actually decrease to a value of about unity at a film temperature of 2500 F, the calorimeter nozzle temperatures predicted with the DEAP model would be very significantly lower than the experimental values.

Core/Film Interaction

Although the film temperature estimates obtained from the Test 003 data have a large uncertainty, they were used with the FILM computer program to obtain an approximate range of values for the psuedo-Lewis number, Le*. This gives another check point for verification of the overall data match. Using the solid curve from Fig. 49, an average value of le^*/c_{p_g} of 7.2 is indicated for Test 003, along with a variation of Le^*/c_{p_g} with distance as shown in Fig. 50. The values used in the upgraded DEAP analytical model are also shown and agree reasonably well with the test data. The average value of 7.2 is quite encouraging when it is recalled that at the outset of the program a value of 11.8 was anticipated for this parameter.

An interesting aspect of these entrainment estimates is that they do not show any evidence of the BOF conversion to B_2O_3, which could cause a large energy release in the film. The film coolant therefore provides effective thermal protection for the wall, a protection that can be predicted reasonably well by the analytical model.

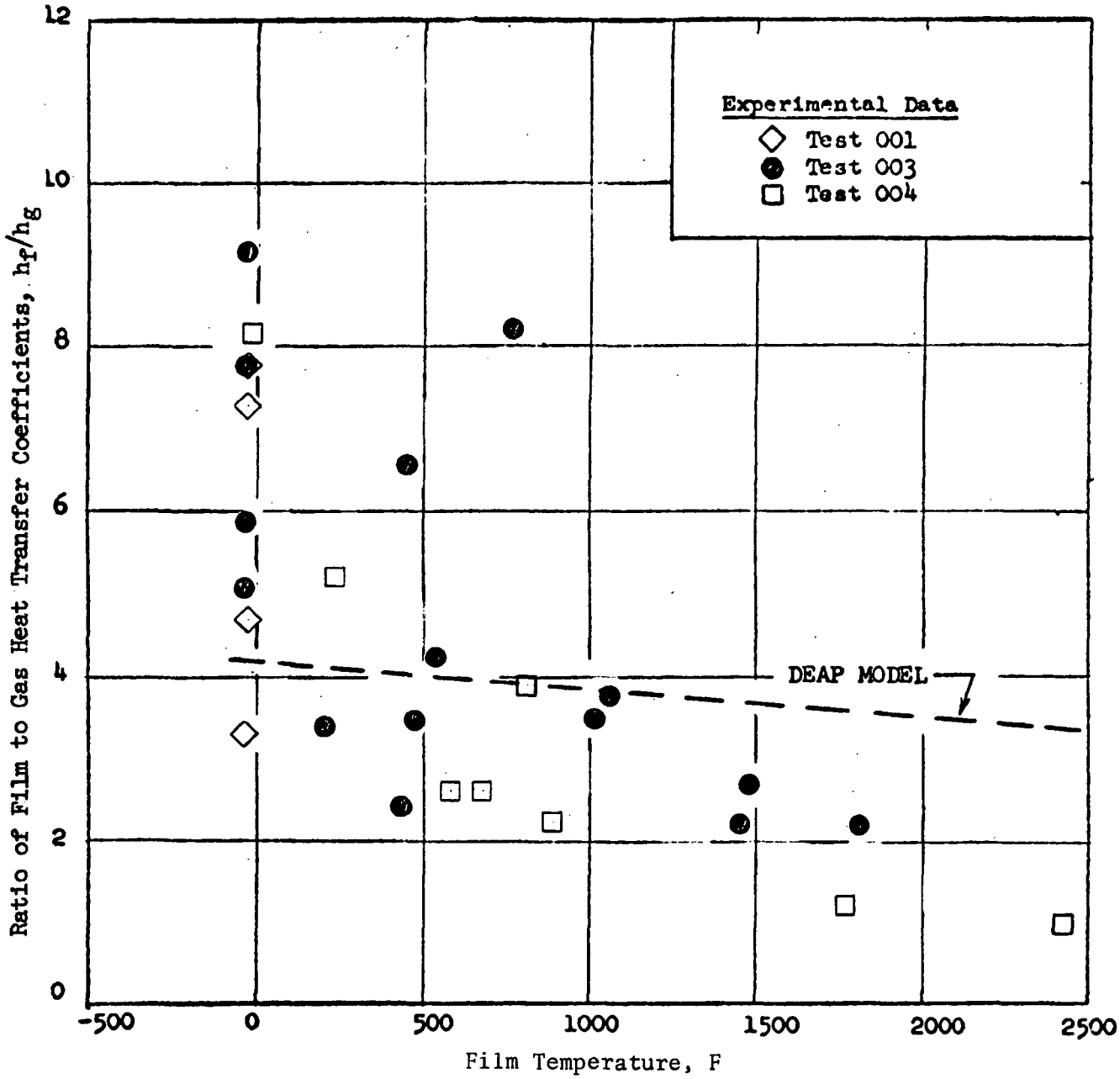

Figure 49. Ratio of Film to Gas Heat Transfer Coefficients vs Film Temperature

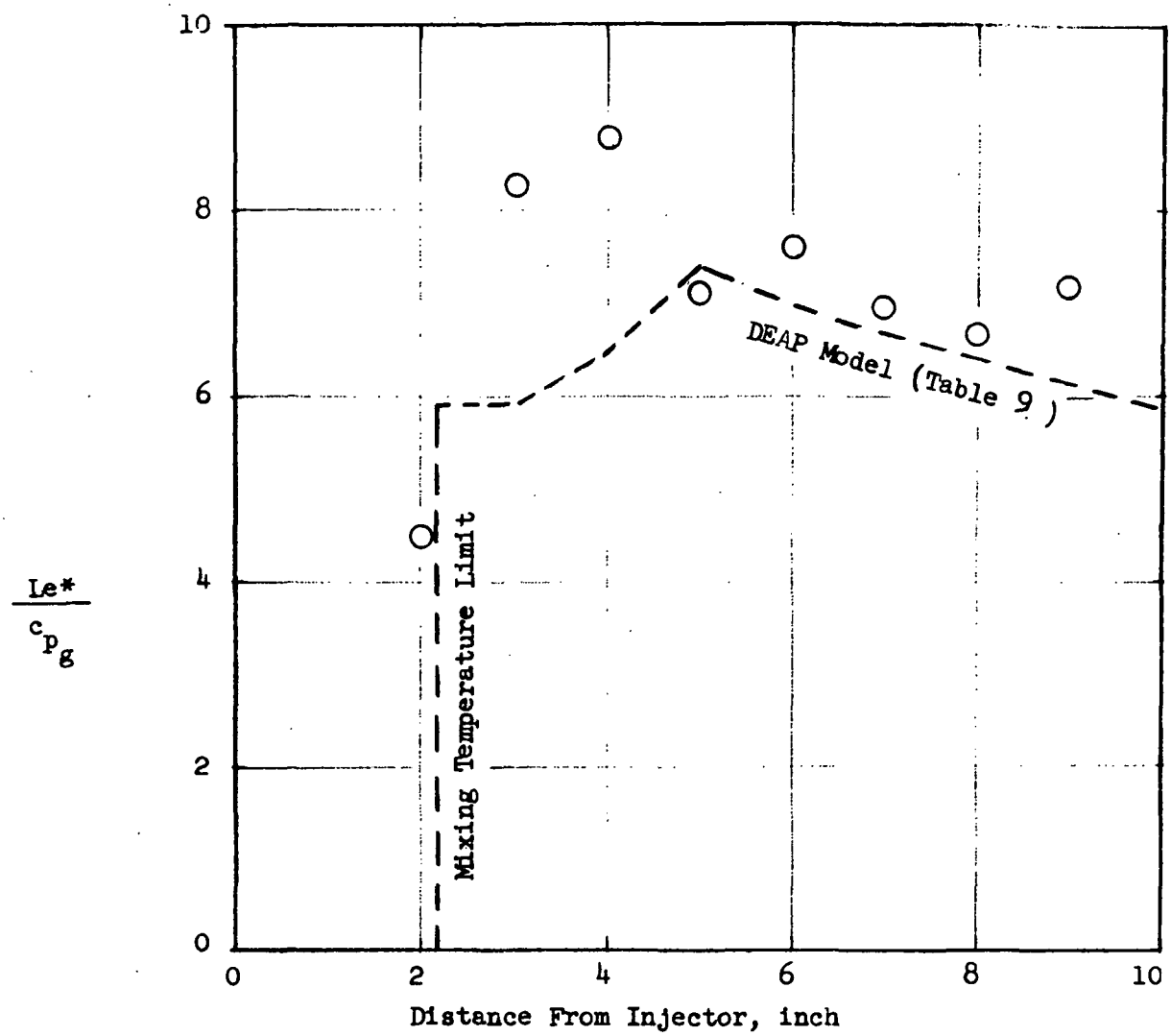

Figure 50. Entrainment Parameter (Le^*/c_{p_g}) vs Distance for Test 003

CONCLUSIONS FROM CALORIMETER HOT FIRINGS (TESTS 001-004)

From calorimeter hot firings (Tests 001-004) analytical DEAP heat transfer model post-predictions which match the experimental data for Tests 001, 003, and 004 were made. Although data obtained from Tests 003 and 004 allowed determination of film heat transfer coefficients, film recovery temperature, and the core/film (Le^*/c_{p_g}) interaction, more data are required before these experimentally measured quantities can be incorporated with a high degree of confidence into the DEAP model. Nonetheless, even at this point, it was concluded that the vapor film cooling is much more effective than originally predicted and that the boundary/conduction cooled heat transfer concept being investigated for OF_2/B_2H_6 propellants under this contract is even more attractive than originally envisioned.

A summary of the chamber damage incurred during Tests 002 and 004 is shown in Fig. 51. The chambers exhibit discoloration, burnthrough, and/or gouging characteristics only within the confines of a 135-degree chamber sector. In the other 225-degree sector, the chambers have remained untarnished, and the heat transfer data have been most encouraging. Because of the consistent anomalous behavior of the injector within the aforementioned 135-degree sector, further use of the NAS7-304 like doublet injector appeared to be unjustified. Furthermore, because of the encouraging thermal data obtained, additional work with the boundary cooling concept appeared totally justified.

NEW INJECTOR DESIGN

The injector (Fig. 52) employed for the initial four calorimeter hot firings was originally fabricated as a 400-pound-thrust injector under Contract NAS7-304. Two major modifications were made to the injector under NAS7-304. The first was a conversion to a 1000-pound-thrust injector through enlargement and addition of orifices, and the second was a conversion from axial boundary layer coolant to swirl boundary layer coolant injection. The NAS7-304 injector is extremely sensitive to oxidizer/fuel misimpingement, contains poor swirl boundary layer coolant

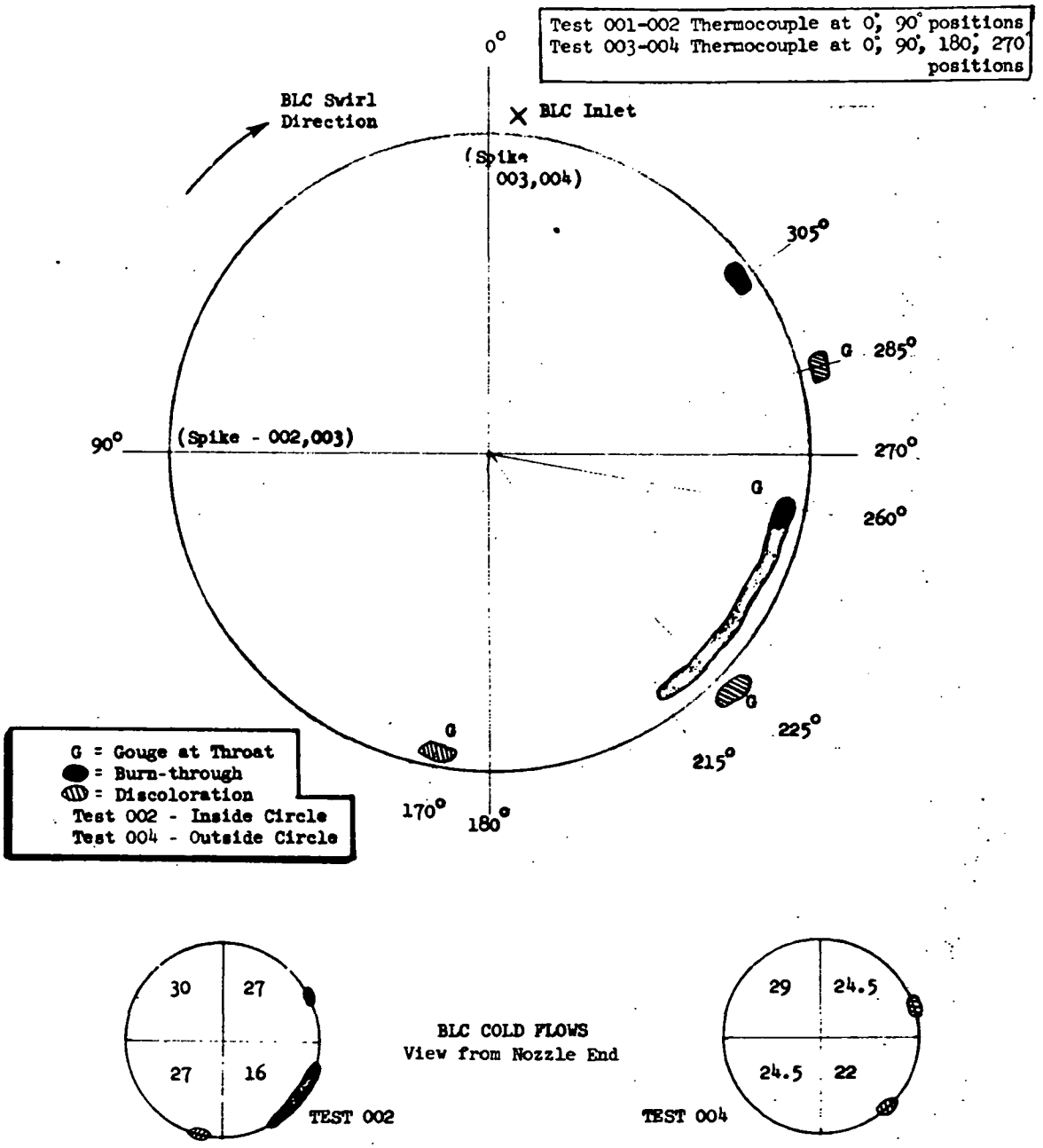

Figure 51. Summary of Chamber Damage Locations

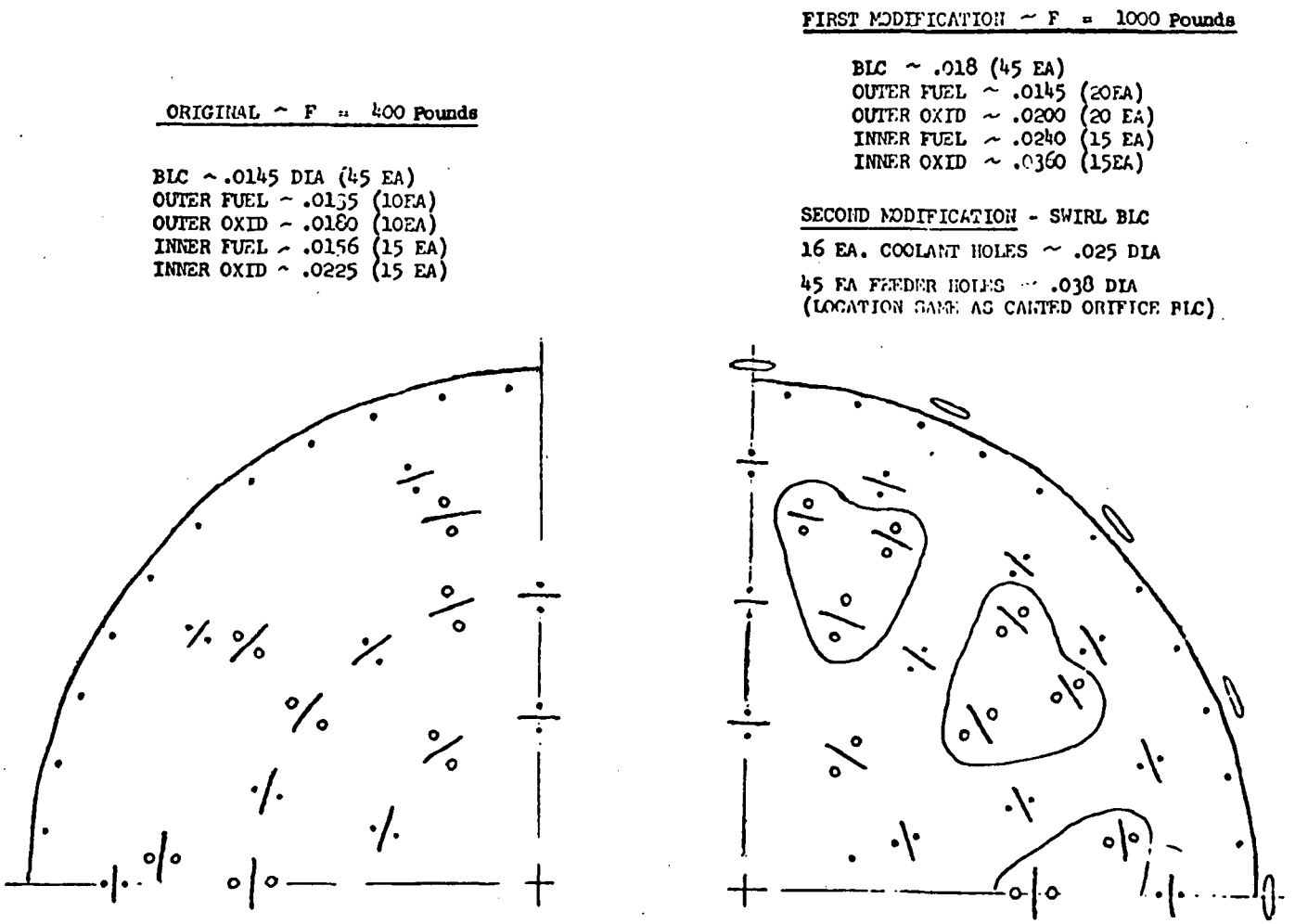

Figure 52. History of NAS7-304 Boundary Layer Coolant Injector

manifolding*, contains small outer row fuel orifices (0.0145-inch-diameter), and has sharp, uncontoured, orifice entrances.

A new injector incorporating the following features was consequently designed: (1) inwardly canted fans (like-on-like) to decrease the injector sensitivity to both chamber fuel fan protection and oxidizer misimpingement, (2) improved boundary layer coolant manifolding, (3) larger outer row orifices, and (4) contoured orifice entrances.

Injector Face Layout

A schematic representation of the new injector face pattern is shown in Fig. 53. The pattern consists of three rings of like doublet elements, where the inner two rings incorporate aligned fuel and oxidizer doublets, while the outer ring of fuel doublets is located 0.17 inch nearer the thrust chamber wall than the oxidizer doublets. This pattern is basically similar to that of the NAS7-304 boundary layer coolant injector, with the most notable change being improved circumferential symmetry. The diameters of each of the rings remain unchanged from the NAS7-304 design. For most injectors of this type (but for use with other propellants), the outer ring of fuel and oxidizer doublets would be located nearer the chamber wall to produce a more favorable mass flux distribution. Previous experience with FLOX/B_2H_6 has shown that when the outer elements are placed near the wall, excessive deposition can occur. Since the NAS7-304 injector produced what was considered a tolerable amount of deposits, the radial dimensions were not altered.

One of the approaches taken to reduce the influence of deposits on injector operation was to cant both the fuel and oxidizer fans away from the chamber wall. Should, for example, oxidizer misimpingement occur, a longer path is traversed before an oxidizer jet can intersect the wall. Over this longer path, the jet would more than likely break up and mix, thereby losing its contiguous streaking characteristics. The cant angles selected for the new design are shown in Fig. 54.

*The manifold for the presently incorporated 16 swirl boundary layer coolant holes were adapted from a manifold for 45 axial boundary layer coolant holes.

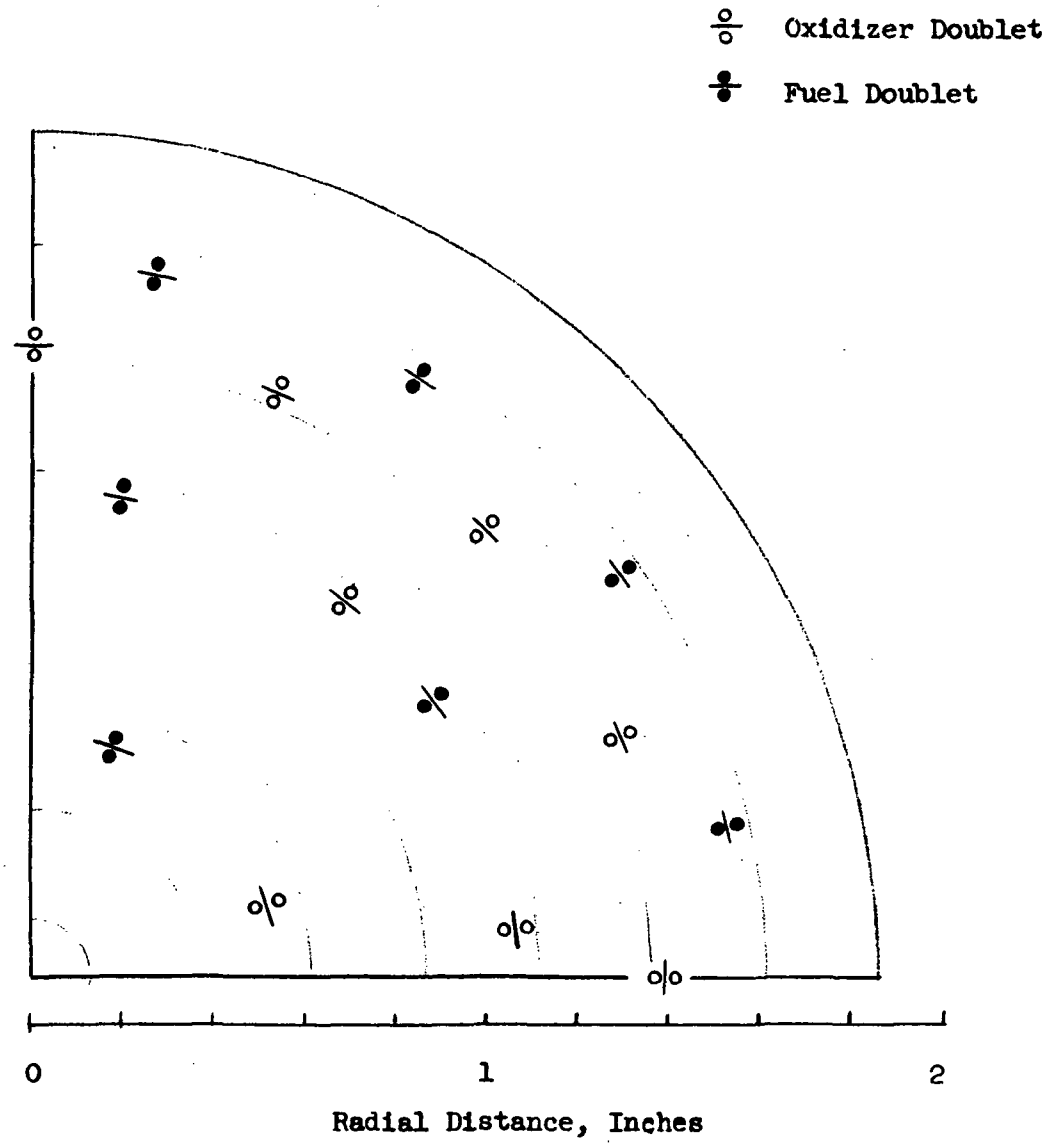

Figure 53. Element Layout for New Injector Design

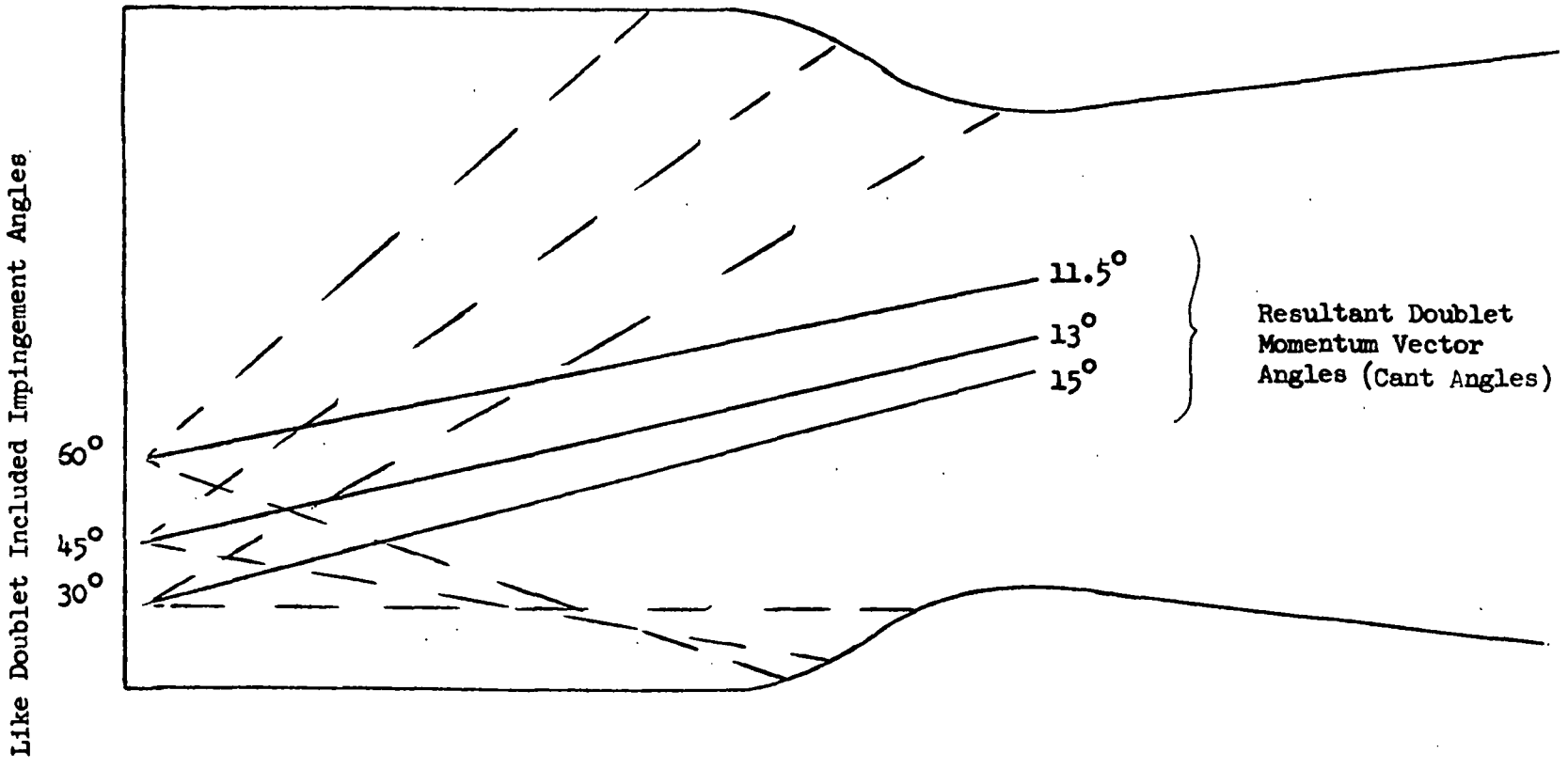

Figure 54. Cant Angles for New Injector Design

In the outer ring, the inner oxidizer jet (which is normally inclined toward the wall) is now directed axially. The outer jet is oriented inward 30 degrees so that the resultant momentum vector is canted 15 degrees toward the thrust chamber axis. The middle ring has an impingement angle of 45 degrees with a cant angle of 13 degrees toward center. The inner ring contains the conventional 60-degree impingement angle and is also canted toward the center.

Performance Analysis

An analysis of the performance characteristics of the new injector was conducted to aid in the selection of certain design parameters. Propellant atomization and vaporization were determined analytically. Cold flow results with the boundary layer coolant injector previously employed were used to provide estimates of performance losses due to incomplete mixing.

The analysis aided in the selection of the following design variables: (1) number of elements, (2) impingement angle, (3) fuel and oxidizer orifice diameters, (4) radial mixture ratio stratification, and (5) injection pressure drop.

Prior to the analysis, a number of assumptions and design restraints were made. These included: (1) maintenance of the existing chamber geometry (5-inch injector-to-throat length, 2.14 contraction ratio), (2) three rings of elements as incorporated in the present injector, (3) minimum orifice diameter of 0.020 inch, (4) maximum injection ΔP of 100 psi, and (5) overall injector mixture ratio of 3.0 (including 6 percent* film coolant).

The performance analyses followed methods of previously described in detail in Ref. 2. For the present analysis, an expression describing the effects of impingement angle on dropsize was also needed. The equation used is that given by Fry, Thomas, and Smart (Ref. 10) and is:

$$D_{30} = 0.775 - 0.000164V_j \sin(\gamma/2) \text{ (CGS Units)}$$

*Targeted value. Actual operating percentages were usually on the conservative side heat-transfer-wise.

where

D_{30} = volume mean dropsize

V_j = injection velocity

γ = included impingement angle

Previous dropsize experiments at Rocketdyne have substantiated this expression for prediction of the change in dropsize over a large range of impingement angles.

A computer program was then written to incorporate the combustion model results and the various dropsize expressions. In addition, the experimental cold flow mixing efficiency of the current film coolant injector was assumed, and stratification efficiencies were incorporated to account for deliberate off-mixture-ratio conditions.

The effect of fan cant angle was examined in the performance analysis; the results of this effort are shown in Table 12, which represents the case run with the selected design parameters, and in Fig. 55, which shows the effect of row impingement angle (or fan cant angle) upon performance. The X-scale on Fig. 55 represents the downstream location at which oxidizer jet intersection with the wall could first occur if an orifice of an oxidizer doublet element misimpinged or plugged. Thus, Fig. 55 indicates the approximate performance penalty associated with "safer" injector designs having greater oxidizer jet intersection distances from the injector face.

The selected design consists of 28 elements (i.e., 28 fuel and 28 oxidizer orifices) with the inner ring (Ring 1) having an impingement angle of 60 degrees, while the middle and outer rings incorporate angles of 45 and 30 degrees, respectively. These impingement angles result in the fan cant angles shown earlier in Fig. 54. Selection of these values appears in good compromise between injector insensitivity and high performance (as shown in Fig. 55).* The orifice diameters

*Lesser impingement angles for each row would result in still greater insensitivity but lower performance.

TABLE 12. FLOX/B_2H_6 PERFORMANCE ANALYSIS - THREE RING INJECTOR

PARAMETER	RING 1	RING 2	RING 3
NUMBER OF ELEMENTS	4	8	16
IMPINGEMENT ANGLE, DEG	60	45	30
OXID ORIFICE DIA, INCH	0.0330	0.0330	0.0260
FUEL ORIFICE DIA, INCH	0.0225	0.0225	0.0225
MASS PERCENT	0.174	0.349	0.477
MIXTURE RATIO	5.107	5.107	3.170
OXID $\bar{D}$, MICRONS	75.0	86.7	88.5
FUEL $\bar{D}$, MICRONS	76.8	94.0	103.6
VAPORIZATION EFFICIENCY	0.9578	0.9331	0.9293

V(OXID)= 90.2 FT/SEC Δ P (OXID)= 90.4 PSID

V(FUEL)= 126.9 FT/SEC Δ P (FUEL)= 53.6 PSID

OVERALL MIXTURE RATIO = 4.00

VAPORIZATION EFFICIENCY (OVERALL) = 0.9356

STRATIFICATION EFFICIENCY = 0.9898

EXPERIMENTAL MIXING EFFICIENCY = 0.9880

OVERALL C STAR EFFICIENCY = 0.9149

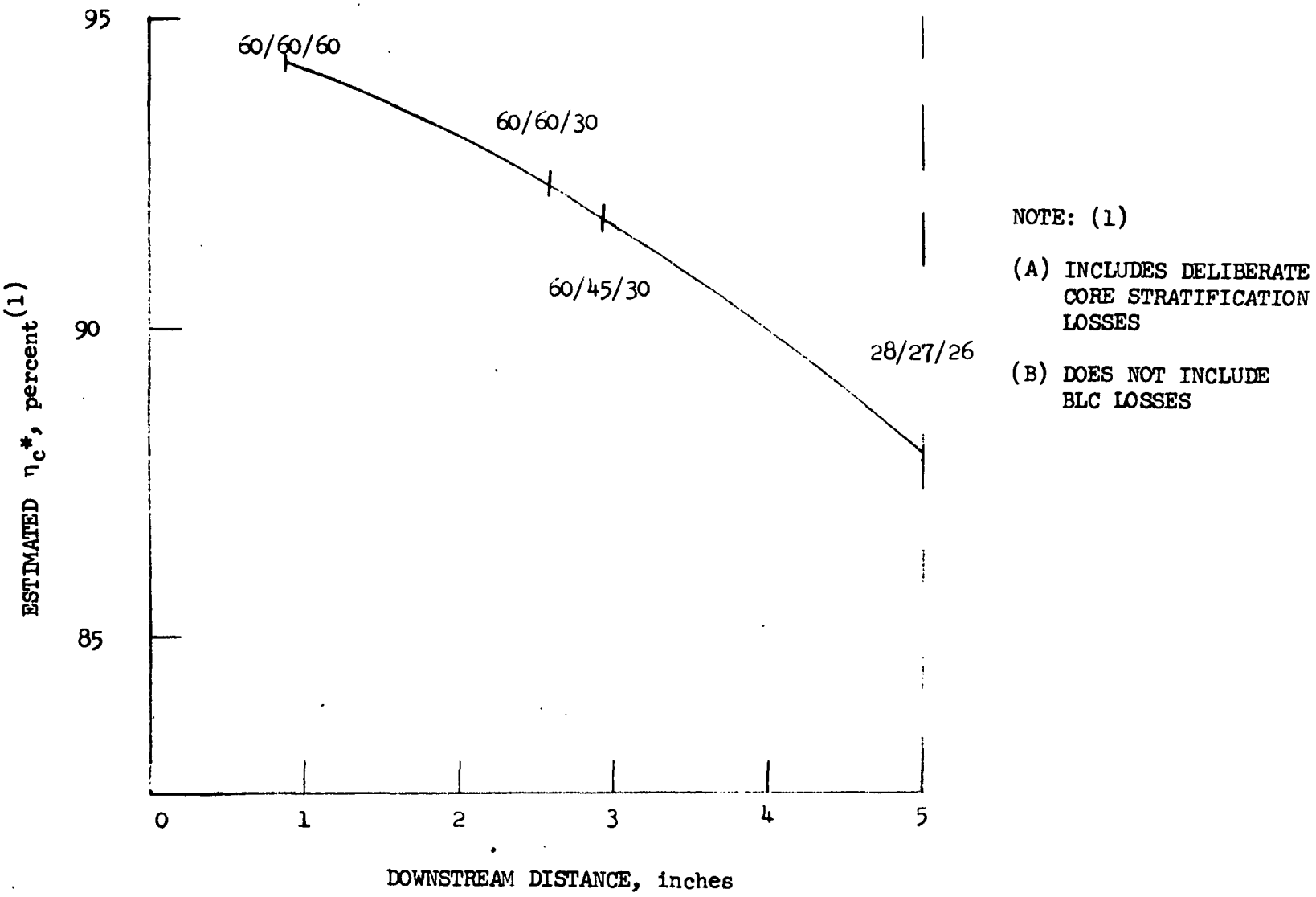

Figure 55. Effect of Row Impingement Angle on Performance

range from 0.0225 to 0.033 inch, with the smaller oxidizer orifice size in the outer ring to produce the desired stratification. The overall core c* efficiency (less boundary layer coolant) for this design is 91.5 percent.

From the data generated in a previous FLOX/B_2H_6 program (Ref. 2), a nearly linear decrease in c* efficiency was found as the amount of boundary layer coolant was increased. The slope of this curve at a core mixture ratio of 4.0 was about -0.5 percent η_{c*} for each +1.0 percent boundary layer coolant (BLC flow/total flow x 100). For a core mixture ratio of 4.0 and 6 percent boundary layer coolant (which results in an overall mixture ratio of 3.0), the predicted c* performance for the selected injector design is

$$91.5 - 6(0.5) = 88.5 \text{ percent.}$$

Similarly, for a core mixture ratio of 4.0 and 10 percent BLC, the predicted c* performance efficiency is 91.5 - 10(0.5) = 86.5 percent.

Radial Mixture Ratio Distribution

To ensure that oxidizer does not contact the chamber wall it is desired that the mixture ratio of the bipropellant spray mass flux fall off rapidly with increasing radial position in the chamber. The LISP (Liquid Injector Spray Patterns) computer program, developed under Air Force Contract F04611-68-C-0043 and described in Ref. 11, was used in conjunction with the new injector element pattern to obtain predictions of spray mass fluxes for each propellant for an array of radial and angular mesh points in an axial plane two inches downstream from the injector face. The two-inch position was selected as representative since angular variations of mixture ratio were nearly nonexistent at this location while marked variations were observed at the one-inch location. The existence of angular variations of mixture ratio at a given radial location near the injector is indicative of propellant spray fans not yet filling the chamber cross section. Experience has shown the LISP analysis to be most effectively employed at the axial location at which the spray fans have just filled the chamber cross-section but not yet

interacted among themselves (Ref. 11). This location appears, in this case, to be just upstream of 2 inches. The mixture ratio distribution was calculated from the bipropellant spray mass fluxes. These results were compared with similar calculations for the NAS7-304 injector design. The angular variations of mixture ratio at various radial positions for both injectors are shown in Fig. 56. It is readily observed from this figure that for the new injector design, mixture ratio decreases rapidly with increasing radial position, thereby adding to the wall protection afforded by the swirl boundary layer coolant injection itself. The mixture ratio decrease with increasing radial position is not nearly as rapid for the NAS7-304 injector design.

Injector Face Heating

A simplified analysis was conducted to assess the cooling capability of the new injector design relative to the previous boundary layer coolant injector. The propellant manifold velocities and areas have been maintained at about the same level, hence, the only significant change in heat removal was assumed to be in the orifice flow. For this analysis the product $h_L A$ was calculated for both the fuel and oxidizer orifices and compared with those of the NAS7-304 injector. The results showed that the coefficients ($h_L A$) were higher by 5 percent and 20 percent (fuel and oxidizer, respectively) for the new design, a result of slightly longer orifice lengths and a higher oxidizer injection velocity. Therefore, the new injector design was predicted to result in somewhat lower injector face temperatures than those experienced with the existing NAS7-304 injector.* Since no injector face heating problems were encountered with the NAS7-304 injector, it was concluded that no such problems would be encountered with the new injector design.

Detailed Injector Design

Detailed drawings of the injector face, injector body, BLC ring and injector assembly are shown in Fig. 57 through 61.

*Injector face temperatures encountered with the injector design were actually found to be higher than previously experienced. The difference was believed due to the much reduced fuel manifold cooling capability.

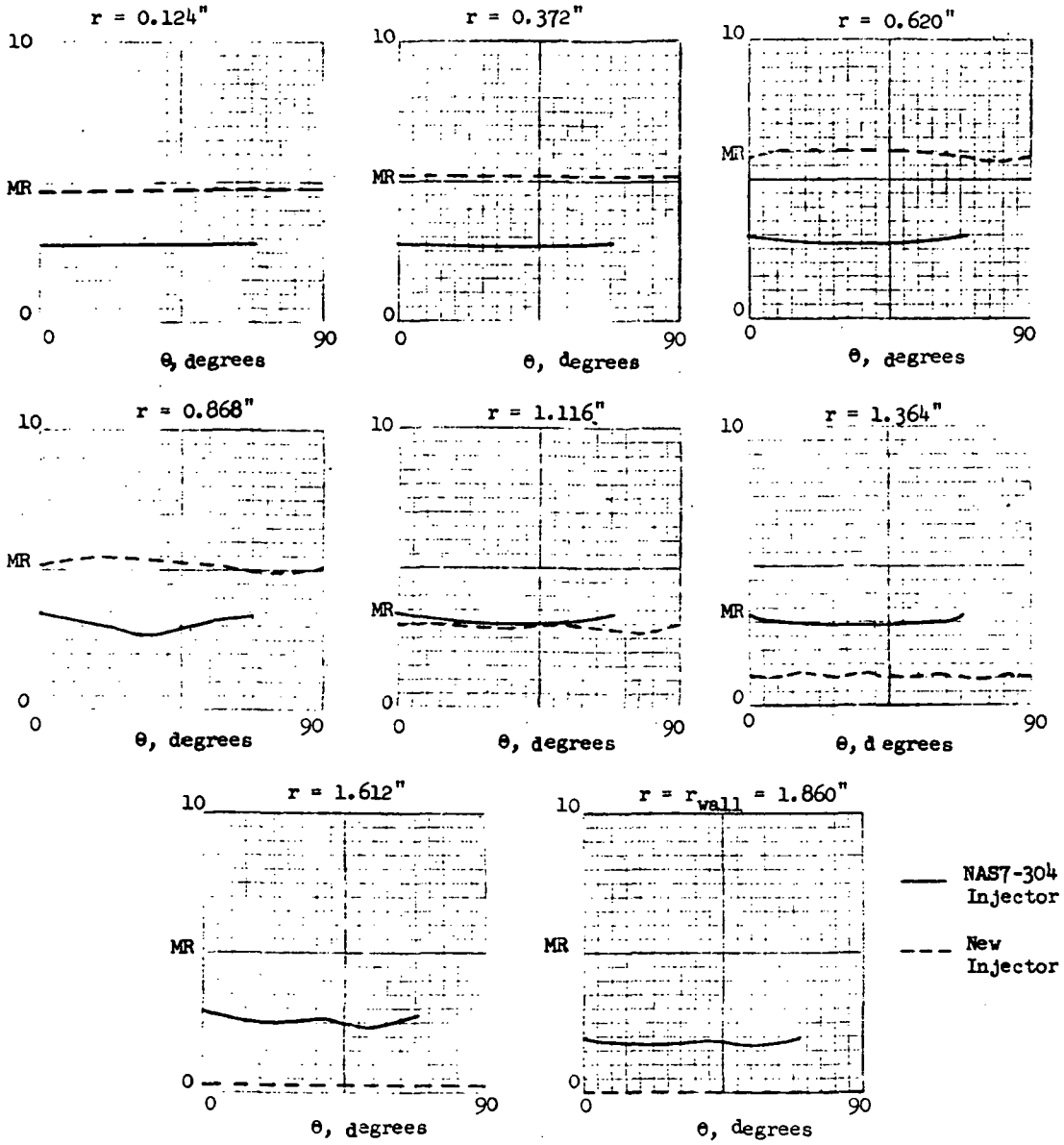

Figure 56. Mixture Ratio Distribution Calculated from LISP Program for New and NAS7-304 Injector Designs

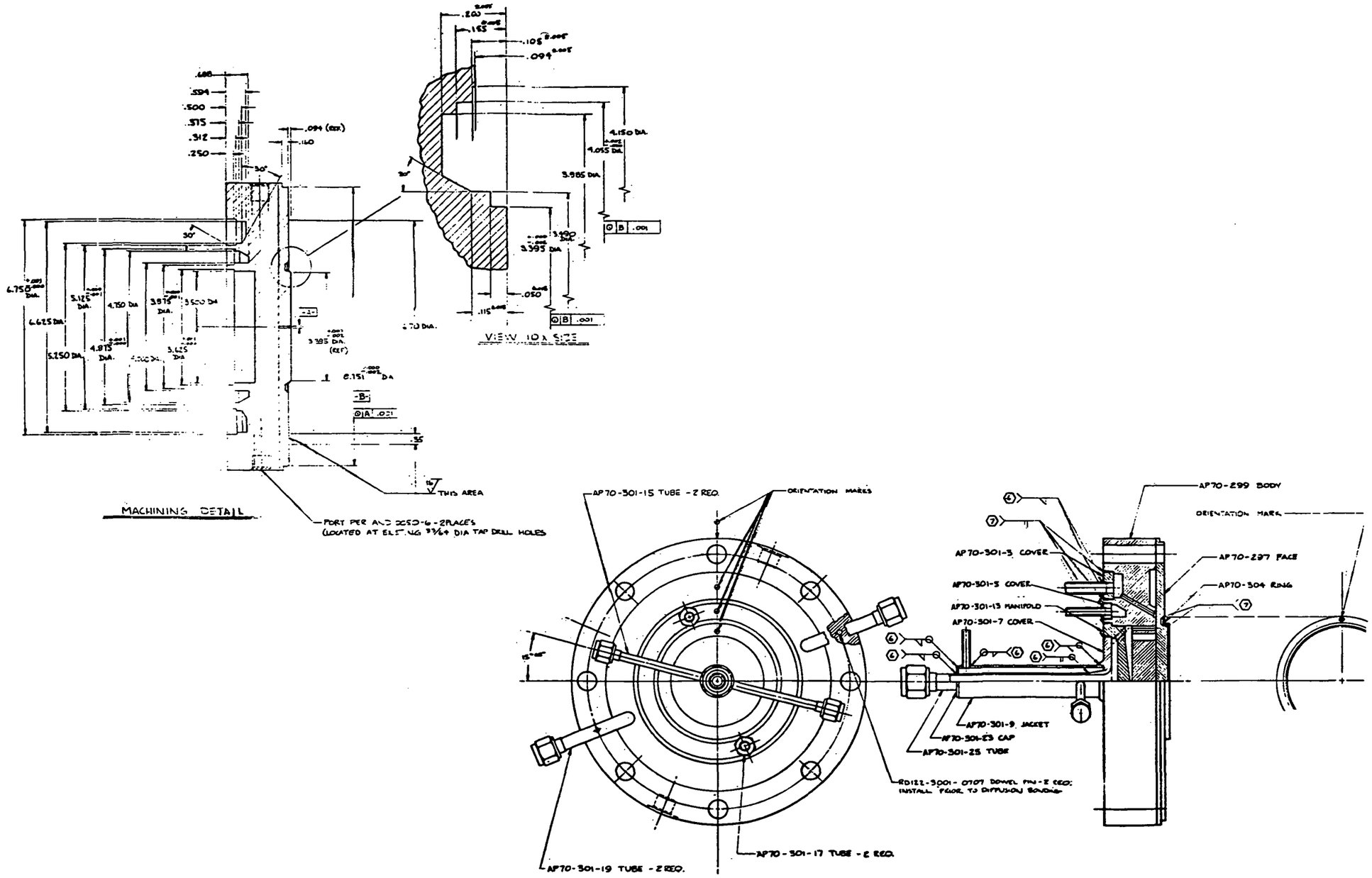

Figure 57. Injector Assembly, OF_2/B_2H_6

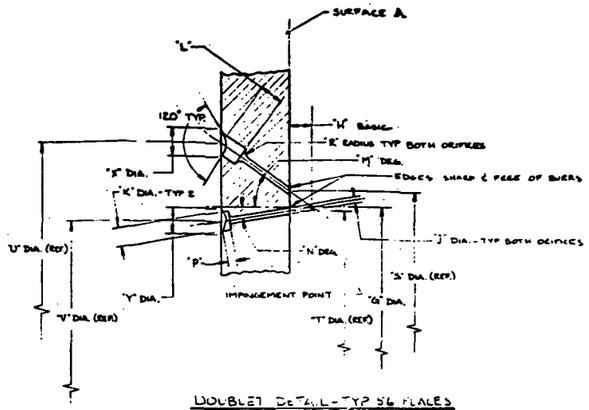

DOUBLET DETAIL - TYP 56 PLACES
APPROX. 4 x SIZE

DOUBLET SET IDENTIFICATION	NUMBER OF EQUALLY SPACED DOUBLETS IN SET	IMPINGEMENT DIAMETER "G" DIA. BASIC	IMPINGEMENT POINT TO FACE DIMENSION "H" BASIC	"J" DIA.	"K" DIA	C'BORE DIAMETER	ANGLE - OUTER ORIFICE "M" DEG.	ANGLE - INNER ORIFICE "N" DEG	PROPELLANT - REF.	"R" RAD.	"S" REF DIA	"T" REF DIA	"U" REF DIA	"V" REF DIA	DOUBLET SET ANGULAR ORIENTATION "W" DEG.	C'SINK DIAMETER - OUTER "X" DIA.	C'SINK DIAMETER - INNER "Y" DIA.	ANGULAR SPACING BETWEEN DOUBLETS - REF.	L	C'BORE DEPTH - OUTER	C'BORE DEPTH - INNER P
A	4	1.067	.111	.0330	.1065	41°30'	18°30'	0%		.033	1.243	.993	1.927	.742	16°30'	.172	.144	90°	.171	.065	
B	4	1.067	.076	.0225	.0730	41°30'	18°30'	FUEL		.022	1.201	1.046	1.865	.765	70°	NONE	NONE	90°	.276	.170	
C	8	2.134	.121	.0353	.1065	35°30'	9°30'	0%		.033	2.307	2.094	2.842	1.868	5°40'	.161	.144	45°	.131	.050	
D	8	2.134	.082	.0225	.0730	35°30'	9°30'	FUEL		.022	2.251	2.107	2.784	1.981	35°	NONE	NONE	45°	.236	.155	
E	16	2.788	.101	.0220	.0820	30	0	0%		.024	2.905	2.748	3.336	2.788	0°	.129	.116	22°30'	.175	.115	
F	16	3.150	.083	.0225	.1150	30	0	FUEL		.022	3.232	3.130	3.664	3.150	12°30'	NONE	NONE	22°30'	.40	.082	

-G-

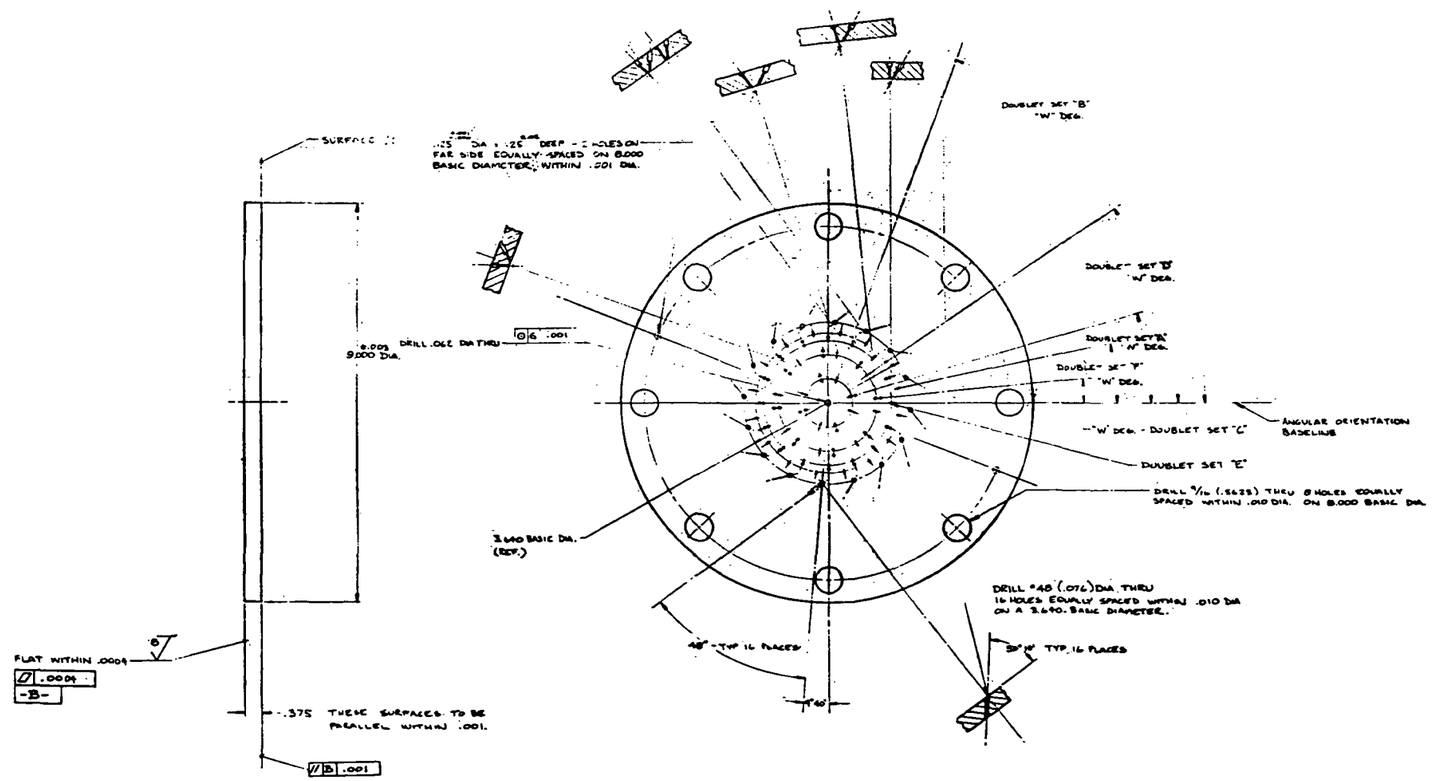

6. STRESS RELIEVE BETWEEN ROUGH & FINISH MACHINING BY BAKING 2 HRS AT 900°F IN ARGON ATMOSPHERE. COOL SLOWLY.
5. DO NOT CLEAN WITH NITRIC ACID OR OTHER ETCHANT.
4. FUEL ORIFICES ARE SHOWN SOLID IN FACE VIEW FOR IDENTIFICATION ONLY.
3. ALL DOUBLETS OF EACH DOUBLET SET ARE EQUALLY SPACED WITH IMPINGEMENT LOCATED AS SHOWN WITHIN .005.
2. ORIFICE CENTERLINES OF EACH INDIVIDUAL DOUBLET TO INTERSECT WITHIN .005.
1. EACH DOUBLET CONSISTS OF TWO HOLES AS SHOWN IN ENLARGED DETAIL.

Figure 58. Face - OF_2/B_2H_6 Injector

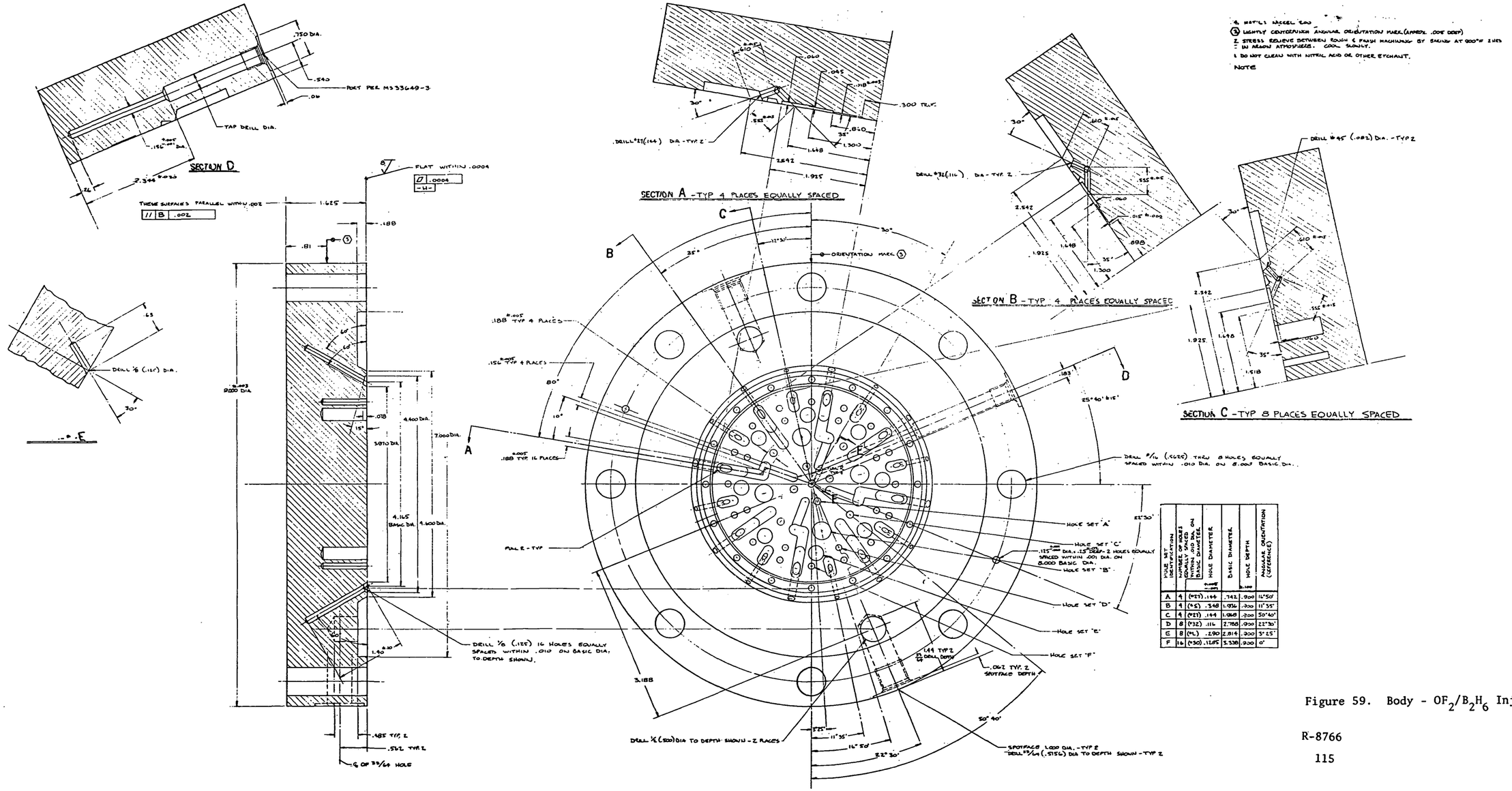

HOLE SET IDENTIFICATION	NUMBER OF HOLES EQUALLY SPACED WITHIN .010 DIA. ON BASIC DIAMETER	HOLE DIAMETER	BASIC DIAMETER	HOLE DEPTH	ANGULAR ORIENTATION (REFERENCE)
A	4	(#27) .144	.742	.900	11°50'
B	4	(#5) .348	1.936	.300	11°55'
C	4	(#27) .144	1.948	.300	50°40'
D	8	(#32) .116	2.788	.900	22°30'
E	8	(#L) .290	2.814	.300	3°25'
F	16	(#30) .1285	3.338	.900	0°

Figure 59. Body - OF_2/B_2H_6 Injector

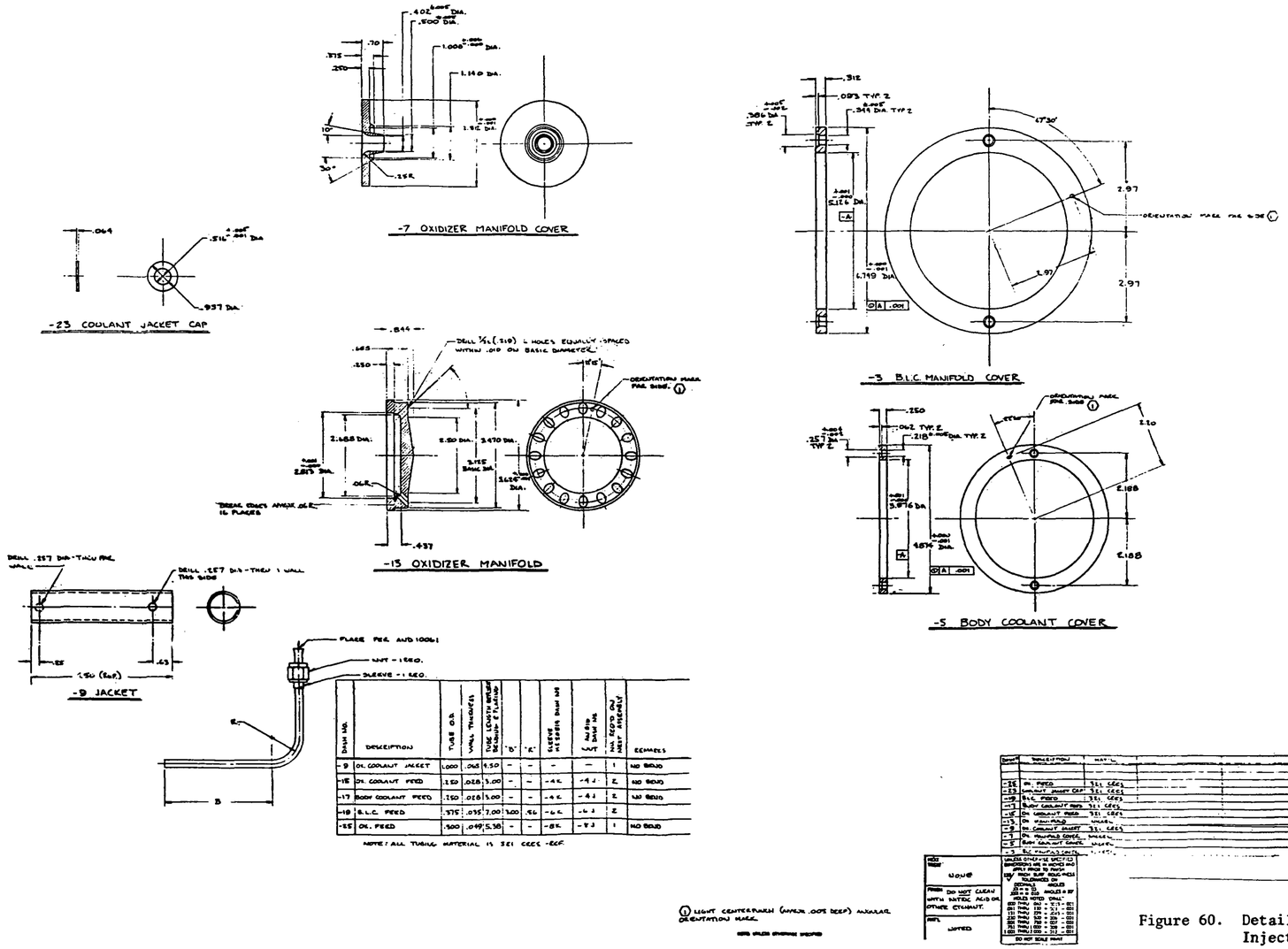

DASH NO.	DESCRIPTION	TUBE O.D.	WALL THICKNESS	TUBE LENGTH BETWEEN BRAZING & FLANGE	"B"	"E"	SLEEVE MATERIAL DASH NO.	"A"	NO. REQ'D ON ASSY.	REMARKS
-9	OX. COOLANT JACKET	.1000	.045	4.50	-	-	-	-	1	NO BRAZE
-15	OX. COOLANT FEED	.150	.028	3.00	-	-	-4 E	-4 J	2	NO BRAZE
-17	BODY COOLANT FEED	.150	.028	3.00	-	-	-4 E	-4 J	2	NO BRAZE
-19	B.L.C. FEED	.375	.035	7.00	3.00	.56	-6 E	-6 J	2	
-25	OX. FEED	.500	.049	5.38	-	-	-8 E	-8 J	1	NO BRAZE

DASH NO.	DESCRIPTION	MATERIAL			NO. REQ'D
-25	OX. FEED	321 CRES			1
-23	COOLANT JACKET CAP	321 CRES			
-19	B.L.C. FEED	321 CRES			2
-17	BODY COOLANT FEED	321 CRES			2
-15	OX. COOLANT FEED	321 CRES			2
-13	OX. MANIFOLD	MONEL			1
-9	OX. COOLANT JACKET	321 CRES			1
-7	OX. MANIFOLD COVER	MONEL			1
-5	BODY COOLANT COVER	MONEL			1
-3	B.L.C. MANIFOLD COVER	MONEL			1

UNLESS OTHERWISE SPECIFIED DIMENSIONS ARE IN INCHES AND TOLERANCES ARE AS FOLLOWS

DECIMALS	ANGLES
.XX ± .03	.XX ± .5°
.XXX ± .010	.XXX ± .25°

FINISH: DO NOT CLEAN WITH NITRIC ACID OR OTHER ETCHANT.

MATL: NOTED

Figure 60. Details - OF_2/B_2H_6 Injector

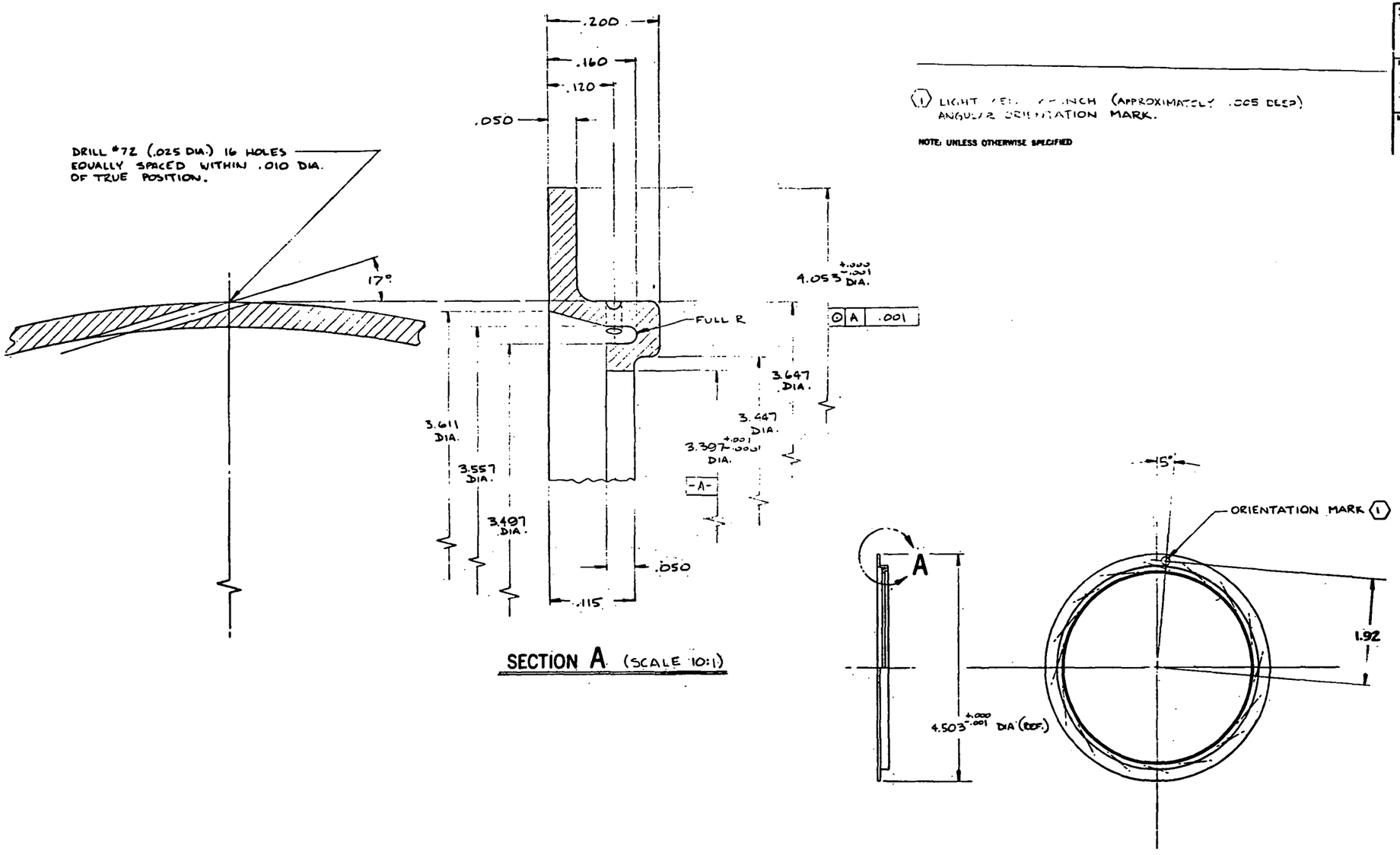

Figure 61. Ring - OF_2/B_2H_6 BLC

FABRICATION TECHNIQUE

The method of fabricating the NAS7-304 film coolant injector consisted of machining the propellant manifolds and orifice pattern from a single piece of material. Manifolding was accomplished by radial feeder passages for the fuel while the oxidizer was fed from the rear of the injector through axial feeders.

This technique is one of the simplest for a like doublet pattern in which fuel and oxidizer fan alignment is required. This method has one serious drawback, however, in that the orifice entrance is not easily accessible for deburring or contouring. For the new injector, prepared orifice inlets were considered necessary to product uniform hydraulic characteristics from orifice to orifice. This requires separate construction of the propellant manifold and orifice plate (or rings) and joining of the separate components after the completion of internal machining.

Several fabrication techniques were reviewed for use in the proposed injector. Due to the fact that the selected orifice pattern requires rather unconventional manifolding, only two techniques were considered in detail. The two methods differed primarily in the manner in which an orifice plate is joined to the manifold assembly, with one consisting of diffusion bonding the plate to the manifold and the second incorporating electron beam welding of the two parts.

Investigation of these two methods revealed that prepared orifice entrances were feasible and that cost and time to fabricate were similar for both techniques. Diffusion bonding allowed for greater versatility with respect to both orifice patterns and propellant manifolding design (no requirements for radially in-line oxidizer doublets). Based on these considerations, the diffusion bonding technique was selected for construction of the new injector.

The technique of diffusion bonding has been widely used in the past, primarily in the manufacture of components for the aircraft and missile industries. The Los Angeles Division of NAR has made significant advances in metal joining through the

use of the solid-state bonding technique. In this method, the two parts to be joined areplaced in a restraining device and subjected to a hard varuum. Pressure is then applied normal to the joining surface. The temperature of the entire system is slowly increased to a level which depends upon the type of metals being used. When the proper combination of pressure and temperature has been applied, the resulting bond joint strength approaches that of the parent metal.

The feasibility of applying diffusion bonding to injector fabrication was initially established during a Rocketdyne IR&D program in 1968 (Ref. 12). Two nonfirable injectors were fabricated and subjected to pneumatic (300 psig) and hydraulic (10,000 psig) pressure checks. Following the successful completion of this effort, a full scale injector was evaluated with FLOX/MMH at a chamber pressure of 100 psia. Ten successful firings were made, with test durations ranging from 2 to 5 seconds each.

The diffusion bonding technique is also being used in injector fabrication on another currently active NASA program (NAS3-12051). This program utilizes the FLOX/methane propellant combination with nominal test conditions of 500 psia chamber pressure and 3000 pounds sea-level thrust. On that program, three diffusion bonded injectors have been fabricated to date. The first injector was severely damaged as a result of oxidizer manifold contamination and subsequent explosion within the oxidizer dome. However, a lead check of the fuel manifold after the explosion revealed that the diffusion bond had remained completely intact, in spite of the extreme overpressure which occurred during the explosion. Including the two diffusion bonded injectors subsequently fabricated, approximately 40 hot firings accumulating 100 seconds duration have been successfully completed without incident.

New Injector Components

The orifice plate and manifold assembly, fabricated from nickel 200, are shown in Fig. 62 and 63. Figure 62 shows the chamber side of the injector orifice face plate. The outer 16 holes shown in this figure are the feeder holes for the BLC manifold. The larger of the core orifices are oxidizer; the smaller orifices are fuel.

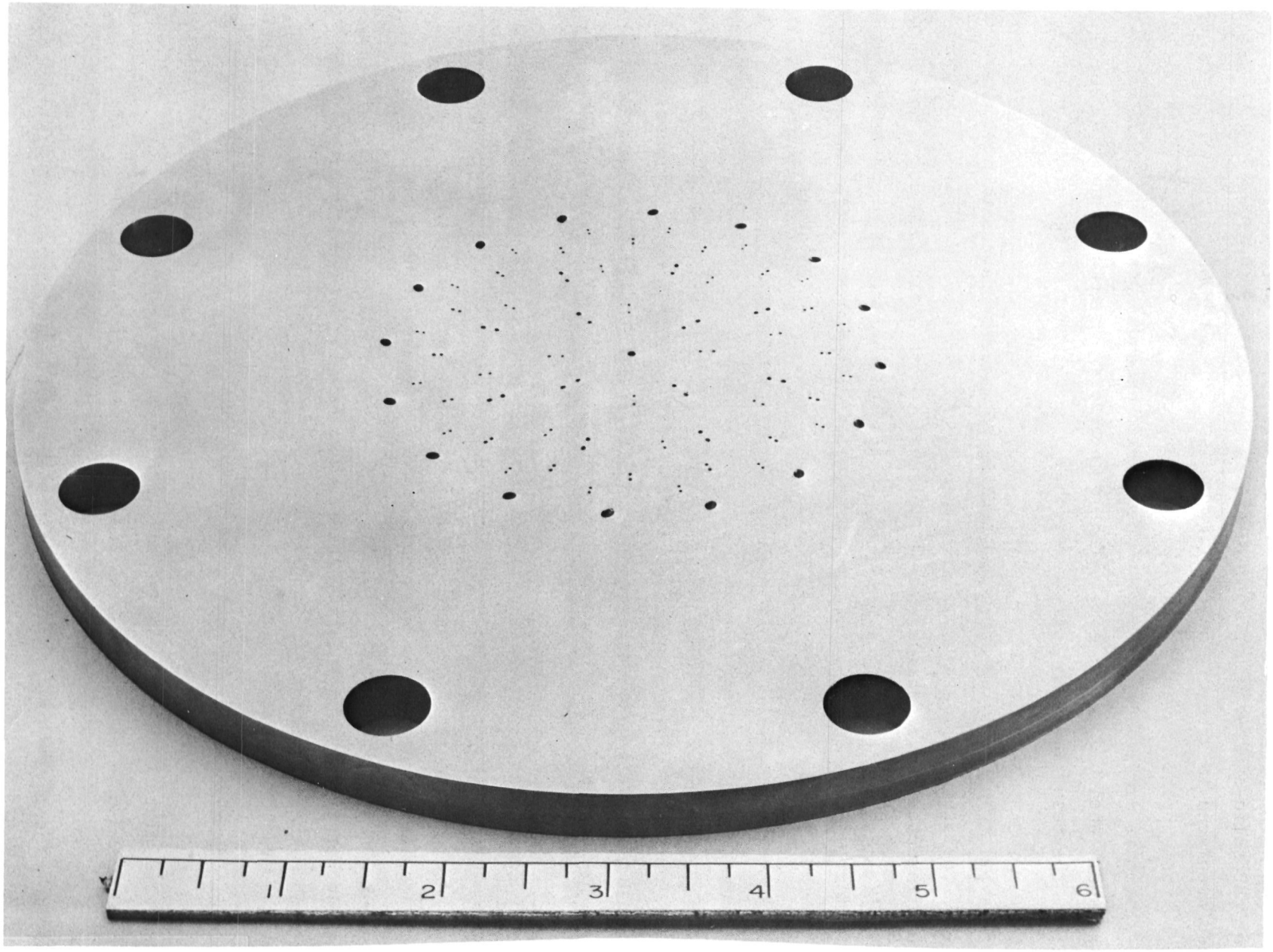

Figure 62. Injector Orifice Face Plate (Chamber Side)

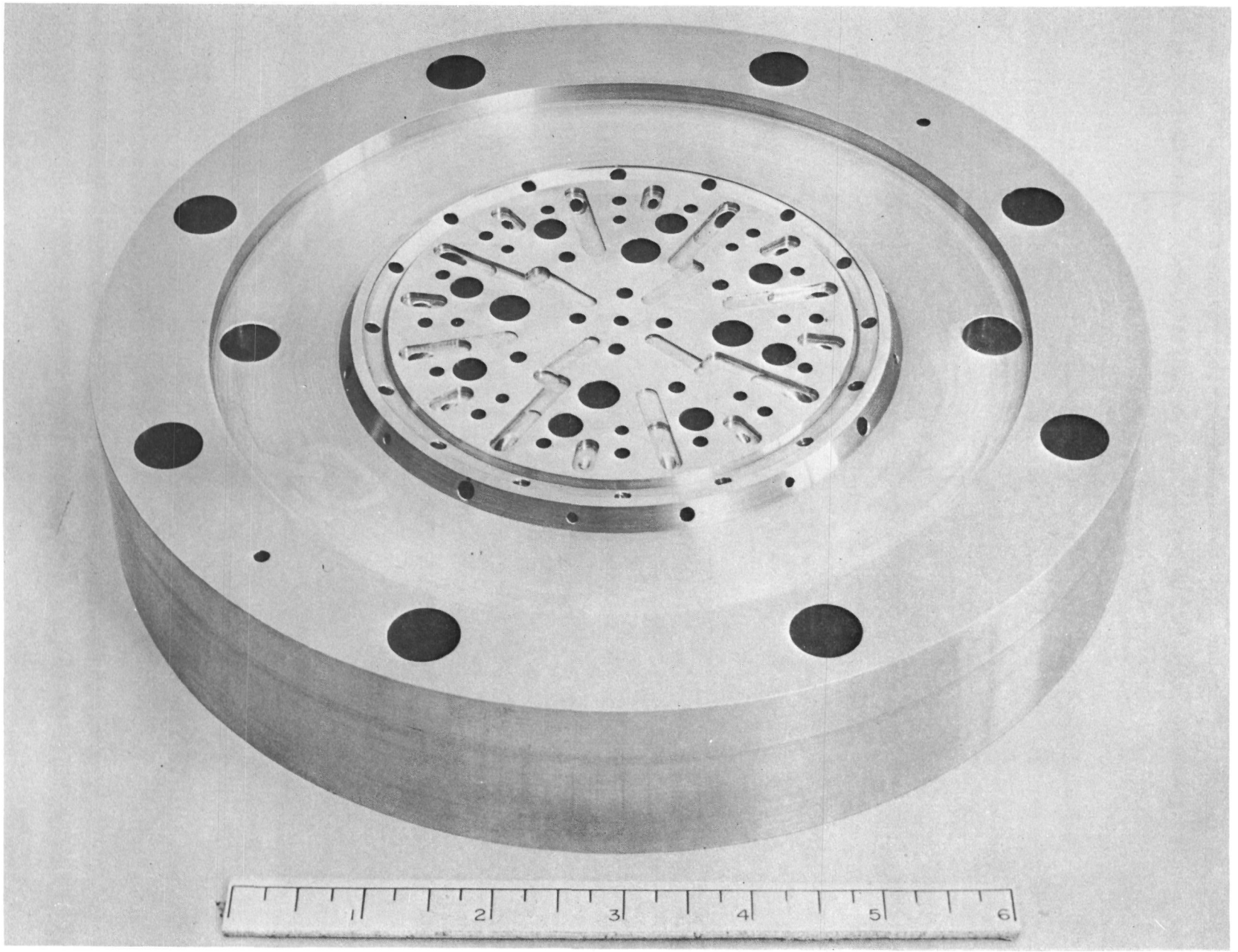

Figure 63. Injector Manifold Body

The hole in the center of the injector is the chamber pressure tap. All the main orifice entrances are recessed and rounded. The manifold body is shown in Fig. 63. The large (outer) grooved ring is the inlet to the main fuel manifold. The smaller annular ring is the boundary layer coolant manifold. The radially milled slots are the main fuel feeder passages. The 44 round holes in the center area are oxidizer feed holes, and the round hole at the geometric center is the chamber pressure top.

The completed injector assembly is shown in Fig. 64 and 65. Prior to hot firing, the individual propellant manifolds were subjected to 300 psig helium leak checks to verify the integrity of the diffusion bond. The helium leak checks indicated no intermanifold leakage.

Cold Flow

Cold flows of the new injector were initiated following hardware completion and helium leak check. A mass distribution water flow was performed with the new BLC ring. The resultant distribution, shown in Fig. 66, indicated a uniform mass flow. The injector core was cold flowed using trichloroethylene and water. The results are shown in Fig. 67 and 68. The canted fan injector design was observed to result, as expected, in a core mass distribution (Fig. 67) confined to the central portion of the injector face. The results of Fig. 67 and 68 corresponds to a predicted c* mixing efficiency of 0.975 for the injector core. That value is in excellent agreement with the prefabrication design estimate of 0.9898 x 0.9880 = 0.978 (see Table 12).

NEW CALORIMETER CHAMBER

Fabrication of a new nickel calorimeter chamber was completed. This calorimeter chamber was identical in all respects to the calorimeter chambers employed in the four hot firings (Tests 001-004) made earlier in the program. Thermal instrumentation similar to that used on Tests 003-004 was provided on this calorimeter chamber to record both axial and circumferential chamber temperatures.

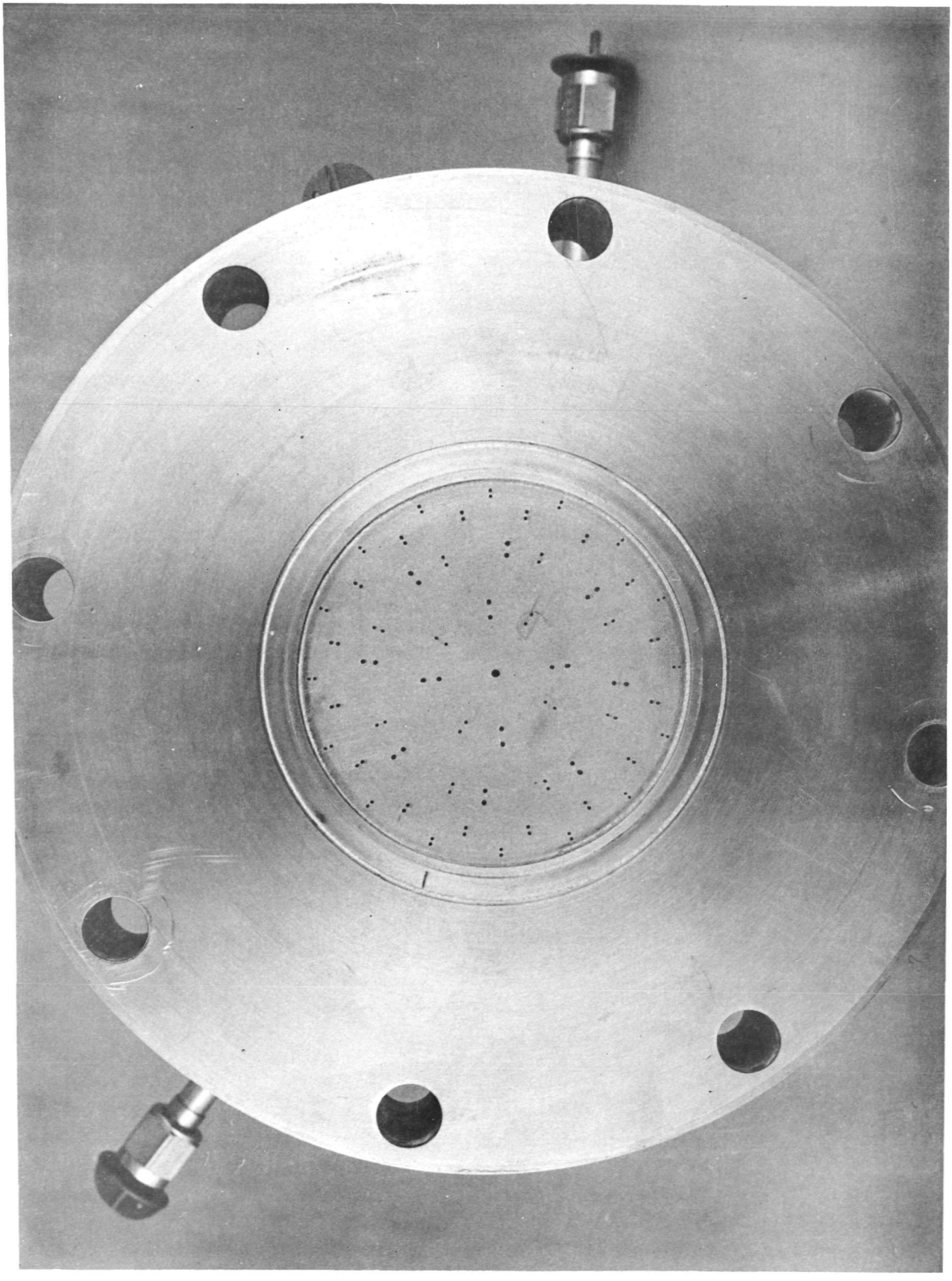

Figure 64. New Injector

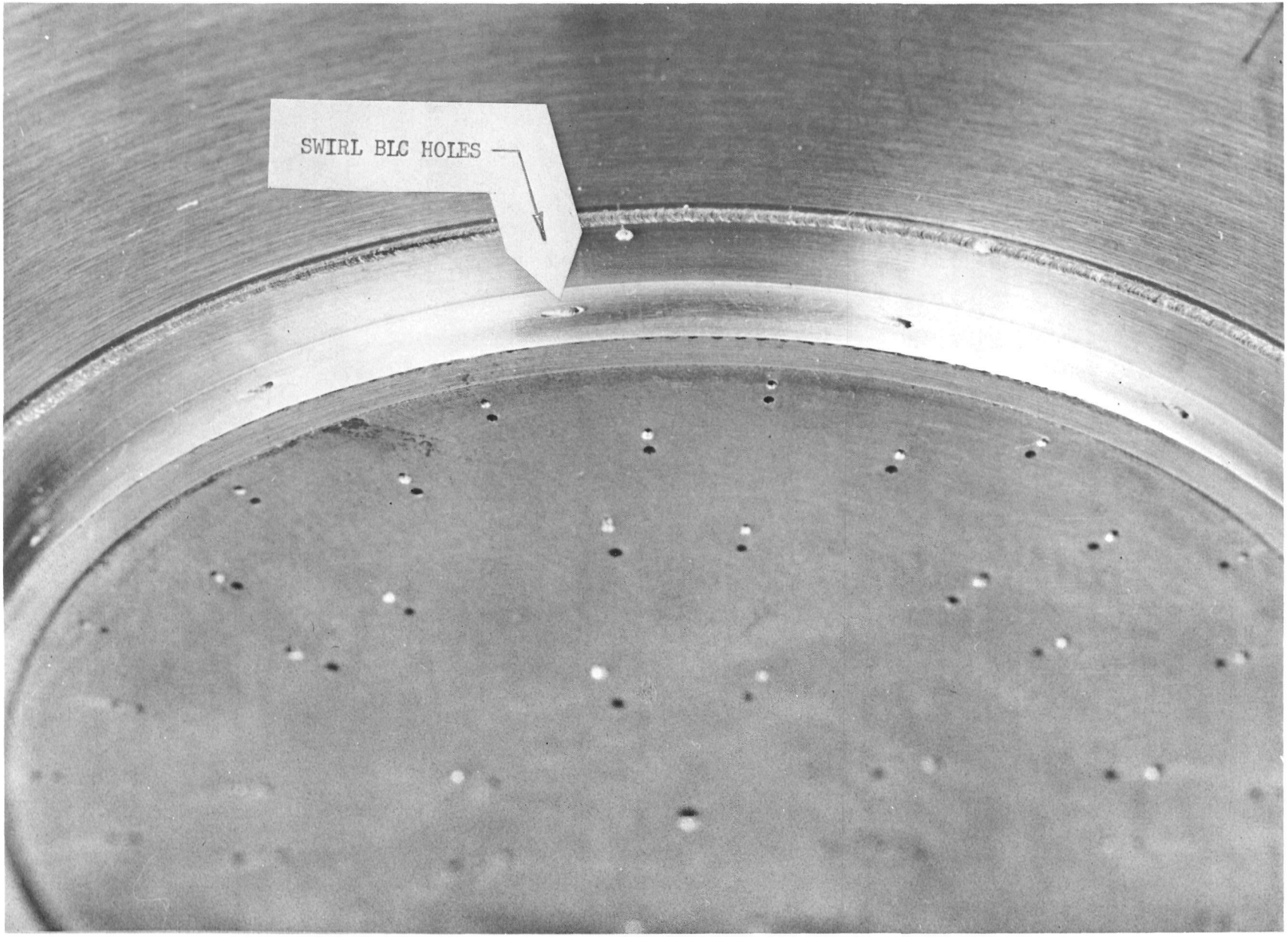

Figure 65. New Injector Showing BLC Holes

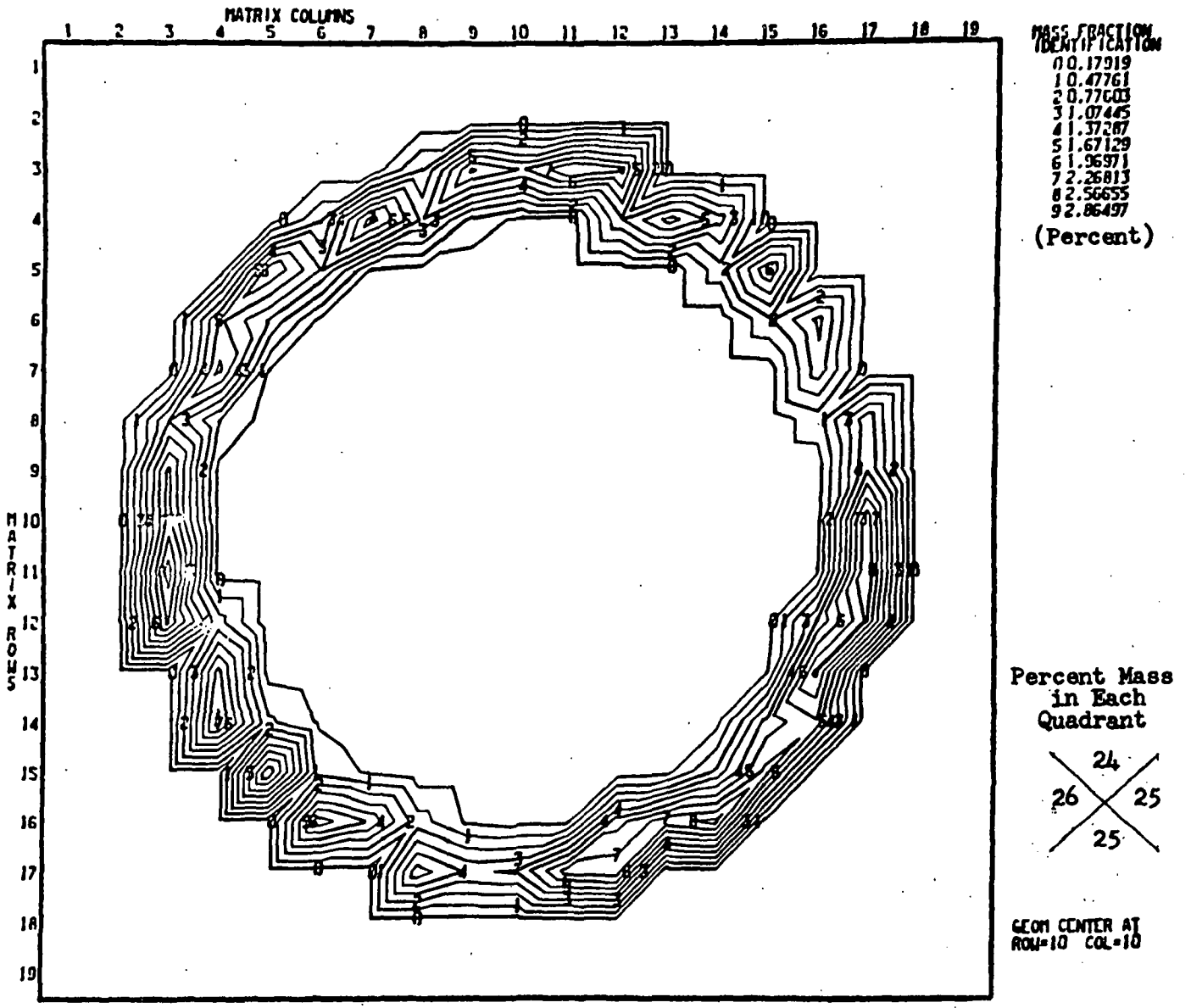

Figure 66. BLC Ring Mass Distribution Pretest Run 005

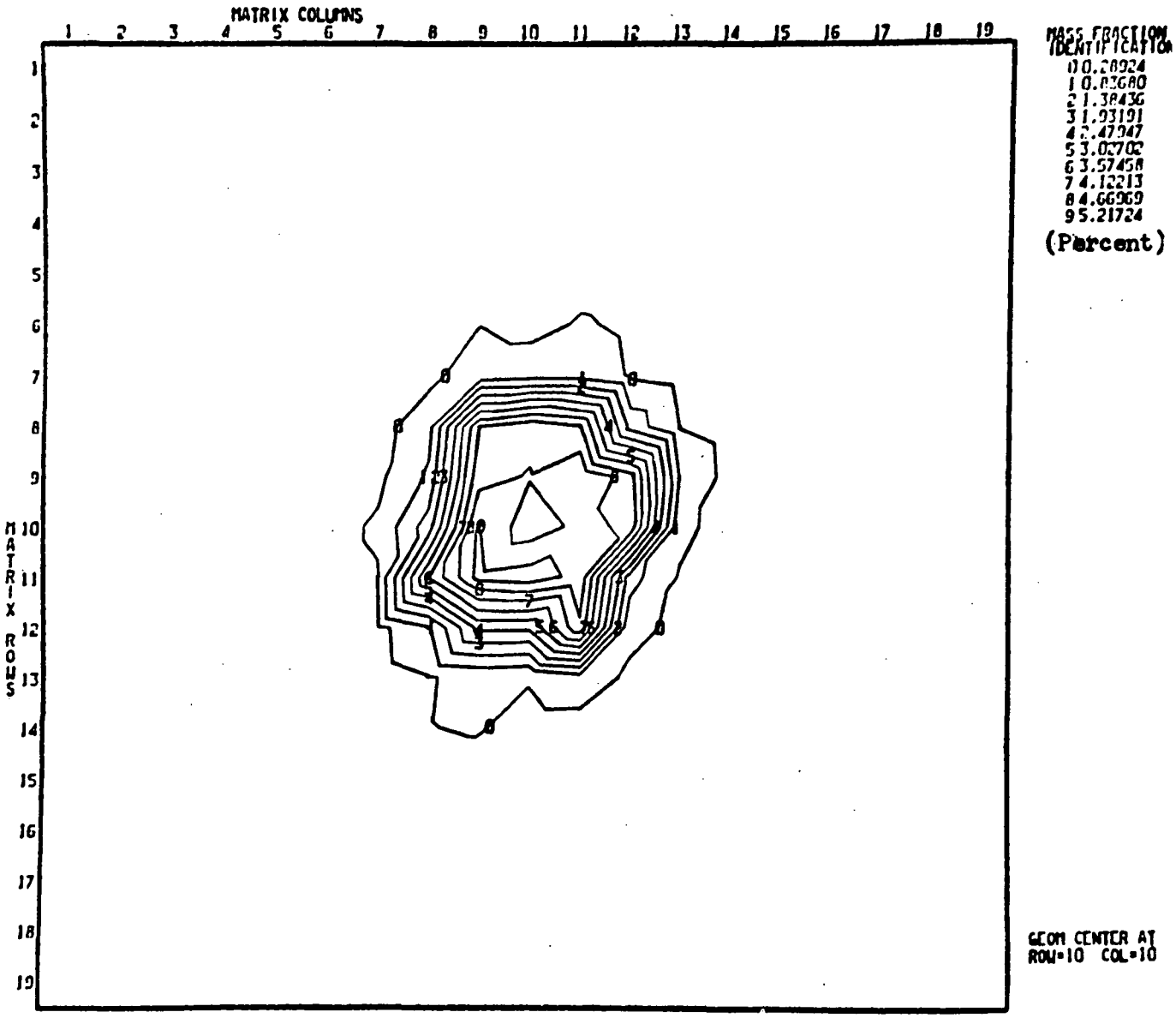

Figure 67. Core Mass Distribution Pretest Run 005

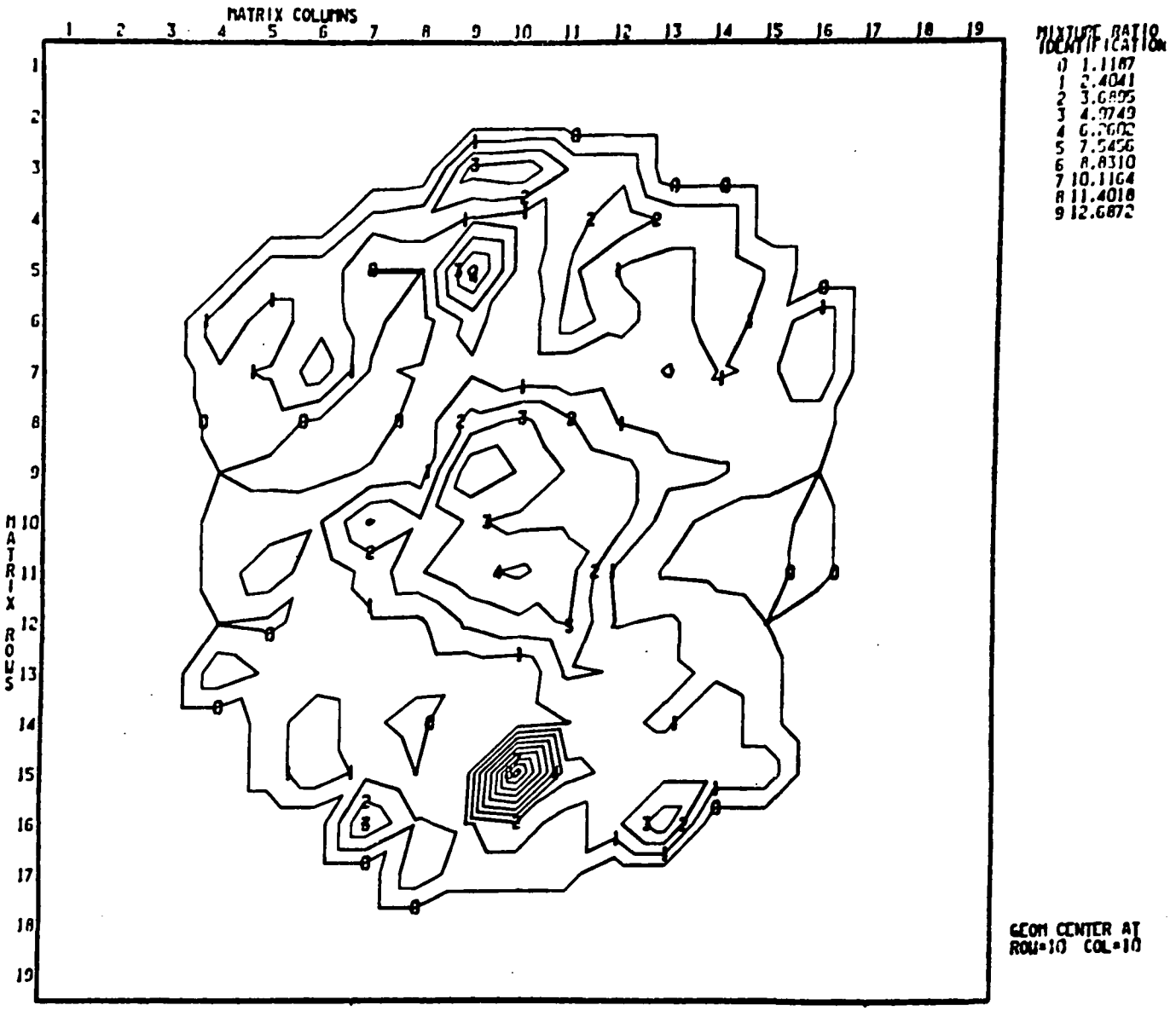

Figure 68. Core Mixture Ratio Distribution Pretest Run 005

Four axial rows of thermocouples were provided at 90-degree intervals around the outside chamber periphery (see sketch below). The zero-degree and 180-degree rows contained 8 thermocouples each at locations of 0.5, 1, 2, 3, 4, 5, 7, and 9 inches from the injector face. The 90-degree and 270-degree rows each contained 5 thermocouples, located 1, 3, 5, 6, and 9-inches from the injector face.

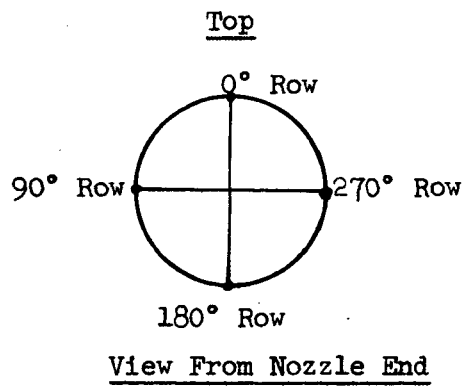

The new nickel calorimeter chamber is shown in Fig. 69, with thermal instrumentation attached.

CALORIMETER CHAMBER HOT FIRINGS (TESTS 005-007)

Test 005

Test 005 was a 2-second checkout hot firing of the new diffusion bonded injector. The test was made at a chamber pressure of 94.7 psia (approximated using c* based on thrust) a core mixture ratio of 4.25 and 4.2 percent BLC. The experimentally measured propellant flowrates and the measured thrust for this test are shown in Fig. 70. Experimental performance is found in Table 8. Temperatures recorded by the thermocouples during the 2-second run did not exceed 500 F.

Following completion of Test 005, the hardware was inspected visually on the stand and then disassembled. No anomalies were observed. The injector face,

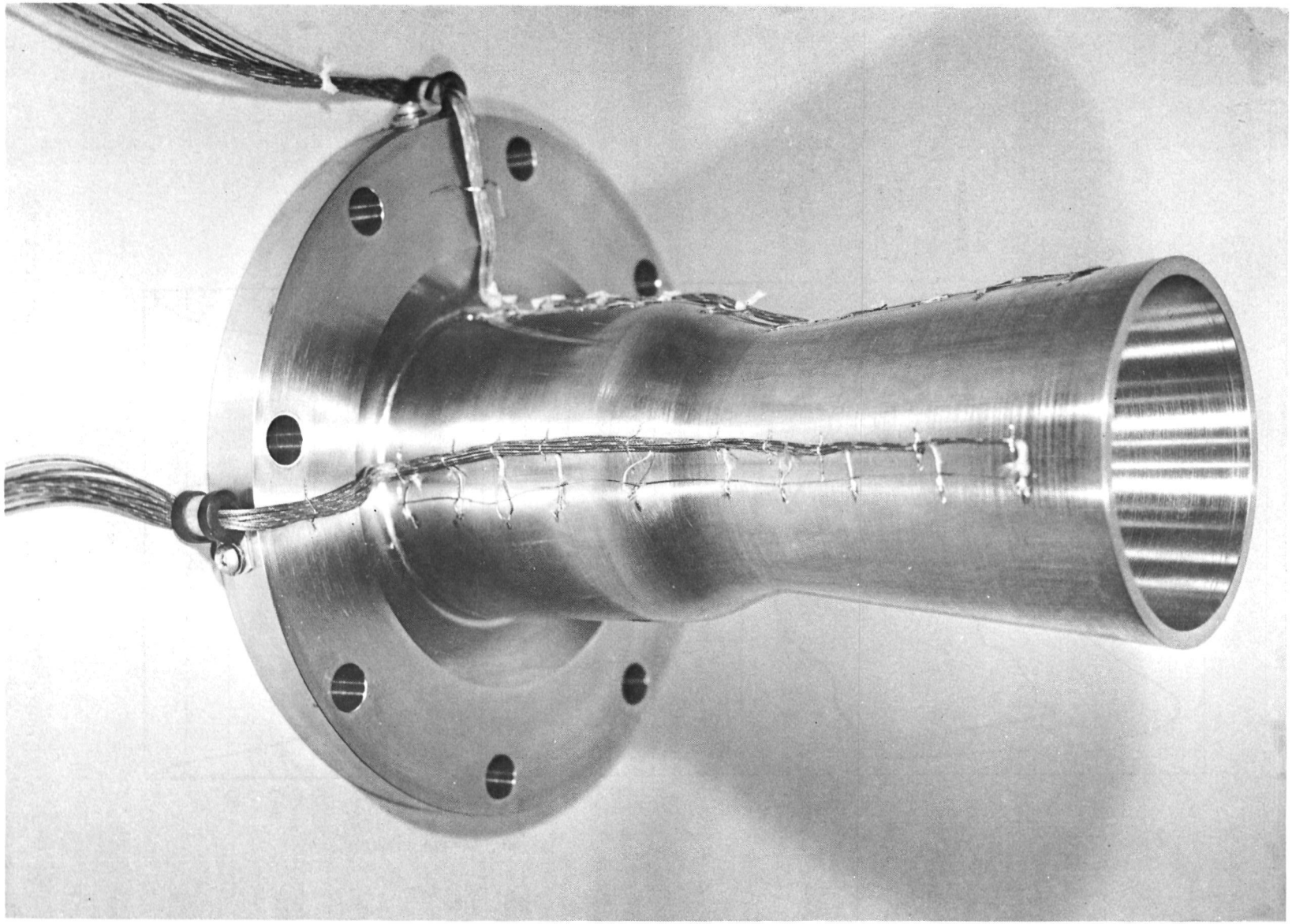

Figure 69. New Nickel Calorimeter Chamber

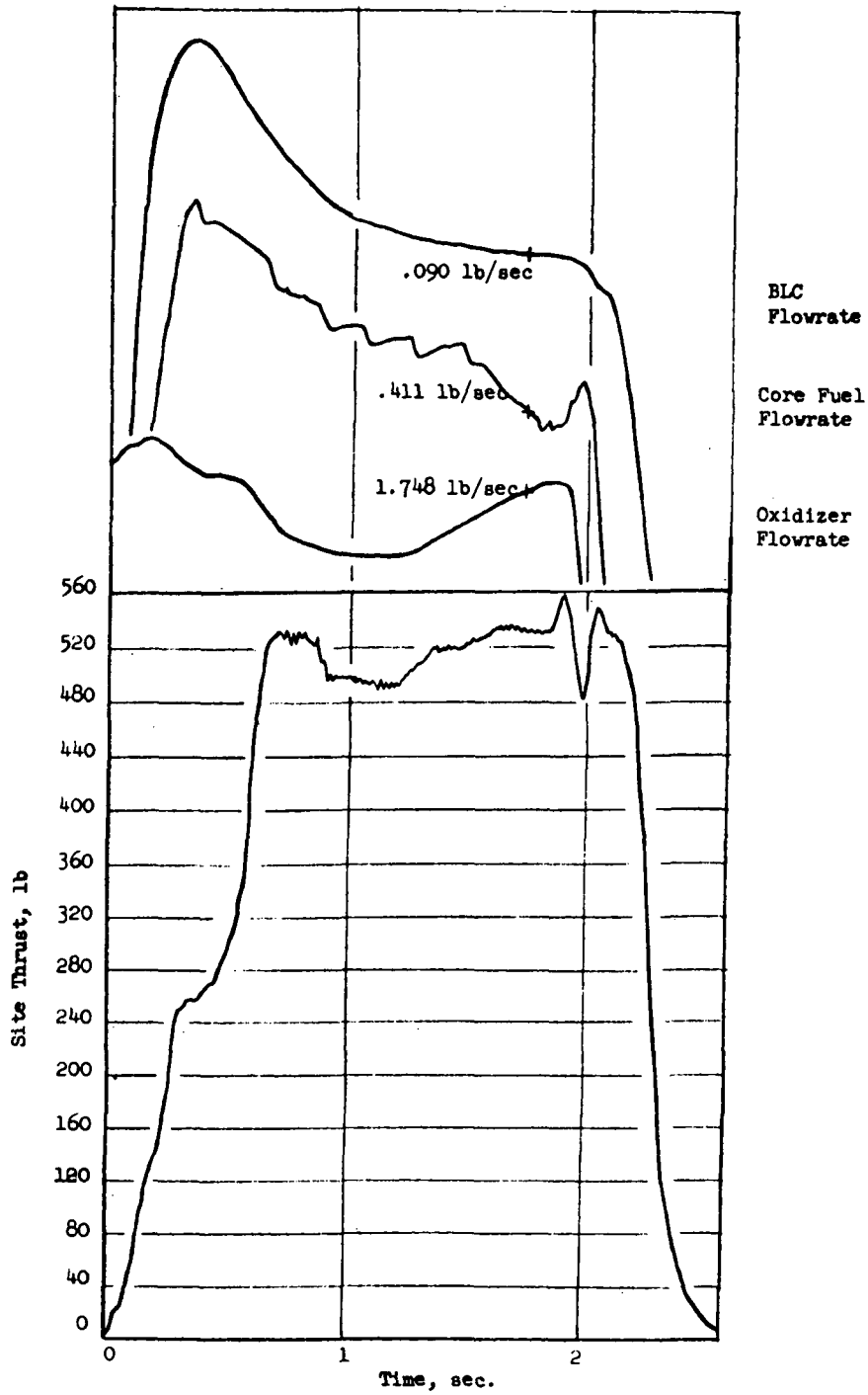

Figure 70. Thrust and Flowrates for Test 005
Core MR = 4.25 4.2% BLC

shown in Fig. 71 prior to cleaning, was found to have much less combustion product deposition than was noted after calorimeter hot firings with the previous (NAS7-304) injector. The nickel calorimeter chamber, Fig. 72, showed no presence of either discoloration or internal gouging.

The excellent condition of the hardware after completion of Test 005 indicated that the firing was a complete success from a compatibility standpoint. The injector and chamber were then cleaned and reassembled for the Test 006-007 firing series.

Test 006

Test 006 was a 10-second hot firing made at relatively high core MR and relatively low BLC mass flowrate. The chamber pressure was 92.7 psia (approximated using c* based on thrust) and the core mixture ratio and percent BLC were 4.80 and 5.3, respectively. The experimentally measured propellant flowrates and the measured thrust for this test are shown in Fig. 73. Experimental performance is shown in Table 8. Temperatures recorded by the thermocouples during Test 006 are shown in Fig. 74-79. These temperatures compare favorably with the pretest thermal predictions, for a core mixture ratio of 4.0 and 6 percent BLC, obtained with the DEAP model (using as input to the DEAP model, those parameters found most successful in postpredicting data from Tests 001, 003 and 004). The absence of the occurrence of "thermal spikes" seen with the previous injector should also be noted.

Following completion of Test 006, the hardware was visually inspected on the stand. The outside surface of the nickel chamber experienced some discoloration of the metal in the throat area (probably as a result of surface oxidation with the atmosphere). However, no gouging or erosion of the chamber interior, such as had occurred with the NAS7-304 injector, was observed. Inspection of the injector face revealed only a minimal amount of disposition.

Figure 71. Injector Face Posttest 005

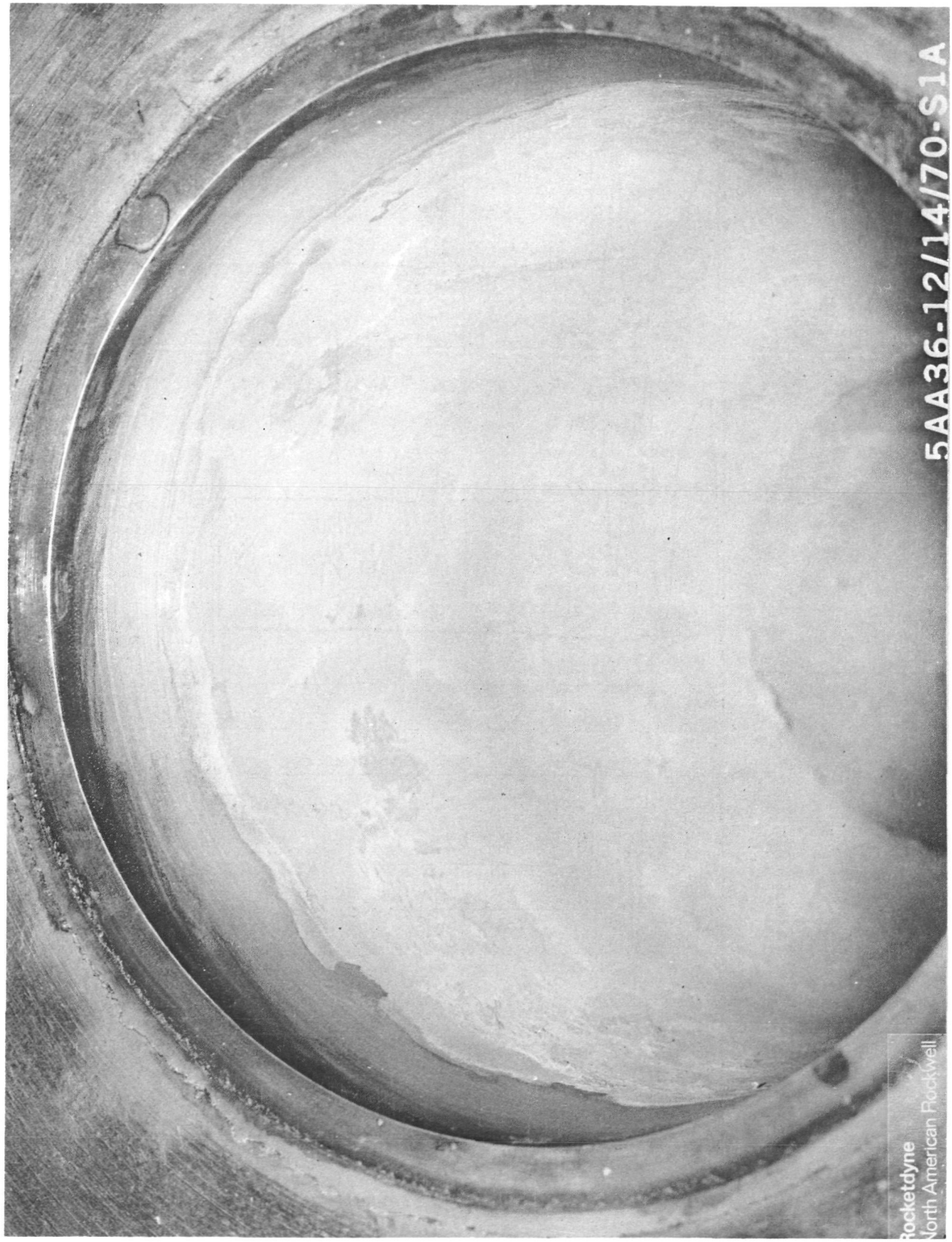

Figure 72. Calorimeter Chamber Posttest 005
(Injector End View)

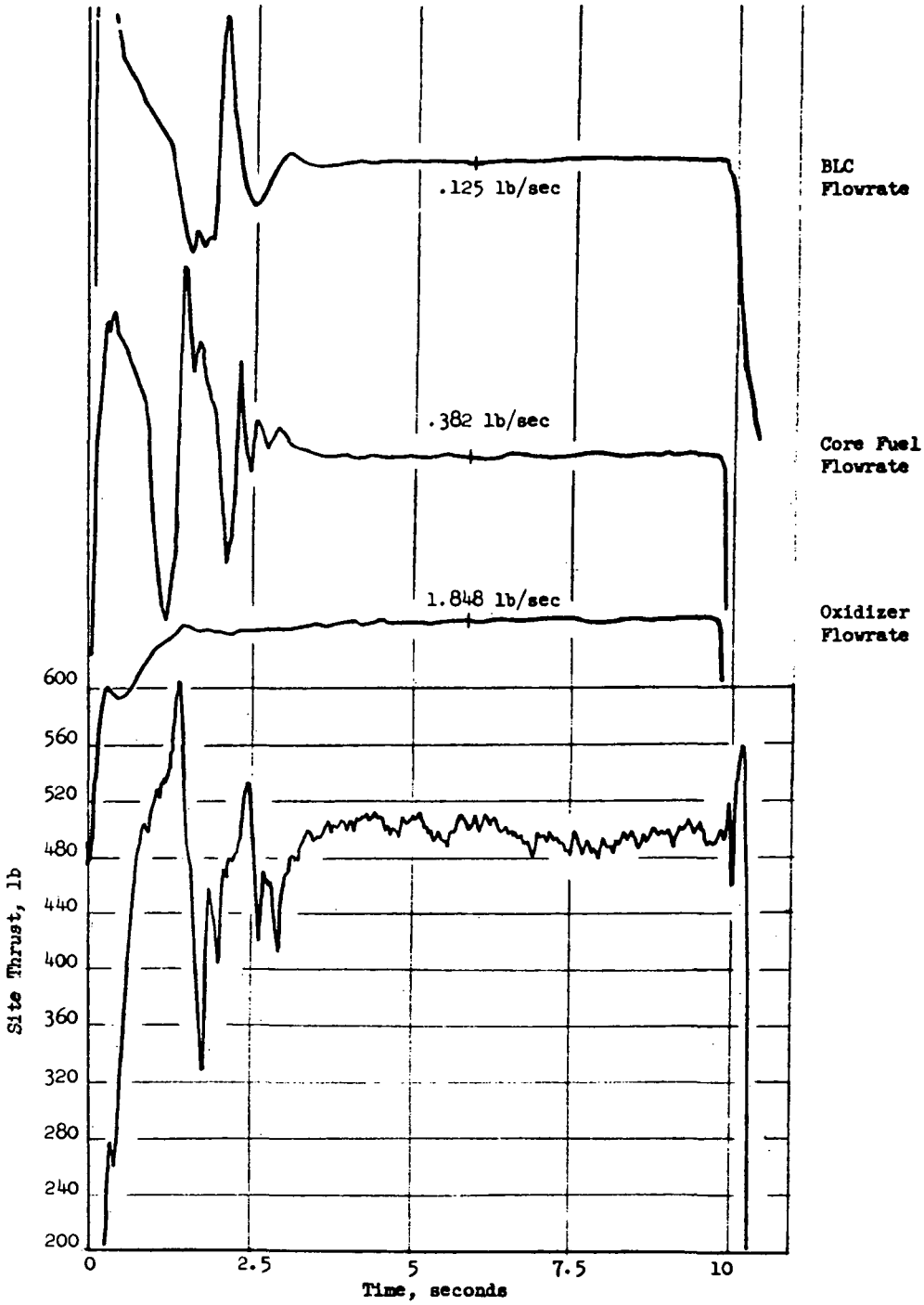

Figure 73. Thrust and Flowrates for Test 006
Core MR = 4.8 5.3% BLC

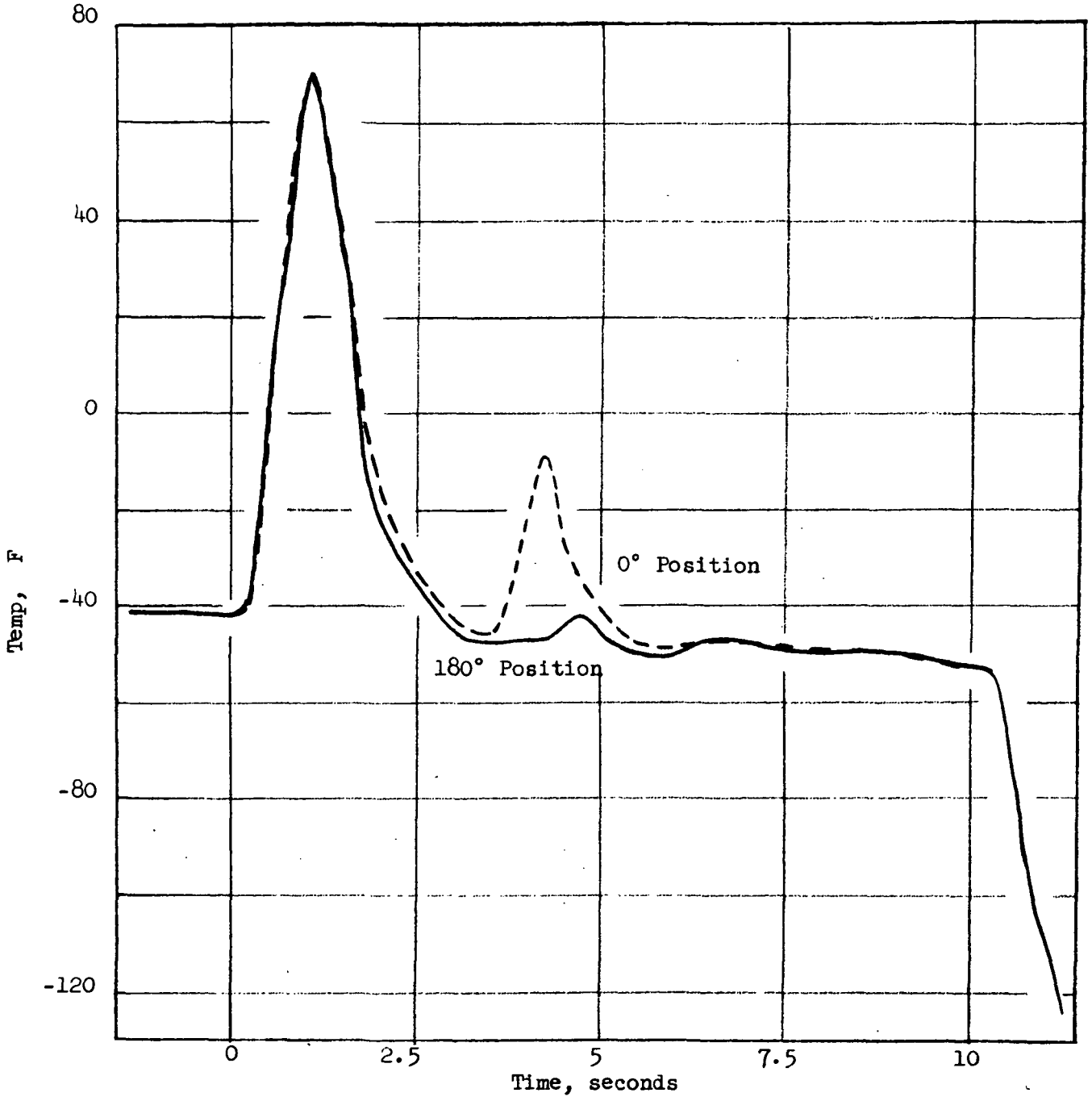

Figure 74. Test 006 - Outside Wall Temperature at 0.50 Inch Axial Location as Function of Thermocouple Position

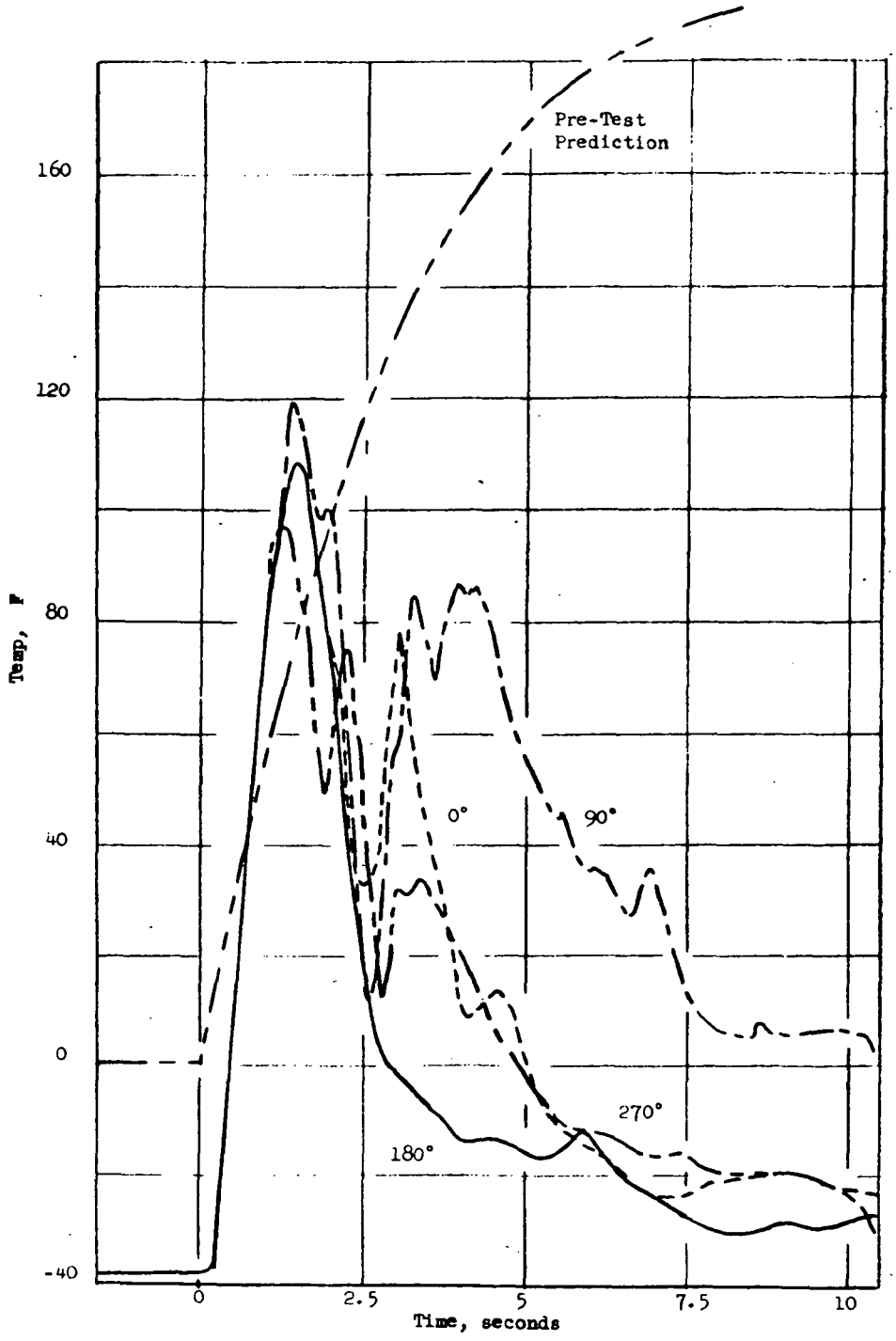

Figure 75. Test 006 - Outside Wall Temperature at 1-Inch Axial Location as Function of Thermocouple Position

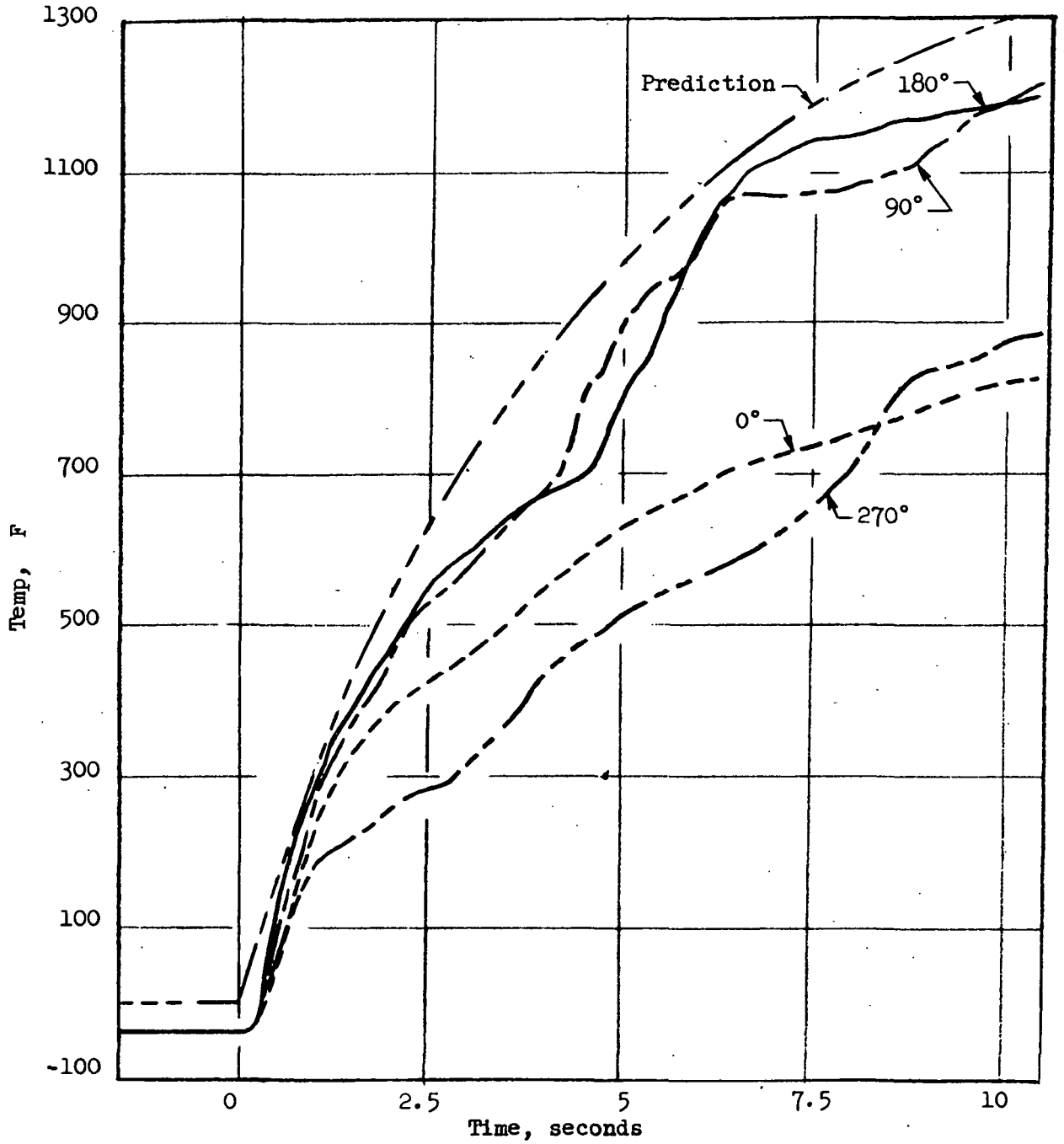

Figure 76. Test 006 - Outside Wall Temperature at 3-Inch Axial Location as Function of Thermocouple Position

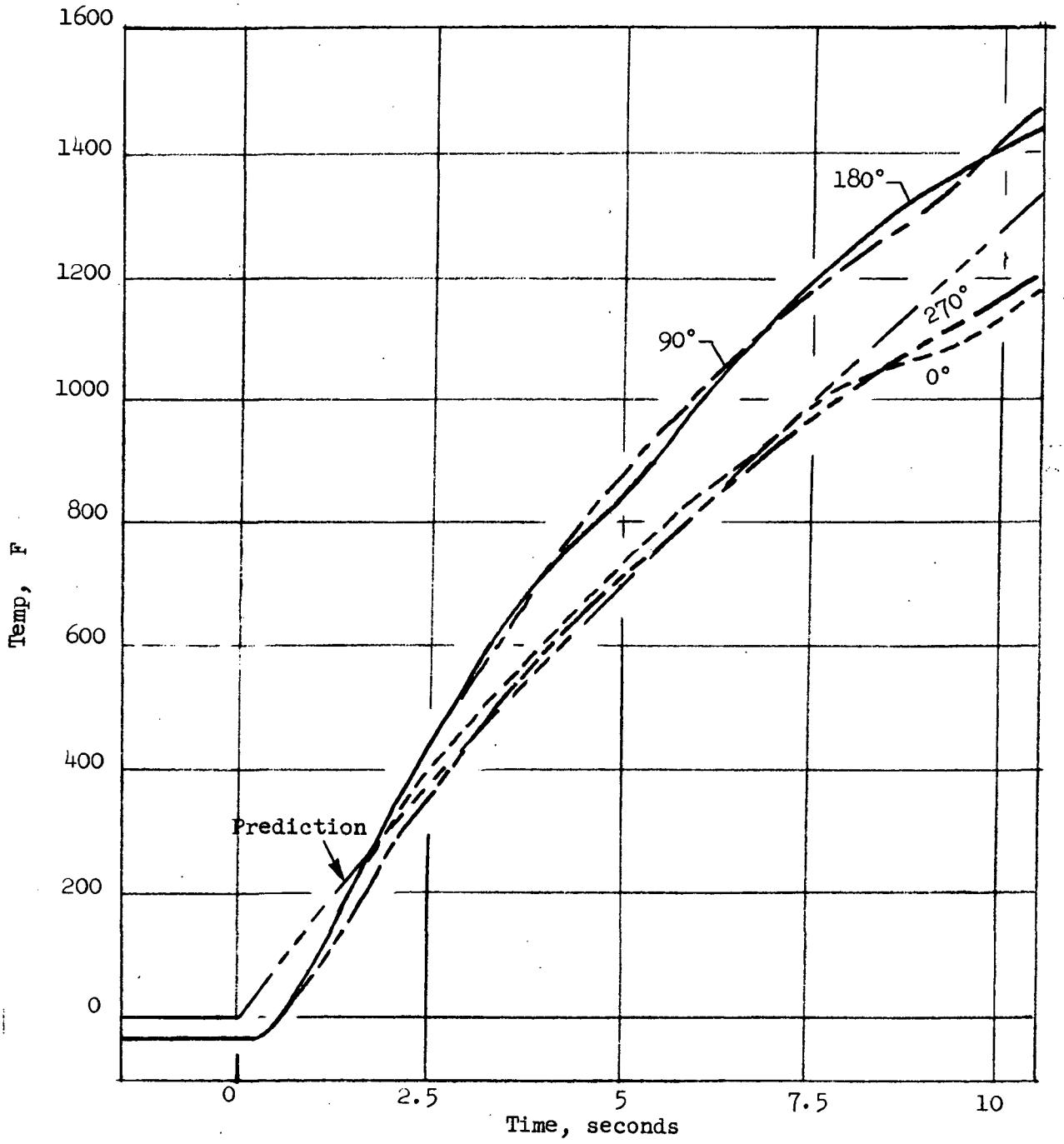

Figure 77. Test 006 - Outside Wall Temperature at 5-Inch Location as Function of Thermocouple Position

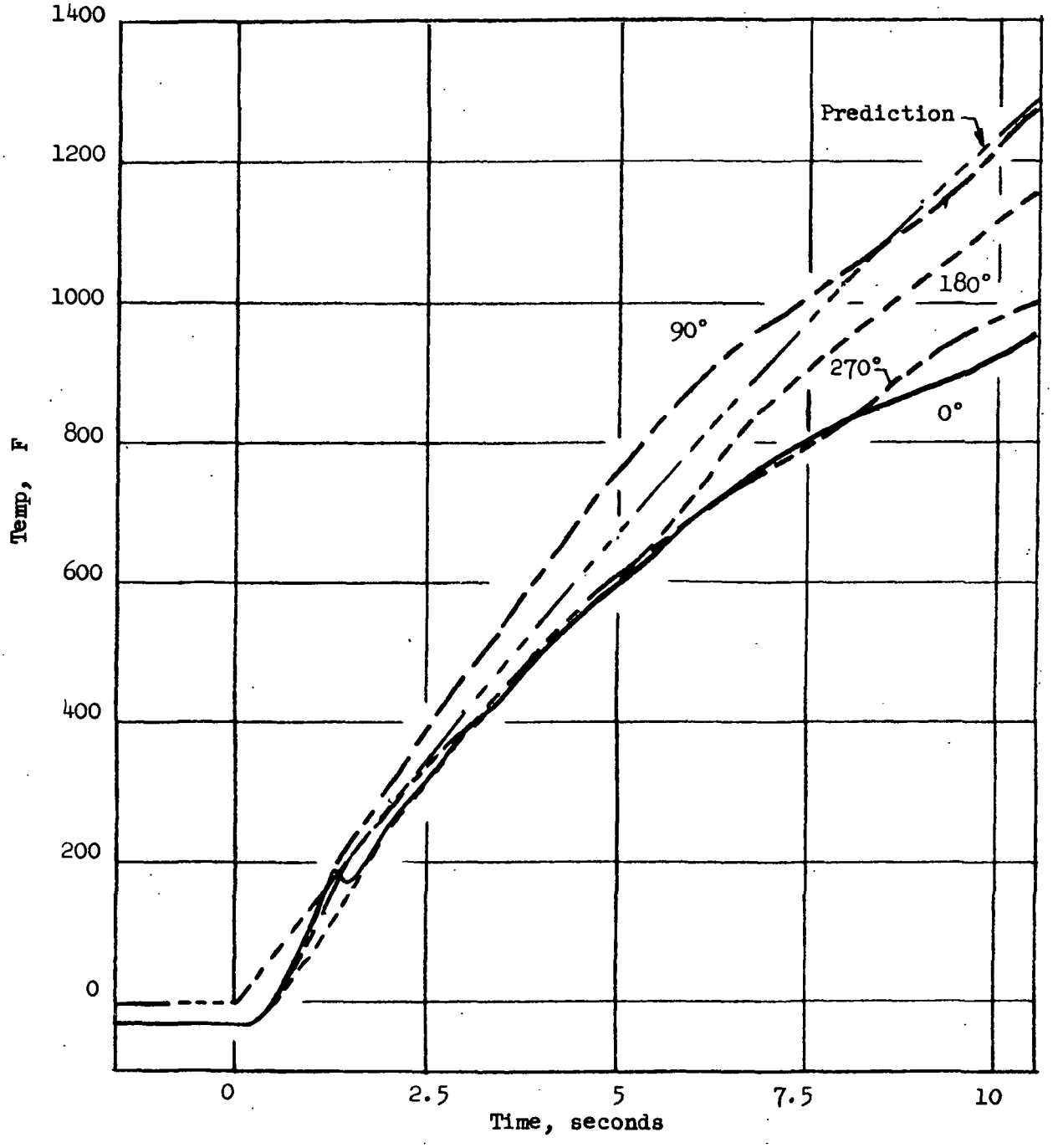

Figure 78. Test 006 - Outside Wall Temperature at 7-Inch Location as Function of Thermocouple Position

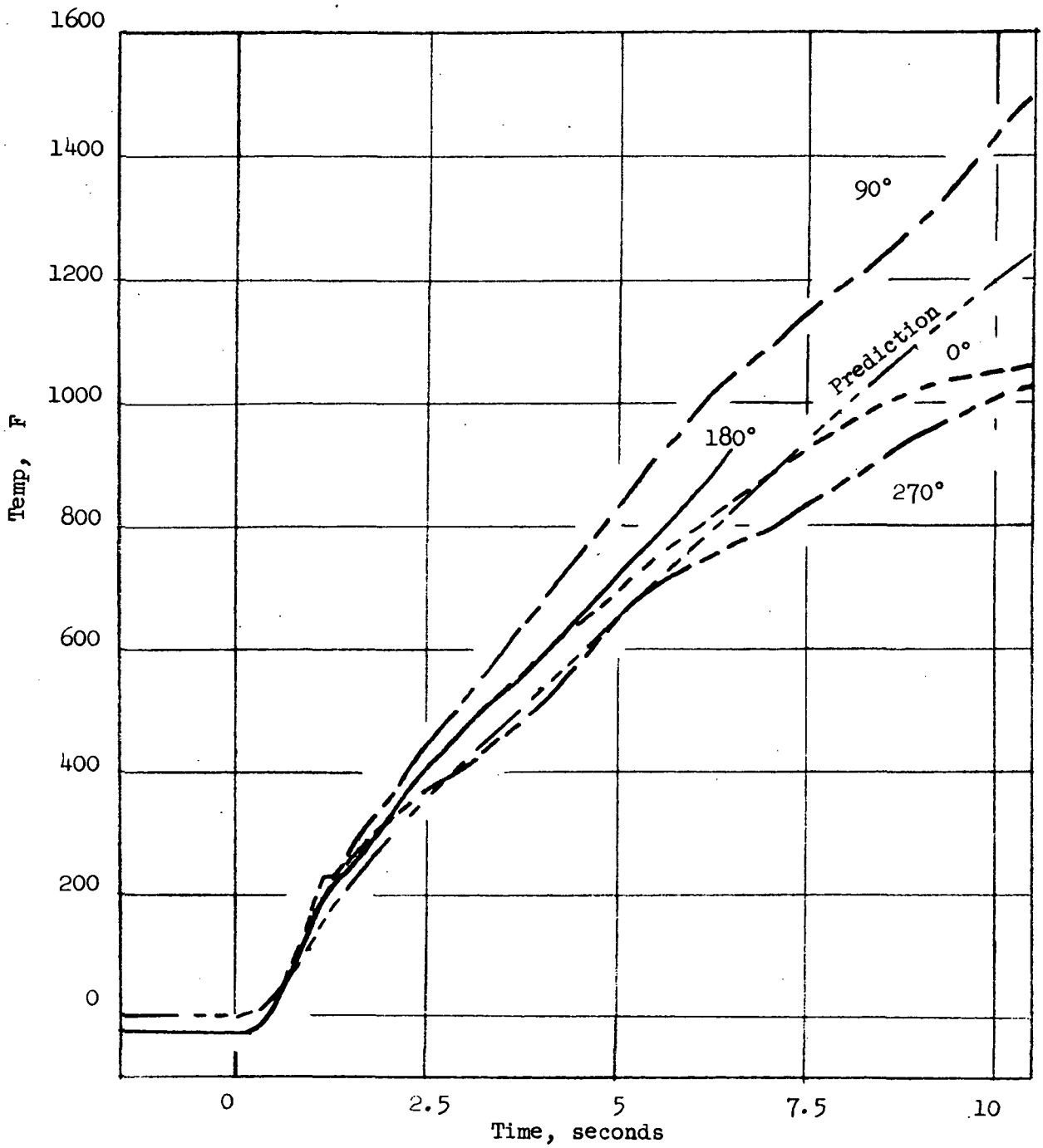

Figure 79. Test 006 - Outside Wall Temperature at 9-Inch Location as Function of Thermocouple Position

Test 007

Test 007 was made immediately following the Test 006 posttest inspection. Run conditions were 127 psia (approximated using c* based on thrust) 2.23 core mixture ratio, and 12.7 percent BLC. This test lasted 2 seconds before automatic run termination caused by a broken thermocouple. The experimentally measured propellant flowrates and the measured thrust for Test 007 are shown in Fig. 80. Experimental performance is shown in Table 8. Temperatures recorded during this 2-second test did not exceed 500 F.

Posttest examination of the hardware on the stand immediately following test completion again indicated success from heat transfer and chamber compatibility standpoints (see Fig. 81 through 83). After posttest injector cleaning, however, localized overheating of the injector was noted in the vicinity of some of the outer row oxidizer orifices (see Fig. 84). Subsequent cold flow tests verified that the impingement characteristics of the injector were unchanged, despite the noted face damage.

USE OF CONTRACT INJECTOR ON IN-HOUSE EFFORT (TEST 008)

The diffusion bonded injector used in the calorimeter chamber hot firings (Tests 005-007) was employed in a company-sponsored FLOX/B_2H_6 long duration hot firing. The chamber utilized for this test contained a POCO graphite inner liner with an ablative outer liner and a stainless steel shell (see Fig. 85). The objective of this test (Test 008) was to investigate the suitability of graphite as a boundary cooled engine liner material. Initial firing conditions were a core mixture ratio of 3.44, 11.8 percent BLC, and a chamber pressure of 102 psia. During the 150-second programmed test duration, thrust was relatively steady (see Fig. 86) and because of the "hard" nature of the feed system, flows appeared relatively constant (see Fig. 87-89). Experimental performance is shown in Table 8.

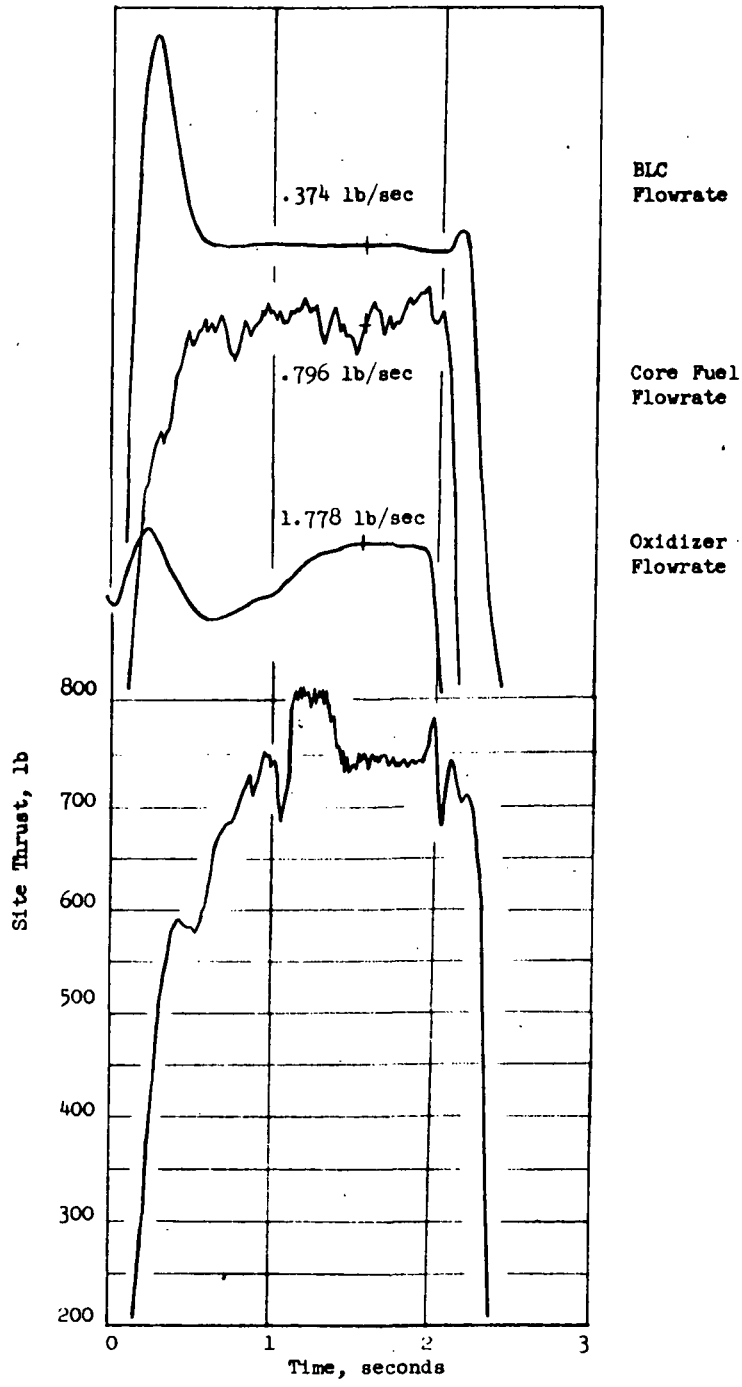

Figure 80. Thrust and Flowrates for Test 007
Core MR = 2.23 12.7% BLC

Figure 81. Injector Face Posttest 007 (Before Cleaning)

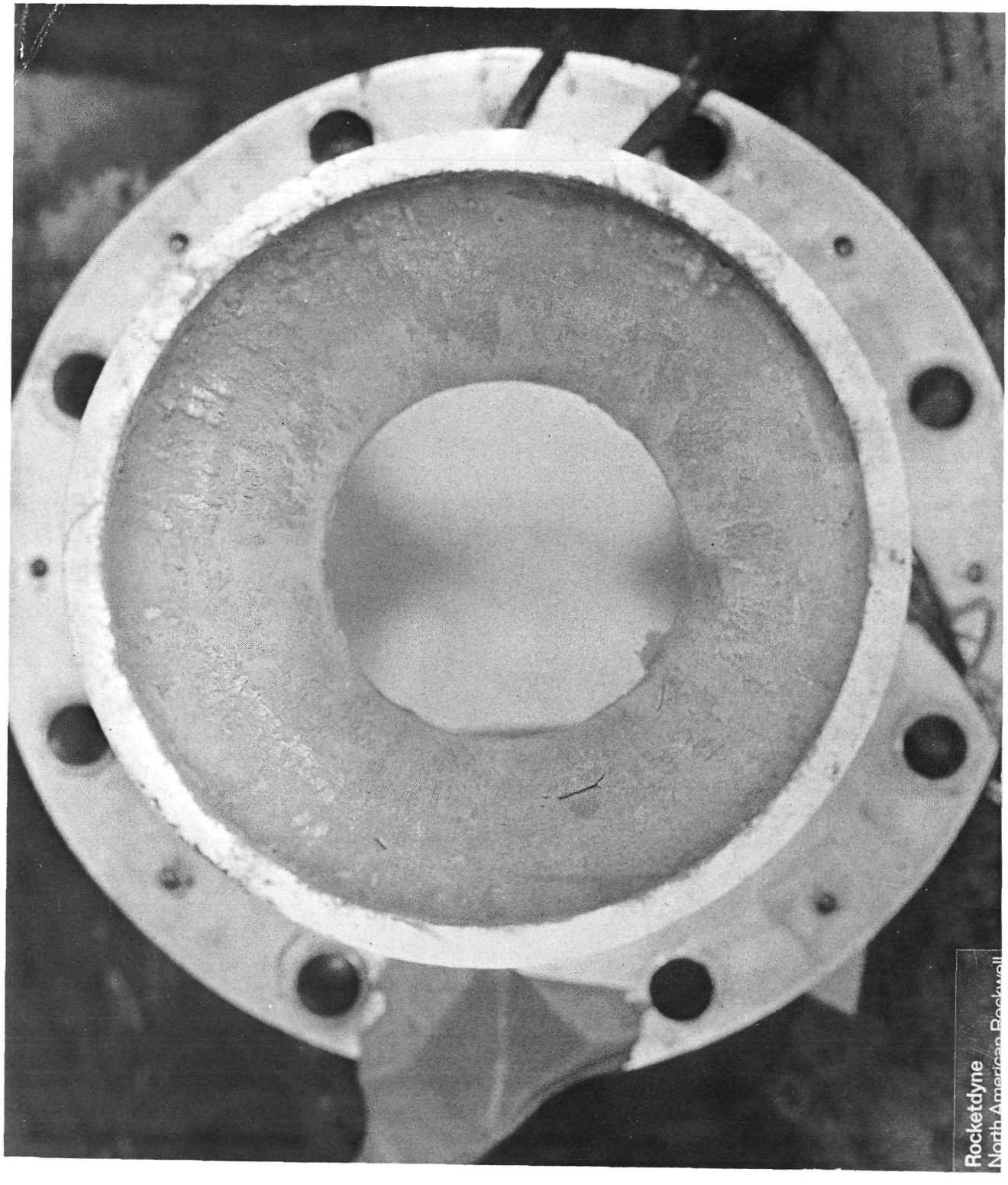

Figure 82. Calorimeter Chamber - Posttest 007 (Nozzle View)

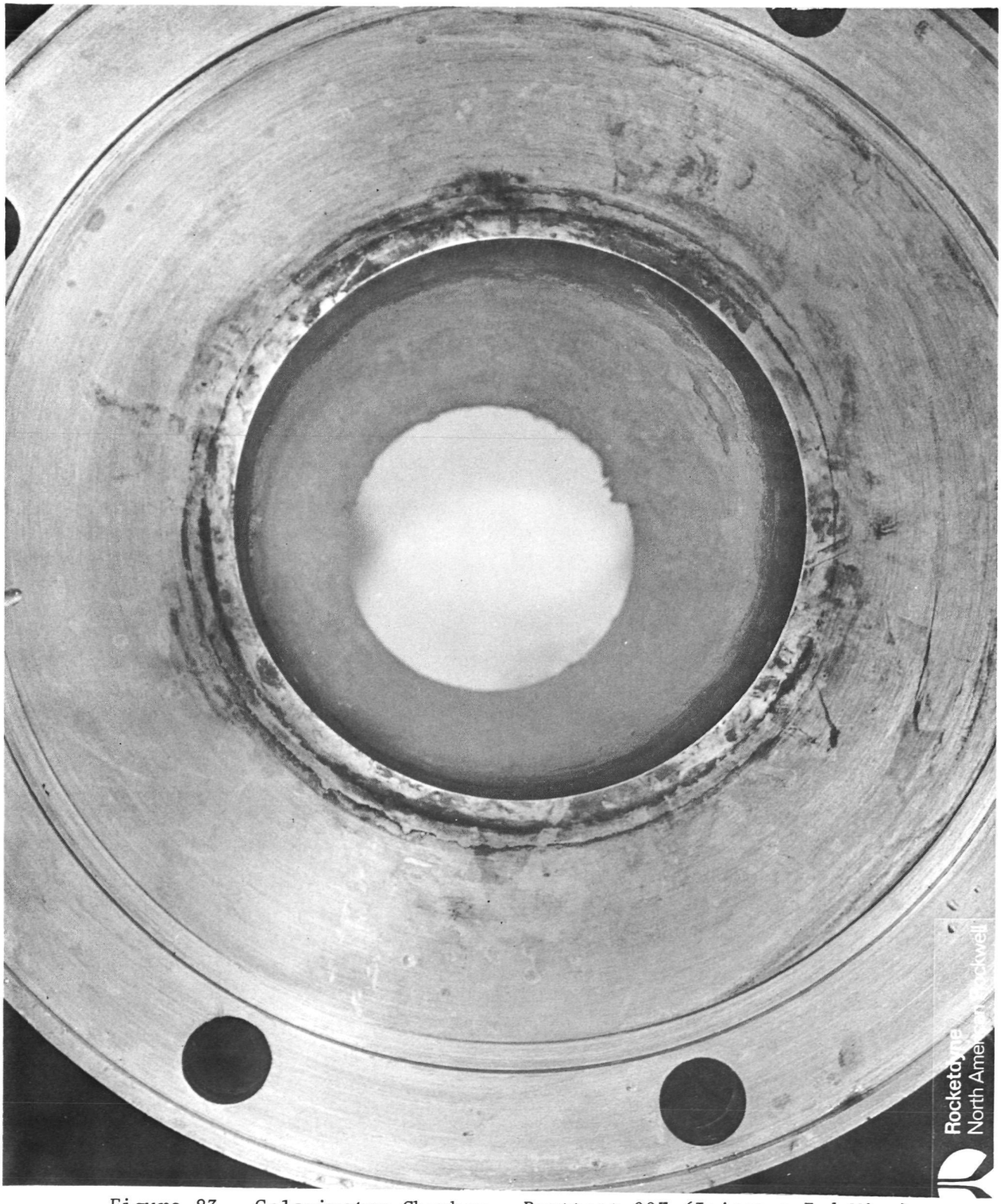

Figure 83. Calorimeter Chamber - Posttest 007 (Injector End View)

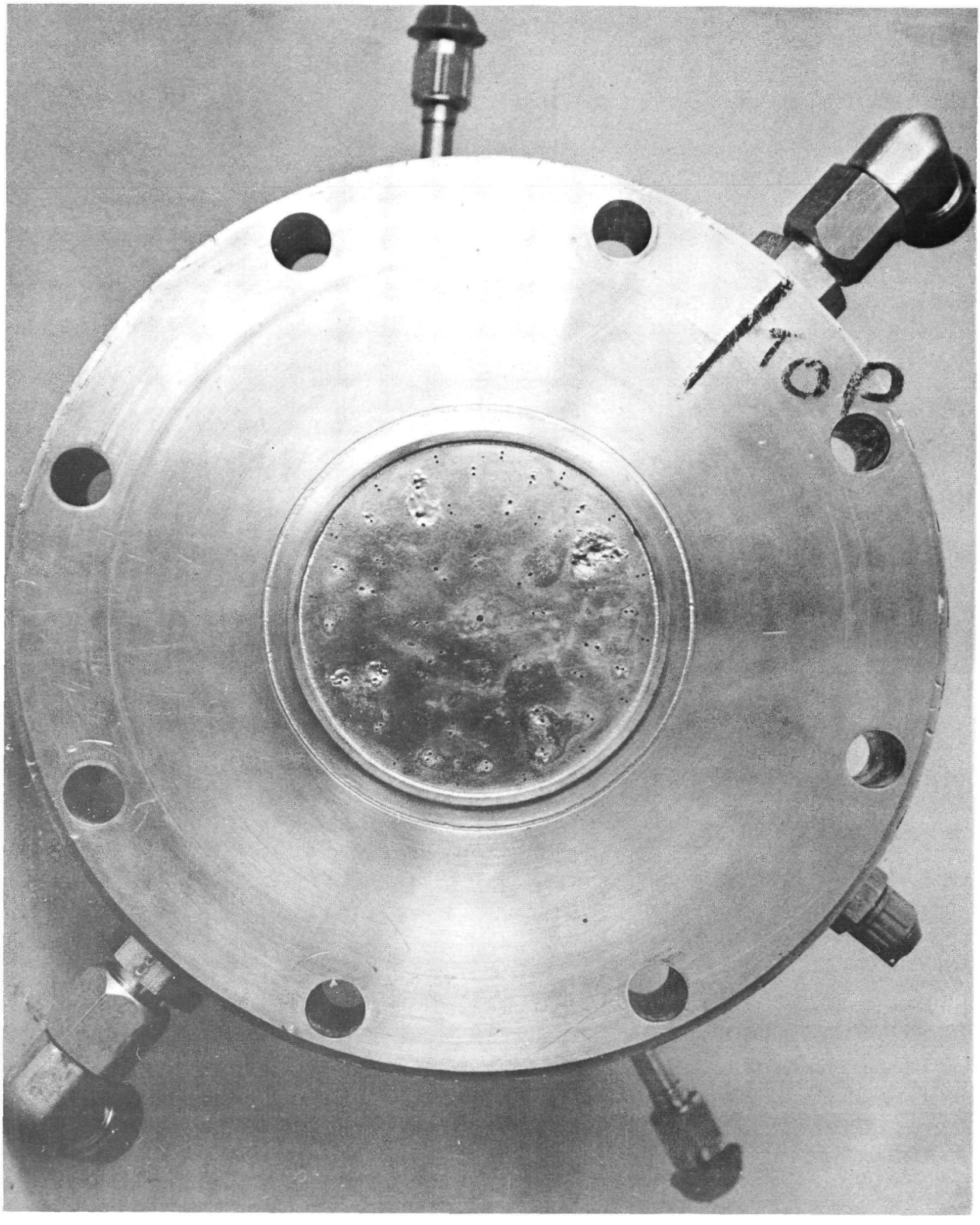

Figure 84. Injector Face - Posttest 007 (After Cleaning)

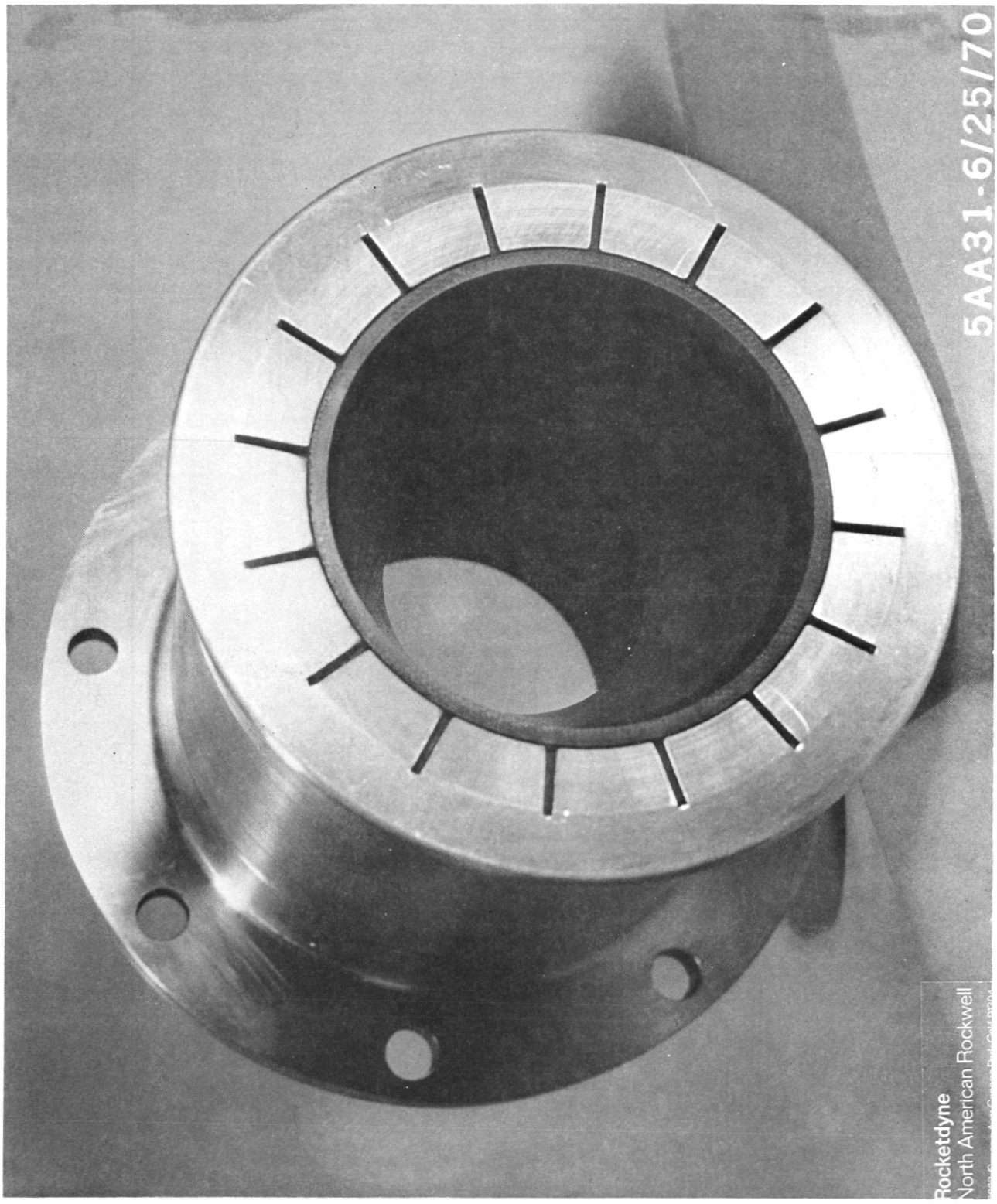

Figure 85. IR&D Chamber - Pretest 008

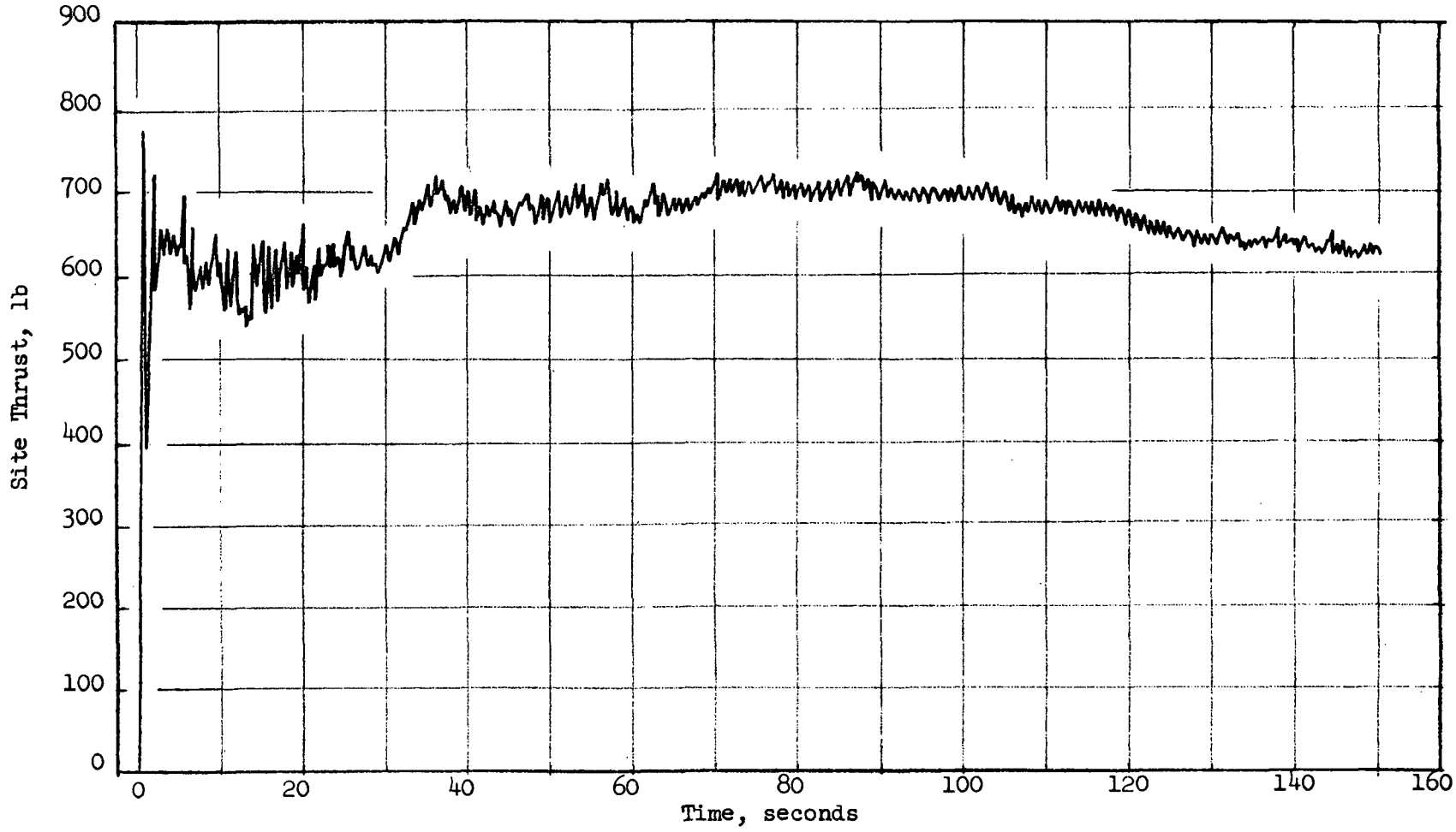

Figure 86. Thrust Versus Time

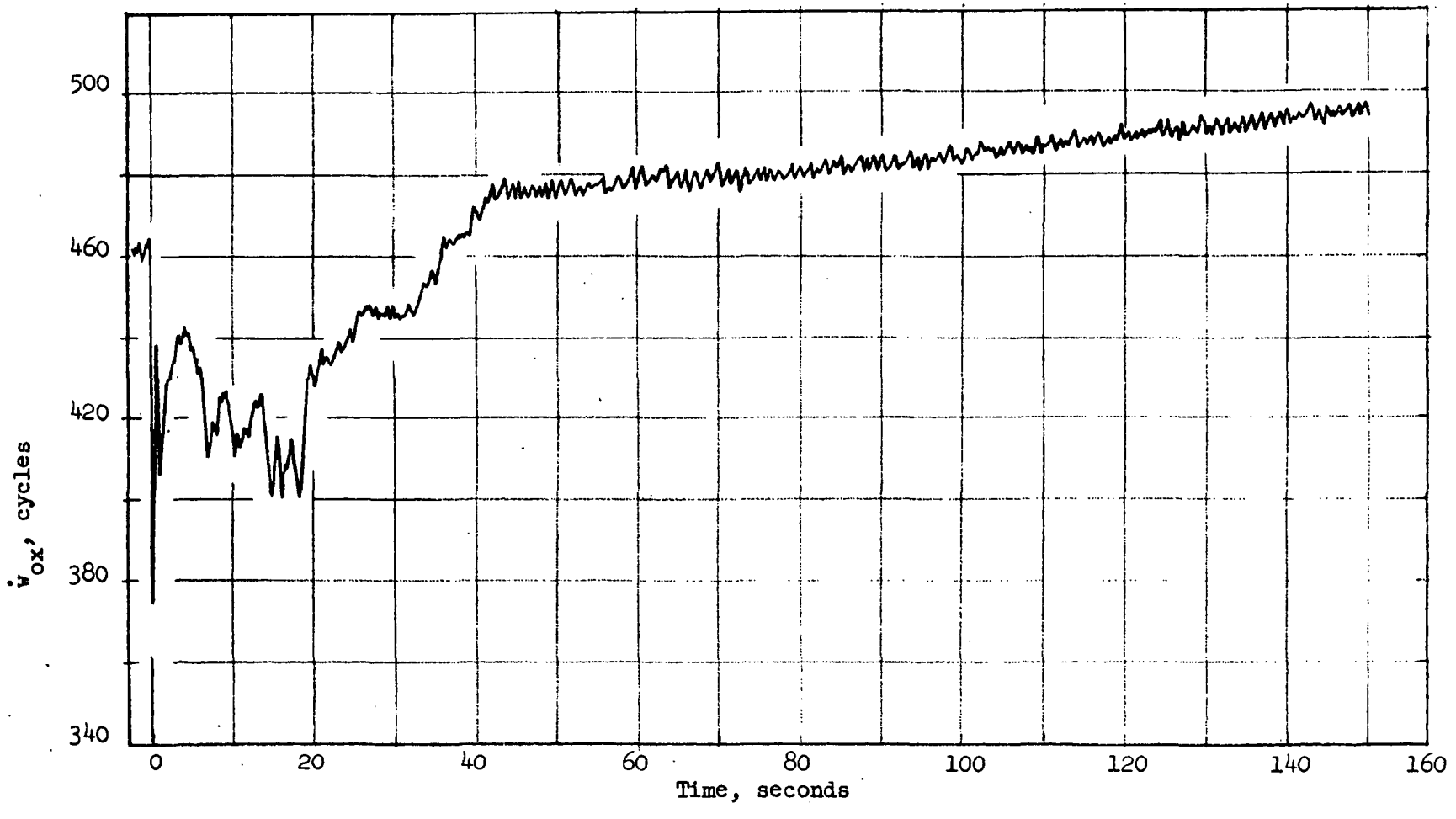

Figure 87. Oxidizer Flowrate Versus Time

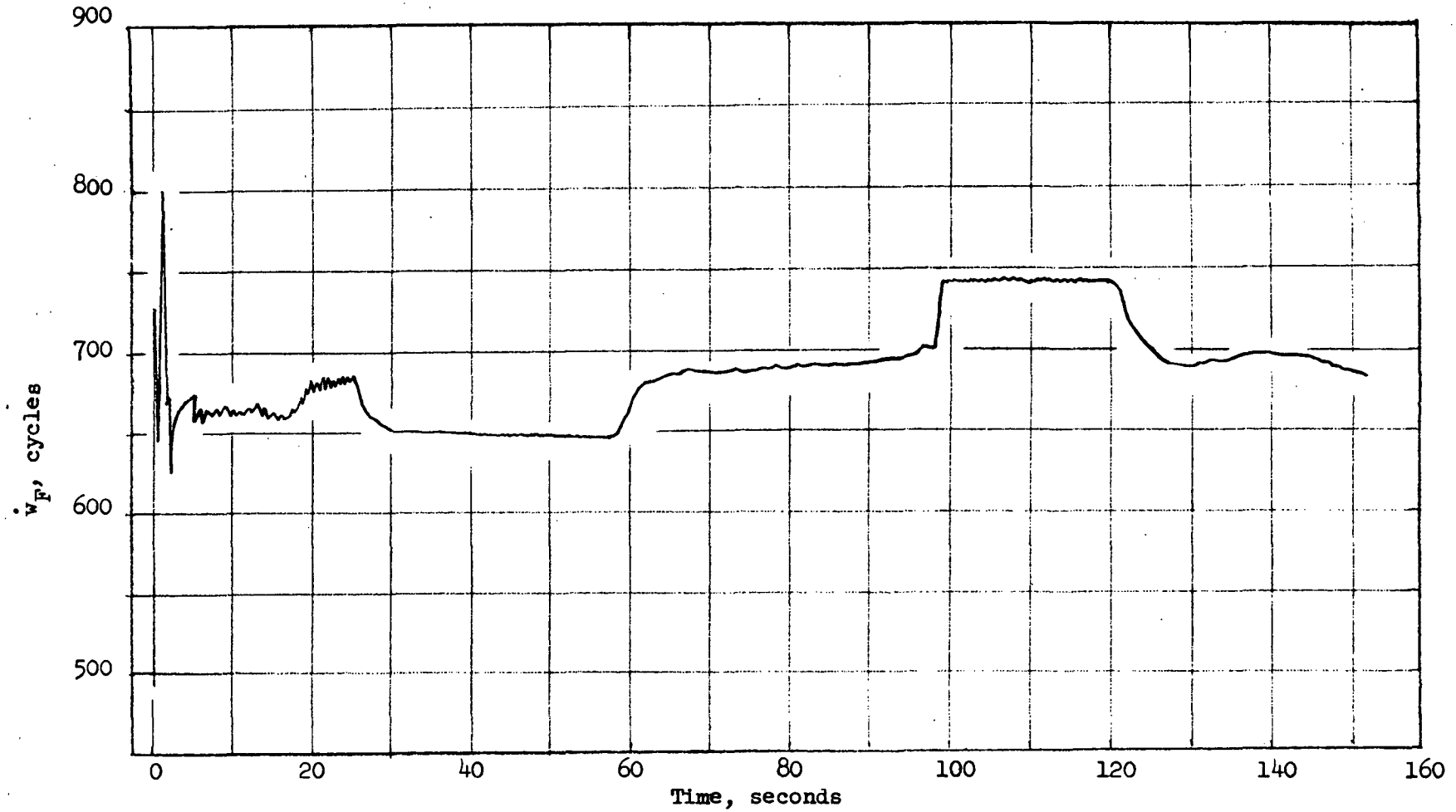

Figure 88. Total Fuel Flowrate Versus Time

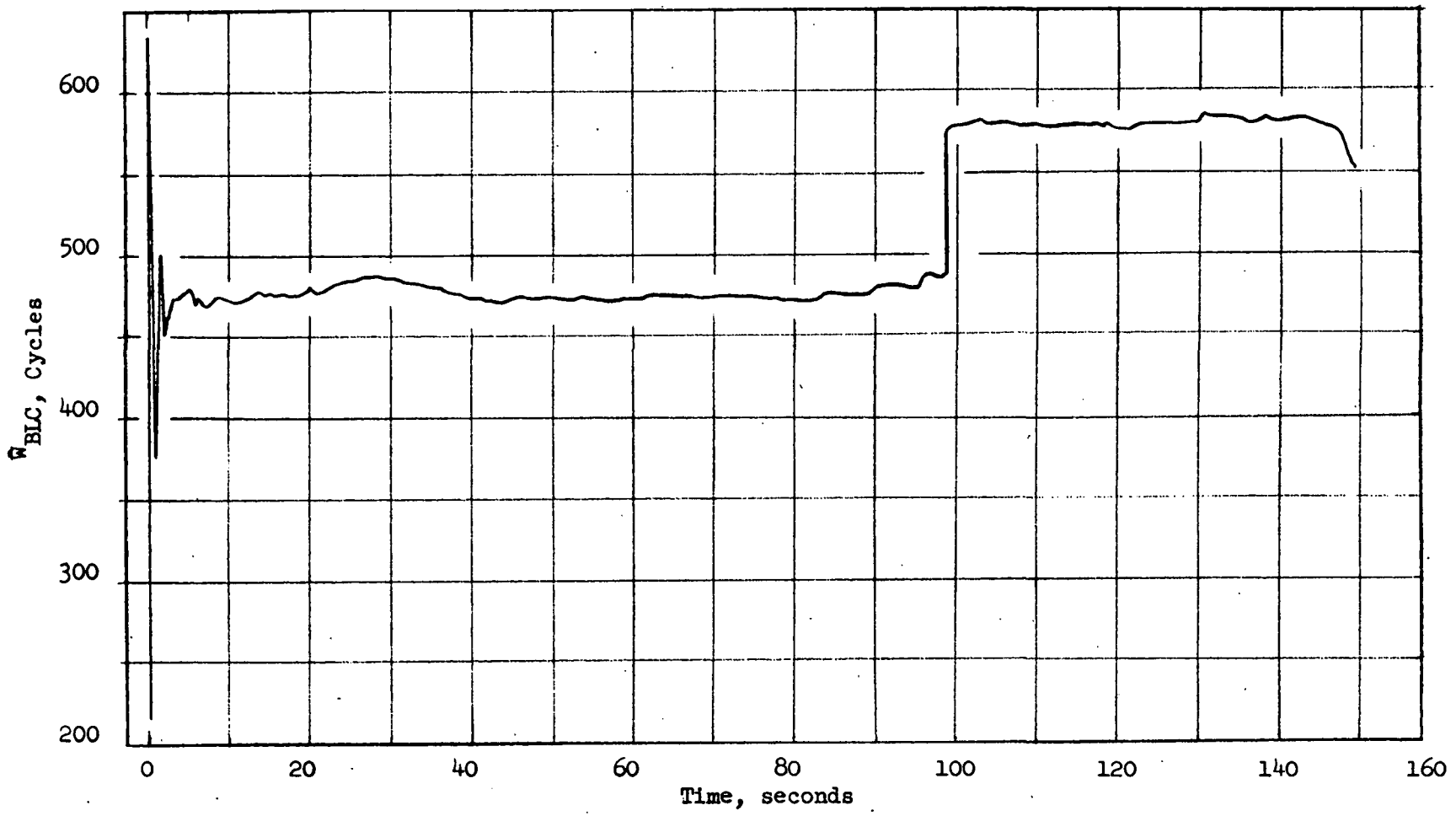

Figure 89. BLC Flowrate Versus Time

Posttest Hardware Condition

A posttest view of the combustion chamber on the test stand is shown in Fig. 90. Posttest examination of the injector indicated melting of a major portion of the injector face plate (see Fig. 91-92). The resultant loss of injector flow control resulted in severe chamber erosion (Fig. 93). Detailed posttest examination of the injector indicated a bond failure of what was an originally marginal bond. This was evidenced by the existence of face plate-manifold cleavage at the bond line as well as by the existence of a number of regions of machined surfaces at the bond cleavage interface. Since diffusion bonding involves intercrystalization of the bonded components, bond failure of a normal bond would not result in a post-cleavage machined surface appearance of bonded surfaces.

At a subsequent hardware review meeting with the fabricator from the Los Angeles Division (LAD), the existence of a bond failure was confirmed. The reason for the marginal bond was poor temperature control due to a malfunction in the bonding facility temperature recorder. (Malfunctioning of the recorder was noted during a subsequent bonding run.) Since the diborane injector experienced what was thought to be a tolerable count of deformation (although the deformation was less than design) during the bonding process, it was felt by LAD personnel at the time of fabrication that the bond was satisfactory, in spite of the fact that a somewhat lower than design bonding temperature had apparently been used*. LAD suggested a helium leak check of the part prior to its use.

As has been standard practice at Rocketdyne with all injectors, a leak check prior to the hot firings was performed. This test indicated no intermanifold leakage. The three hot firings proceeding the long duration firing further confirmed this condition. The duration firiing did, however, experience a comparatively hard start as measured by pressure transducers located at the inlets to the injector manifold (see Fig. 94). This hard start, in conjunction with possible bond weakening during the previous three hot firings, most likely caused the marginal bond to fail.

*LAD has since revised their operational procedures to preclude the possibility of poor temperature control on future bonds.

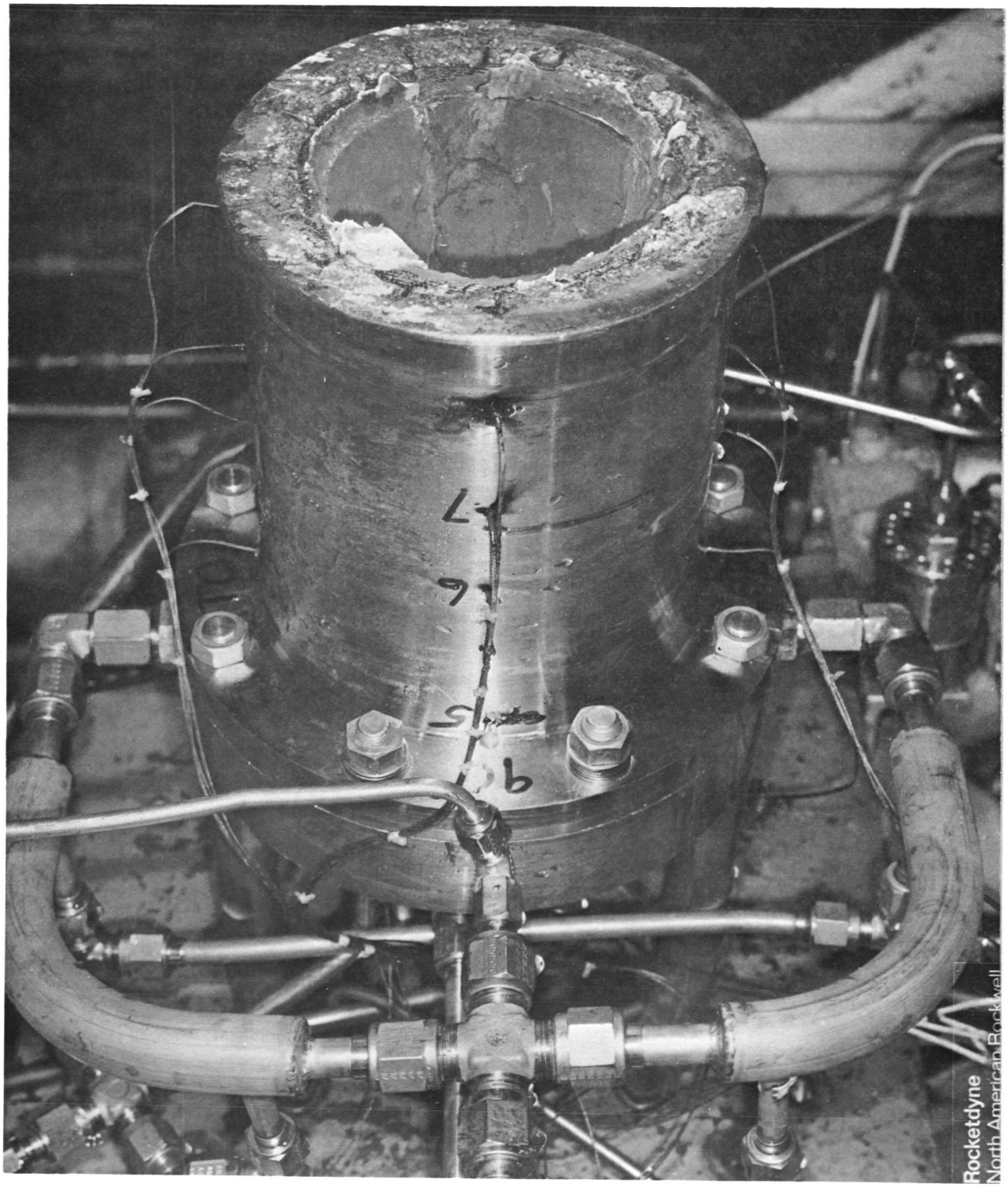

Figure 90. IR&D Chamber on Stand - Posttest

Figure 91. Injector Face - Posttest

Figure 92. Injector Face - Posttest 008

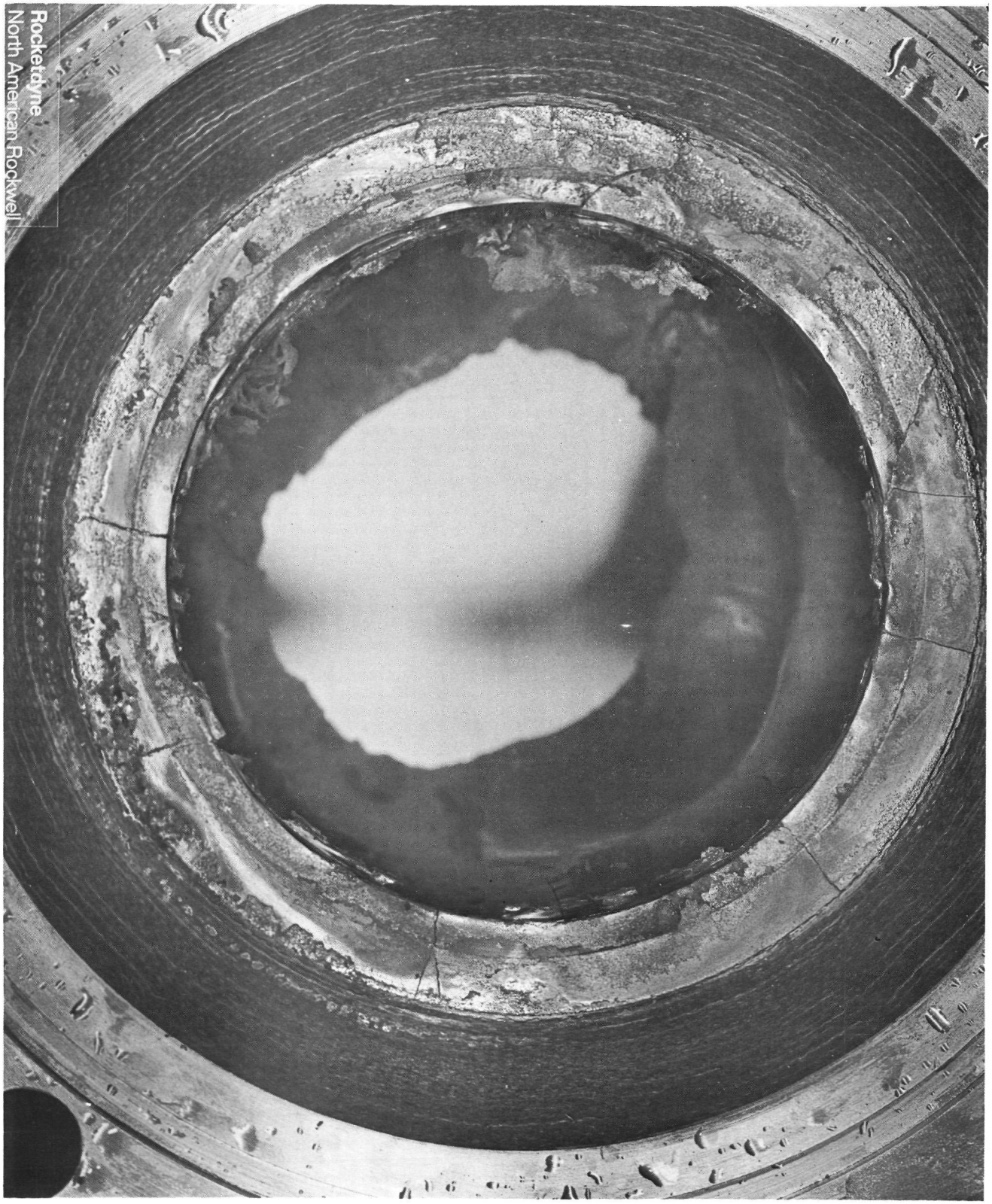

Figure 93. IR&D Chamber - Posttest (Injector End View)

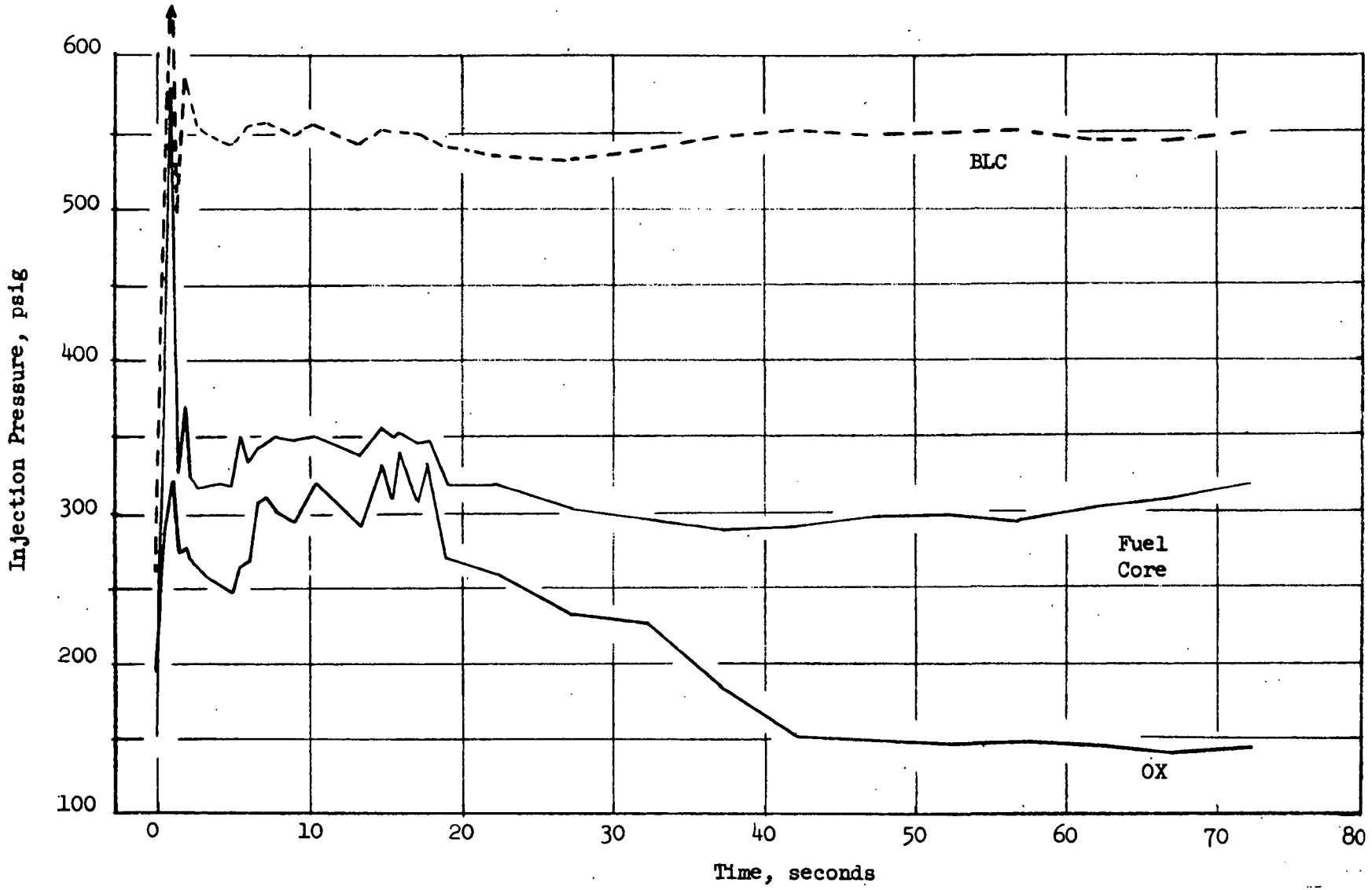

Figure 94. Manifold Injection Pressures Versus Time

Additionally, bond failure may have been related to P_c tap burning, resulting from the purge pressure cycling employed to ensure deposit-free operation of the P_c tap during the 150-second run. A purge cycling procedure had not been used on previous tests with the diffusion bonded injector. On the other hand, the observed P_c tap burning may have been the result of bond failure and subsequent intermanifold leakage. (See subsequent sections for detailed discussions of possible failure modes).

Probable Sequence of Injector Failure

On Test 008 about one second into the test a pressure spike occurred in the fuel manifold (see Fig. 94), resulting in approximately a 300 psi pressure differential between the oxidizer and fuel manifolds. (Previous tests, see Fig. 95, revealed no large oxidizer and fuel injector manifold pressure differentials.) This pressure spike could have caused a bond failure, most probably in the area of the large oxidizer feeder passages where the bond interface distance between the oxidizer downfeeder and the surrounding fuel feeders is a minimum (see Fig. 96). A localized bond failure could have allowed a small smount of interpropellant leakage between the oxidizer and fuel manifolds, with formation of B_2O_3 particles in both the fuel and oxidizer manifolds, plugging the narrow fuel feeder passage and the innermost oxidizer orifices (see Fig. 94). This would have caused the decrease in observed $\dot{w}/\sqrt{\Delta P}$ (which is proportional to orifice area) at about 5 seconds into the test (see Fig. 97). This reduction could then have caused a massive burnout to start at the center of the injector. Examination of Fig. 97 reveals that between 5 and 8 seconds into the run the fuel $\dot{w}/\sqrt{\Delta P}$ decreased about 11 percent and the oxidizer $\dot{w}/\sqrt{\Delta P}$ decreased about 18 percent. These figures correspond to starvation of all four of the inner row oxidizer doublets and three of the inner row fuel doublets. At approximately 20 seconds into the run, massive burnthroughs of the oxidizer and fuel manifolds began to occur, as evidenced by large increases in $\dot{w}/\sqrt{\Delta P}$. Observations of the P_c vs time trace (discussed below) are also consistent with the postulated sequence of events.

In an effort to circumvent plugging of the P_c tap, which occurred on Tests 006 and 007, a GN_2 OFF-ON purge was applied through the P_c tap on Test 008. The purge was

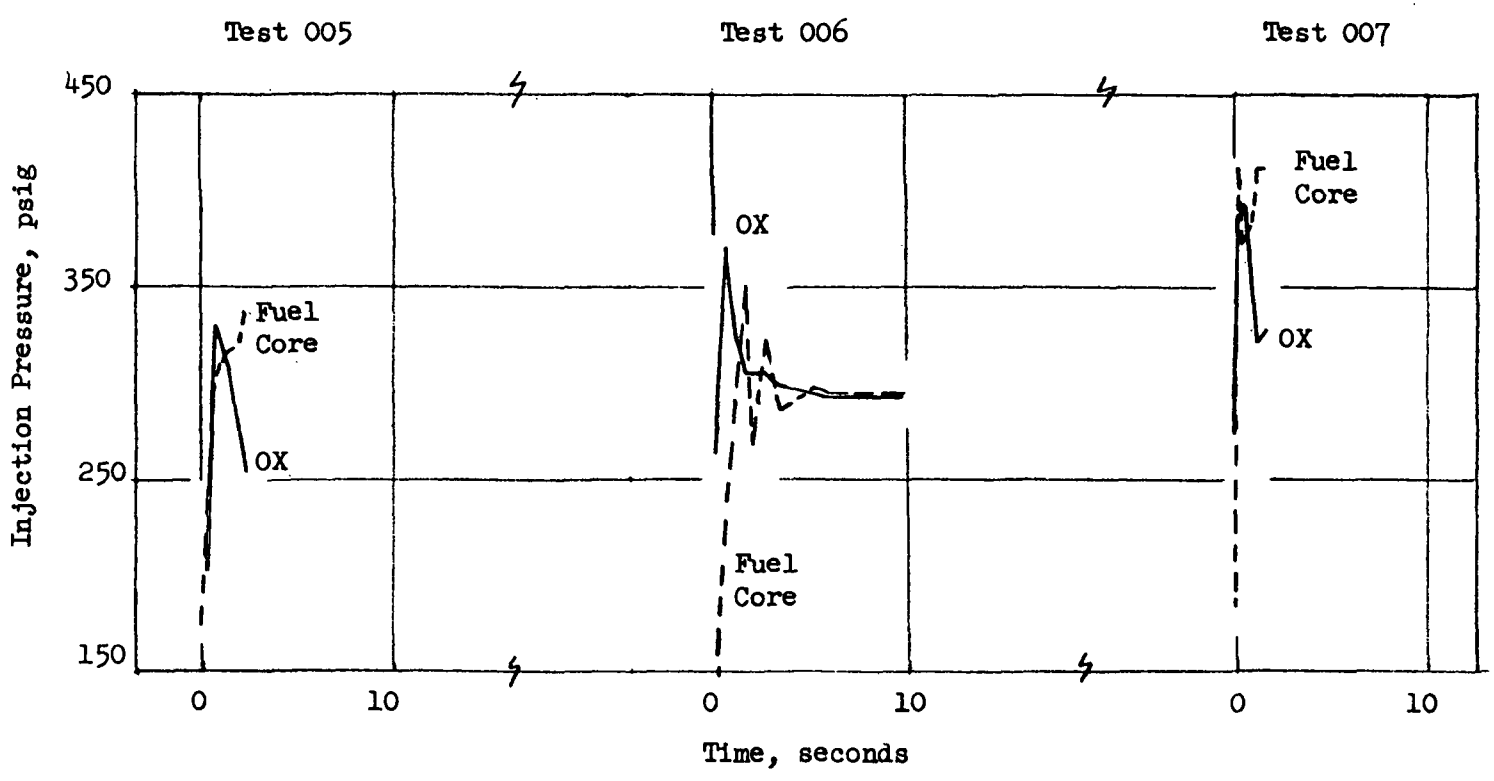

Figure 95. Injection Pressures Versus Time - Tests 005 through 007

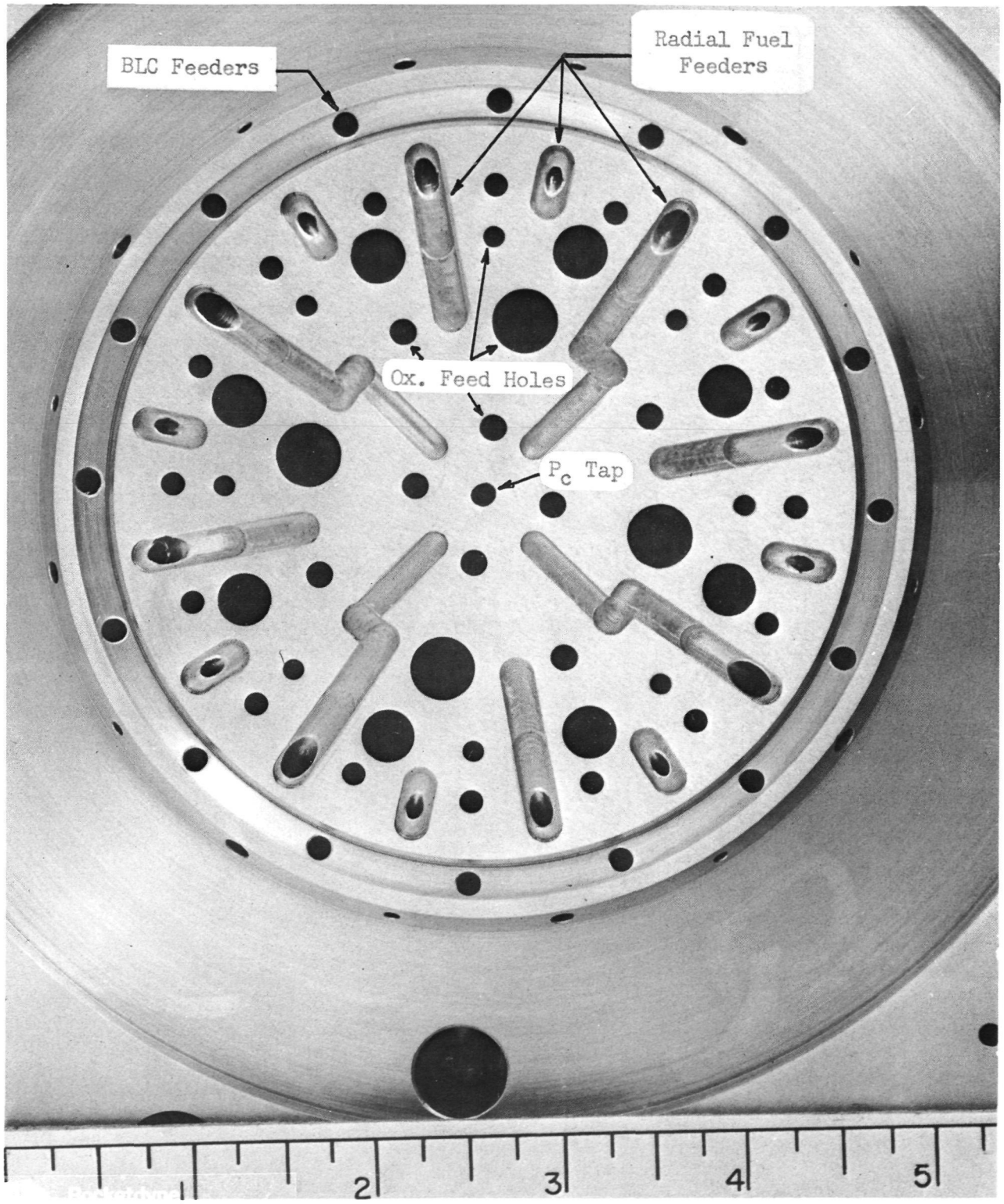

Figure 96. Injector Manifold

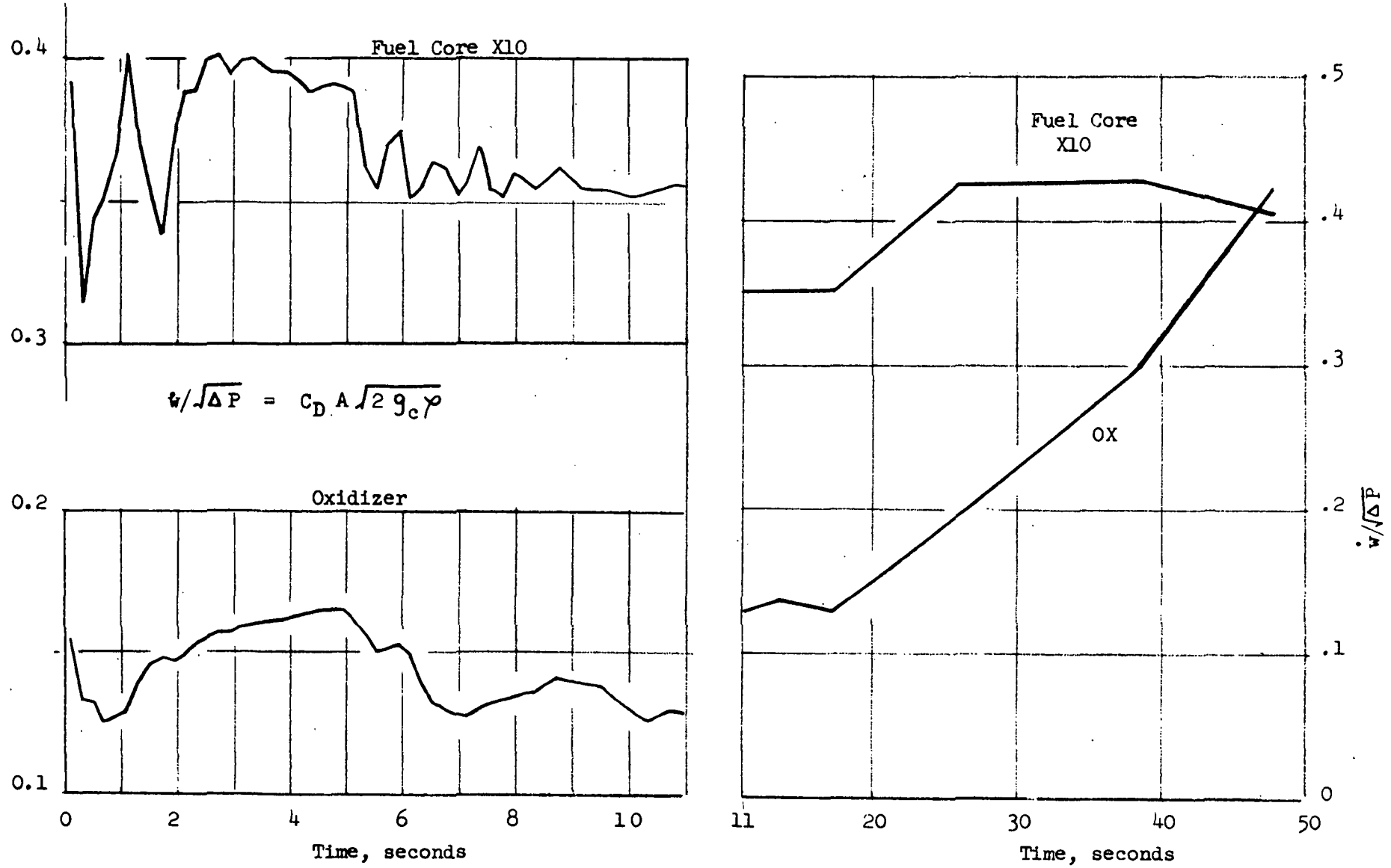

Figure 97. $\dot{w}/\sqrt{\Delta P}$ Versus Time

operated on a 2.5-second ON and 3.2-second OFF cycle. The purge pressure was 375 psi. Operation of the purge may be understood by referring to the P_c vs time trace shown in Fig. 98. Figure 36 indicates that plugging of the P_c tap occurred just prior to 10 seconds and at 15 seconds into the run. This is indicated by an increase in measured P_c to a value equal to the purge pressure. Ignoring the periods at which plugging is evidenced, there appears to be a systematic decrease in the P_c trace during the ON purge periods from a value of 360 psig at the start of the test to a value of about 160 psig at about 33 seconds into the run. This represents a decrease in the flow resistance between the purge inlet to the manifold and the injector face which was caused by burning of the injector face plate in the region of the P_c tap. At about 33 seconds into the run, the P_c trace during periods of ON purge operation was observed to reach a constant value. This time was interpreted as being the time at which burn-through of the injector face plate was completed.

Thermal History and DEAP Model Comparison

Chamber wall temperatures (measured on the outer surface of the graphite inner liner) recorded during Test 008 for the first 30 seconds are shown for various stations as a function of time and circumferential position in Fig. 99 through 102. These traces indicate circumferentially uniform thermal behavior prior to a sharp temperature rise at about 33 seconds into the run. This time was shown to correspond to the time at which burnthrough of the injector face plate occurred and injector control was subsequently lost. The analytical heat transfer model DEAP found successful in post-predicting the calorimeter heat transfer in Tests 001, 003, and 004, was used in conjunction with measured operating parameters (i.e., chamber pressure, flowrate, initial wall temperature, etc.) from Test 008 to obtain an analytical prediction of the temperature behavior of the graphite wall for this test. The results obtained from the DEAP model are superimposed on the measured traces in Fig. 99 through 102. Excellent agreement between theory and experiment is noted at each axial thermocouple location. With the exception of the measured operational parameters, no additional changes were made in the DEAP model which has previously given satisfactory posttest predictions of the early calorimeter hot firings (Tests 001, 003, 004).

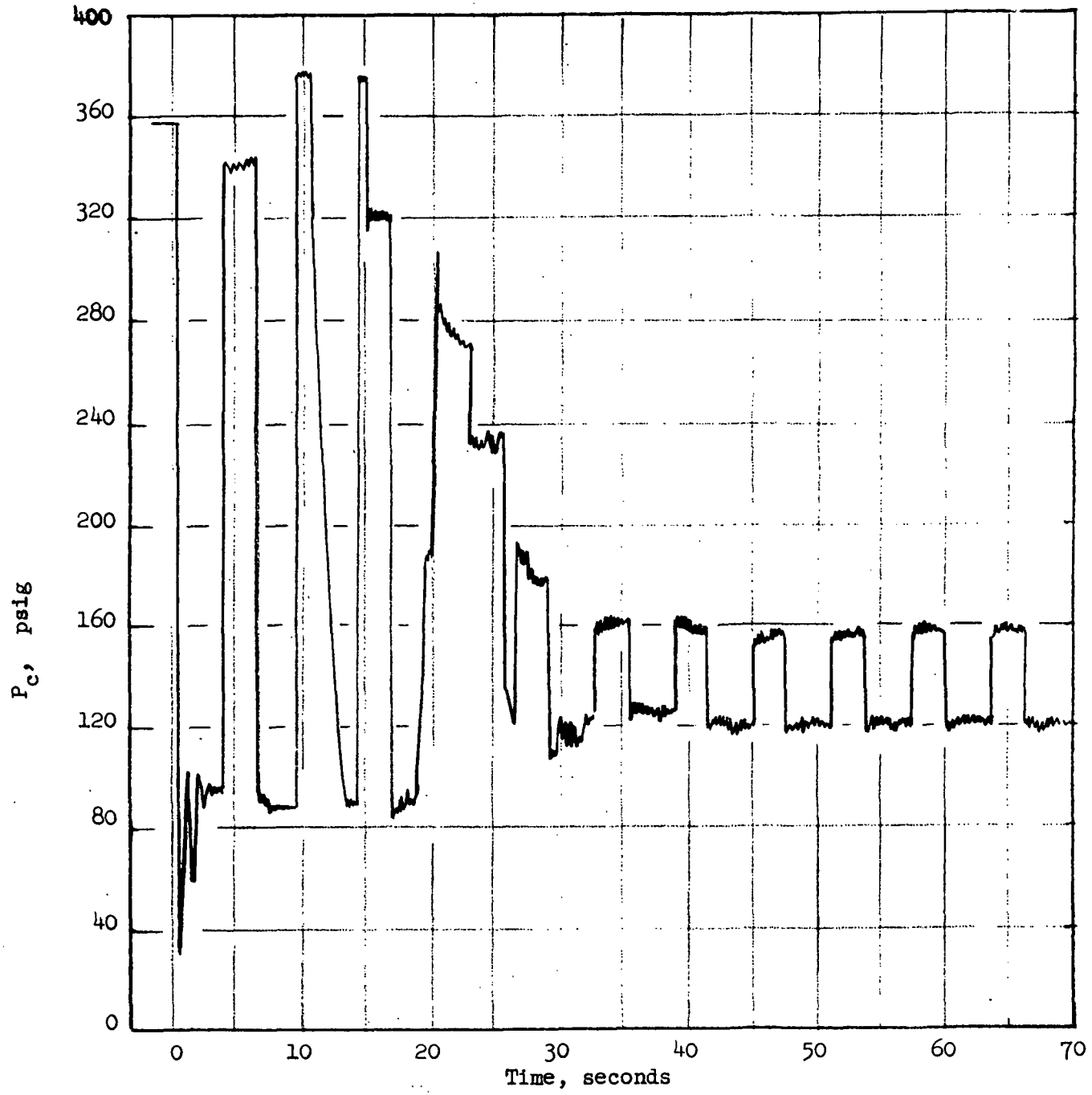

Figure 98. Chamber Pressure Versus Time

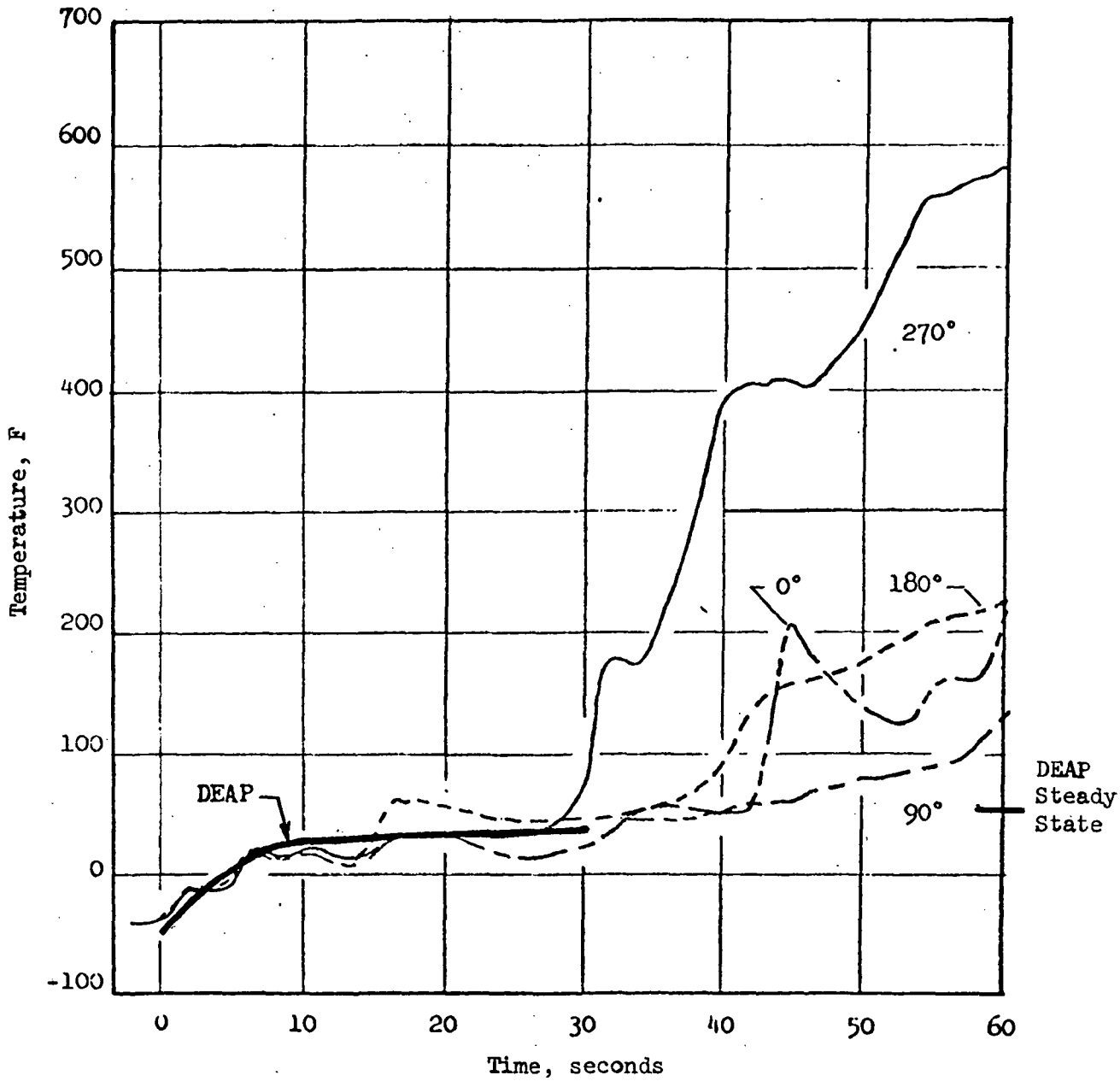

Figure 99. Graphite Outside Wall Temperature at 1-Inch Axial Location as Function of Thermocouple Position - Test 008

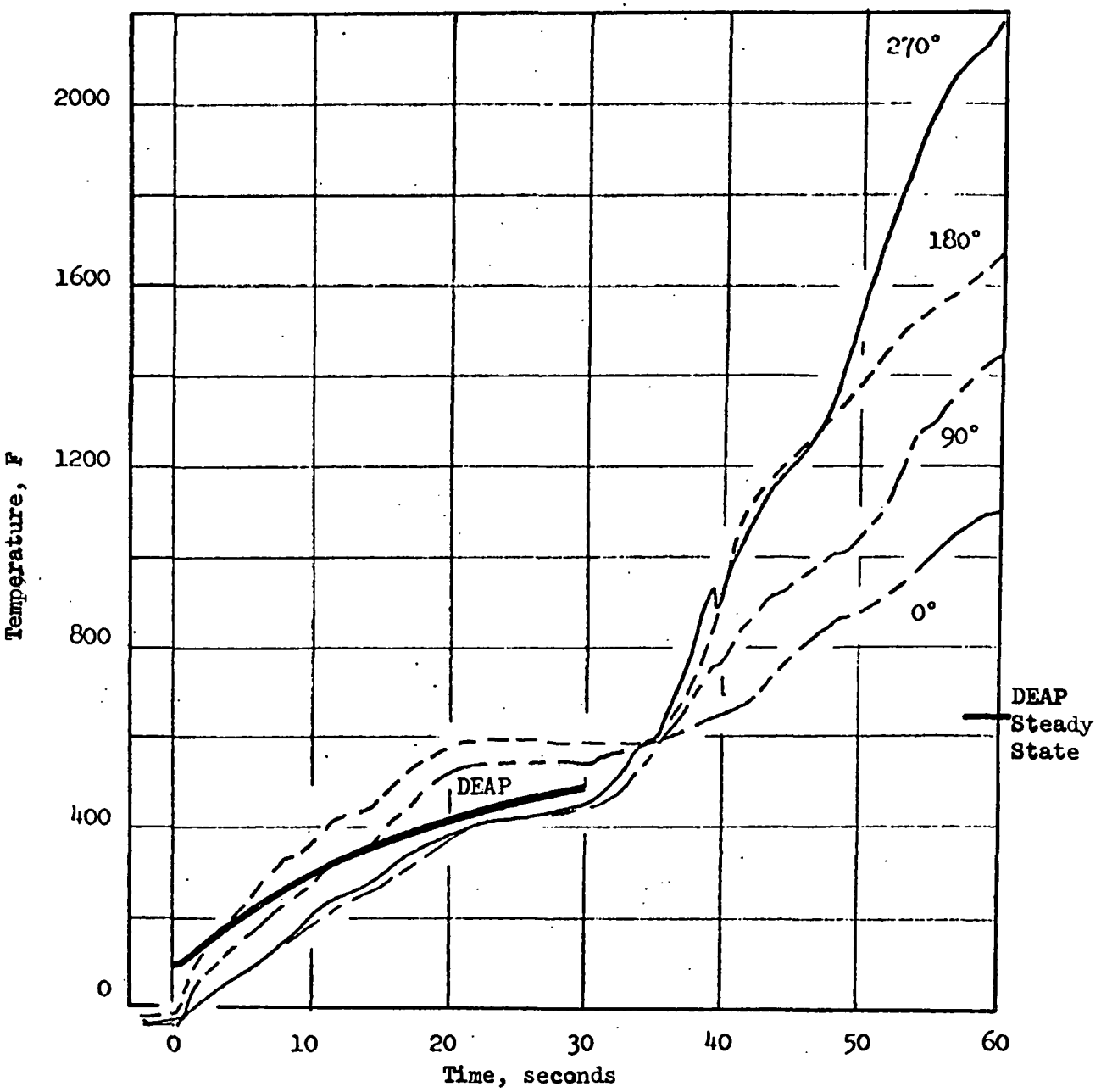

Figure 100. Graphite Outside Wall Temperature at 3.5-Inch Axial Location as Function of Thermocouple Position - Test 008

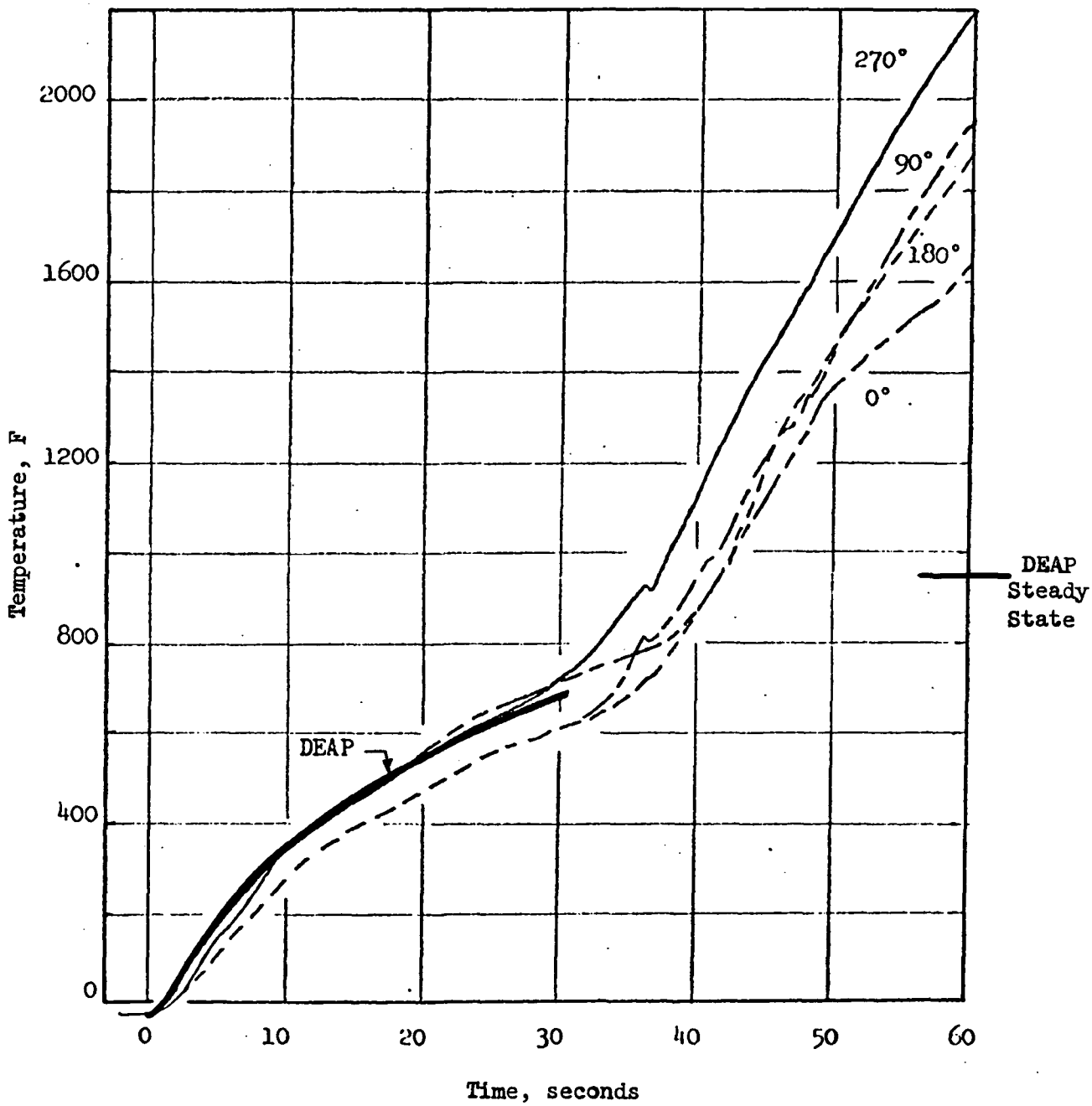

Figure 101. Graphite Outside Wall Temperature at 5-Inch Axial Location as Function of Thermocouple Position - Test 008

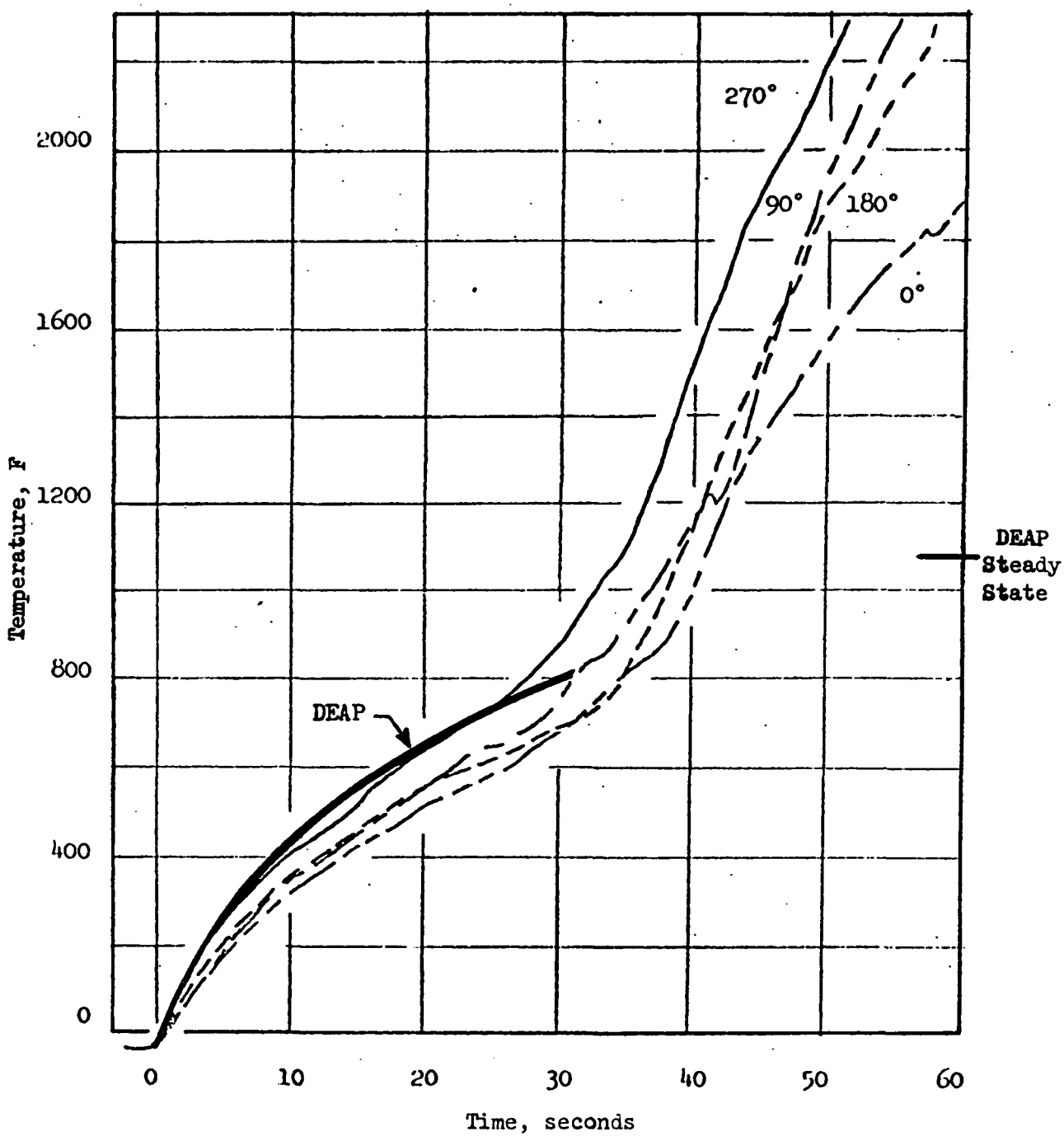

Figure 102. Graphite Outside Wall Temperature at 6.75-Inch Axial Location as Function of Thermocouple Position - Test 008

The DEAP model, which accurately predicts the measured wall temperatures during the first 33 seconds of Test 008, also predicts that, if the test had proceeded to 150 seconds without injector incident, the maximum temperature in the graphite inner liner would not have exceeded 1310 F. (Steady-state temperatures predicted to occur at the temperature measurement stations are shown in Fig. 99 through 102.) The results of this DEAP model prediction, therefore, generate optimism regarding the feasibility of obtaining a completely successful long duration OF_2/B_2H_6 hot firing with a graphite lined chamber.

POSTTEST SYNOPSIS OF NEW INJECTOR DESIGN

A comparison of the cross-sectional views of both the NAS7-304 injector design and the NAS7-767 injector design is shown in Fig. 103. The NAS7-767 injector design, which employs diffusion bonding of the injector face plate to the manifold, was improperly bonded as a result of poor temperature control during the bonding operation. The Los Angeles Division has since revised operational procedures to preclude the possibility of poor temperature control on future bonds. Since past operation with properly diffusion-bonded injectors at Rocketdyne has been found to be entirely satisfactory, no further discussion of this problem area will be presented.

The occurrence of two-phase oxidizer flow during, at least, the three calorimeter test firings with the NAS7-767 injector (Tests 005 - 007) resulted in higher than anticipated injector face heating. Calculating the vapor pressures existing in the oxidizer injection manifold and comparing them to the operating chamber pressures clearly indicated that two-phase flow occurred in the calorimeter hot firings (Tests 005 - 007) with the NAS7-767 injector. The results of this comparison for Tests 005, 006, 007, and also 008 (where the two-phase problem was probably eliminated), are shown in Fig. 104 along with the oxidizer flowrate, ΔP characteristics of the diffusion bonded injector in hot fire, and cold flow. The existence of "hot" FLOX is most apparent in Test 005, although FLOX temperatures in Tests 006 and 007 are also unacceptably high, and indicate that two-phase flow did occur in the oxidizer manifold and/or orifices in those tests also. The fact that localized face overheating did not occur on Test 005, which was of 2-second duration, but did occur during the Test 006 - 007 series was probably due to the fact that the latter series contained a relatively long run duration of 10 seconds (Test 006). The face overheating was localized. Since the injector ran two-phase during Test 006, cooling of the whole face was probably marginal. The reason the damage was localized is that the new injector manifold design accentuated the problem in these local areas.

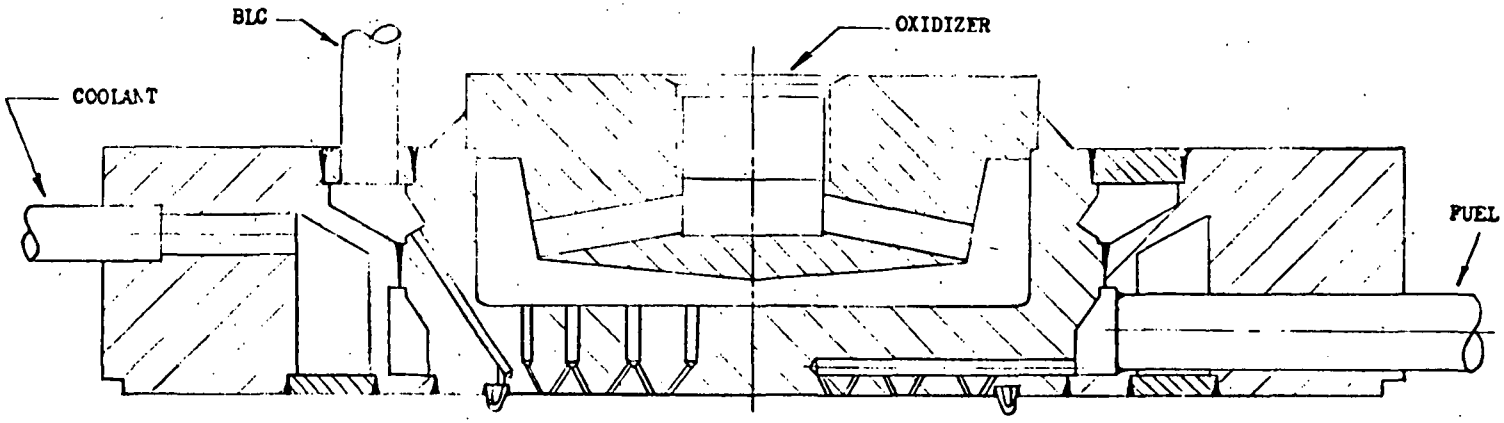

NAS7-304 INJECTOR

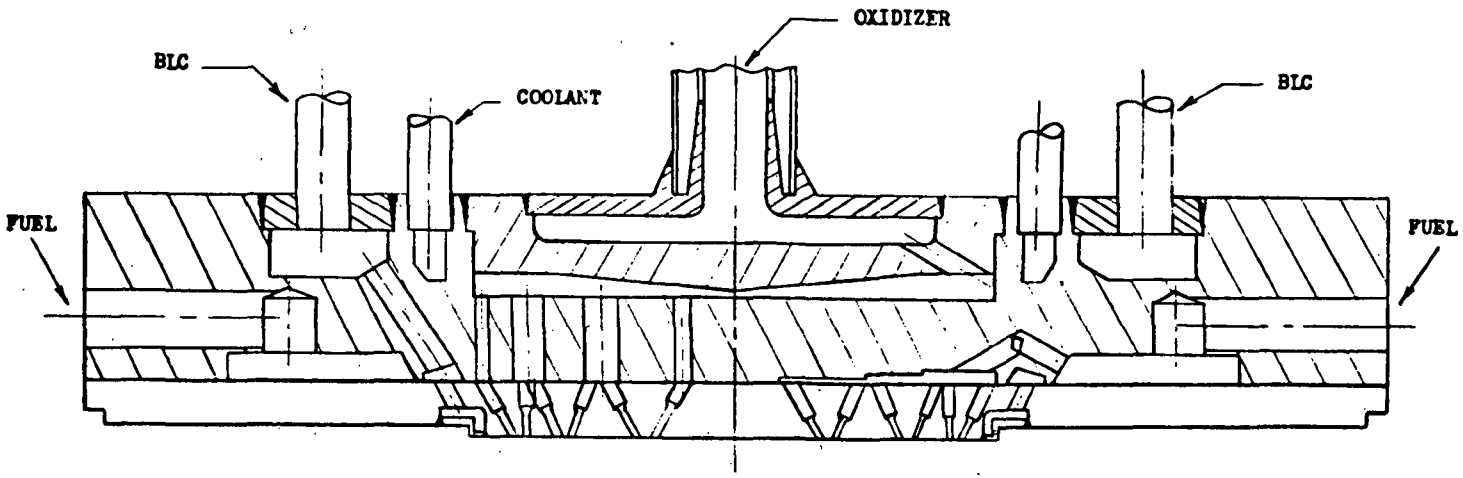

NAS7-767 INJECTOR

Figure 103. Comparison between NAS7-304 and NAS7-767

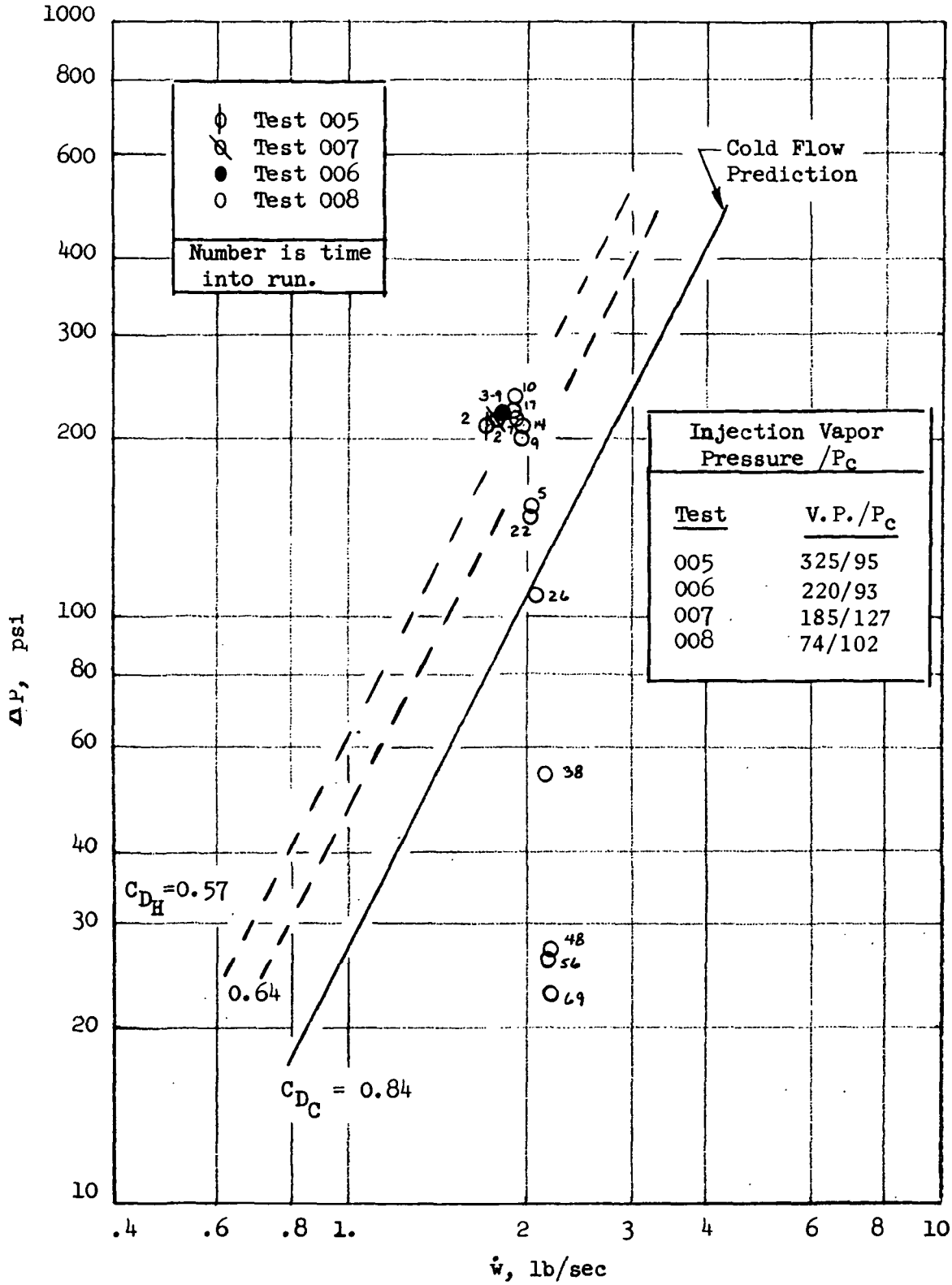

Figure 104. Oxidizer Flowrate - ΔP Characteristics of New Injector

The face overheating of the injector during Test 006, shown in Fig. 84, was observed to occur predominantly at those oxidizer orifices fed through the two large downfeed passages as shown in Fig. 96. There was also some slight erosion in those orifices fed by one large downfeed passage. The large downfeed passages have a surface area per unit flowrate about four times that of the small downfeed passages. The enthalpy change of the oxidizer in these large passages would be approximately 15 percent more than that in the smaller passages. This amount of additional localized energy absorption in the large downcomers might have aggravated the already marginal cooling situation to cause localized increased two-phase flow. That would cause localized decreased mass flowrate through the affected orifices through a worsening of the two-phase flow condition. Calculations made using a very simplified thermal model indicated that this type of failure mode (i.e., two-phase flow) could produce injector face temperatures high engough to initiate melting of the injector face (2000 F). A more detailed thermal re-analysis was consequently felt necessary (see following section).

It is obviously most desirable to avoid any possibility of two-phase flow in the oxidizer manifold and/or orifices. Prior to Test 008, improvements were made to the LN_2 jacketing around the FLOX line to decrease the possibility of two-phase flow. As observed in the vapor pressure/chamber pressure comparison shown in Fig. 104, no indication of the occurrence of two-phase oxidizer flow is evident in Test 008*. On future tests, however, to preclude the occurrence of two-phase oxidizer flow, it was decided to remove the methyl cyclohexane (MCH) injector cooling jacket and pre-chill the injector by flowing LN_2 directly through the oxidizer manifold.

INJECTOR HEAT TRANSFER RE-ANALYSIS

A more detailed heat transfer analysis of the diffusion bonded injector design was made to more fully assess the operating characteristics of this injector. A three-dimensional heat transfer model (TAP) of a one-quarter segment of the

* Further indication of no two-phase flow occurring on Test 008 is derived from the visual observation that those oxidizer holes showing most erosion after Tests 006 - 007 (due to two-phasing) did not appear to be much further damaged after Test 008.

injector face plate and manifold was set up, using a network of approximately 300 nodes to describe the heat transfer interaction between combustion gas and the fuel and oxidizer orifices and feed passages. Figure 105 shows a cross-sectional representation of the nodal network used in the computer model, and identifies the location of fuel and oxidizer nodes. Utilizing this model, both the transient and steady-state heat transfer characteristics of the injector were determined as functions of various gas-side and propellant feed-side conditions. These results are described below.

Interpretation of Test 006 Local Overheating

To aid in the interpretation of the localized face overheating observed after test series 006 - 007, the operating conditions of Test 006* were used to obtain input data for the TAP model of the injector. Values of the gas-side heat transfer coefficient at the injector face (h_g) and the combustion gas temperature at the injector face, T_g, were selected to be 0.0006 Btu/in.^{2}-sec F and 3210 F, respectively. These values are identical to those employed in the DEAP heat transfer model of the combustor which were effective in post-predicting the thermal behavior of the chamber wall in Tests 006 and 008. Using these values of h_g and T_g and the run conditions of Test 006, the TAP injector model (ignoring the occurrence of two-phase flow) predicted a steady state temperature distribution across the injector face as shown in Fig. 106**. As shown in Fig. 106, the injector is predicted to operate at a temperature ranging from 1300 to 1500 F, depending on injector face location.

---

* Test 006 was a 10-second run. Test 007 was a 2-second run. It is felt that the localized overheating occurred during Test 006.

** Heat transfer between the BLC coolant and the coolant orifices was accounted for. However, no account was made for heat transfer from the liquid film to the BLC ring gap. Therefore, temperatures predicted at the outer periphery of the model are somewhat conservative.

Manifold storage conditions of 170 R FLOX and 270 R B_2H_6 were assumed for all computer cases. The presence of two-phase flow occasioned by inadequate subcooling was treated through adjustment of the heat transfer coefficients.

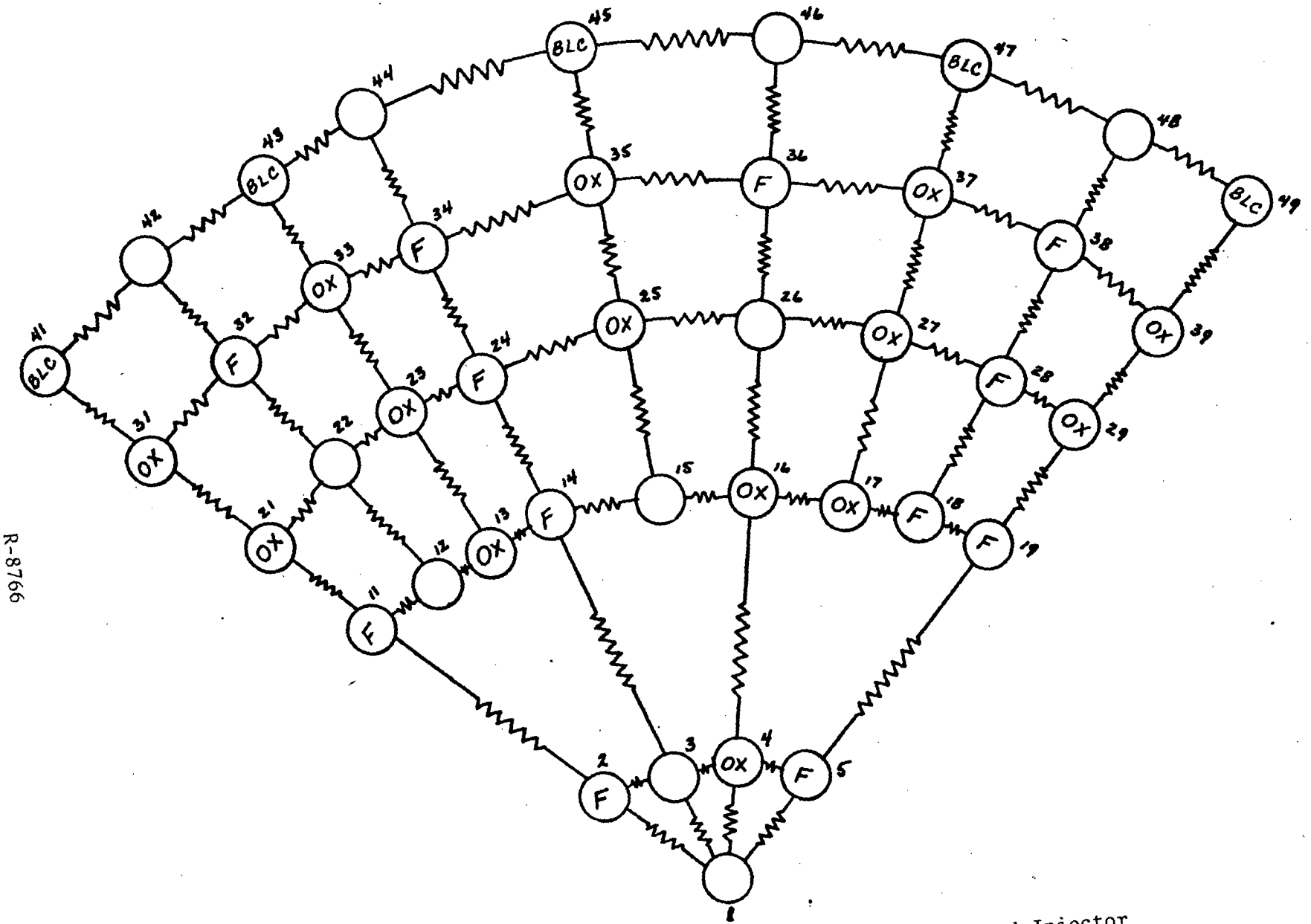

Figure 105. TAP Model Nodal Network for Diffusion-Bonded Injector

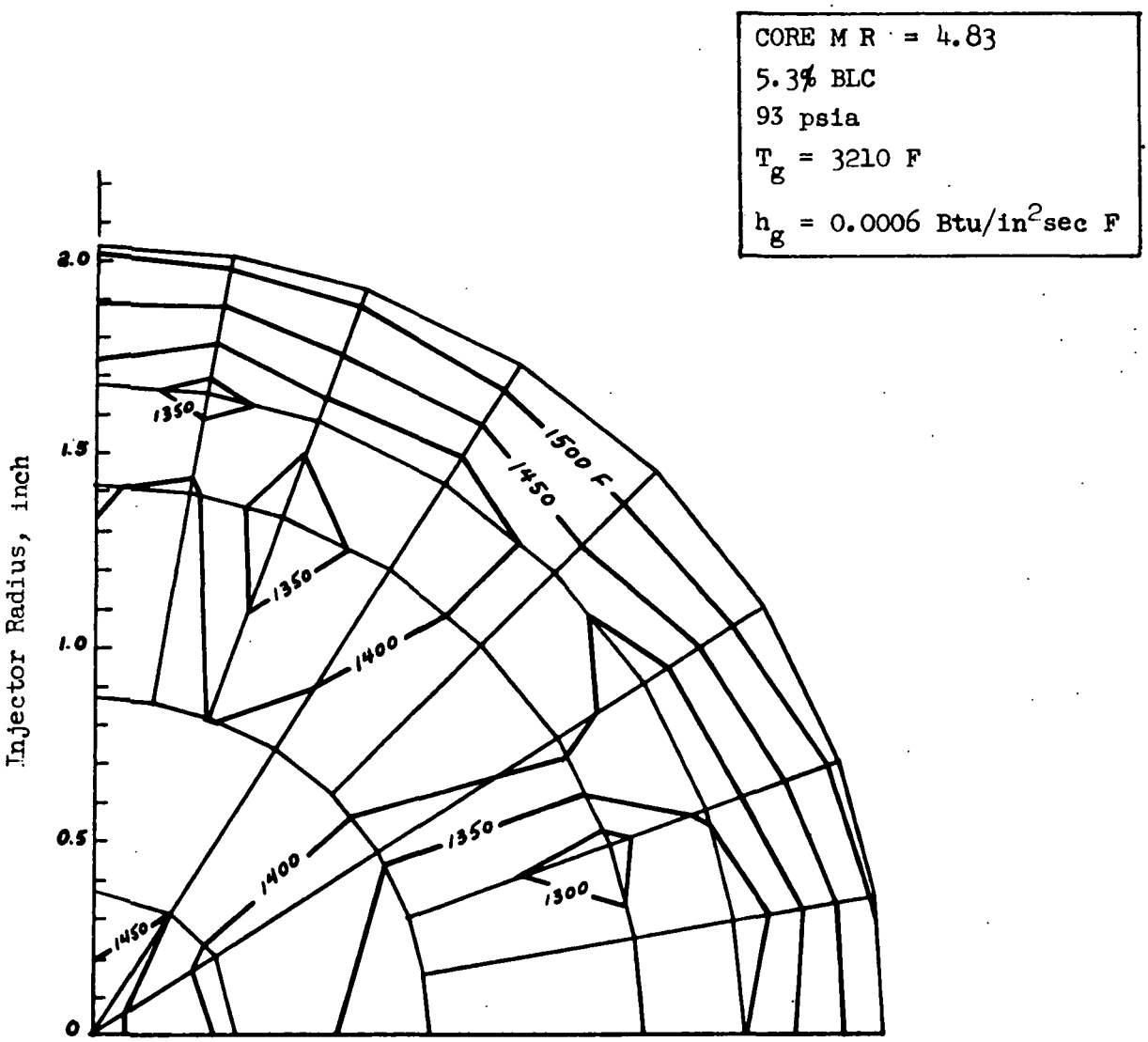

Figure 106. Predicted Steady-State Temperature Distribution (without two-phase flow) for Diffusion-Bonded Injector - Test 006 Conditions

As mentioned above, the results shown in Fig. 106 do not account for the possibility of two-phase flow occurring in the fuel or oxidizer orifices. The fact that two-phase flow did occur in the oxidizer orifices on Test 006 was dicusssed earlier*. Using the computer results for the base case shown in Fig. 106, the amount of heat transferred from the metal surface to the oxidizer flows in the various nodes was then determined. Assuming the oxidizer entering the back of the manifold to be at saturation conditions, it was then possible to calculate the quality (vapor weight fraction of the oxidizer stream at each orifice exit. The quality was found to vary from a high of 0.081 at the node 35 orifice to a low of 0.047 at the node 17 orifice, with an average value over the injector face of 0.062. Thus, two-phase oxidizer flow, should it occur, is predicted to occur not in preferential orifices, but in all orifices.

Assuming that two-phasing is occurring in all of the oxidizer orifices, a calculation was made using the Martinelli parameter to determine the reduction in cooland side heat transfer coefficient for two-phase flow. A two-phase FLOX mixture having a quality of 0.06 was calculated to have a coolant side heat transfer coefficient of 0.12 times the single liquid phase value. Using this reduced value of oxidizer coolant coefficient in the TAP injector model, the steady state temperature distribution across the injector face shown in Fig. 107 is predicted. A similar prediction for 10 seconds is shown in Fig. 108. While an increased face temperature is predicted with two-phase oxidizer flow, especially in the vicinity of the oxidizer nodes, the localized overheating observed after Test 006 - 007 (see Fig. 84) is not predicted.

In the above analyses, no account was taken of the possibility of increased gas-side heat transfer coefficients in the vicinity of the oxidizer orifices. Such gas-side heat transfer enhancement might well be expected since the presence of two-phase flow might encourage recirculation and, therefore, increase h_g.

---

* On Test 006, the injection vapor pressure of the oxidizer was 220 psia compared to a chamber pressure of 93 psia.

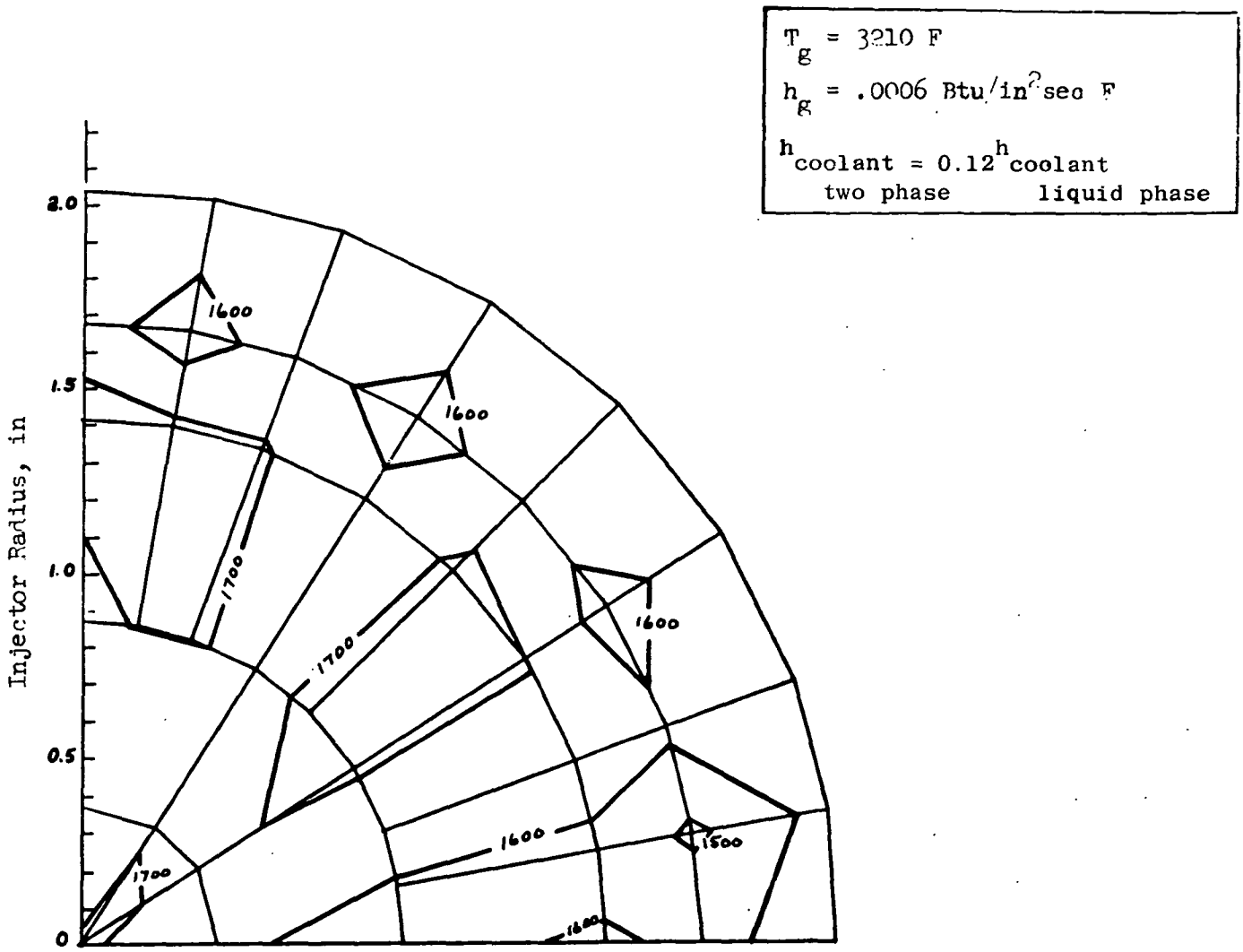

Figure 107. Predicted Steady-State Temperature Distribution (Including Two-Phase Flow) for Diffusion-Bonded Injector

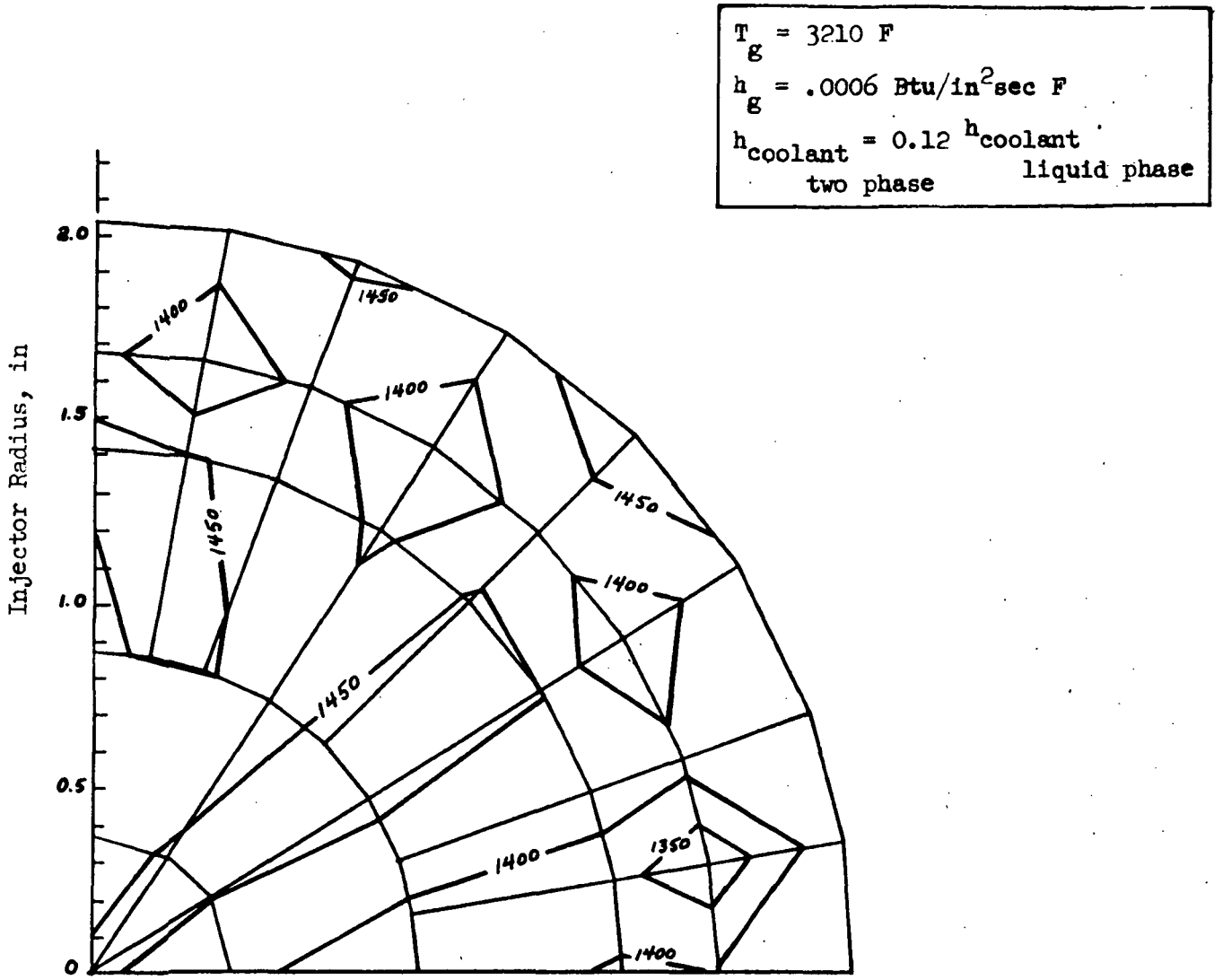

Figure 108. Predicted 10-Second Temperature Distribution (Including Two-Phase Flow) for Diffusion-Bonded Injector - Test 006 Conditions

By doubling the h_g at the oxidizer nodal locations, the predicted 10-second injector face temperature distribution shown in Fig. 109 was obtained with the TAP injector model. This prediction closely approximates the localized overheating observed in Test 006. The predicted temperature of 1800 F at these locations is close to the value necessary to initiate reaction between the nickel face and fluorine (1800 - 2000 F). It is, therefore, believed that the occurrence of two-phase flow in the oxidizer orifices can adequately explain the localized overheating observed after the Test 006 - 007 test sequence.

The above predictions obtained with the TAP injector model indicate that successful operation of this injector under two-phase (oxidizer) conditions is not possible. To estimate the degree of oxidizer subcooling required to avoid the occurrence of two-phase flow, the computer results for the case shown in Fig. 106 were again employed. The maximum amount of heat transferred to the worst oxidizer orifice feed passage was calculated ($q/\dot{w}$ = 6.09 Btu/lb, node 35) and the required amount of subcooling was calculated from the relation

$$\Delta T = \frac{q}{\dot{w}\, C_p}$$

where

$$\Delta T = T_o - T_i$$

T_o = maximum exit temperature of FLOX (i.e., saturation at P_c)

T_i = FLOX temperature at inlet to manifold

For the case shown in Fig. 106, the amount of subcooling required to avoid two-phase oxidizer flow in the "worst" orifice is 16 F. It should be noted that 16 F oxidizer subcooling is entirely consistent with present operational plans for the OF_2/B_2H_6 system. A common propellant storage temperature of 250 R is anticipated (Ref. 13). For OF_2, this represents 35 F of subcooling for 100-psia chamber pressure operation. Improvements made to the LN_2 jacketing around the FLOX line prior to Test 008 enabled a FLOX manifold temperature of 170 R or less to be maintained. This represents 24 F of subcooling for 100-psia chamber pressure operation.

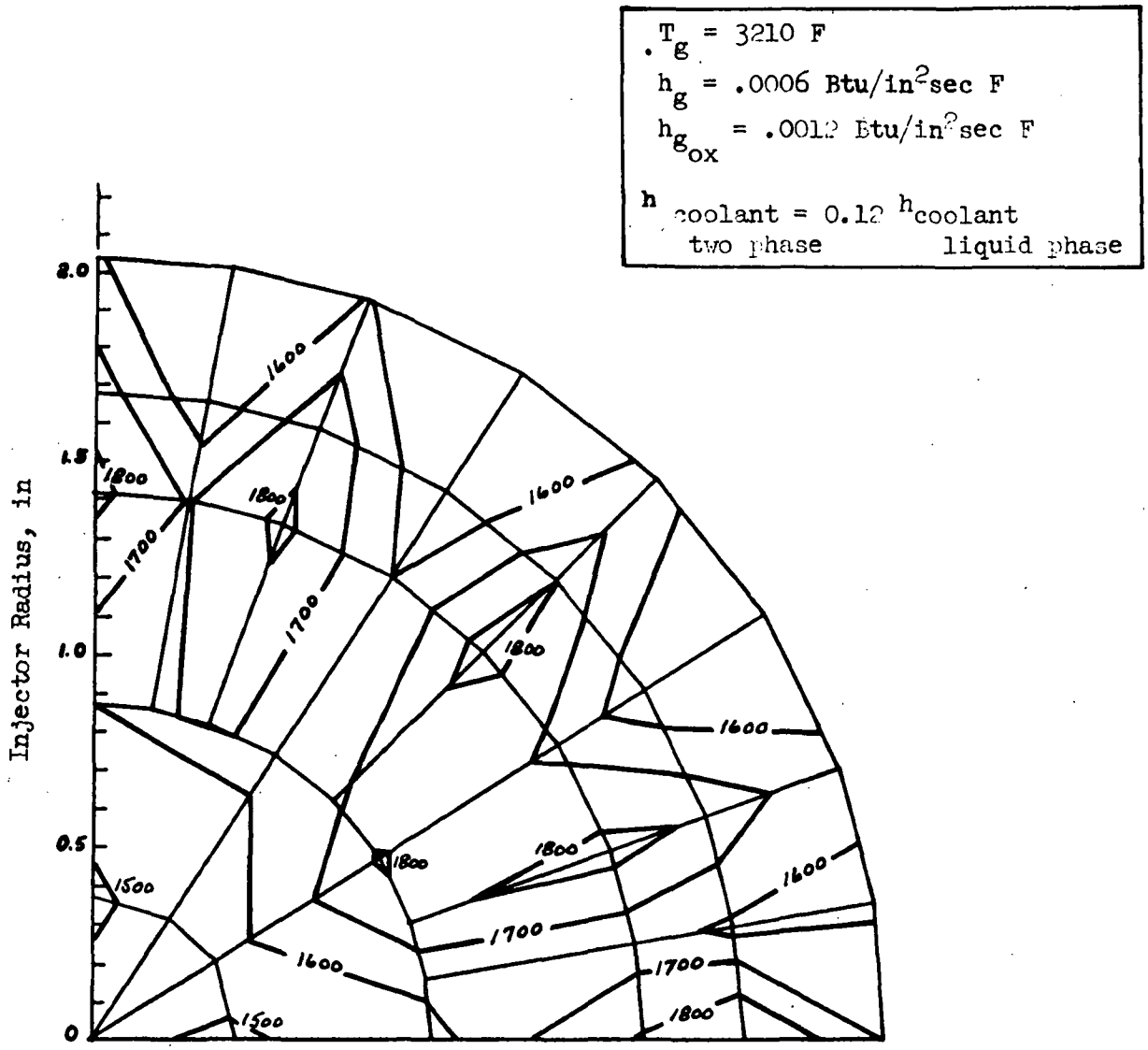

Figure 109. Predicted 10-Second Temperature Distribution (including two-phase flow and local gas side film enhancement in the vicinity of two-phase flowing orifice) for Diffusion-Bonded Injector

Effects of Injector Operating Conditions

A steady state prediction made with the TAP injector model for operating conditions of 3.0 core MR, 10 percent BLC, and 100-psia chamber pressure (see Fig. 110) can be compared with the steady state prediction for Test 006 conditions (4.83 core MR, 5.3 percent BLC, 93-psia chamber pressure) (see Fig. 106). An injector temperature reduction of about 75 F is predicted.

Effect of Manifold Design Changes

Among the possible manifold design changes considered for the diffusion bonded injector were the following:

1. Decreased diameter of "large" oxidizer feeders
2. Radial oxidizer feed toward center of injector from sixteen tangentially uniform downcomers near the injector periphery
3. Radial star pattern oxidizer feed from eight downcomers, spaced at equal tangential positions about six-tenths of the radial distance from the center to the periphery of the injector
4. Radial oxidizer feed from one downcomer located at the center of the injector.

Each one of these possible oxidizer manifold modifications was examined using the TAP injector model, and was found to have no appreciable effect on the predicted injector face temperature distribution.

Comparison With NAS7-304 Injector

To compare the NAS7-767 diffusion-bonded injector design (which allowed for essentially face deposition-free operation and eliminated the "thermal spiking" problems encountered with the NAS7-304 injector) to the NAS7-304 injector (which performed most acceptably from an injector heat transfer standpoint), the NAS7-304 injector was also analyzed with the TAP injector model under operating conditions identical to those used to obtain the predictions for the NAS7-767

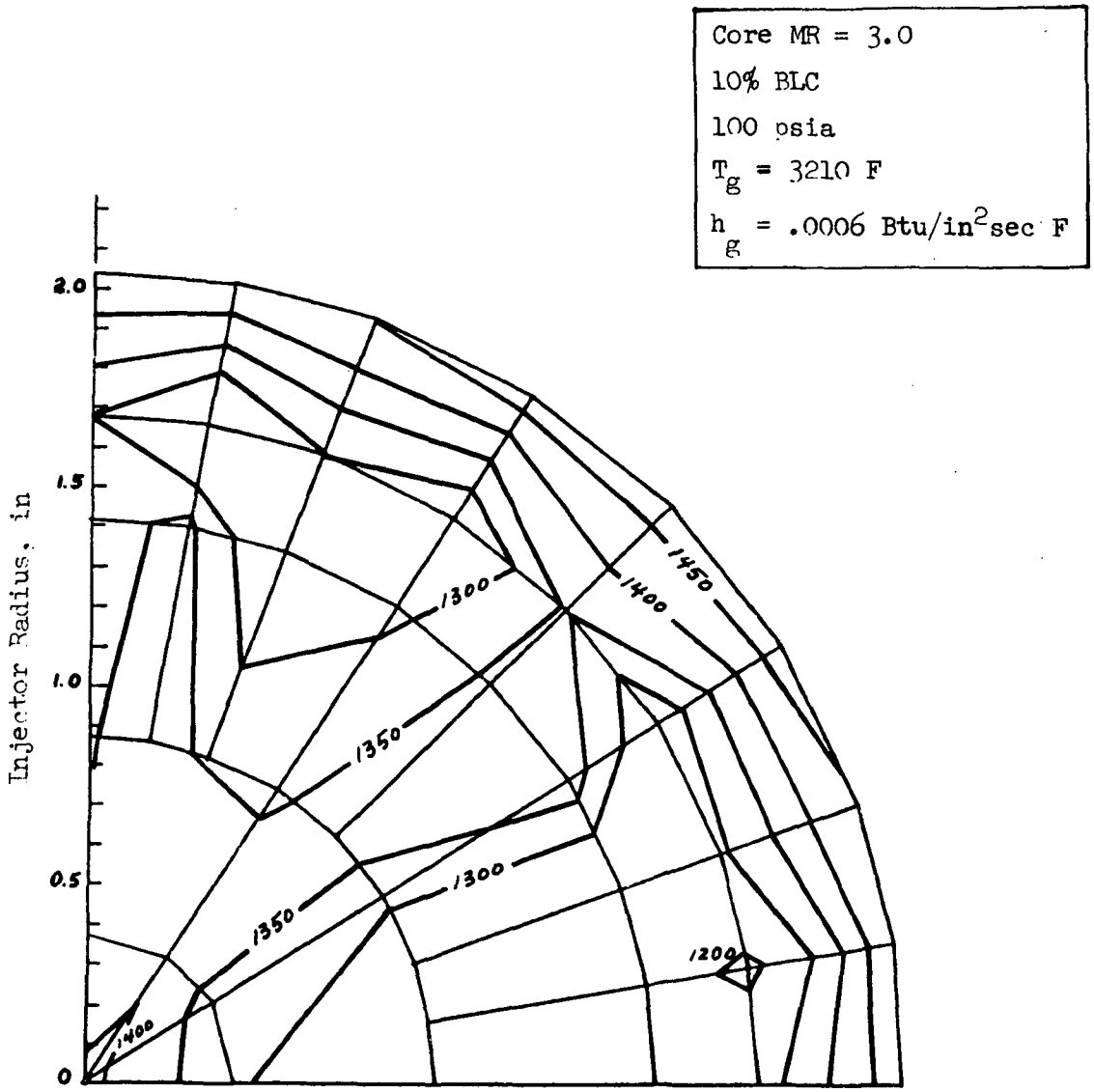

Figure 110. Effect of Operating Conditions on Predicted Steady-State Temperature Distribution

injector shown in Fig. 106. The nodal network used in the computer model of the NAS7-304 injector is shown in Fig. 111. The predicted injector face temperature distribution for the NAS7-304 injector is shown in Fig. 112. Comparison between Fig. 112 and Fig. 106 reveals that the NAS7-304 injector is predicted to operate about 250 F cooler than the diffusion bonded injector. This margin of safety might indeed have been sufficient to allow thermally acceptable NAS7-304 injector operation, even if two-phasing in the oxidizer orifices did occur.

Effect of Face Plate Thickness

One of the major differences between the NAS7-304 injector and the NAS7-767 diffusion bonded injector design is the distance from the injector face to the radial fuel feeders (see Fig. 103). This distance is 0.205 inch for the NAS7-304 injector, and 0.375 inch for the diffusion bonded injector*. To assess the possible heat transfer advantage that might be gained by employing a decreased injector face plate thickness, the TAP computer model was run with inputs calculated for a 0.205-inch face plate thickness. The resultant predicted temperature distribution at steady state is shown in Fig. 113. Comparison of Fig. 106 and Fig. 113 shows that by decreasing the injector face plate thickness from 0.375 to 0.205 inch, an injector face temperature decrease of 200 F is predicted.

The hypothesis that the decreased distance between the injector face and the radial fuel feeder is responsible for the beneficial decrease in injector face temperature is verified through a comparison of the various heat flow components for the two face plate thicknesses. The total heat flow (Btu/sec) into the injector face can be divided into heat flows to the: (1) fuel orifices (2) oxidizer orifices, (3) fuel manifold, and (4) oxidizer manifold. This division of the total heat flow for the 0.375-inch face plate is shown in Fig. 114a. A similar division for the 0.205-inch face plate is shown in Fig. 114b. With both configurations, approximately 2.1 Btu/sec is absorbed by

* The diffusion bonded injector face plate thickness of 0.375 inch was selected to maintain a minimum L/D of 10 for both fuel and oxidizer orifices.

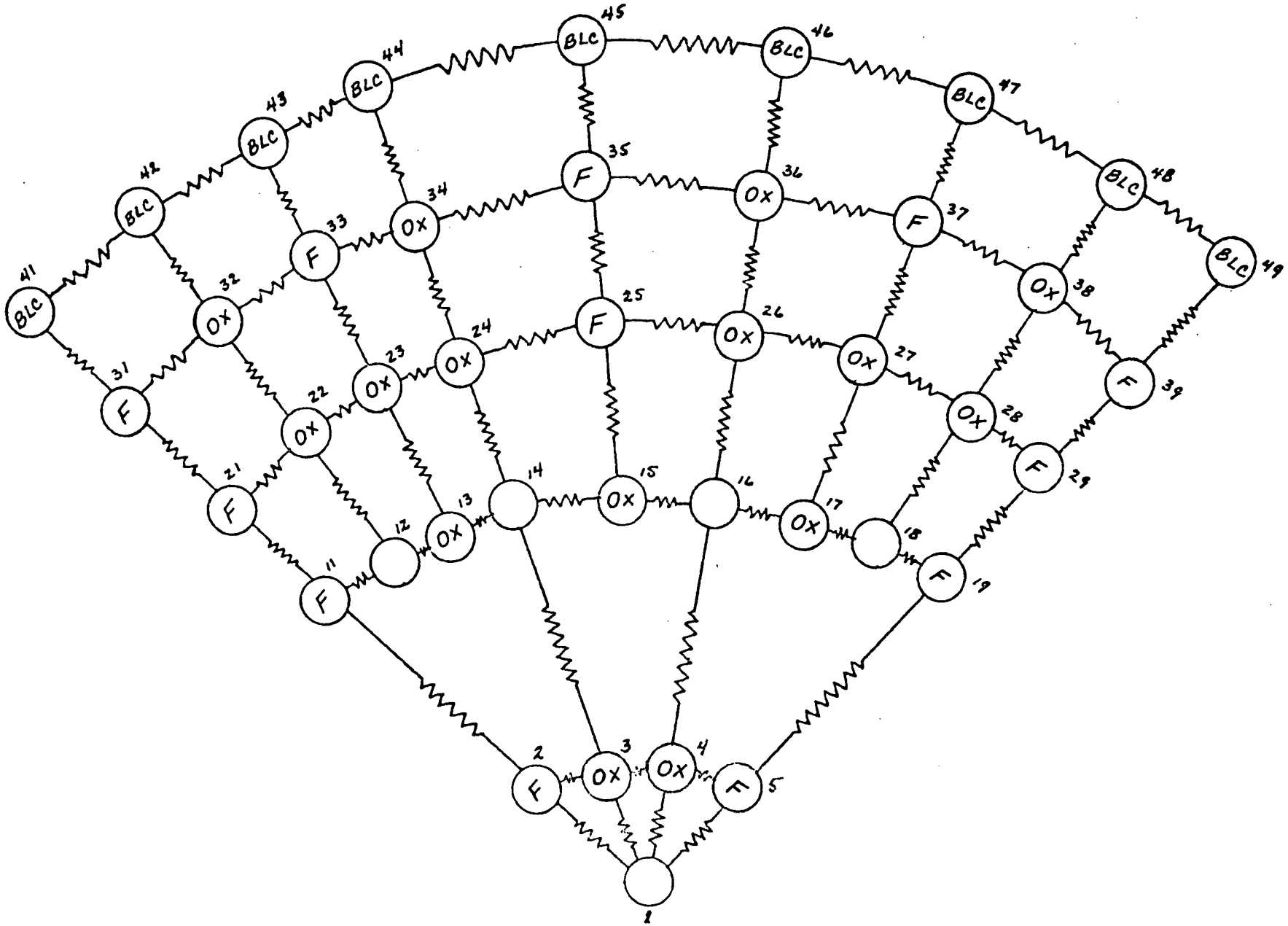

Figure 111. TAP Model Nodal Network for NAS7-304 Injector

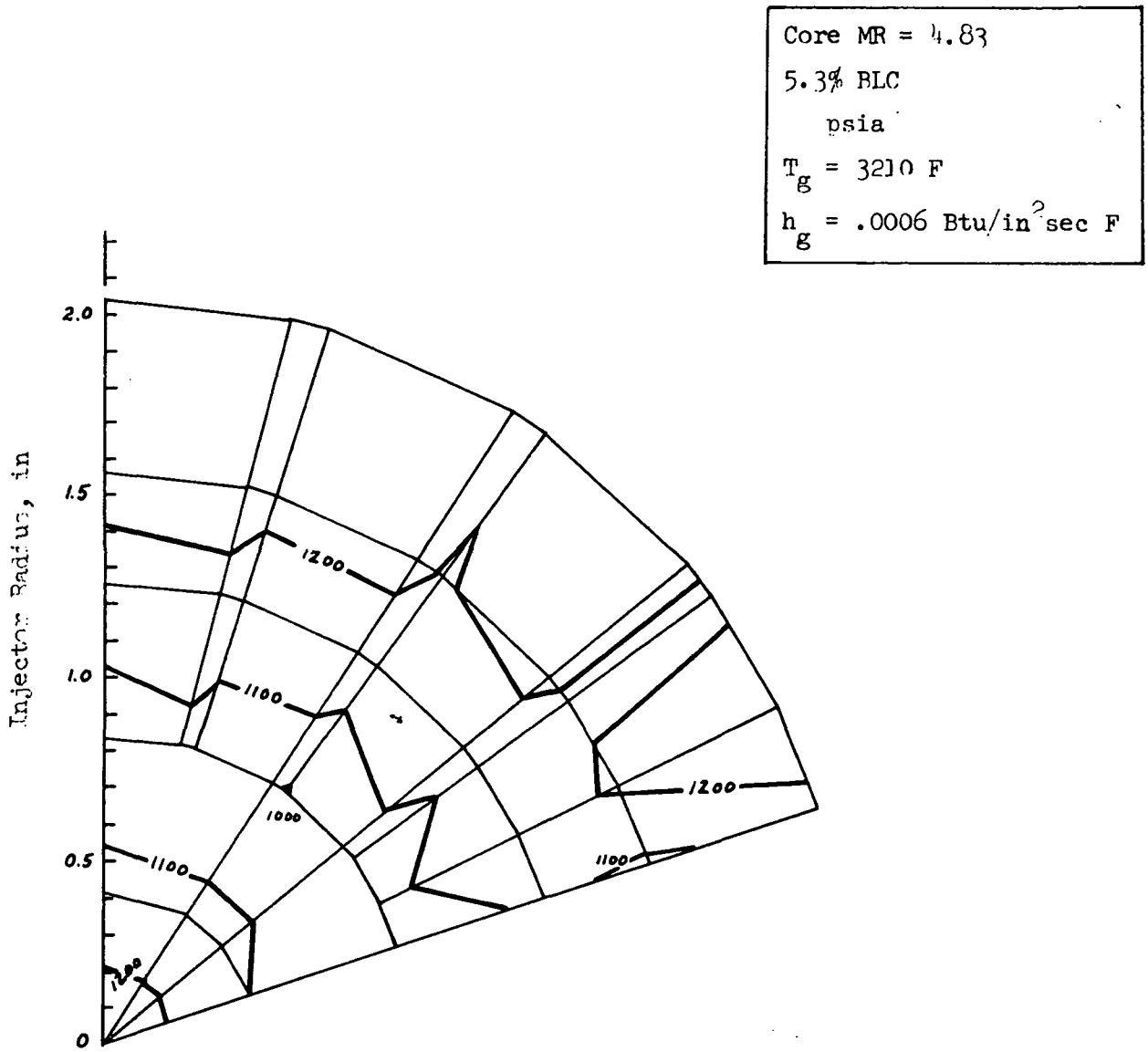

Figure 112. Predicted Steady-State Temperature Distribution for NAS7-304 Injector Under Test 006 Conditions

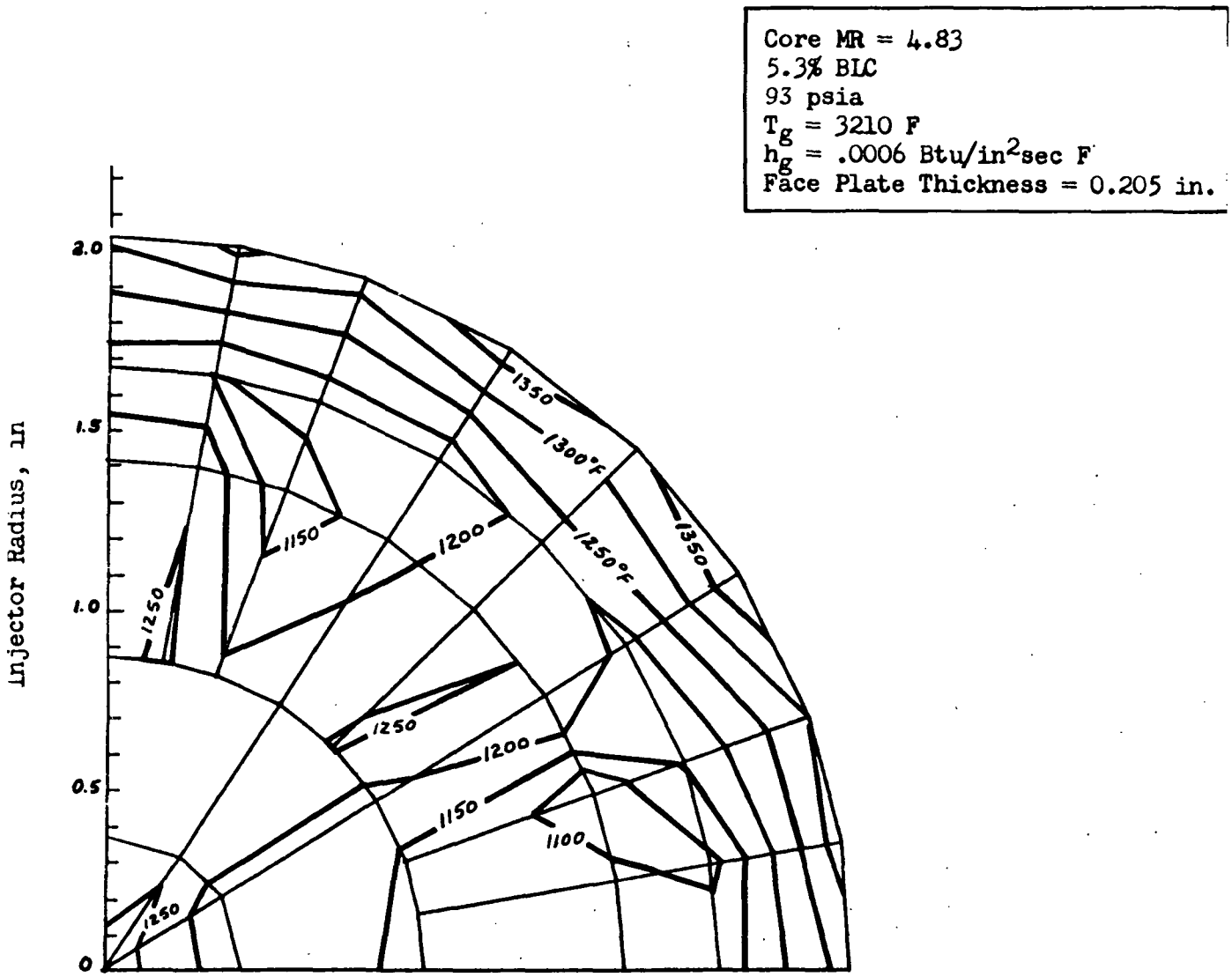

Figure 113. Effect of Decreased Injector Face Plate Thickness on Steady-State Temperature Distribution for Diffusion-Bonded Injector

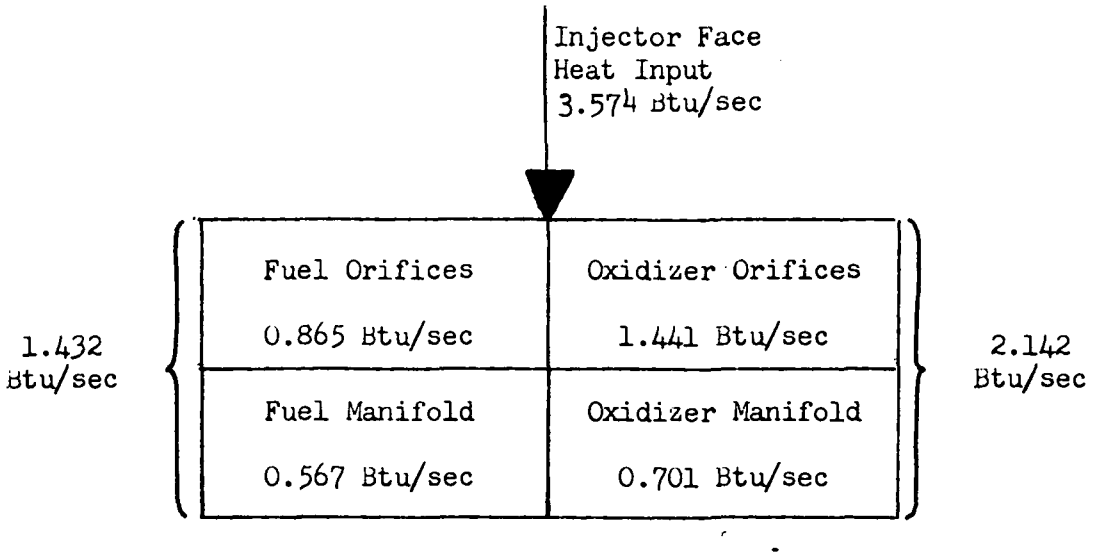

a. 0.375-Inch Face Plate

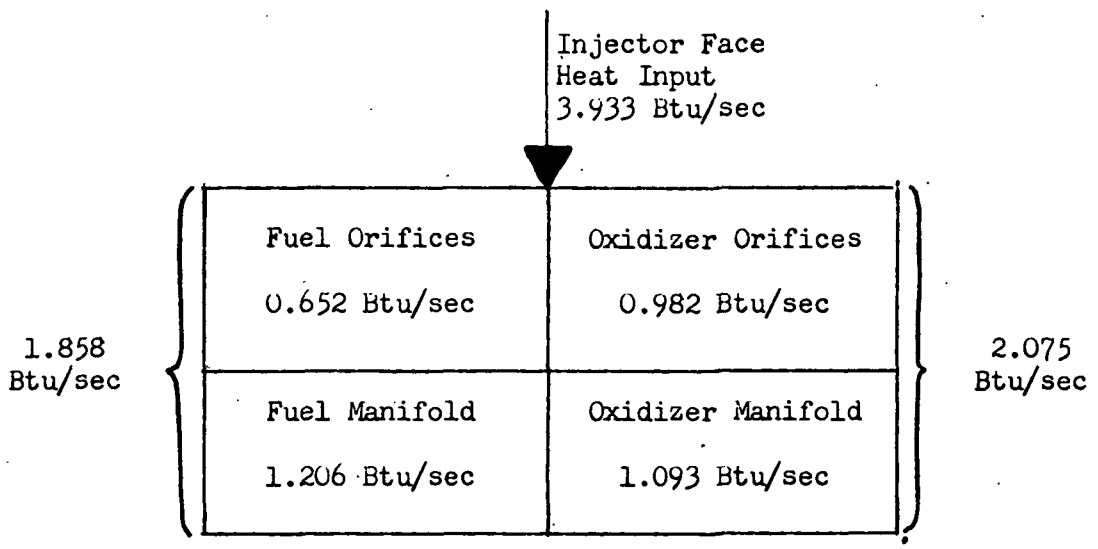

b. 0.205-Inch Face Plate

Figure 114. Comparison of Heat Flows in Injectors of Different Face Plate Thicknesses

the oxidizer. With the thinner plate configuration, however, approximately 30 percent more heat is absorbed by the fuel. As is evident from Fig. 114b, this increased capability of the fuel to absorb the heat passing into the injector face having the thinner face plate is due primarily to the greatly increased value of the fuel manifold contribution. The lower operating temperature of the thinner plate injector results directly from this increased fuel manifold cooling capability.

INJECTOR MODIFICATION SUBSEQUENT TO TEST 008

In accord with the results of the injector heat transfer re-analysis described above, the diffusion bonded injector was redesigned to incorporate an 0.0205-inch injector face plate thickness at the expense of the long (10) orifice L/D's. Additionally, the redesign necessitated a non-flow distribution compromising change in the number of BLC manifolds from three to two. The injector face pattern itself was left unaltered. Instead, the back side of the face plate and the manifold body were redesigned to reflect the thinner face plate. Oxidizer orifice L/D's were set at a constant value of 8.7. As in the previous design, the orifice entrances were contoured. The modified design, therefore, allowed for a greater margin of safety from a heat transfer standpoint with very little sacrifice in propellant flow characteristics. An additional design modification relative to fuel feed was also made. This modification eliminated the 180-degree reverse flow previously necessary for feed of the outermost row of fuel orifices.

Detailed drawings of the injector face plate, injector manifold body, BLC ring, and injector assembly are shown in Fig. 115 through 119. These drawings may be compared with the detail drawings for the original diffusion bonded injector shown in Fig. 57 through 61.

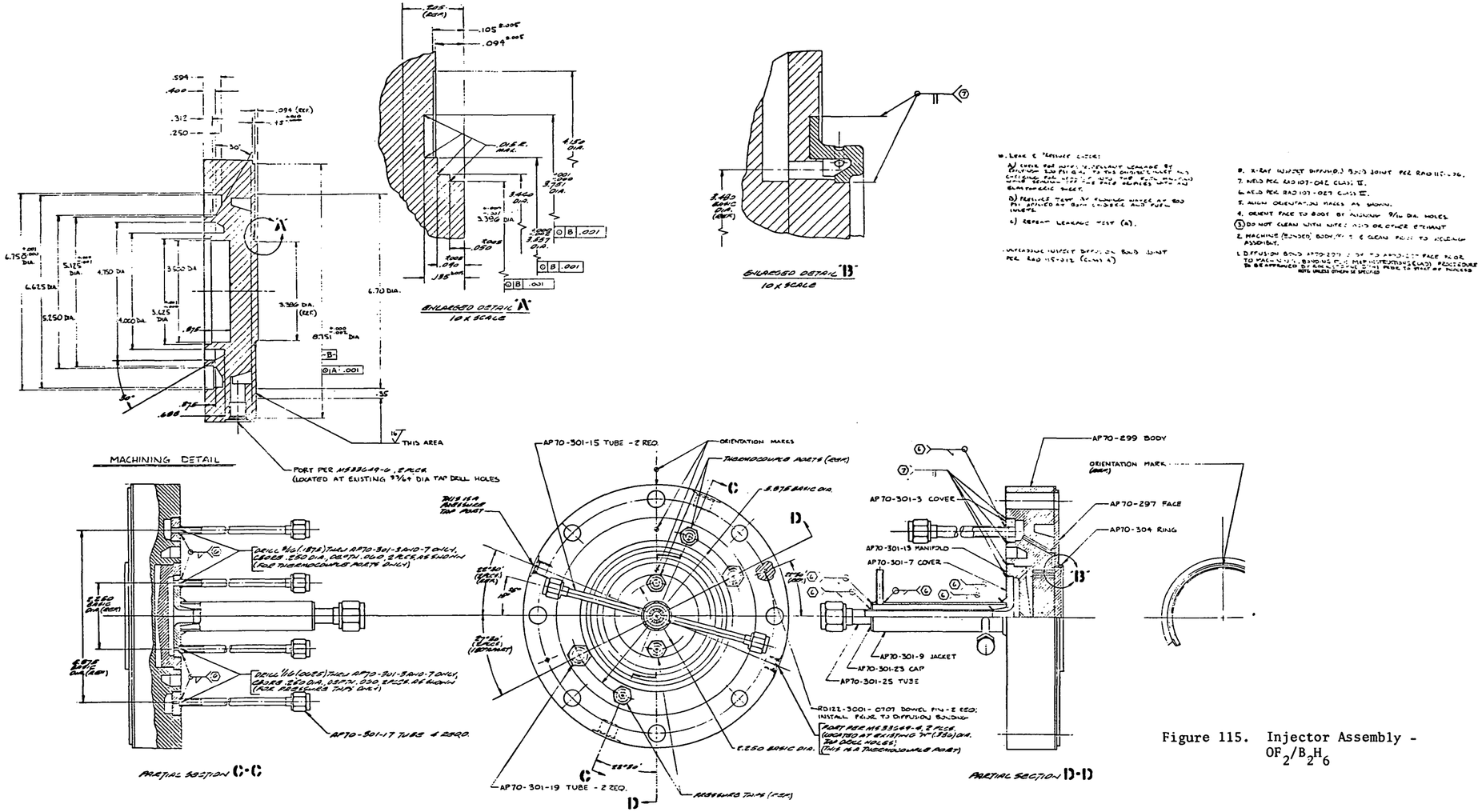

Figure 115. Injector Assembly - OF_2/B_2H_6

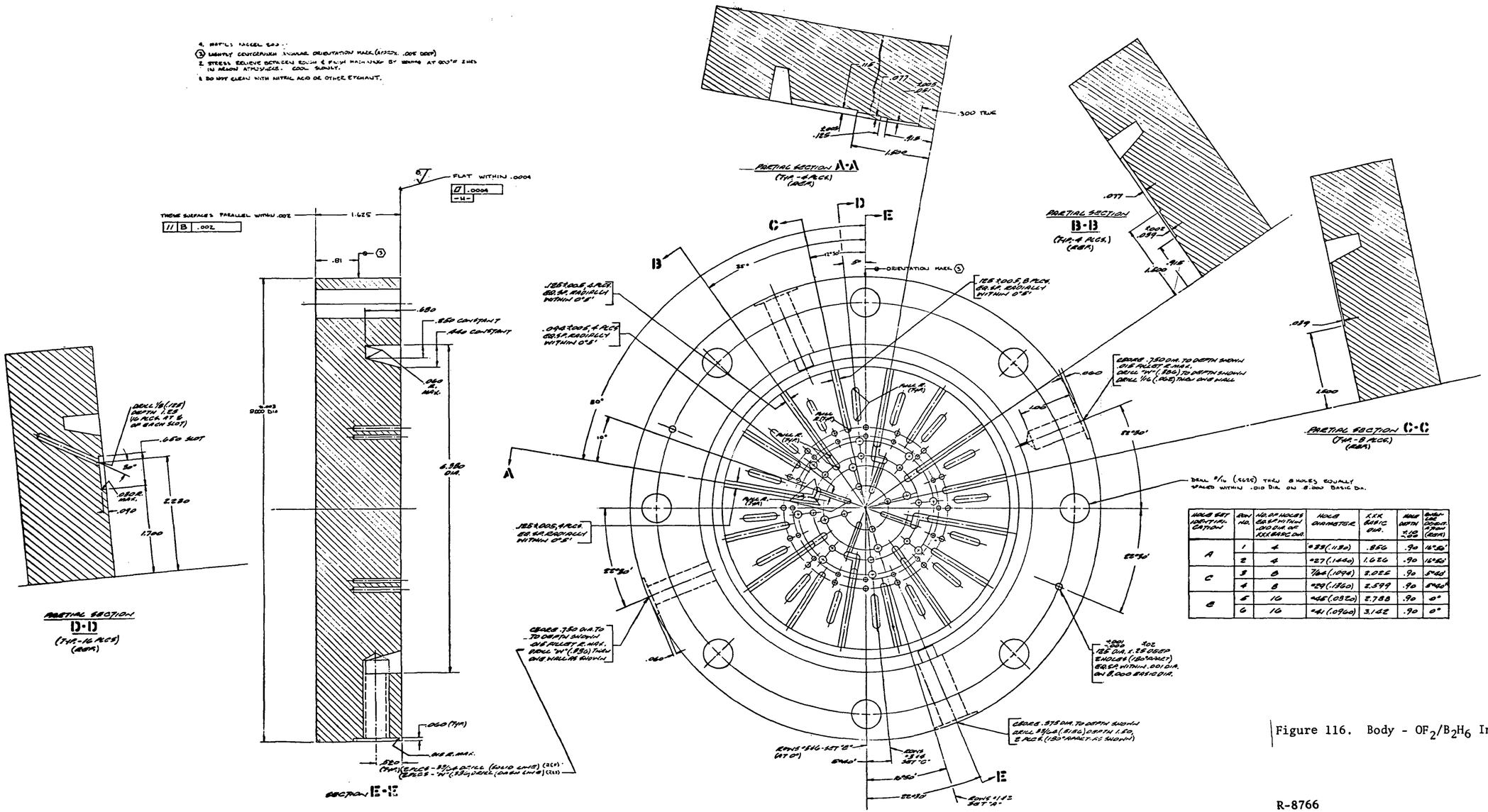

HOLE SET IDENTIFICATION	ROW NO.	NO. OF HOLES EQ. SP. WITHIN .010 DIA. OF XXX BASIC DIA.	HOLE DIAMETER	XXX BASIC DIA.	HOLE DEPTH +.10 -.00	ANGULAR ORIENTATION (REF.)
A	1	4	#33 (.1130)	.856	.90	16°50'
	2	4	#27 (.1440)	1.626	.90	16°50'
C	3	8	7/64 (.1094)	2.025	.90	5°40'
	4	8	#29 (.1360)	2.599	.90	5°40'
E	5	16	#45 (.0820)	2.788	.90	0°
	6	16	#41 (.0960)	3.142	.90	0°

Figure 116. Body - OF_2/B_2H_6 Injector

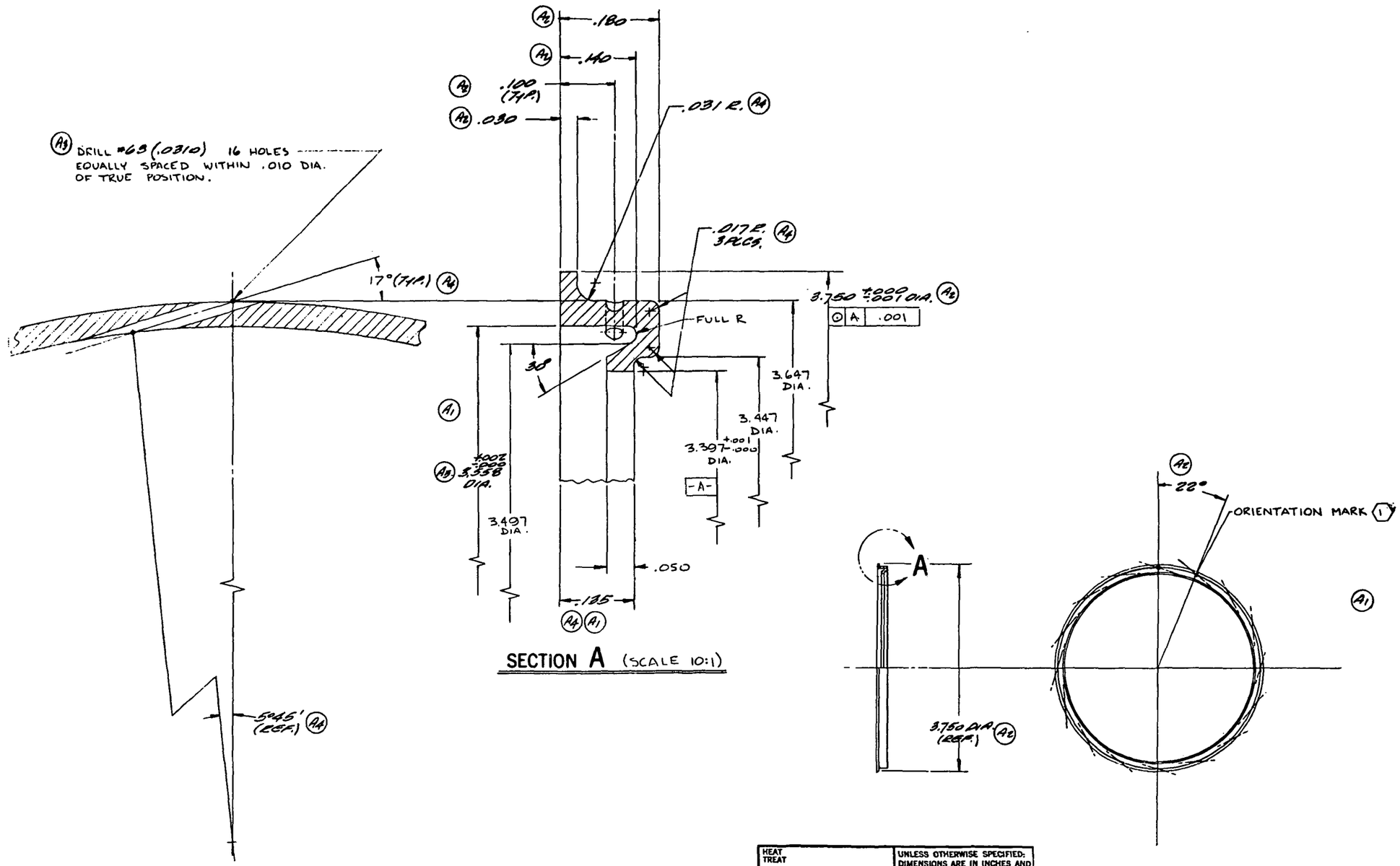

LIGHT CENTERPUNCH (APPROXIMATELY .005 DEEP) ANGULAR ORIENTATION MARK IN .031 FILLET R. ONLY

NOTE: UNLESS OTHERWISE SPECIFIED

HEAT TREAT —	UNLESS OTHERWISE SPECIFIED: DIMENSIONS ARE IN INCHES AND APPLY PRIOR TO FINISH. 125/ MACH. SURF. ROUGHNESS
FINISH DO NOT CLEAN WITH NITRIC ACID OR OTHER ETCHANT.	TOLERANCES ON: ANGLES ± 0° 30' DECIMALS .XX ± .03 .XXX ± .010 HOLES NOTED "DRILL"
MATL NICKEL 200	OVER THRU TOLERANCE .0000 .0400 + .0015 — .0010; .0400 .1300 + .0030 — .0010; .1300 .2290 + .0045 — .0010; .2290 .5000 + .0060 — .0010; .5000 .7500 + .0070 — .0010; .7500 1.0000 + .0090 — .0010; 1.0000 2.0000 + .0120 — .0010
	DO NOT SCALE PRINT

Figure 117. Ring - OF_2/B_2H_6

R-8766

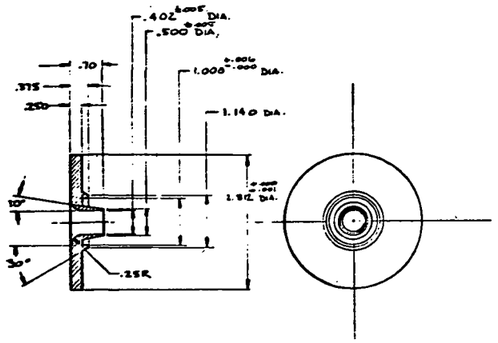

-7 OXIDIZER MANIFOLD COVER

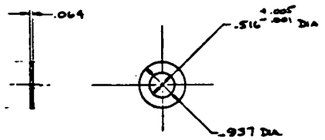

-23 COOLANT JACKET CAP

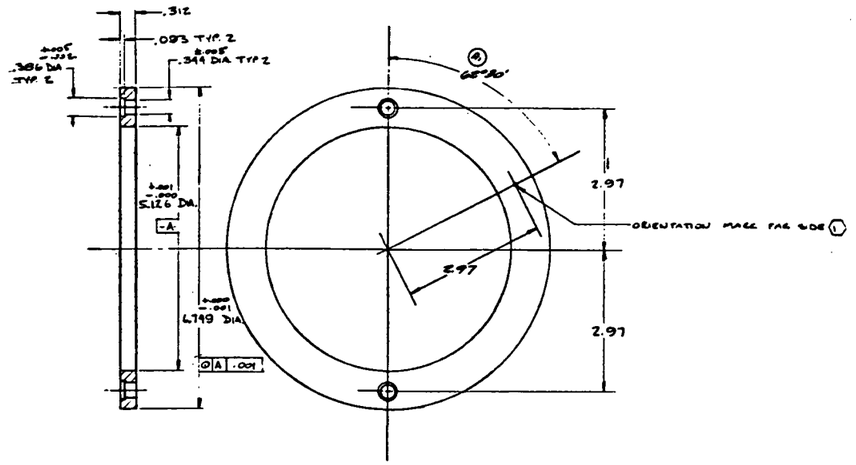

-3 B.L.C. MANIFOLD COVER

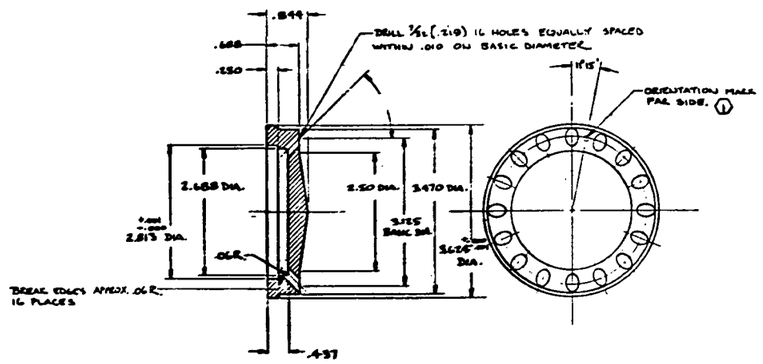

-13 OXIDIZER MANIFOLD

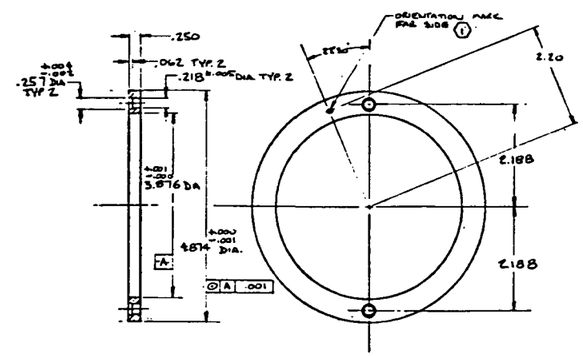

-5 BODY COOLANT COVER

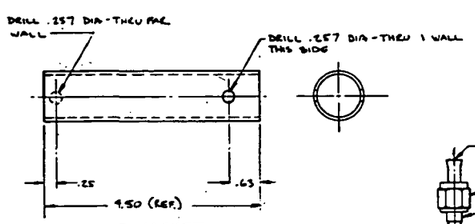

-9 JACKET

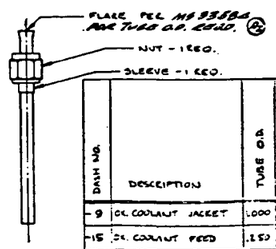

DASH NO.	DESCRIPTION	TUBE O.D.	WALL THICKNESS	TUBE LENGTH BEFORE FLARING			SLEEVE MS 33584 DASH NO	NUT AN 818 DASH NO	NO. REQD. ON INLET ASSEMBLY	
-9	OX. COOLANT JACKET	.000	.065	4.50			—	—	1	
-15	OX. COOLANT FEED	.250	.028	3.00			-4K	-4J	2	
-17	OX. TRANS. T/C INLET	.250	.035	3.00			-4K	-4J	4	
-19	B.L.C. FEED	.375	.035	8.00			-6K	-6J	2	
-25	OX. FEED	.500	.049	5.38			-8K	-8J	1	

NOTE: ALL TUBING MATERIAL IS 321 CRES -ECF.

-15 TUBE
-17 TUBE
-19 TUBE
-25 TUBE

DASH NO.	DESCRIPTION	MATERIAL	NO. REQD. PER ASSY.
-25	OX. FEED	321 CRES	1
-23	COOLANT JACKET CAP	321 CRES	
-19	B.L.C. FEED	321 CRES	2
-17	BODY COOLANT FEED	321 CRES	2
-15	OX. COOLANT FEED	321 CRES	2
-13	OX. MAN FOLD	NICKEL	1
-9	OX. COOLANT JACKET	321 CRES	1
-7	OX. MANIFOLD COVER	NICKEL	1
-5	BODY COOLANT COVER	NICKEL	1
-3	B.L.C. MANIFOLD COVER	321 CRES	1

HEAT TREAT: NONE
FINISH: DO NOT CLEAN WITH NITRIC ACID OR OTHER ETCHANT
MATL: NOTED

UNLESS STATED OTHERWISE SPECIFIED DIMENSIONS ARE IN INCHES AND APPLY PRIOR TO FINISH
125 MACH. SURF. RQ. UNLESS TOLERANCES ON
DECIMALS: .XX = ± .03, .XXX = ± .010
ANGLES = ± 30'
HOLES NOTED "FOR LIST"
.000 THRU .040 = +.005 -.001
.041 THRU .130 = +.007 -.001
.131 THRU .279 = +.009 -.001
.280 THRU .500 = +.011 -.001
.501 THRU .750 = +.013 -.001
.751 THRU 1.500 = +.015 -.001
1.501 THRU 2.500 = +.017 -.001
DO NOT SCALE PRINT

① LIGHT CENTER PUNCH (WITH .005 DEEP) ANGULAR ORIENTATION MARK

NOTE: UNLESS OTHERWISE SPECIFIED

Figure 118. Details - OF_2/B_2H_6 Injector

R-8766

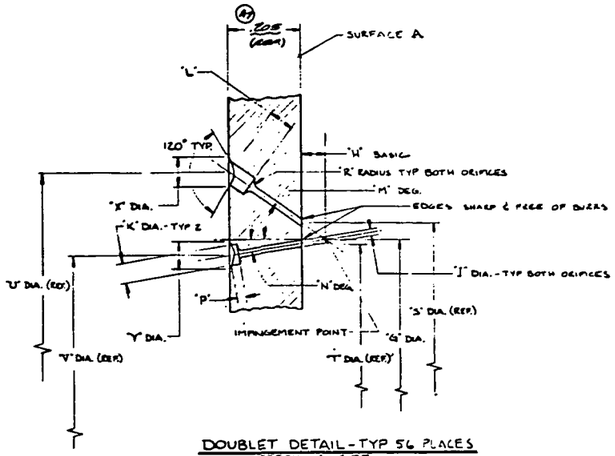

DOUBLET DETAIL - TYP 56 PLACES
APPROX. 4 x SIZE

DOUBLET SET IDENTIFICATION	NUMBER OF EQUALLY SPACED DOUBLETS IN SET	IMPINGEMENT DIAMETER BASIC "G" DIA.	IMPINGEMENT POINT TO FACE DIMENSION BASIC "H"	ORIFICE DIAMETER "J" DIA.	C'BORE DIAMETER "K" DIA.	ANGLE-OUTER ORIFICE "M" DEG.	ANGLE-INNER ORIFICE "N" DEG.	PROPELLANT-REF.	±.005 "R" RAD.	"S" REF DIA	"T" REF DIA	"U" REF DIA	"V" REF DIA	DOUBLET SET ANGULAR ORIENTATION ±10' "W" DEG.	C'SINK DIAMETER-OUTER "X" DIA.	C'SINK DIAMETER-INNER "Y" DIA.	ANGULAR SPACING BETWEEN DOUBLETS - REF.	C'BORE DEPTH-OUTER L ±.030	C'BORE DEPTH-INNER P ±.010
A	4	1.067	.111	.0330	.1065	41°30'	18°30'	OX	.033	1.263	.993	1.626	.856	16°30'	.172	.144	90°	.076	.018
B	4	1.067	.076	.0225	.0730	41°30'	18°30'	FUEL	.022	1.201	1.016	1.664	.879	70°	NONE	NONE	90°	.079	.021
C	8	2.134	.121	.0330	.1065	35°30'	9°30'	OX	.033	2.307	2.094	2.699	2.025	5°40'	.161	.144	45°	.056	.010
D	8	2.134	.082	.0225	.0730	35°30'	9°30'	FUEL	.022	2.251	2.107	2.643	2.038	35°	NONE	NONE	45°	.057	.013
E	16	2.788	.101	.0260	.0820	30	0	OX	.026	2.905	2.788	3.142	2.788	0°	.129	.116	22°30'	.081	.049
F	16	3.130	.088	.0225	.0730	30	0	FUEL	.022	3.232	3.130	3.464	3.130	12°30'	NONE	NONE	22°30'	.042	.010
		-G-										A2	A3					A4	A5

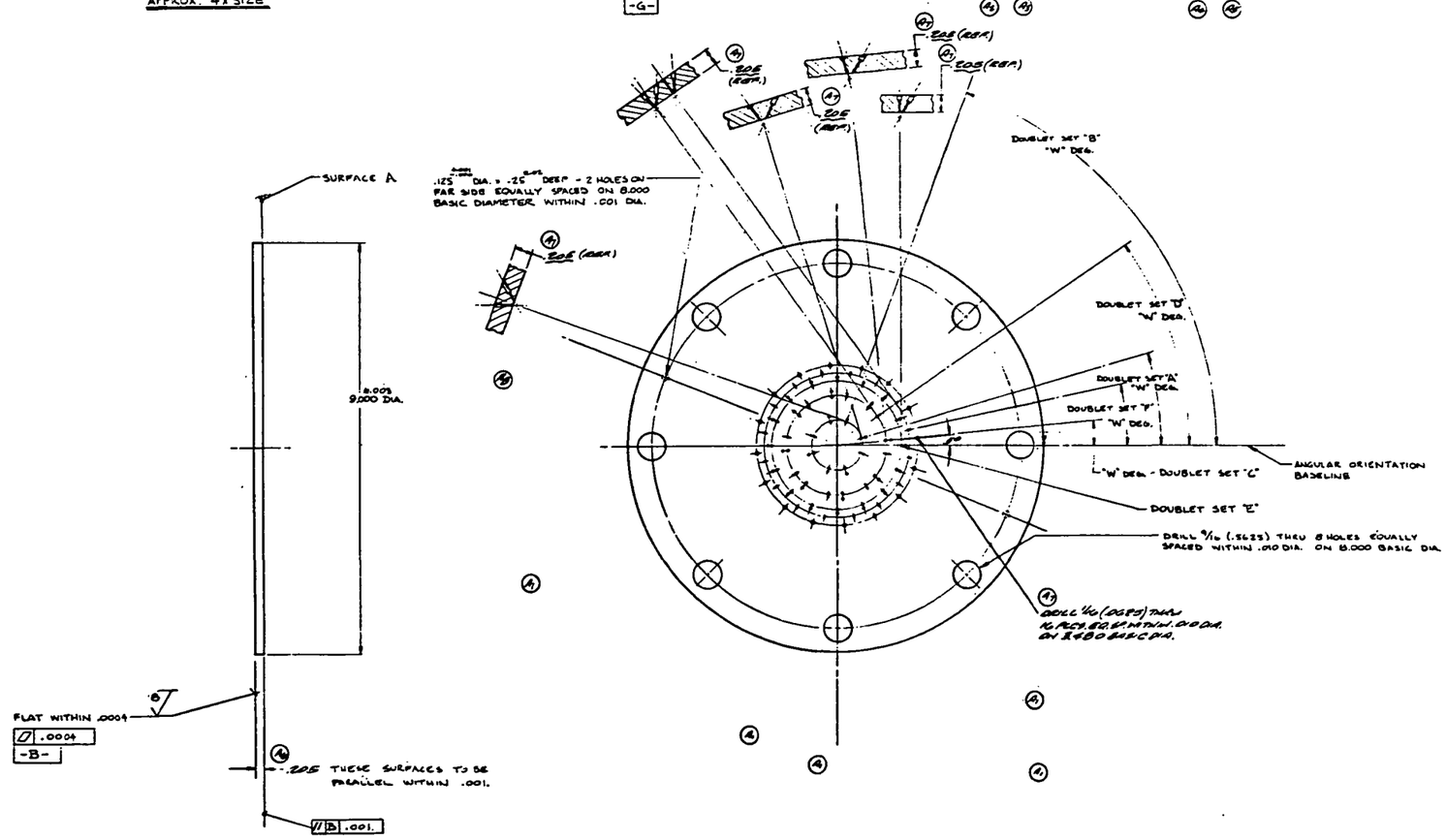

(6) STRESS RELIEVE BETWEEN ROUGH & FINISH MACHINING BY HEATING 2 HRS AT 900°F IN ARGON ATMOSPHERE. COOL SLOWLY.

(5) DO NOT CLEAN WITH NITRIC ACID OR OTHER ETCHANT.

4. FUEL ORIFICES ARE SHOWN SOLID IN FACE VIEW FOR IDENTIFICATION ONLY.

3. ALL DOUBLETS OF EACH DOUBLET SET ARE EQUALLY SPACED WITH IMPINGEMENT LOCATED AS SHOWN WITHIN .005.

2. ORIFICE CENTERLINES OF EACH INDIVIDUAL DOUBLET TO INTERSECT WITHIN .0015.

1. EACH DOUBLET CONSISTS OF TWO HOLES AS SHOWN IN ENLARGED DETAIL.

NOTE: UNLESS OTHERWISE SPECIFIED

HEAT TREAT (6)	UNLESS OTHERWISE SPECIFIED DIMENSIONS ARE IN INCHES AND APPLY PRIOR TO FINISH 125/ MACH. SURF. ROUGHNESS
FINISH (5)	TOLERANCES ON ANGLES ± 0°10' DECIMALS .XX ± .03 .XXX ± .010 HOLES NOTED "DRILL"
MATL. NICKEL 270	DO NOT SCALE PRINT

Figure 119. Face - OF_2/B_2H_6 Injector

The modified injector components are shown in Fig. 120 through 122. Figure 120 shows the chamber side of the injector orifice face plate (nickel type 270). The outer 16 holes shown in this figure are the feeder holes for the BLC manifold. The larger of the inner orifices are oxidizer; the smaller of the inner orifices are fuel. The P_c tap was eliminated altogether to preclude any possible additional risk relative to injector operation. All of the main (non-BLC) orifice entrances are recessed and contoured (see Fig. 121). The manifold body (nickel type 200) is shown in Fig. 122. The large (outer) grooved ring is the inlet to the main fuel manifold. The radially milled slots extending from the large grooved ring are the main feeder passages. The remaining 16 symmetric radially milled slots are the boundary layer coolant feed passages. The 56 round holes in the center area are oxidizer feed holes.

The nickel 270 orifice plate was diffusion-bonded to the nickel 200 manifolds. Ultrasonic inspection of the bond interface indicated a satisfactory joining of the two components. In addition, three core samples were machined from the bonded injector for the purpose of determining the ultimate tensile strength of the bond interface. The ultimate strengths of the center and two outer samples were 43.4, 53.1, and 35.3 kpsi. The strength values for the two outer samples are only approximate, since these two specimens inadvertently contained a portion of the dowel pins which are used for accurate alignment of the face plate and manifold. As a result, it was necessary to estimate the cross-sectional area of these two specimens.

The most significant result of the tensile tests was the fact that each of the three samples broke in the nickel 270 region, not at the bond interface. The average tensile strength of the three samples (44 kpsi) is lower than the reported ultimate strength of nickel 270 (70 - 80 kpsi). The effect of the bonding process on the strength of this material is not known; however, the fact that the bond interface did not rupture at a stress of approximately 44 kpsi indicated that the bond was more than satisfactory.

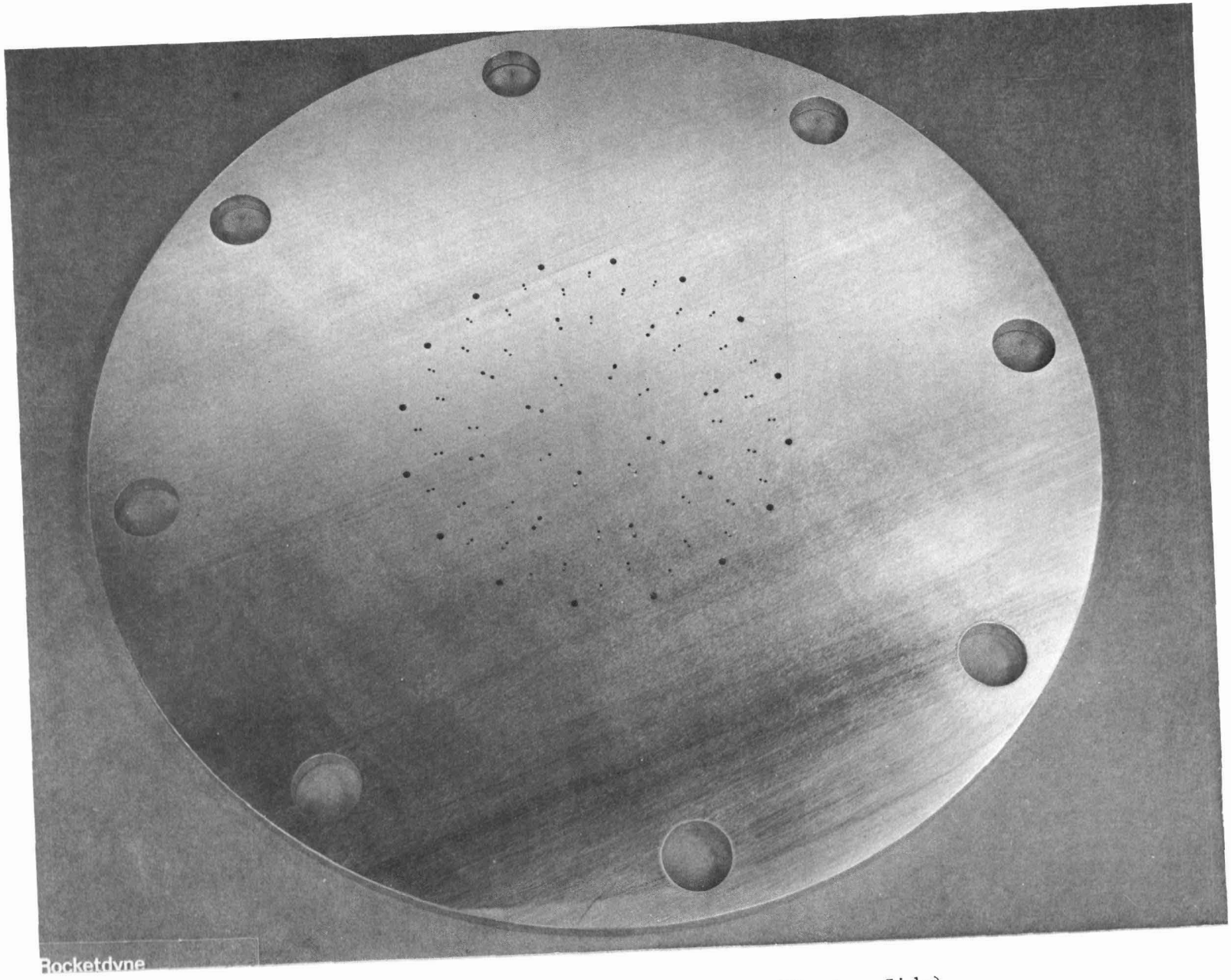

Figure 120. Injector Orifice Face Plate (Chamber Side)

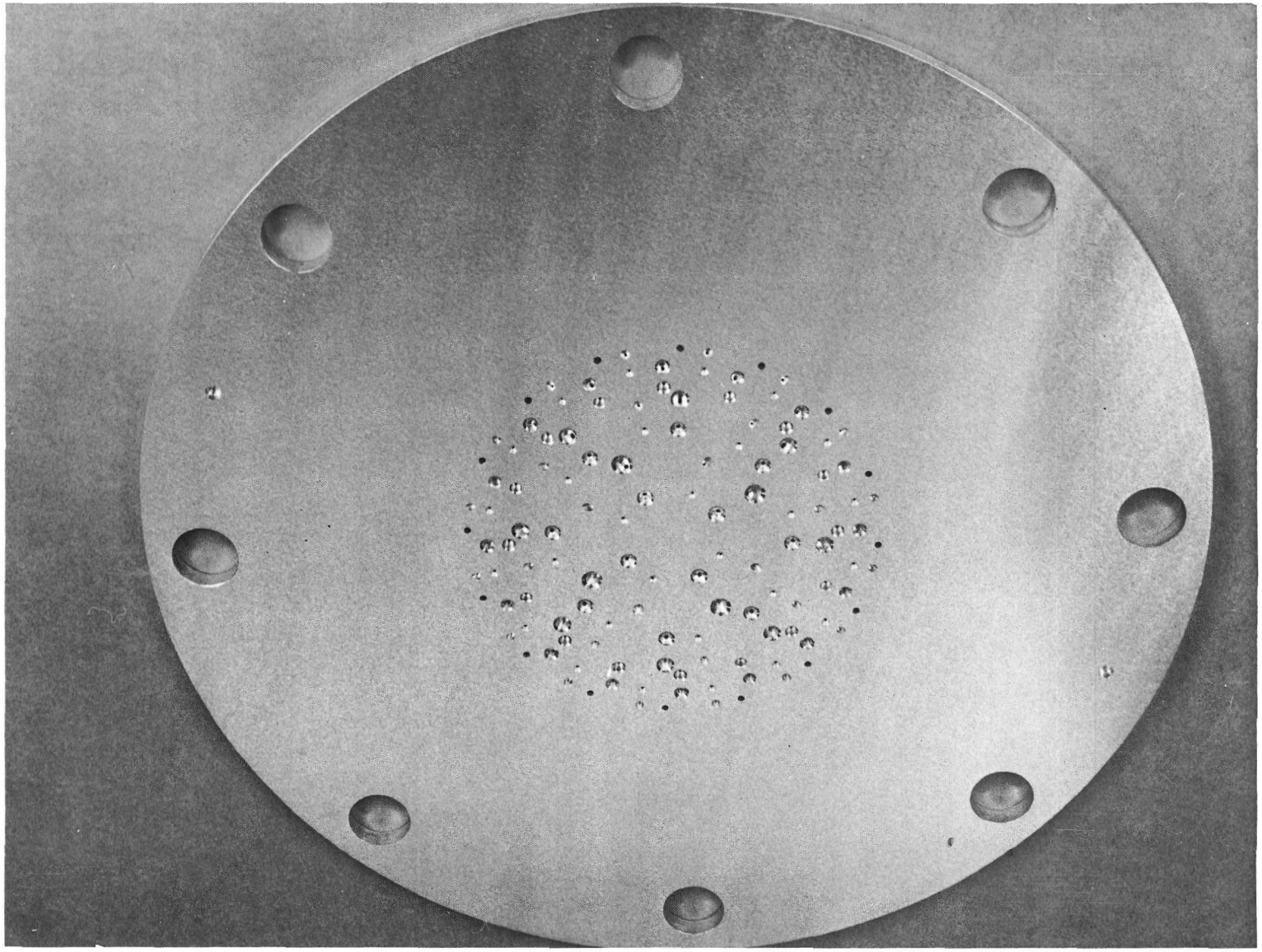

Figure 121. Injector Orifice Face Plate (Manifold Side)

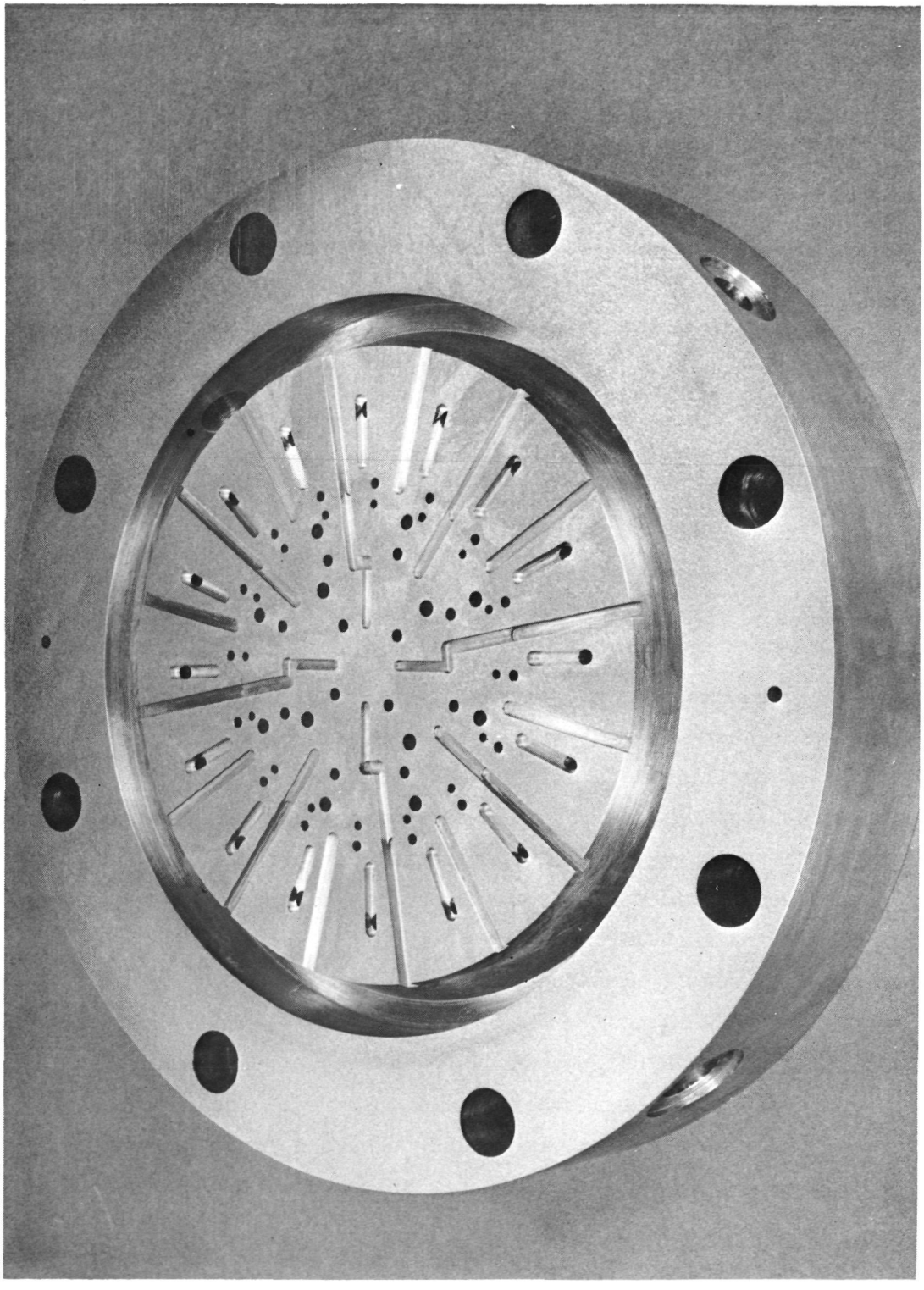

Figure 122. Injector Manifold Assembly

The diffusion-bonded assembly was then final machined, which included the cutting of the oxidizer manifold and the two BLC manifolds. EB welding of the manifolds and feeder tubes completed the fabrication cycle.

Cold Flow

Cold flows of the new diffusion bonded injector were made following hardware completion and leak check. A mass distribution water flow was performed with the new BLC ring. The resultant distribution, shown in Fig. 123, indicated a fairly uniform mass flow. The injector core and BLC were cold-flowed together using trichloroethylene and water. These results are shown in Fig. 124 and 125. No abnormalties were indicated.

CALORIMETER HOT FIRINGS (TESTS 009 - 010)

Test 009

Test 009 was a 3-second checkout hot firing of the new, modified diffusion-bonded injector. The test was made at a chamber pressure of 88.5 psia (approximated using c* based on thrust), a core mixture ratio of 4.0, and 8.3 percent BLC. The experimentally measured propellant flowrates and the measured thrust for this test are shown in Fig. 126. Experimental performance is shown in Table 8. Temperatures recorded by the thermocouples during the 3-second run are shown in Fig. 127 through 130. The pronounced thermal symmetry of the calorimeter chamber is readily apparent.

Following completion of Test 009, the hardware was inspected visually on the stand and then disassembled. No anomalies were observed. The injector face, shown in Fig. 131 prior to cleaning, was found to have a minimal amount of combustion product deposition similar tot that observed after Test 005 with the original diffusion-bonded injector. The nickel calorimeter chamber again showed no evidence of internal gouging or deterioration. The injector and chamber were then cleaned and reassembled for Test 010.

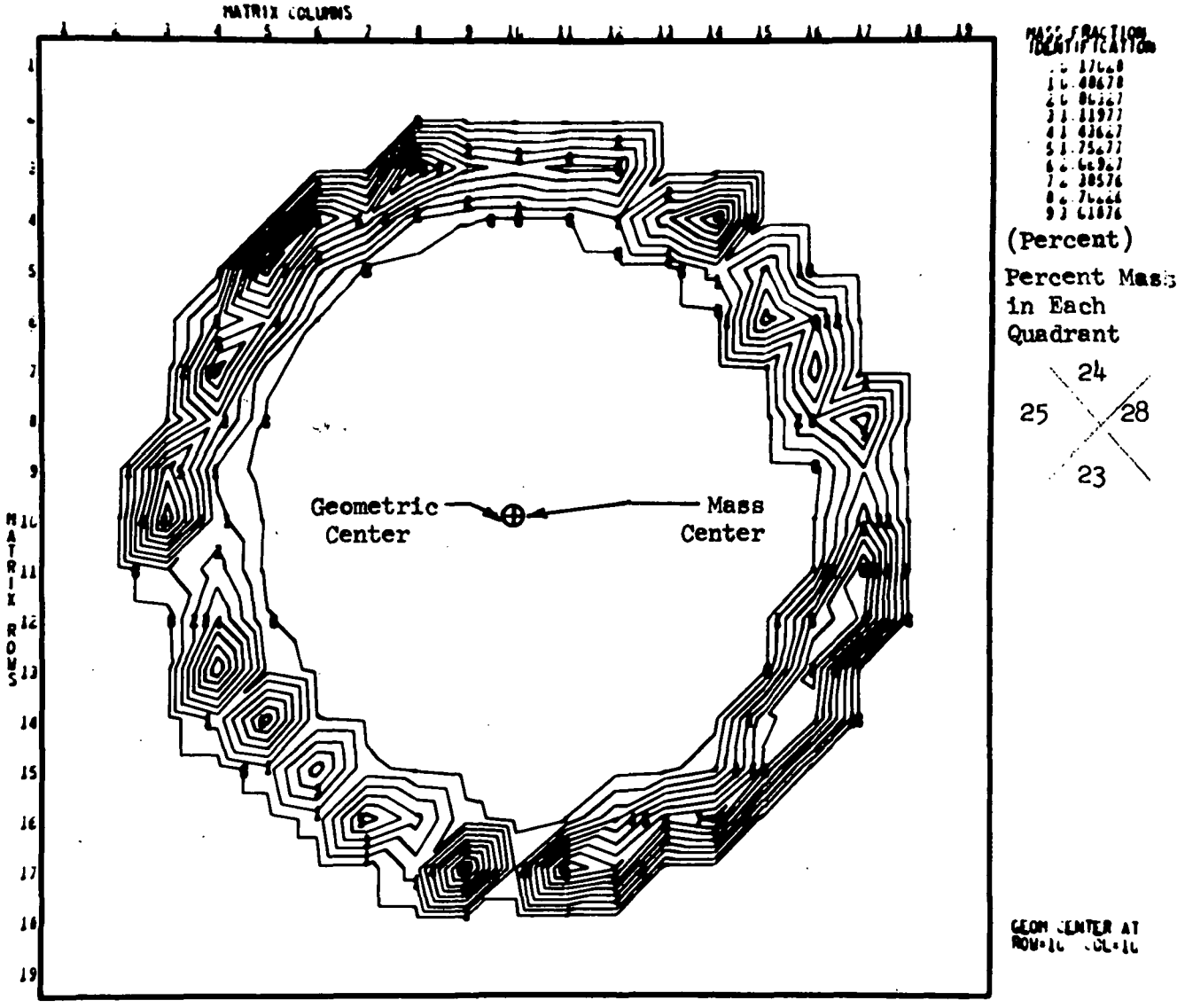

Figure 123. BLC Ring Mass Distribution Pretest Test 009

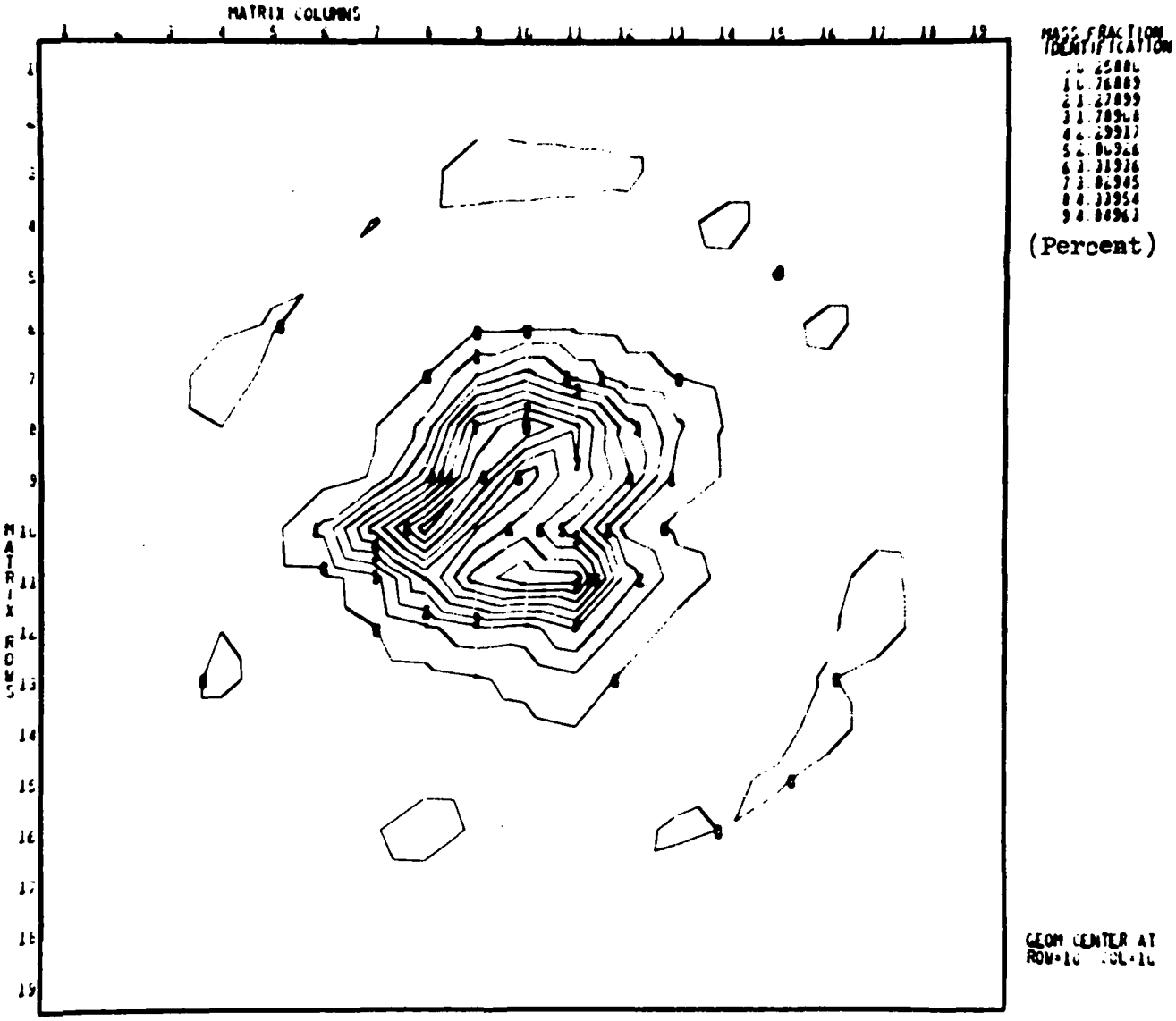

Figure 124. Combined Core/BLC Mass Distribution
Pretest Test 009

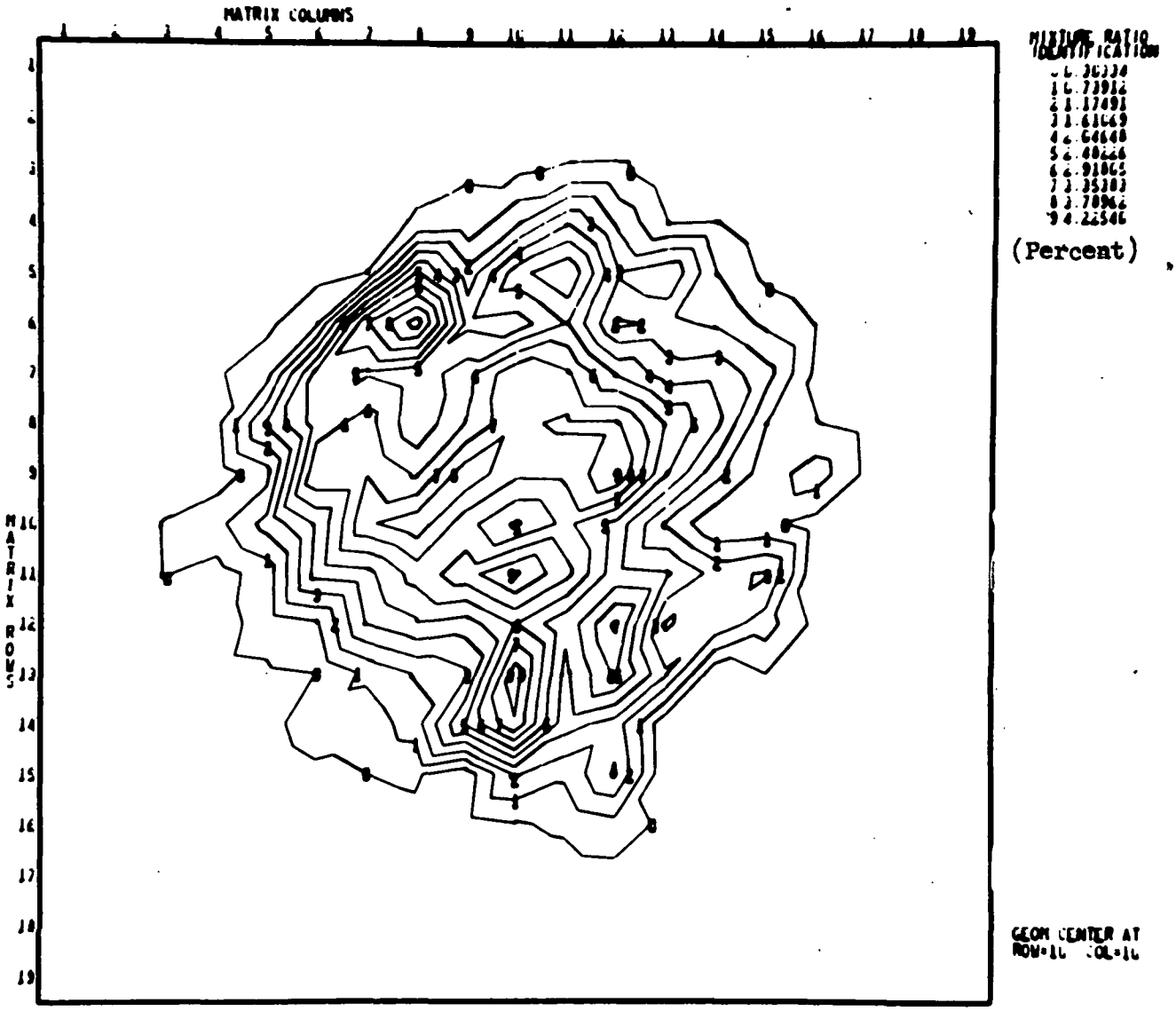

Figure 125. Combined Core/BLC Mixture Ratio Distribution
Pretest Test 009

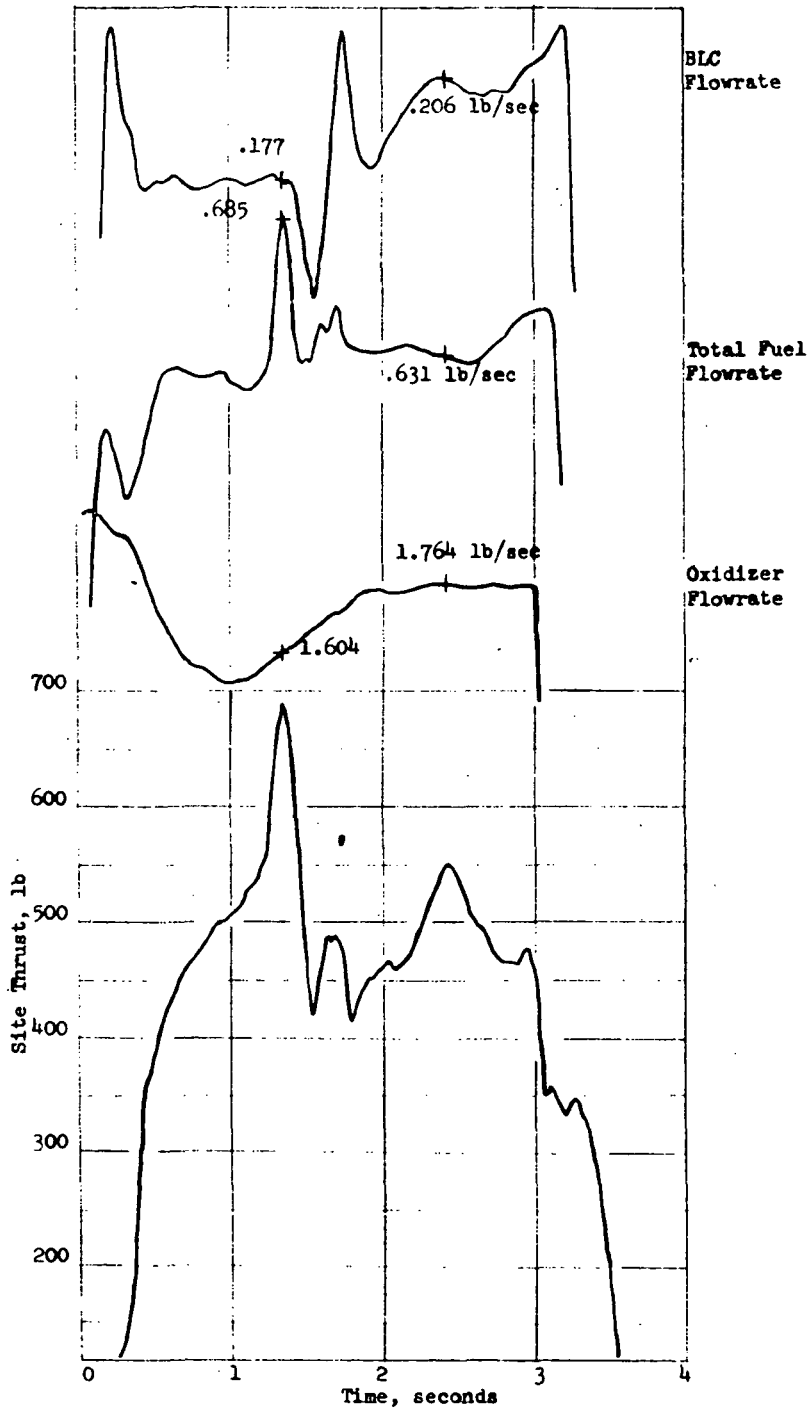

Figure 126. Thrust and Flowrates for Test 009
Core MR = 4.0 8.3% BLC

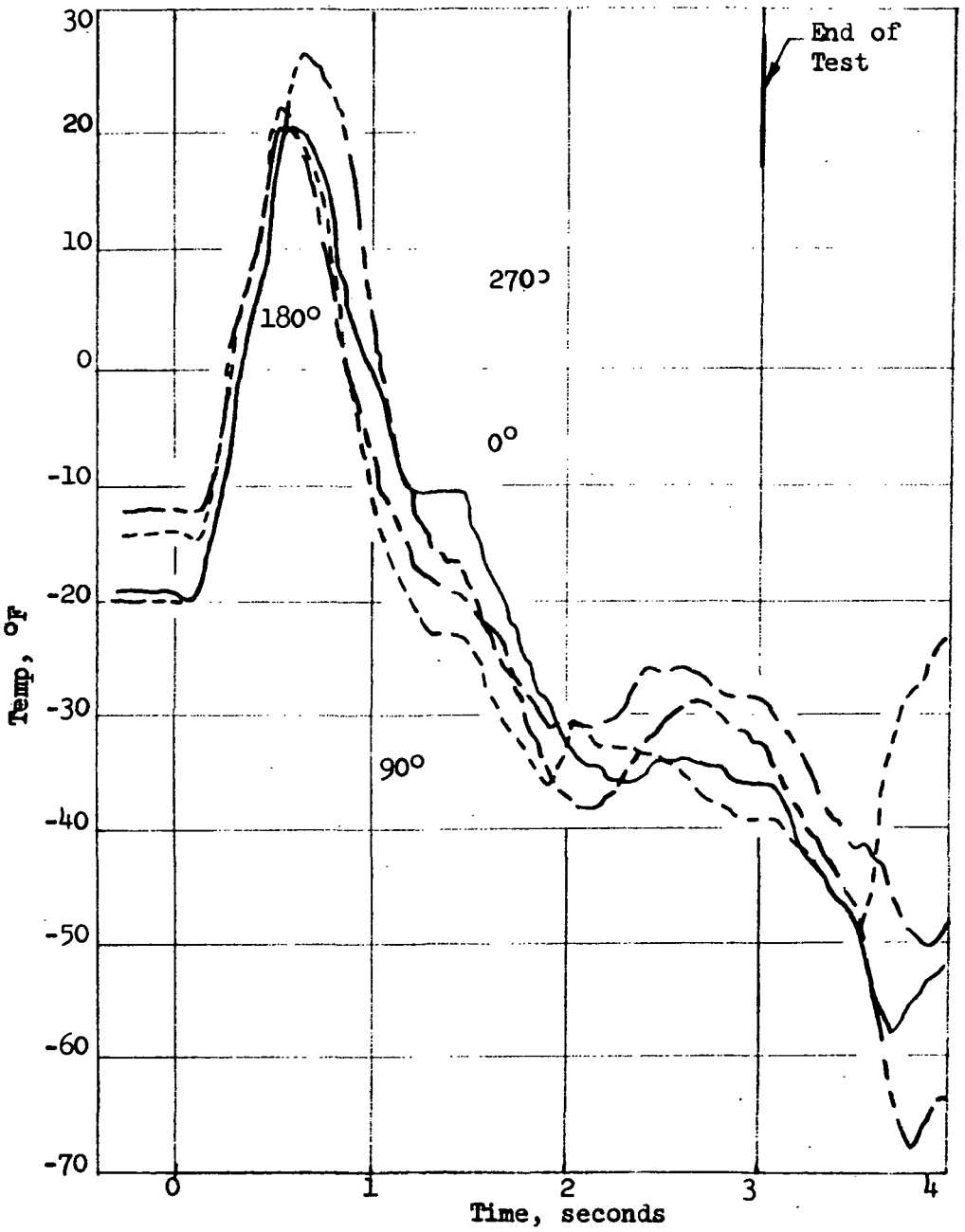

Figure 127. Test 009 - Outside Wall Temperature at 1-Inch Axial Location as Function of Thermocouple Position

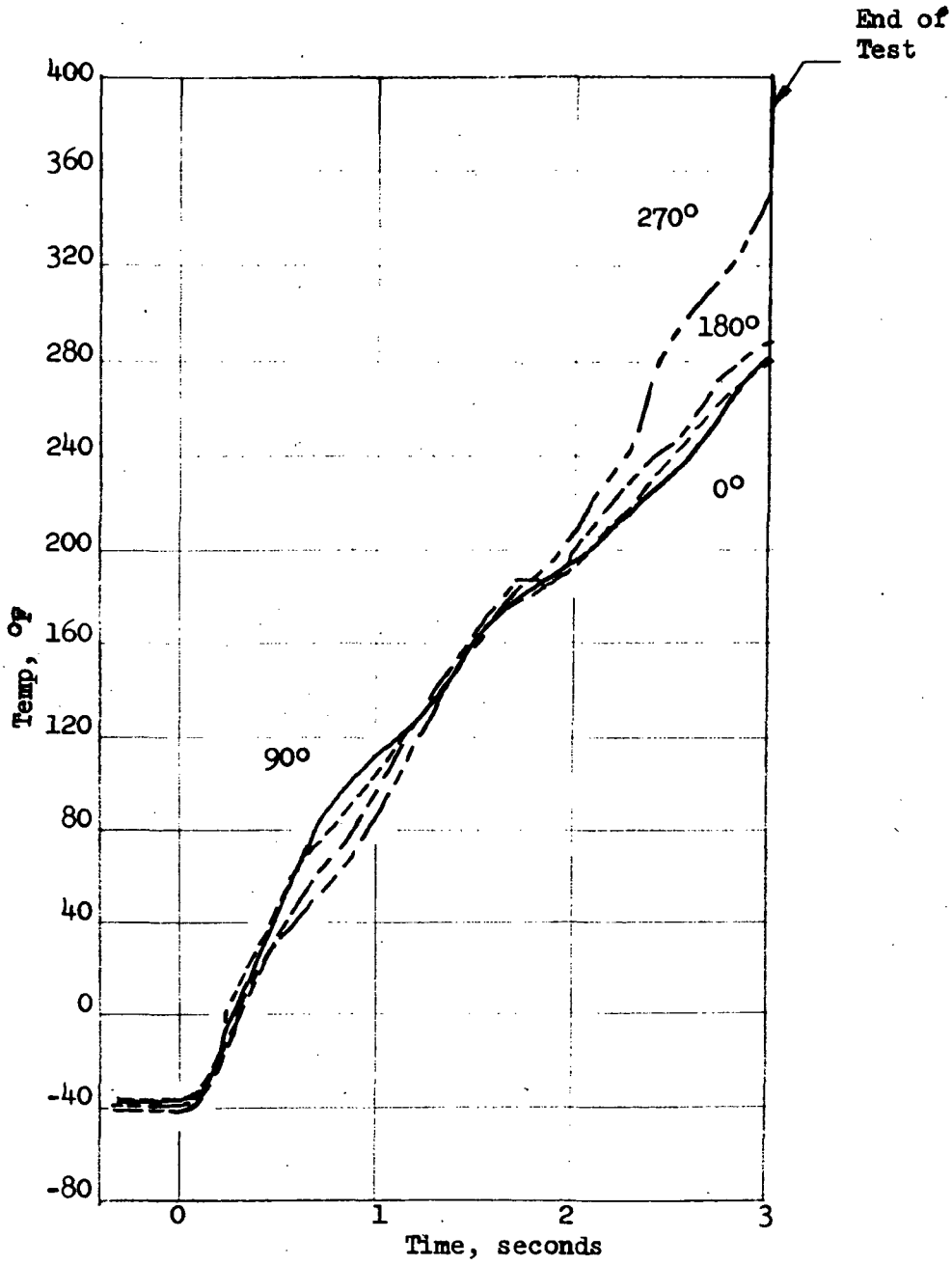

Figure 128. Test 009 - Outside Wall Temperature at 3-Inch Axial Location as Function of Thermocouple Position

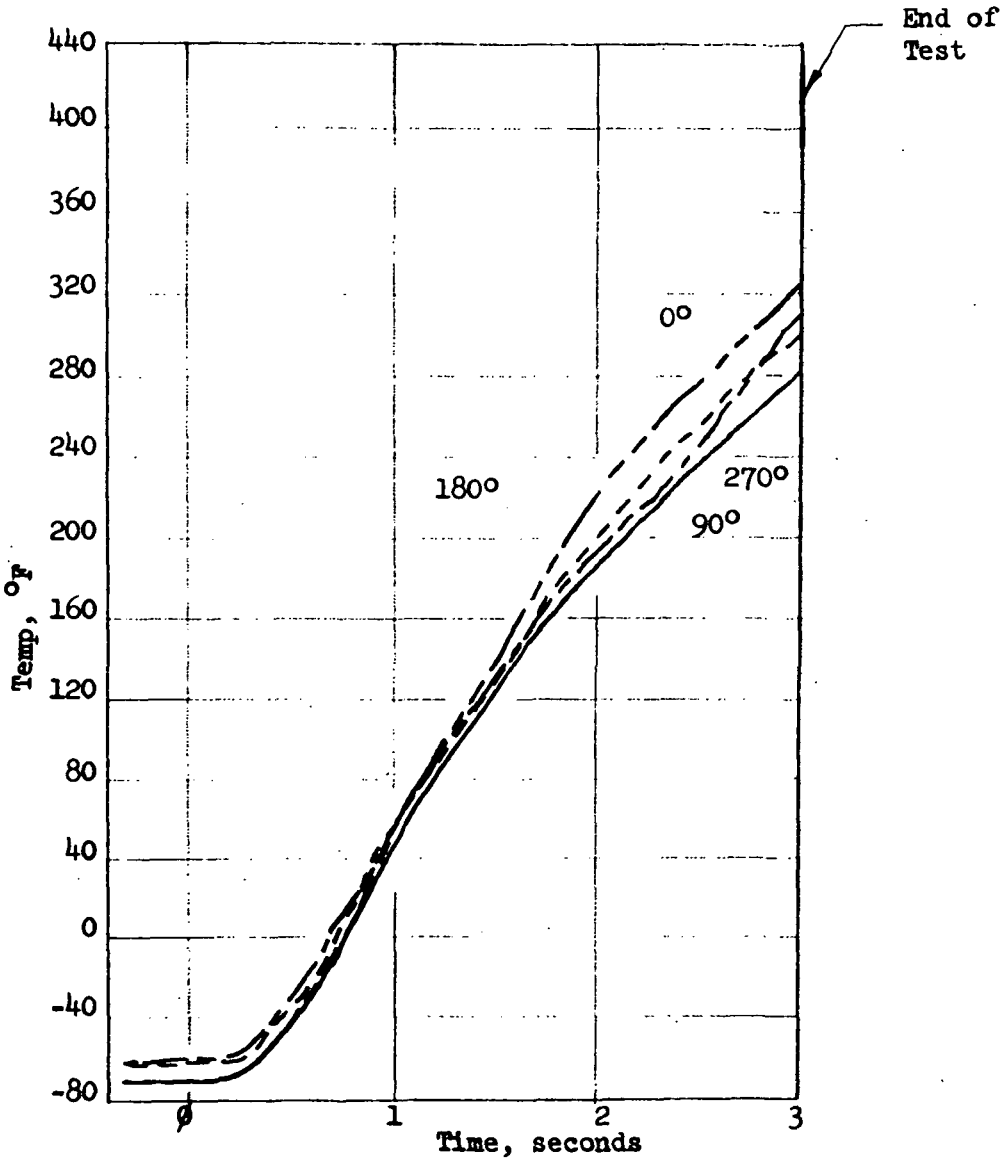

Figure 129. Test 009 - Outside Wall Temperature at 5-Inch Axial Location as Function of Thermocouple Position

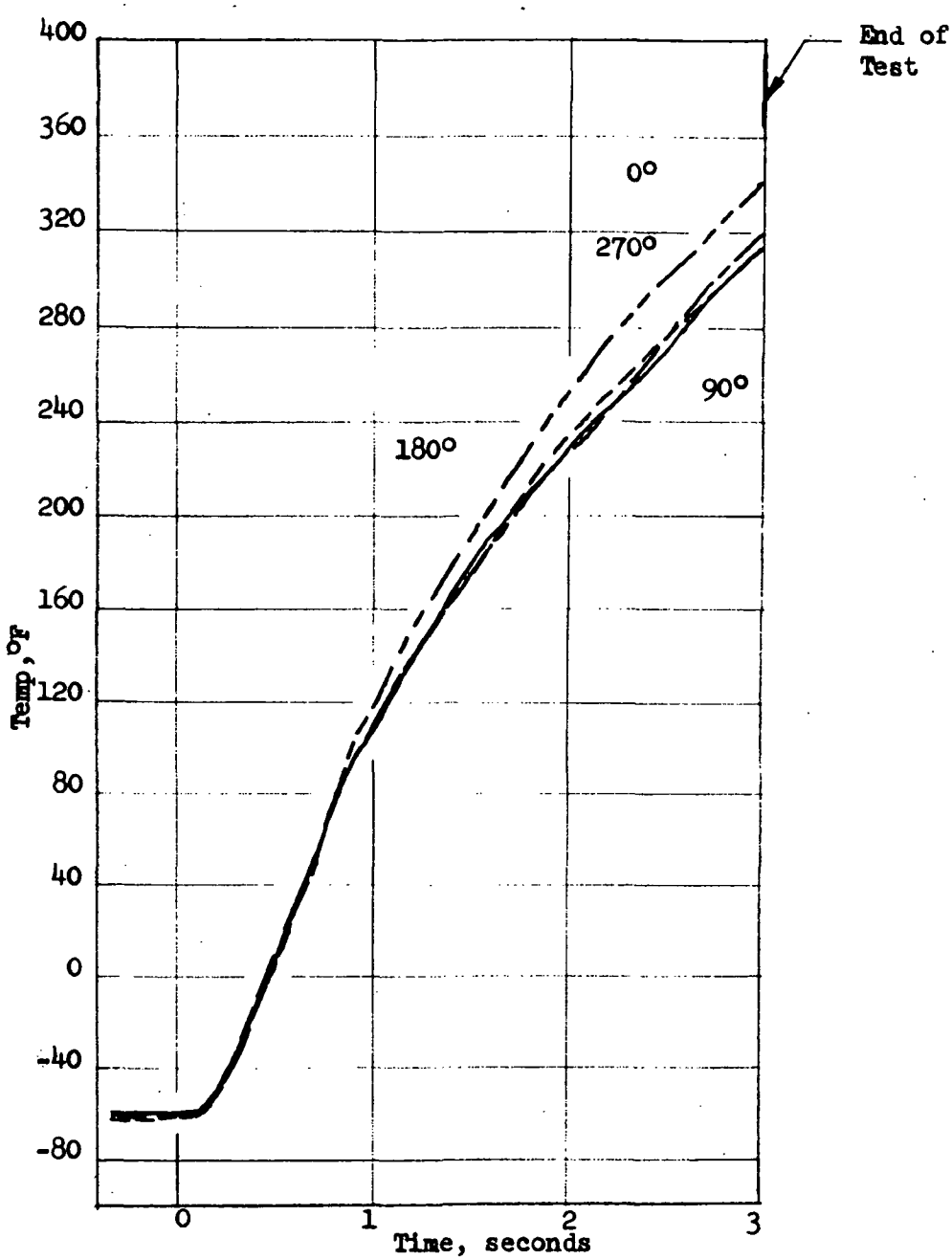

Figure 130. Test 009 - Outside Wall Temperature at 9-Inch Axial Location as Function of Thermocouple Position

5AA36-6/22/71-S1C

Figure 131. Injector Face Post Test 009

Test 010

Test 010 was programmed for a 10-second run duration. The chamber pressure was 101 psia, and the core mixture ratio and percent BLC were 3.6 and 12.5, respectively. This test was prematurely sequence cut at 7 seconds into the run when a small external diborane fire, occasioned by a fitting leak (see Fig. 132) caused fusion of the thermocouple leads.

The experimentally measured propellant flowrates and the measured thrust for Test 010 are shown in Fig. 133. Experimental performance is shown in Table 8. Temperatures recorded by the thermocouples during Test 010 are shown in Fig. 134 and 135. Thermal departures from the initially symmetric thermal history evidence the burnthrough of certain thermocouple leads as early as 2.5 seconds into the run.

With the exception of the burned leads, no other damage was noted and the hardware (see Fig. 136) appeared in excellent condition posttest. Indeed, the plexiglas jacket surrounding the chamber was not melted and had only small amounts of diborane combustion product deposition on its outer surface.

The thermal symmetry observed in Tests 009 and 010 is indicative of successful injector operation. The abbreviated run durations, however, did not warrant a comprehensive comparison of the measured thermal histories with the DEAP model predictions.

LONG DURATION TEST USING GRAPHITE LINED THRUST CHAMBER

The diffusion bonded injector utilized successfully in the calorimeter hot firings (Tests 009 - 010) was next set up for a long duration hot firing (Test 011) using a graphite lined INTEREGEN chamber (see Fig. 137). This long-duration thrust chamber, whose detail design is shown in Fig. 138, was identical to that employed in a previous in-house effort, Test 008, and

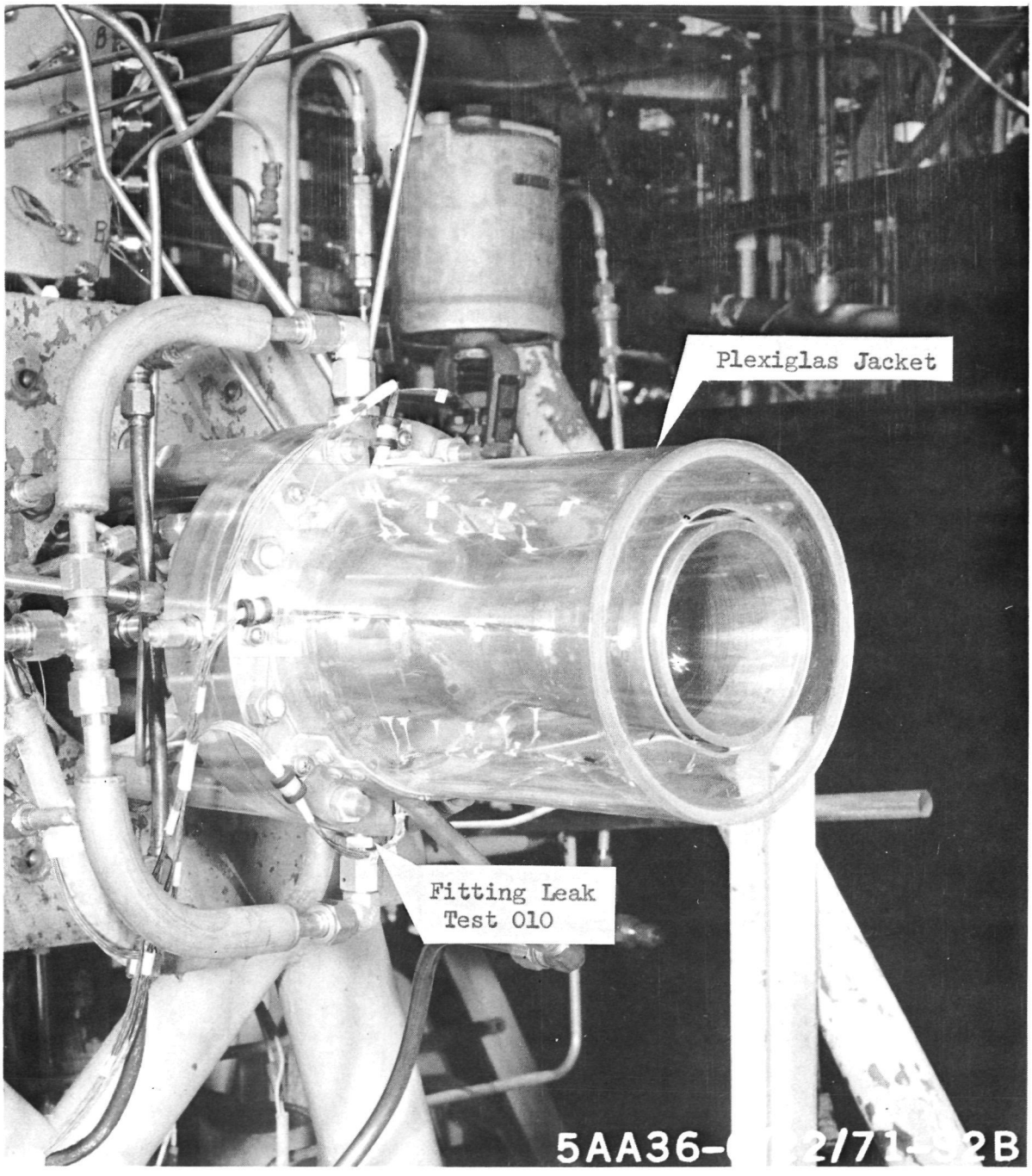

Figure 132. Calorimeter on Stand Pretest Test 010

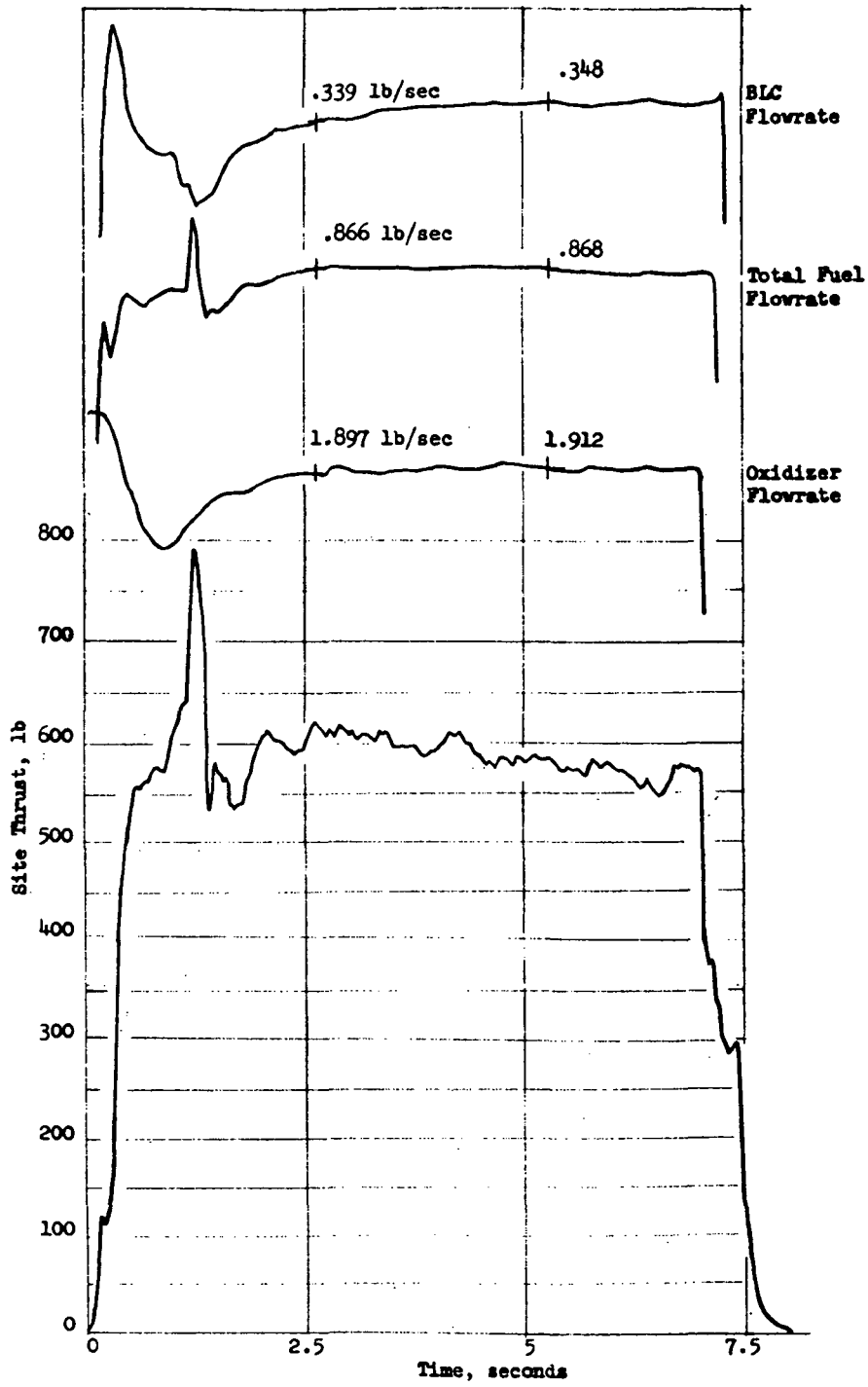

Figure 133. Thrust and Flowrates for Test 010
Core MR = 3.6 12.5% BLC

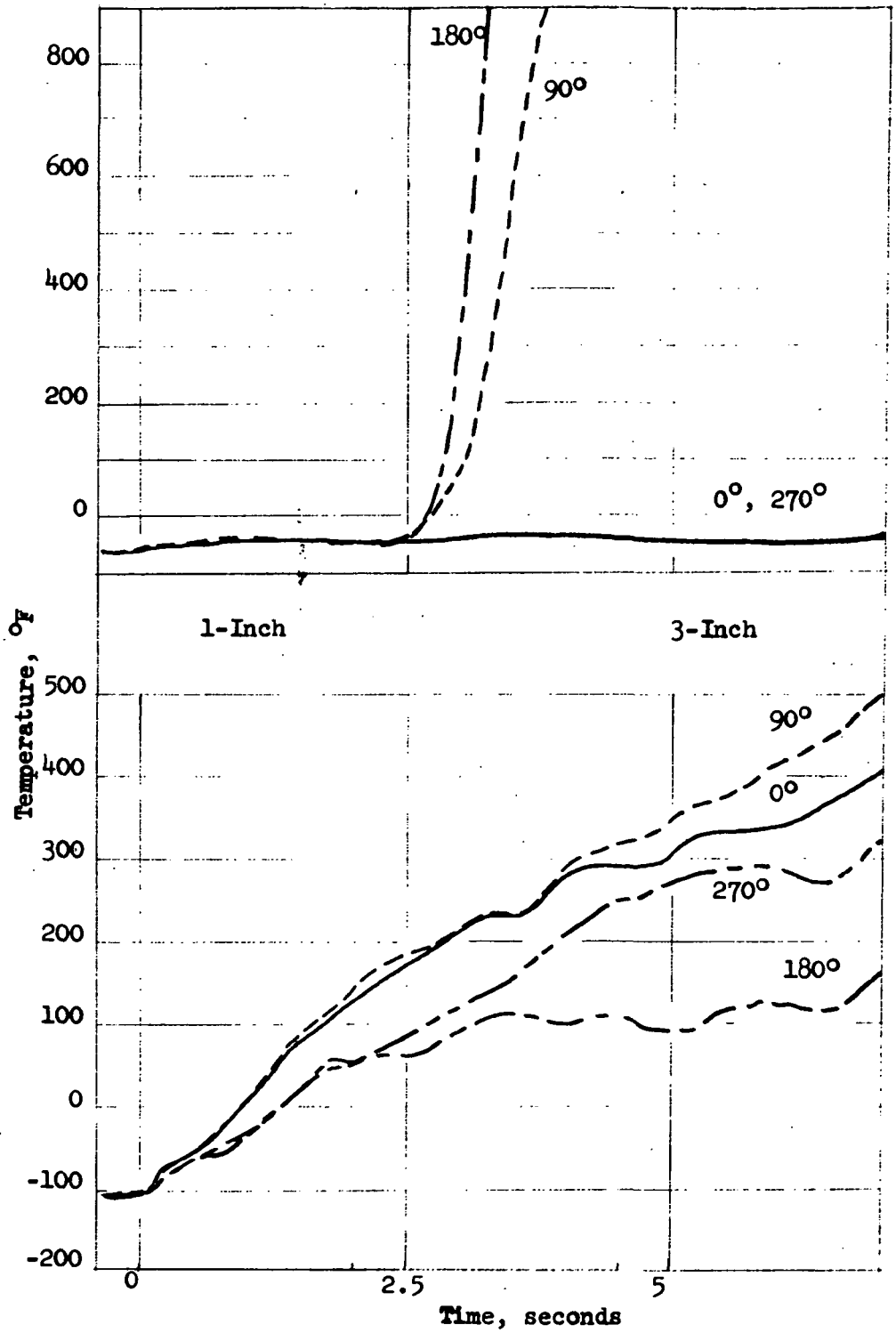

Figure 134. Test 010 - Outside Wall Temperature at 1-Inch and 3-Inch Axial Locations as Function of Thermocouple Position

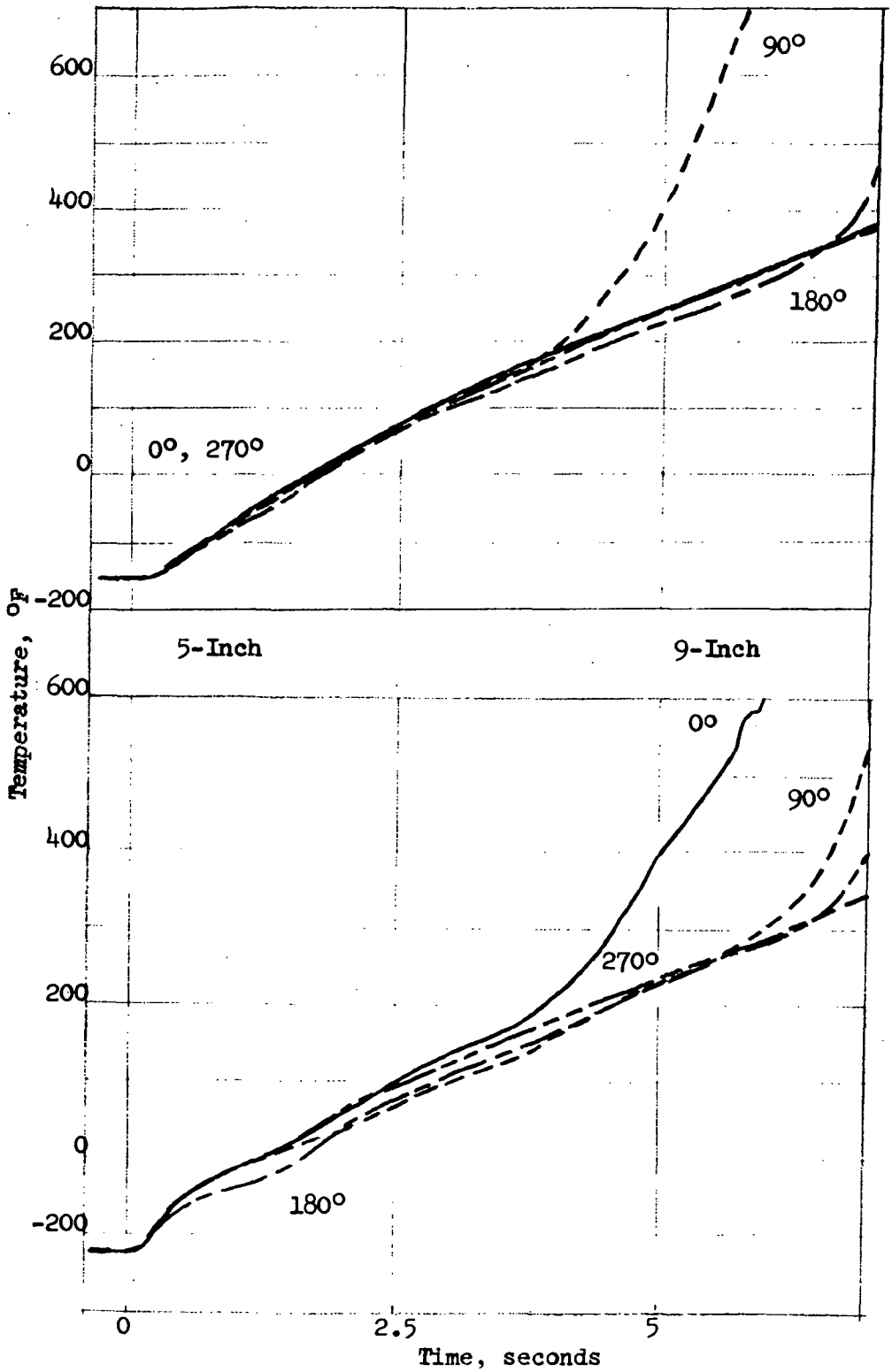

Figure 135. Test 010 - Outside Wall Temperature at 5-Inch and 9-Inch Axial Locations as Function of Thermocouple Position

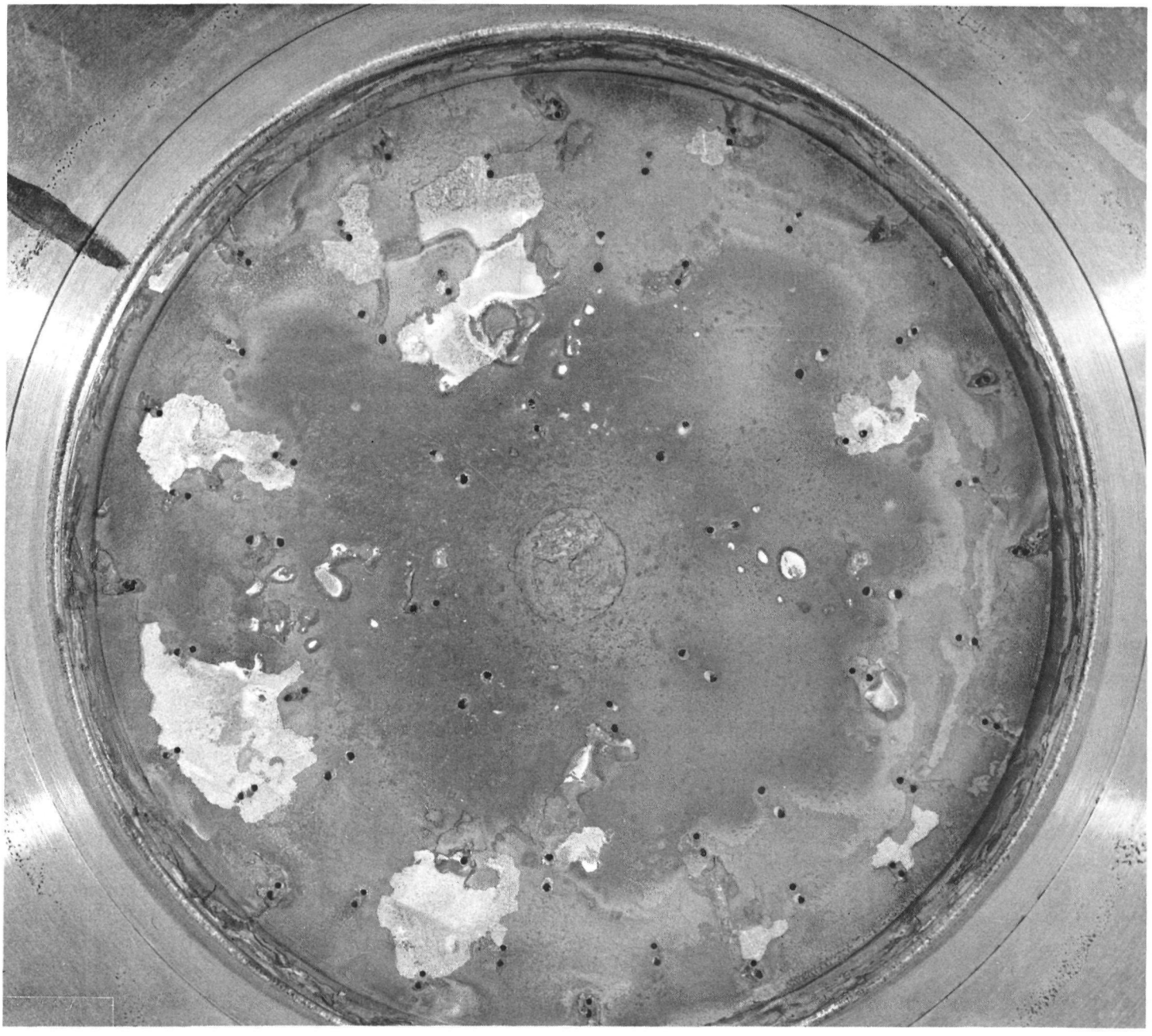

5AA36-6/22/71-S21

Figure 136. Injector Face Posttest 010

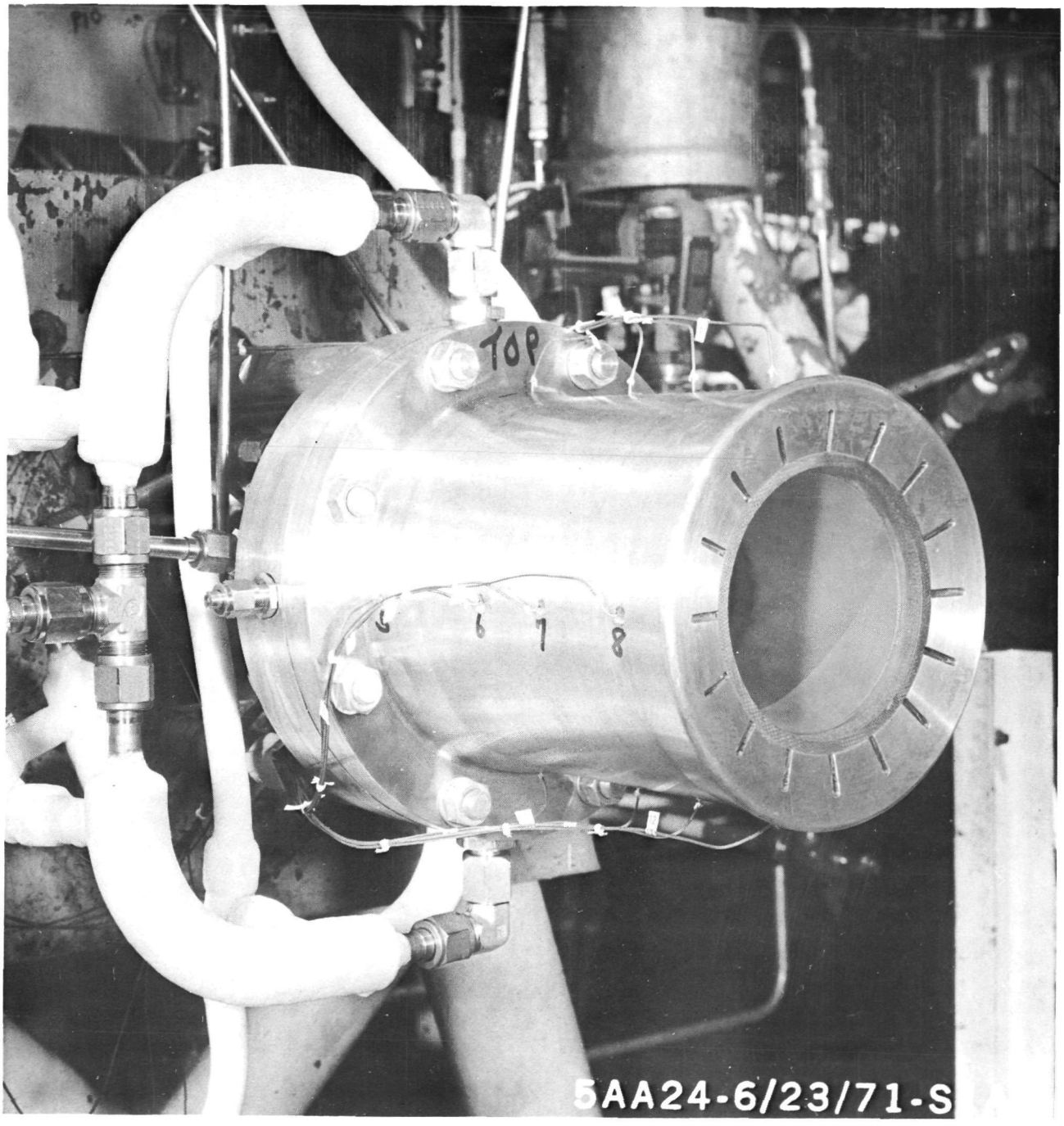

Figure 137. Boundary-Cooled Graphite Lined Chamber on Stand Pretest 011

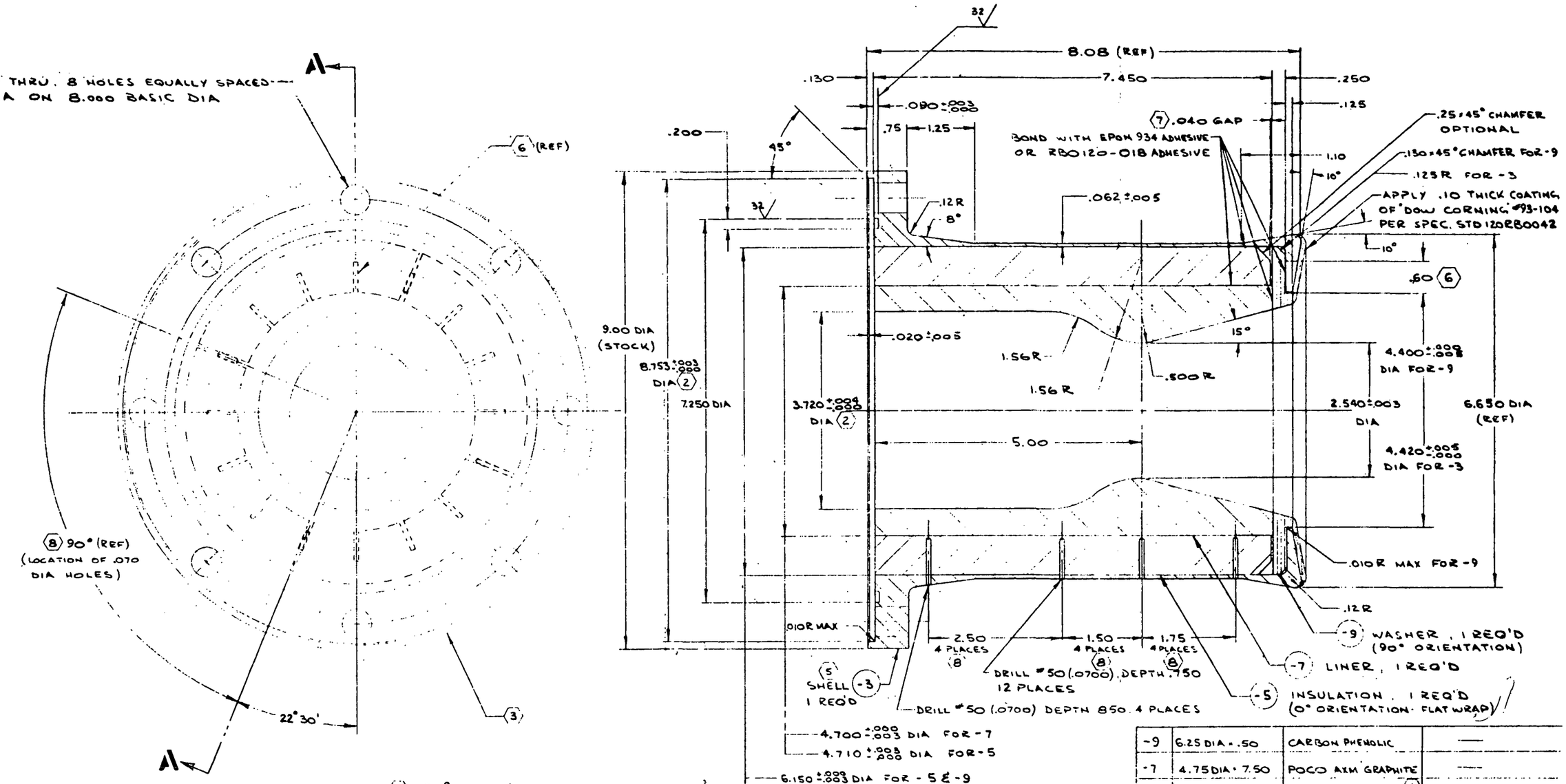

8 90° APART (LOCATION OF .070 DIA HOLES)

7 TAKE CARE NOT TO FILL .040 GAP WITH ADHESIVE DURING ASS'Y

6 16 SLOTS EQUALLY SPACED .090±.040 WIDE x .60 DEEP

5 SHELL MAY BE WELDED UTILIZING 100% WELD PENETRATION

4 CURED AT 50 PSI PRESSURE AND 300°F TEMP FOR 70±10 MIN.

3 IDENTIFY PER RAO 104-008

2 CONCENTRIC WITHIN .003 TIR

1. MACHINE PER RAO 103-002

NOTE: UNLESS OTHERWISE SPECIFIED

SECTION A-A

NO	SIZE	MATERIAL	SPECIFICATION
-9	6.25 DIA x .50	CARBON PHENOLIC	—
-7	4.75 DIA x 7.50	POCO AXM GRAPHITE	—
-5	6.25 DIA x 7.50	NARMCO #4065 4	—
-3	9.00 DIA x 8.12	300 SERIES CRES	—

UNLESS OTHERWISE SPECIFIED: DIMENSIONS ARE IN INCHES AND APPLY PRIOR TO FINISH.

125 MACH. SURF. ROUGHNESS

TOLERANCES ON: ANGLES ± 0° 30' DECIMALS .XX ± .03 .XXX ± .010

HOLES NOTED "DRILL" OVER	THRU	TOLERANCE
.0000	.0400	+ .0015 — .0010
.0400	.1300	+ .0030 — .0010
.1300	.2250	+ .0045 — .0010
.2250	.5000	+ .0060 — .0010
.5000	.7900	+ .0070 — .0010
.7900	1.0000	+ .0090 — .0010
1.0000	2.0000	+ .0120 — .0010

DO NOT SCALE PRINT

Figure 138. Thrust Chamber Assembly (OF_2/B_2H_6 IR&D)

R-8766

consisted of a 0.5-inch-thick graphite liner (POCO grade AXM), a lightweight, low-strength ablative overwrap (NARMCO No. 4065), and a thin-wall (1/16 inch) stainless steel shell. Selection of a graphite lined INTEREGEN chamber for the long duration test was made after comparison of the thermal characteristics of both graphite and nickel chamber walls using the upgraded thermal analysis model (DEAP). Predicted values of the maximum chamber temperature versus time for various nickel chamber designs are shown in Fig. 139 for a 4.0 core mixture ratio and 10% BLC. A comparison between the one-inch thick walled nickel chamber (operating at 4.0 core MR and 10% BLC) and the Test 008 graphite chamber design (Test 008 conditions) is shown in Fig. 140*. While both materials appear satisfactory from a heat transfer standpoint, the graphite design was selected because its predicted maximum temperatures, as compared to its melting point, offered a greater safety factor.

The Test 011 long duration hot firing, programmed for 75-second duration, was prematurely terminated after unexpected depletion** of the contents of the diborane tank at about 7 seconds into the run. Before the test was manually cut, engine operation at high mixture ratio and insufficient fuel cooling of the injector resulted in considerable injector damage to the central fuel orifices (see Fig. 141). The chamber, however, was in excellent condition after the run. No throat erosion nor any other evidence of damage was evident (see Fig. 142 and 143). Only a small amount of readily removable deposits were noted.

The experimentally measured propellant flowrates and the measured thrust for Test 011 are shown in Fig. 144. Test conditions consisted of a chamber pressure of 87.8 psia, a core mixture ratio of 3.9, and 11.2 percent BLC. The thermal history of Test 011 is summarized in Fig. 145 and 146. It is observed in these figures that the temperature of the outside graphite wall increased a maximum

---

* The comparison shown in Fig. 140 is not direct, since the core MR and percent BLC vary between the two cases. If common values of these parameters were used for both chamber designs, the predicted temperature-time traces for the two designs should show even closer correspondence than indicated in Fig. 140.

** An accounting of the diborane usage on this program is given in Appendix B.

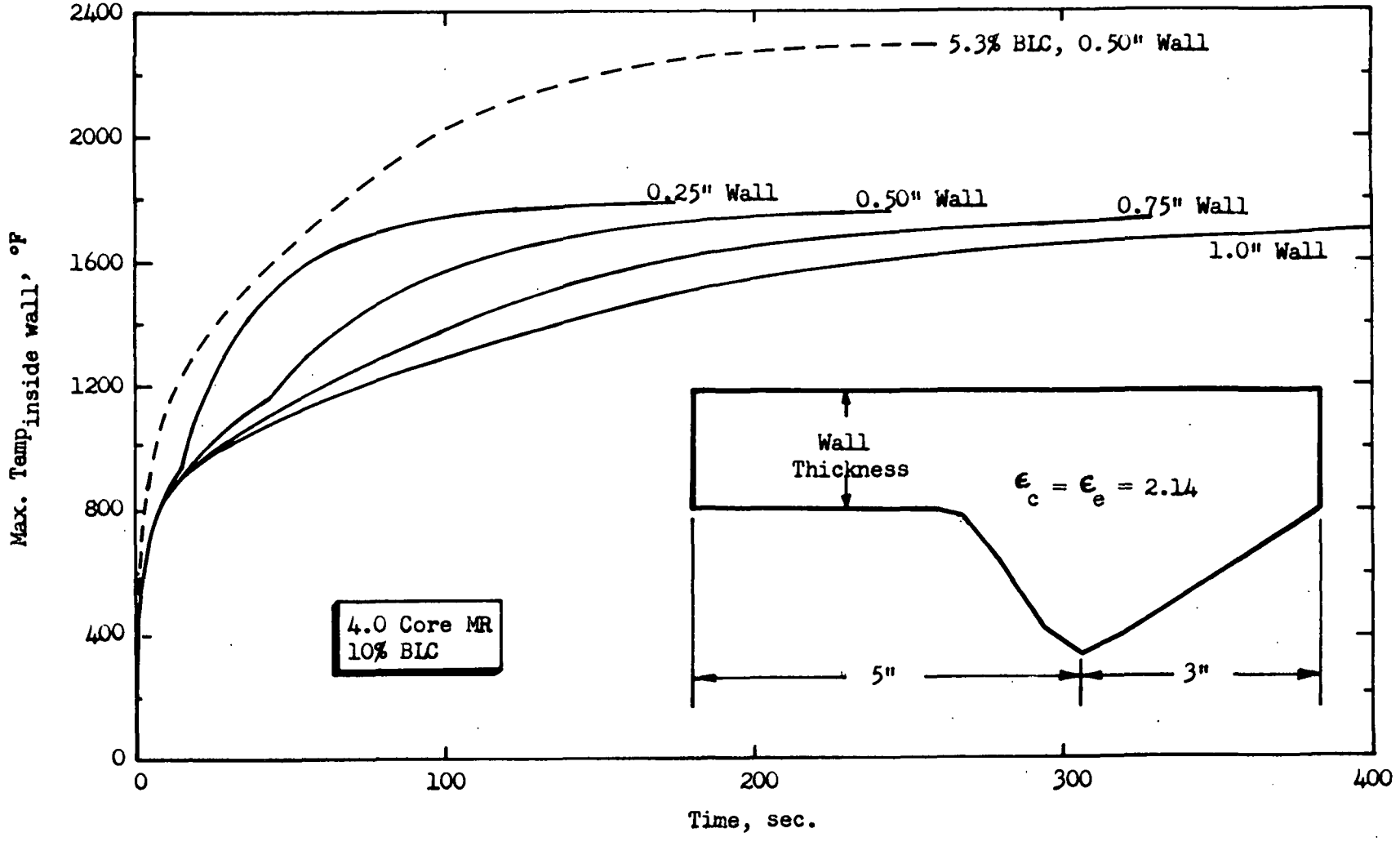

Figure 139. Maximum Chamber Temperature vs Time for Various Nickel Chamber Designs

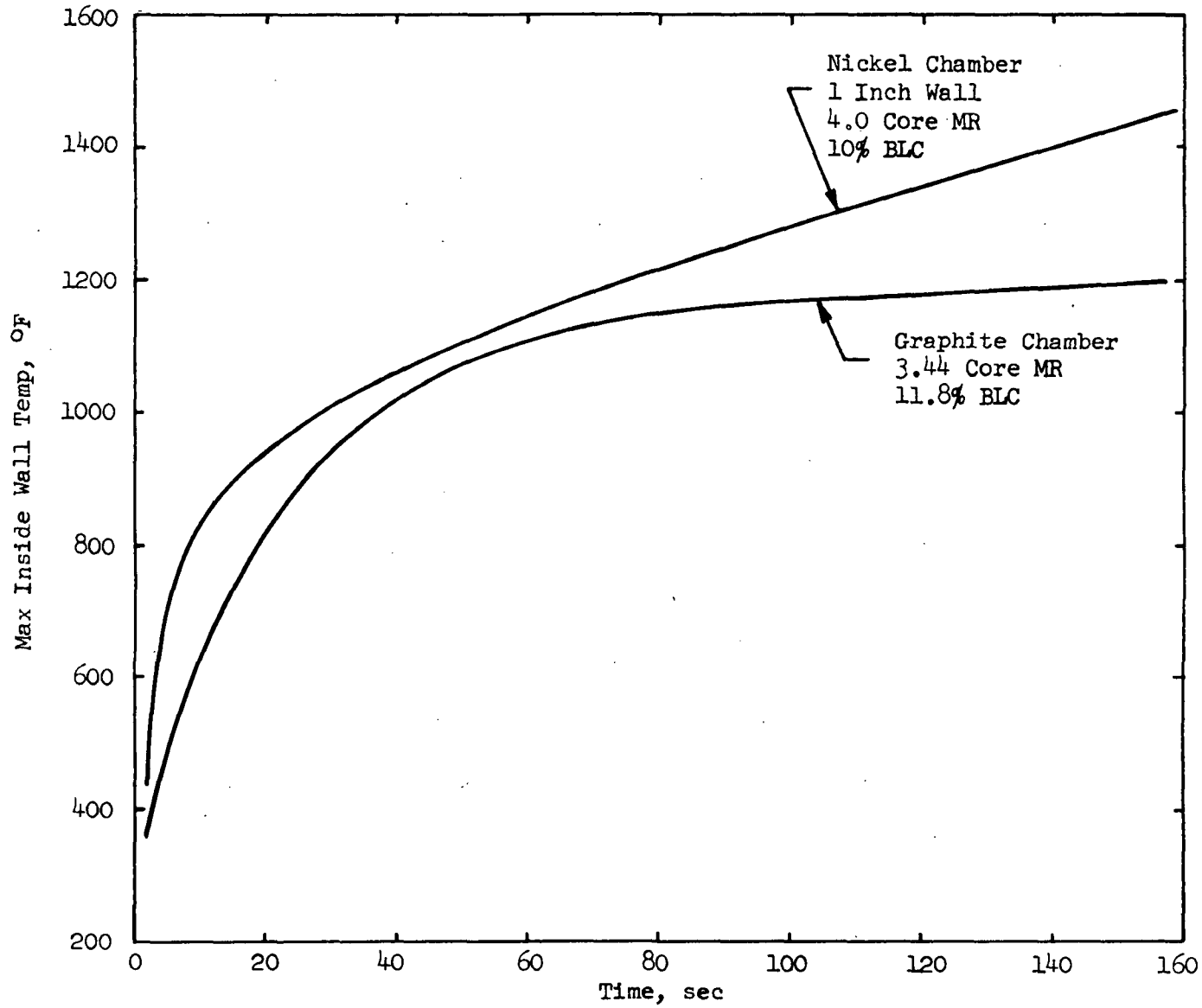

Figure 140. Nickel and Graphite Chamber Comparison

-6/24/71-S1B

Figure 141. Injector Face Posttest 011

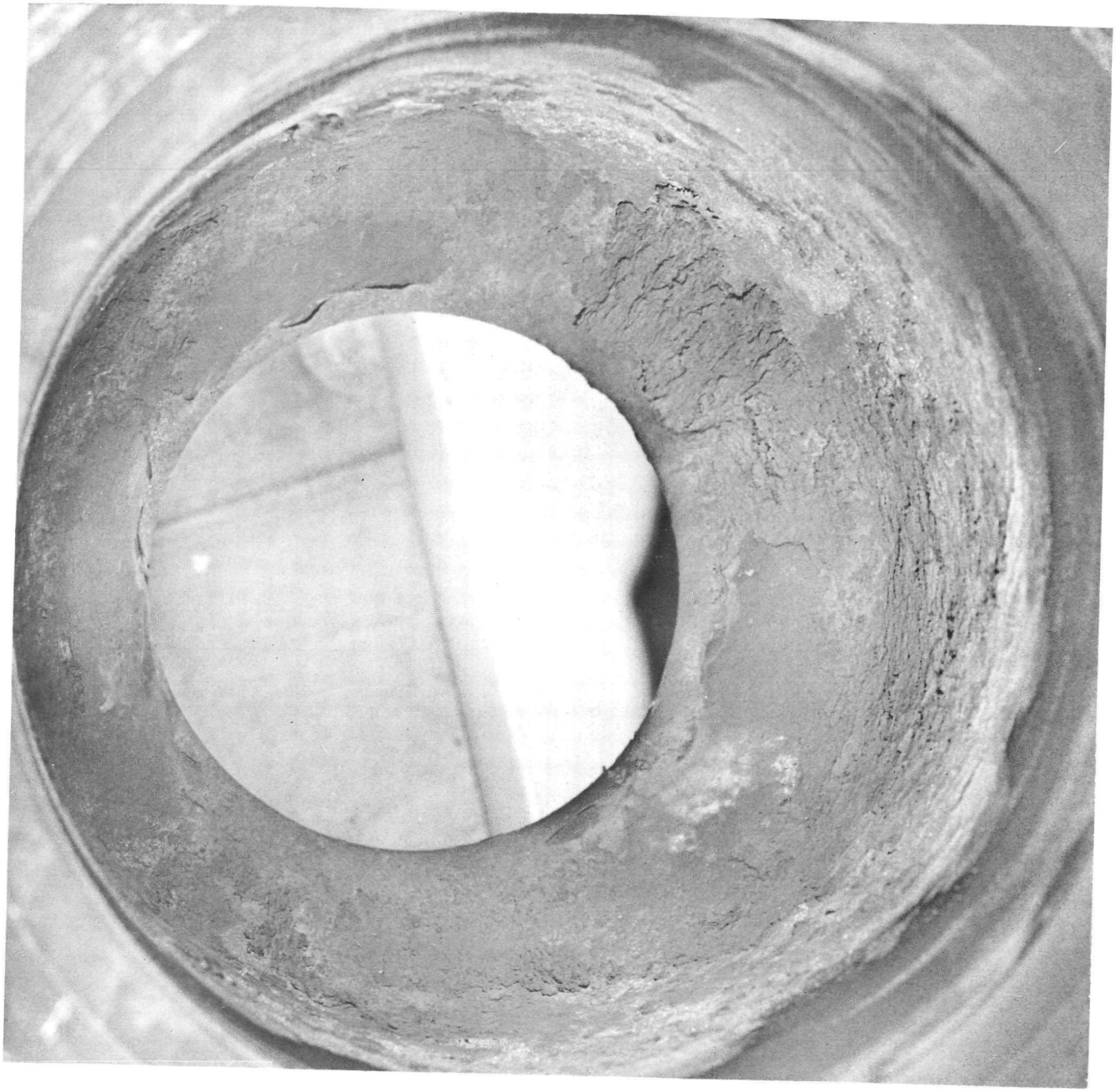

5AA36-6/24/71-S1C

Figure 142. Boundary Cooled Chamber - Injector End View
Posttest 011

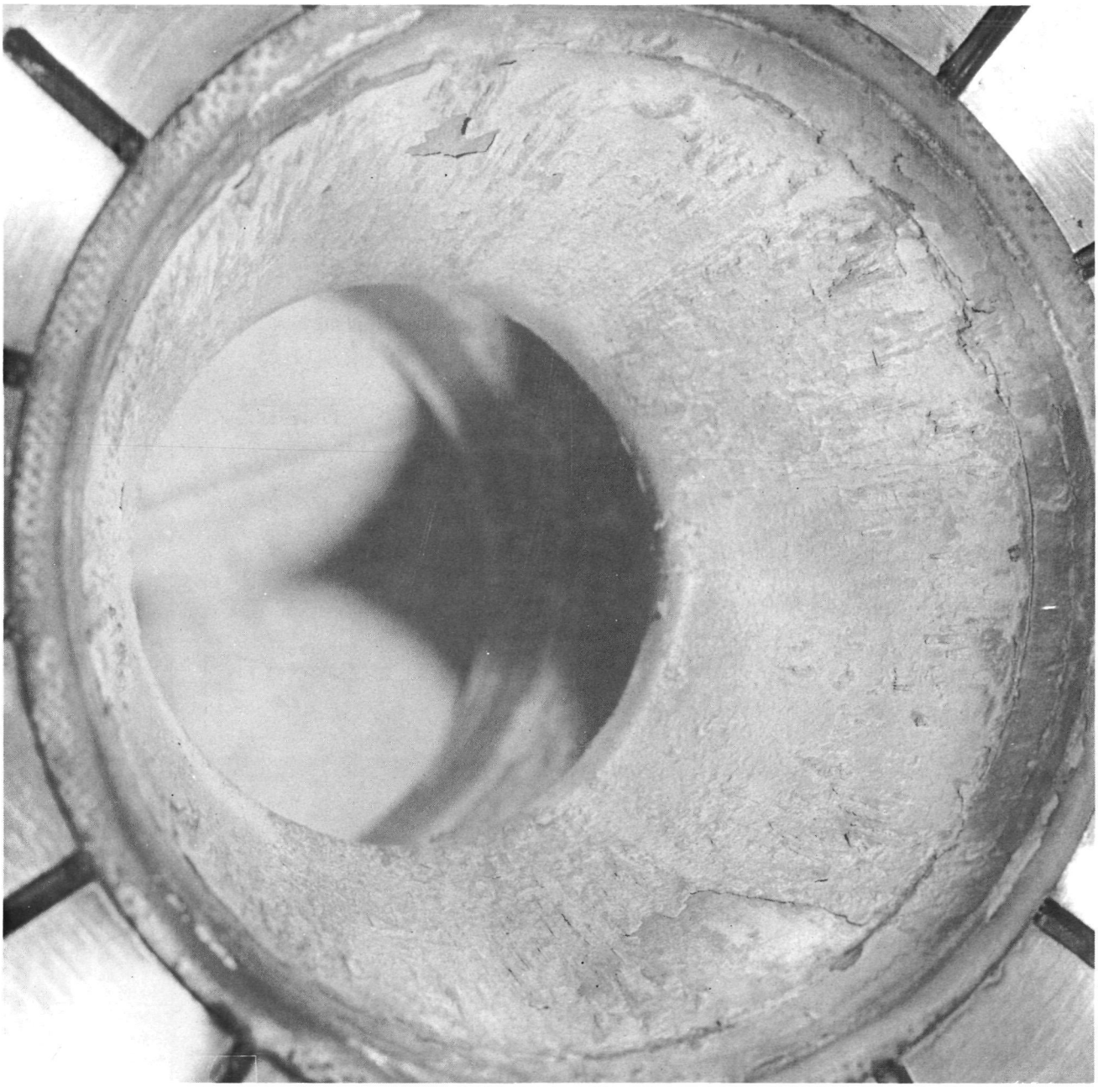

5AA36-6/24/71-S1D

Figure 143. Boundary Cooled Chamber - Nozzle End View
Posttest 011

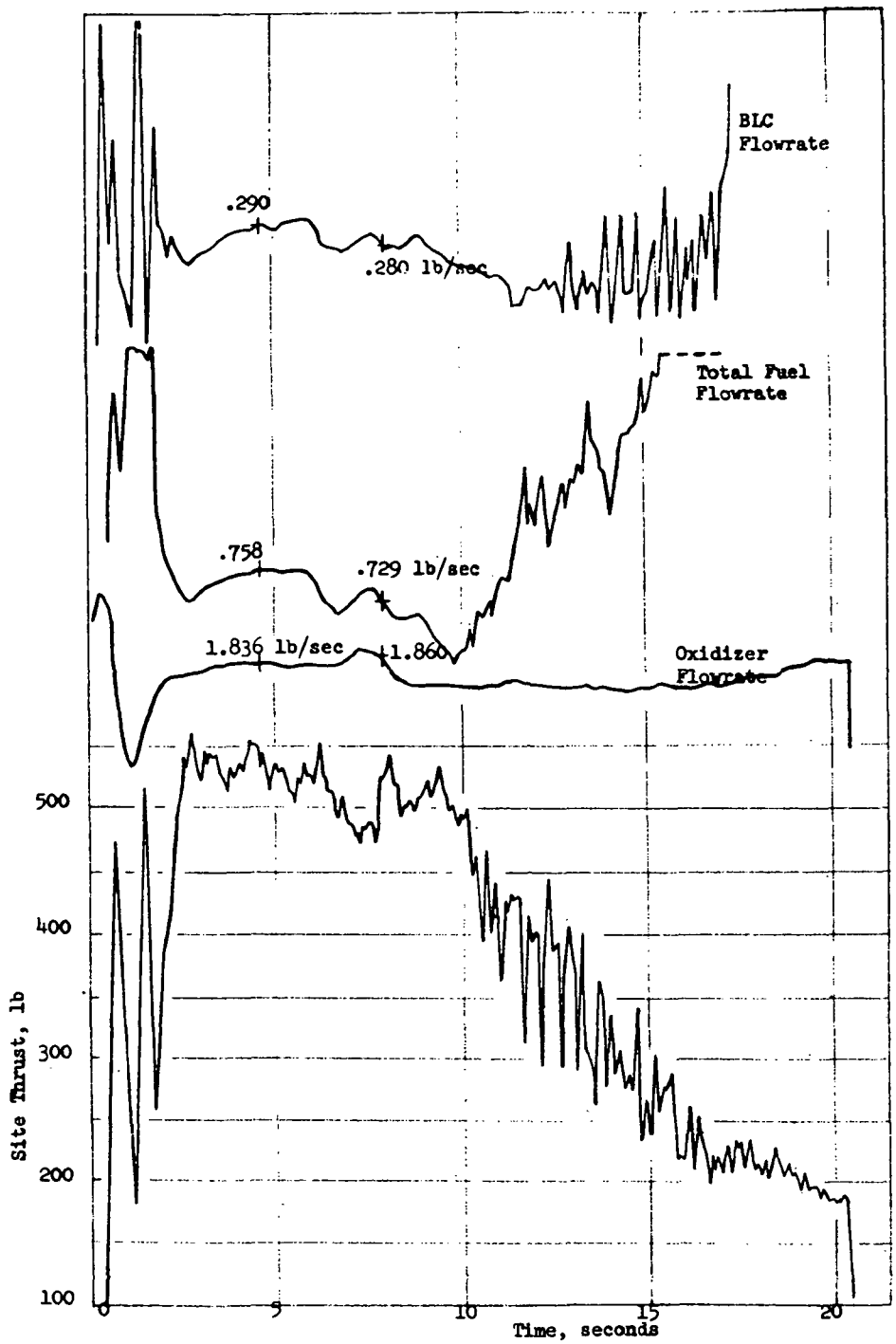

Figure 144. Thrust and Flowrates for Test 011
Core MR = 3.9 11.2% BLC

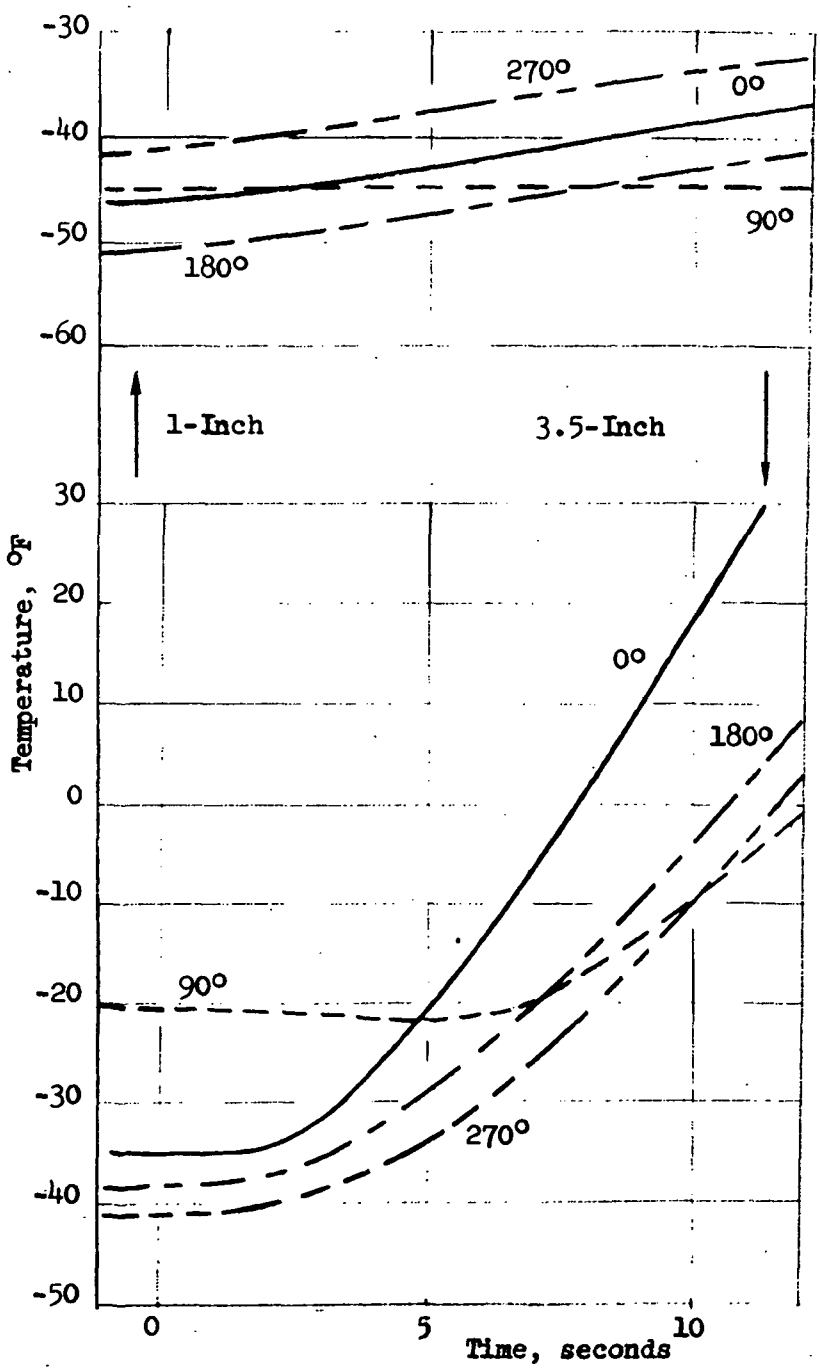

Figure 145. Test 011 - Outside Graphite Wall Temperature at 1-Inch and 3.5-Inch Axial Locations as Function of Thermocouple Position

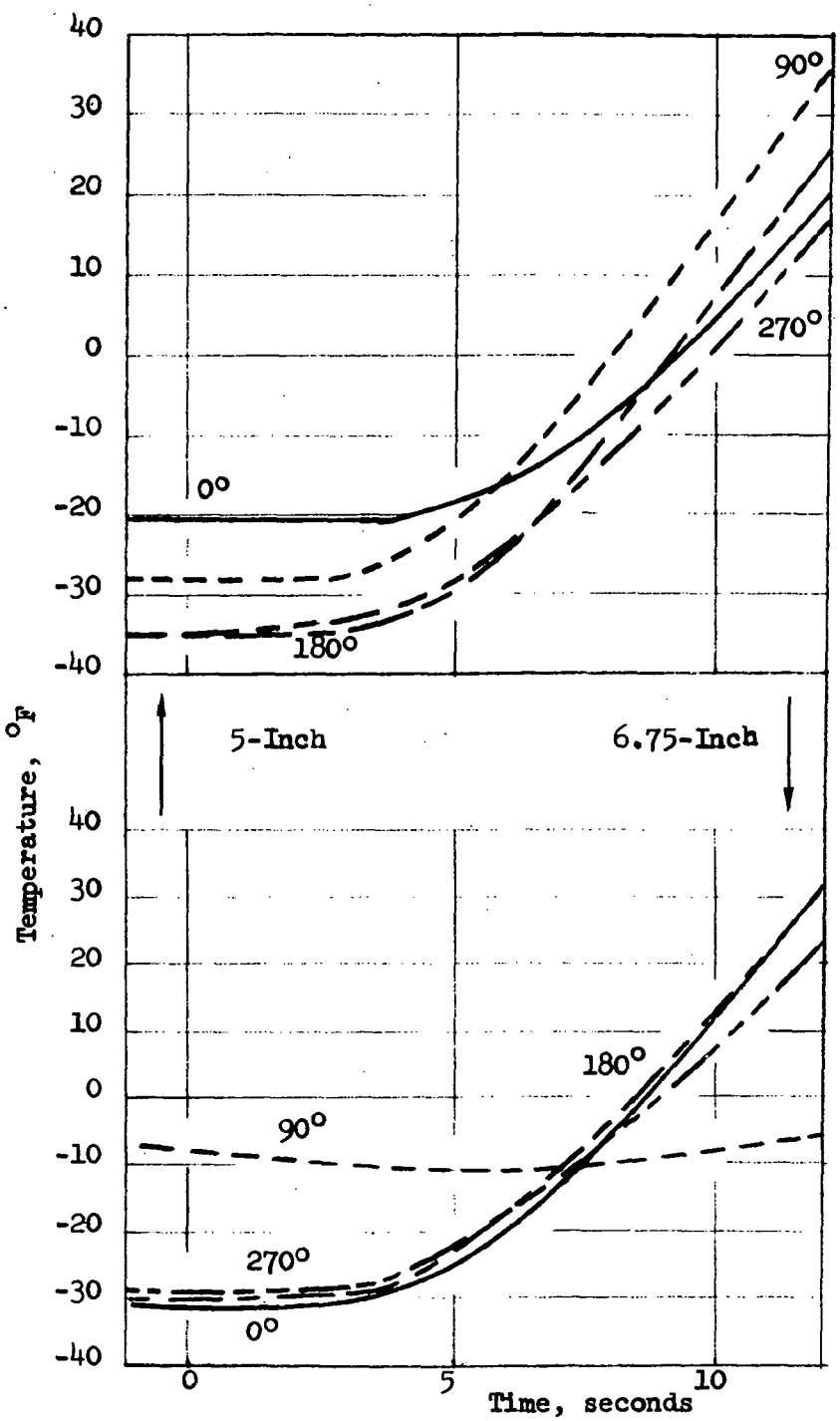

Figure 146. Test 011 - Outside Graphite Wall Temperature at 5-Inch and 6.75-Inch Axial Locations as Function of Thermocouple Position

of only about 30 - 40 F during the initial 7 seconds of test duration before depletion of the diborane tank and thus did not permit meaningful heat transfer evaluation. Experimental performance is shown in Table 8 (page 75). It is observed in Table 8 that the average I_{sp} efficiency calculated for the two graphite chamber hot-firings (Tests 008 and 011) made at similar operating conditions was 86.6 percent compared to a pre-test η_{c*} prediction of 91.5.

SUMMARY OF RESULTS

Although plagued by a number of problems, the subject effort was successful in a number of respects.

The thin-wall, nickel calorimeter chambers, in conjunction with a number of thermal data analysis computer models developed during this program, most adequately provided a sensitive means of establishing injector operating characteristics and obtaining basic heat transfer data as a function of such variables as percent film cooling, injector core mixture ratio, and chamber length.

The initial four calorimeter hot firings, made with an existing like-doublet injector, resulted repeatedly in unsymmetrical heat transfer, thermal spikes, and chamber deterioration or burnthrough. For the greater sector of the chamber, streaking/burnout characteristics were not evident; in fact, the experimental chamber temperatures were lower than originally predicted with the analytical heat transfer model. Data analysis revealed that this was due predominantly to significantly lower (than previously estimated) rates of entrainment of combustion gas into the vapor film. The heat transfer model (DEAP) was thus upgraded to successfully post-predict the results of the initial four calorimeter hot firings.

A new diffusion-bonded injector was designed and fabricated which incorporated: (1) inwardly canted fans (like-on-like) to decrease the injector sensitivity to both chamber fuel fan protection and oxidizer misimpingement, (2) improved BLC manifolding, (3) large outer-row fuel orifices to decrease combustion product deposition on the injector face, and (4) contoured orifice entrances. Three calorimeter hot firings were made with the new diffusion-bonded injector. Although in one of the tests, non-orifice-damaging localized overheating was observed following operation with insufficiently sub-cooled FLOX, all calorimeter tests evidenced (1) no injector streaking (absence of local hot spots, thermal spikes and/or chamber gouging), (2) minimal amounts of injector face deposition, and (3) analytically predictable chamber heat trasnfer using the upgraded model.

Further use of the diffusion-bonded injector in a long-duration hot firing with a graphite-lined chamber (designed through use of the upgraded anlaytical heat transfer model) resulted in loss of the hardware due to the failure of an originally substandard diffusion bond undetected in the short calorimeter firings. In spite of the hardware loss, good data were obtained during the first 30 seconds of run duration. These data, like the calorimeter data, showed symmetric and analytically predictable heat transfer results.

Another diffusion-bonded injector was fabricated. This injector was redesigned slightly to effect a reduction in the operating temperature of the injector face, thereby reducing injector sensitivity to FLOX subcooling. This was accomplished primarily through use of a reduced injector face plate thickness which allowed the fuel flow in the orifices and manifold to assume a proportionately greater share of the cooling load.

Two short calorimeter tests with the modified diffusion-bonded injector successfully resulted in symmetric heat transfer and no injector face overheating.

Another long-duration test using a graphite-lined chamber, however, was prematurely terminated after unexpected depletion of the contents of the diborane tank at 7 seconds into the run. Before the test was manually cut, engine operation at high mixture ratio and insufficient fuel cooling of the injector resulted in injector damage to the central fuel doublets. This occurrence was indeed unforunate since all previous evidence gave indication of:

1. Injector operationg resulting in only minimal combustion product deposition on the face
2. No injector streaking
3. No thermal spikes
4. No injector face overheating
5. Symmetric heat transfer to the chamber wall
6. Analytically predictable heat transfer to the chamber wall.

In summary, the efforts on this program are believed to have resulted in:

1. Demonstration of the utility of calorimeter chambers
2. Detailed design of a satisfactory FLOX/B_2H_6 injector
3. An upgraded FLOX/B_2H_6 analytical heat transfer model whose validity has been demonstrated numerous times and which can be used to design FLOX/B_2H_6 thrust chambers for indefinite periods of operation.

CONCLUSIONS

1. The thermal feasibility of a boundary-cooled OF_2/B_2H_6 chamber capable of operating for indefinite periods of time has been analytically predicted by extrapolation of results from an upgraded thermal analysis model (DEAP) whose predictions were experimentally verified with short-duration calorimeter test data obtained during the subject program. The design for such a chamber is presented in Fig. 138. Operation of that graphite chamber with the injector pictured in Fig. 64 at 102 psia, 3.4 core mixture ratio, and 11.8 percent BLC resulted in a measured I_s efficiency of 86.6 percent with a predicted maximum inside wall temperature of 1200 F (indefinite operation).

2. Injector design criteria capable of providing indefinite OF_2/B_2H_6 boundary-cooled operation have been developed, though not yet adequately demonstrated.

3. The material (graphite, nickel, etc.) feasibility of a boundary-cooled OF_2/B_2H_6 chamber for indefinite periods of time remains to be evaluated.

4. Calorimetric test and data reduction techniques for high-temperature boundary-cooled combustor operation have been developed and verified. Such data allowed a thermal analysis model (DEAP) for OF_2/B_2H_6 boundary-cooled combustor operation to be upgraded and verified.

NOMENCLATURE

c	Specific heat of wall material
C_p	Specific heat at constant pressure
h	Heat transfer coefficient
k	Thermal conductivity
G_m	Mass transfer rate per unit area into film
L	Wall thickness
Le^*	Pseudo Lewis number $= \frac{G_m C_{p_g}}{h_g}$
N	Number of equations
n	Time index
p	Wetted perimeter
q_s	Heat flux at gas surface $= h\ (T_{aw} - T_s)$
q_c	Axial heat flux from conduction
T	Temperature
T_s	Hot gas surface temperature
T_{theo}	Temperature corresponding to the theoretical flame temperature of the chamber core
T_o	Back wall temperature
$\dot{T}_o$, $\ddot{T}_o$	First and second time derivatives of back well temperature
$\dot{W}$	Flowrate
x	Coordinate through wall
y	Coordinate along wall
η_{c^*}	Characteristic velocity efficiency $= c^*_{measured}/c^*_{theoretical}$
α	Density

REFERENCES

1. R-7998, "Chamber Technology for Space Storable Propellants, Final Report," Rocketdyne, a division of North American Rockwell Corporation, Canoga Park, California, September 1969.

2. LAP 69-564, "Thermal Analysis Procedure for INTEREGEN Thrust Chambers Using the Boundary Layer Cooling (BLC) Subroutine with the Thermal Analyzer Program (TAP)," Rocketdyne, a division of North American Rockwell Corporation, Canoga Park, California, September 1969.

3. R-7281, "Advanced Experimental Thrust Chambers," Final Report, Phases III and IV, Rocketdyne, a division of North American Rockwell Corporation, Canoga Park, California, 1968.

4. Giedt, W. H.: Principles of Engineering Heat Transfer, Van Nostrand Co., N. Y., 1957.

5. Goodman, T. R.: "The Heating of Slabs with Arbitrary Heat Inputs," AFOSR-7N-58-52, May 1958.

6. PR9227-12, "Thrust Chambers for Space Storables," Contract NAS3-12071, Rocketdyne, a division of North American Rockwell Corporation, Canoga Park, California, 22 July 1970.

7. McFarland, B. L.: "Heat Transfer Considerations in Interegen Thrust Chambers," ASME Paper 70-HT/Spt 41.

8. R-2403, "Analytical and Experimental Evaluation of Ejectors with 90° Turns," Aerojet General Corporation, November 1962.

9. R-7022, "Designers Guide and Computer Program for Ablative Materials in Liquid Rocket Thrust Chambers Final Report," Rocketdyne, a division of North American Rockwell Corporation, Canoga Park, California, June 1967.

10. Fry, F., P. Thomas, and P. Smart (Title Unknown): Institute of Fire Engineers, Edinborough, England, 1954.

11. Hines, W. W., L. P. Combs, W. M. Ford, and R. Van Wyk: "Development of Injector Chamber Compatibility Analysis," Final Report, AFRPL-TR-70-12, Rocketdyne, a division of North American Rockwell Corporation, Canoga Park, California, March 1970.

12. Knight, R. M., and R. N. Gurnitz: "Advanced Solid-State Diffusion-Bonded Injectors," Rocketdyne, a division of North American Rockwell Corporation, Canoga Park, California, Paper presented at Sixth AIAA Propulsion Specialist Conference, San Diego, Calfiornia, June 1970.

13. Personal communication, D. Young, JPL, with R. N. Gurnitz, Rocketdyne, 10 March 1971.

APPENDIX A

LEAST SQUARES EVALUATION OF VAPOR FILM ENTRAINMENT RATES IN TERMS OF DIFFERENTIAL EQUATION MODELS

In the stream tube model of the film cooling process, the temperature rise of the coolant is assumed to be governed by the following equation

$$\frac{\dot{w}_f C_{P_f}}{p} \frac{\partial T_{ft}}{\partial x} = hg' \left(T_{gr} - T_{fr}\right) + C_{P_g} G_{mg} \left(T_{gt} - T_{ft}\right) \tag{A-1}$$

In most cases, the differences between recovery and total temperature can be neglected so that the second subscript can be dropped. The thermal capacity of the film is approximated by

$$\dot{w}_f C_{P_f} - \dot{w}_c C_{P_c} + \int_o^x p G_{mg} C_{P_g} dx - \int_o^x p G_{mc} C_{P_c} dx \tag{A-2}$$

Analyses made to date generally assumed $G_{m_c} = 0$, and this assumption has been included here. Substitution of Eq. A-2 into Eq. A-1 gives:

$$\left(\dot{w}_c C_{P_c} + \int_o^x p G_m C_{P_g} dx\right) \frac{\partial T_f}{\partial x} = hg' \; p \left(T_g - T_f\right) + p C_{P_g} G_m \left(T_g - T_f\right) \tag{A-3}$$

Test data will define values of the film temperature at various locations along the coolant path so that if the spatial derivative in Eq. A-3 is approximated by a finite difference expression, Eq. A-3 can be converted into an algebraic equation in terms of the measured temperatures and a summation of entrainment flowrates.

$$\dot{w}_c C_{P_c} \left[\frac{T_{n+1} - T_{n-1}}{x_{n+1} - x_{n-1}}\right] \sum_{-}^{+} p_i G_i C_{P_g} \left[\frac{T_{n+1} - T_{n-1}}{x_{n+1} - x_{n-1}}\right] \Delta x_i = \left(h'_n + C_{P_g} G_n\right)_{p_n} \Delta T \tag{A-4}$$

In Eq. A-4 all quantities are known except for the entrainment flowrates, G_i. If both the measurement errors and the finite difference approximation errors were negligible, then Eq. A-4 could be solved directly for the entrainment flowrates.

Since this will not usually be the case, Eq. A-4 is rewritten as:

$$\sum p_i G_i \Delta x_i C_{p_g} \left[\frac{T_{n+1}-T_{n-1}}{x_{n+1}-x_{n-1}}\right] - C_{p_g} (T_g - T_n) G_n - h_g' (T_g - T_n) + \frac{\dot{w}_c C_{p_c}}{p_n}$$

$$\left[\frac{T_{n+1}-T_{n-1}}{x_{n+1}-x_{n-1}}\right] = \varepsilon_n \tag{A-5}$$

Squaring Eq. A-5 and summing yields an error parameter, $\sum \varepsilon_n^2$, which gives equal weighting to every data point and serves as a quantitative measure of how well the test data fit Eq. A-1 after evaluation of the entrainment mass flux, G_i. To evaluate G_i, the condition of minimum total error in Eq. A-5 is selected so that

$$\sum_1^N \varepsilon_n^2 = \text{minimum} \tag{A-6}$$

Therefore, for all n data points

$$\frac{\partial}{\partial G_n} \left(\sum \varepsilon^2\right) = 0 \tag{A-7}$$

When Eq. A-5 is expanded with G_n as the independent variable, a set of linear equations is formed of the type

$$a_{1n} G_1 + a_{2n} G_2 + a_{3n} G_3 + \ldots a_{nn} G_n - b_n = \varepsilon_n \tag{A-8}$$

$$a_{in} = a_{1n} = a_{2n} = a_{3n} = C_{p_g} \left[\frac{T_{n+1}-T_{n-1}}{x_{n+1}-x_{n-1}}\right] \frac{p_i \Delta x_i}{p_n \Delta x_n} \tag{A-9}$$

$$ann = C_{p_g}' \left\{\left[\frac{T_{n+1}-T_{n-1}}{x_{n+1}-x_{n-1}}\right] - T_g + T_n\right\} \tag{A-10}$$

$$b_n = h'_g (T_g - T_n) + \frac{\dot{w}_c C_{p_c}}{p_n} \left[\frac{T_{n+1}-T_{n-1}}{x_{n+1}-x_{n-1}}\right] \tag{A-11}$$

Squaring Eq. A-8 and differentiating with respect to G_j gives

$$\frac{\partial \varepsilon_n^{\,2}}{\partial G_j} = 2a_{jn}\varepsilon_n \tag{A-12}$$

Summing Eq. A-12 and setting the result equal to zero gives for the jth equation

$$\sum_{1}^{N} a_{jn}\,(a_{1n}G_1 + a_{2n}G_2 + \ldots\, a_{nn}G_n) = \sum_{1}^{N} a_{jn}b_n \tag{A-13}$$

Equation A-13 can then be solved for the mass entrainment fluxes, G_n, to give a minimum total error between the data and the prediction equation. Since no assumptions have been made as to the relationship between h_n, G_n, and T_n, the results can be used to test the various correlations relating to film behavior.

The effect of truncation errors on the spatial derivative approximation can be easily evaluated by use of successively more accurate approximations for the derivative.

APPENDIX B

SUMMARY OF DIBORANE TANKING OPERATIONS AND TEST USAGE

The final hot-firing (Test 011) of NAS7-767 was programmed for a duration of 75 seconds with a required diborane usage of 56 pounds; however, after 7 seconds of operation, the supply of the B_2H_6 (assumed at start to be approximately 100 pounds) was depleted from the 150-gallon run/storage tank and the test was terminated. There was no damage to the test stand nor the ablative thrust chamber; however, damage to the injector face occurred around the four inner fuel doublets. This damage most likely resulted from the high mixture ratio/two-phase floe conditions which occurred prior to engine cutoff.

An examination of previous B_2H_6 tanking operations and test usage on NAS7-767 has resulted in an unaccounted loss of approximately 95 pounds of B_2H_6. A review of the tanking operations and test usage are given below.

B_2H_6 TANKING

At the completion of the NAS7-304 program, 200 pounds of B_2H_6 were estimated to be remaining in the 150-gallon storage tank. This entire amount was scheduled to be depleted during the final test of 300 seconds duration; however, the firing was terminated at about 40 seconds due to engine failure. Upon request of JPL, 160 pounds of B_2H_6 were flow metered from the storage tank and transferred to four dipleg (volume below dipleg estimated to be 1/2 pound) shipping cylinders and shipped to JPL. During the subsequent negotiations on the current contract, it was decided that this unused propellant would be returned to Rocketdyne. The four cylinders were returned and the propellant was transferred (as discussed below) to the storage tank.

An estimated additional 100 pounds of B_2H_6 were obtained for use on the current program from the Rocketdyne Nevada Field Laboratory. This propellant, left over from the NAS7-741 contract, was transferred (as discussed below) from three shipping cylinders to the storage tank.

The criteria used to estimate the amount of B_2H_6 transferred from the dipleg shipping cylinders to the storage tank involved measurement of the length of time before a noticeable rise in storage tank pressure (indicating end of transfer of liquid and subsequent transfer of gas) occurred (at a constant cylinder-tank ΔP). For a ΔP of 100 psi, the time required to transfer as-received 40-pound cylinders from the supplier is about 4 minutes. During the tanking of the four cylinders received from MPL, it appeared that all of the cylinders were full. The same was true for two of the three cylinders obtained from Reno, with the third indicating approximately half-full (20 pounds).

The amount of B_2H_6 then estimated in the tank was as follows:

Previously left in tank	40 pounds
Received from JPL	160 pounds
Received from Nevada Field Laboratory	100 pounds
	300 pounds

PROPELLANT FILL DETERMINATION OPTIONS

Three basic options exist for determining the amount of diborane transferred to the storage vessel:

(1) Storage vessel level indication

(2) Pre-fill and post-fill cylinder weighing

(3) Direct-fill flow measurement

Option 1 could only be accomplished with float, acoustic, or bubble indicator systems. Because of the single-outlet (dipleg) construction of the tank, simple sight-glass indication could not be employed. Option 2 was not considered to be practical since the difference between pre- and post-fill weighing would only be 40 pounds out of a total steel cylinder, wood crate, and dry ice weight of 1500 pounds. Option 3 was complicated by the fact that the shipping cylinders have

dipleg construction which requires substantial purging with the helium pressurant to ensure that the maximum available amount of expensive liquid has been removed. This rules out the use of turbine flowmeters if the cylinders are to be emptied to completion through a single transfer line. As previously noted, the technique of measuring, at constant shipping cylinder-storage tank ΔP, the time for depletion of each shipping cylinder was chosen.

TEST USAGE

A total of 10 hot firings had been conducted prior to the final run (Test 011) on 23 June 1971. The estimated test usages and vent losses are summarized in Table B-1. The total accounted usage is about 205 pounds, or about 95 pounds short of the quantity believed tanked.

POSSIBLE CAUSES OF ACCOUNTING ERROR

There are a number of possible explanations for the accounting error; however, one single cause has been pinpointed. Leakage from the storage tank was recognized as a candidate cause. This possibility was discounted for the following reasons: 1) there was no indication of leakage (in the form of white deposits) around valves or flanges, 2) the tank pressure remains at 150 psig during periods of inactivity, and 3) there was no odor in the storage area.

Other possible explanations include:

(1) Substantial error in the assumed 40 pounds remaining in the storage tank after the 160-pound detanking.

(2) Small errors in the assumed amounts in the supposedly full cylinders which were tanked (due to initial fill errors, cylinder valve leakage, transfer leakage, and decomposition)

(3) Substantial error in the estimation of the quantity remaining in the supposedly half-full container obtained from the Nevada Field Laboratory.

TABLE B-1. B_2H_6 USAGE - NAS7-767

(Original Estimate)

Test No.	$\dot{W}_{B_2H_6}$ lb/sec	Duration, sec.	Test Usage, pounds	Vent Loss**, pounds	Total Usage, pounds
001	0.93	10	9.3	0.8	10.1
002	0.80	9	7.2	0.8	8.0
003	0.86	8.5	7.3	0.8	8.1
004	0.90	10	9.0	0.8	9.8
005	0.55	2	1.1	0.8	1.9
006	0.51	10	5.1	0.8	5.9
007	1.17	2	2.4	0.8	3.2
008	0.92	150	138.0	4.5	142.5
009	0.65	3	2.0	0.8	2.8
010	0.88	7	6.1	0.8	6.9
011	0.78	7*	5.5	---	4.7
		218.5	193.0	11.7	204.7

Amount on hand from NAS7-304 (incl. JPL) 200 lbs
Amount from Nevada Field Laboratory (NAS7-741) 100 lbs
300 lbs

* To B_2H_6 depletion

** Assumes full ullage and diptube loss for 25-gallon tank when employed; similar assumption for 150-gallon run/storage vessel when it was employed (Runs 008, 011)

(4) Small errors in the estimates of the amounts used during the eleven program tests

(5) Moderate errors in the estimation of vent losses

Potential propellant availability errors are summarized in Table B-2. Potential propellant usage errors are summarized in Table B-3. It can be seen that an unfortuitous combination of all errors could account for the observed propellant discrepancy.

PREVENTION OF PROPELLANT DEPLETION

The best means of prevention of propellant depletion would be to install a liquid-level gage in the 150-gallon run/storage tank*. Additionally, it is recommended that propellant from the 40-pound shipping cylinders be flow metered during the fill operation. Since, as previously discussed, emptying of the dipleg shipping cylinders to completion would cause flowmeter ram (due to flow of the pressurization gas), it is recommended that these cylinders be only 3/4 emptied, decoupled from the flowmeters, and subsequently fully depleted. Similar precautions should be taken relative to the usage of FLOX propellant.

*It should be noted that liquid level gages are not without problems. One such system is presently installed on a FLOX tank, is inoperative, and qill require considerable expense in terms of tank disassembly to repair.

TABLE B-2. PROPELLANT AVAILABILITY

Item	Nominal Tanked Propellant Estimate, pounds	Tanked Propellant Error Estimate, pounds	Minimum Tanked Propellant Estimate, pounds
Propellant Remaining in Tank	40	30	10
Four 40-pound Containers Returned from JPL	160	16	144
Unopened Container from Nevada Field Laboratory	40	4	36
Opened Container #1 from Nevada Field Laboratory	40	4	36
Half-Full Container from Nevada Field Laboratory	20	8	12
	300 pounds	62 pounds	238 pounds

TABLE B-3. PROPELLANT USAGE

Item	Nominal Usage Estimate, pounds	Usage Error Estimate, pounds	Maximum Usage Estimate, pounds
11 Runs	193	19	212
10 Vents	12	14	26
	205 pounds	33 pounds	238 pounds

APPENDIX C

DISTRIBUTION LIST

COPIES	RECIPIENT	DESIGNEE
	NASA HEADQUARTERS WASHINGTON, D.C. 20546	
1	PATENT OFFICE	(X)
	NASA LEWIS RESEARCH CENTER 21000 BROOKPARK RD. CLEVELAND, OHIO 44135	
1	OFFICE OF TECHNICAL INFORMATION	(X)
1	MR. IRV JOHNSON	(X)
	NASA MANNED SPACECRAFT CENTER HOUSTON, TEXAS 77058	
1	OFFICE OF TECHNICAL INFORMATION	(X)
	NASA MARSHALL SPACE FLIGHT CENTER HUNTSVILLE, ALABAMA 35812	
2	OFFICE OF TECHNICAL INFORMATION, MS-IP	(X)
1	TECHNICAL LIBRARY	(X)
1	DALE BURROWS S+E-ASTN-PJ	(X)
	NASA AMES RESEARCH CENTER MOFFET FIELD, CALIF. 94035	
1	PATENTS AND CONTRACTS MANAGEMENT	(X)
	JET PROPULSION LABORATORY 4800 OAK GROVE DR. PASADENA , CALIF. 91103	
2	WALTER B. POWELL	(X)
1	R. RIEBLING	(X)
3	MANAGER, LIQUID ROCKET PROPULSION TECH., CODE RPL OFFICE OF ADVANCED RESEARCH AND TECHNOLOGY NASA HEADQUARTERS WASHINGTON, D.C., 20546	(X)
1	DIRECTOR, TECHNOLOGY UTILIZATION DIVISION OFFICE OF TECHNOLOGY UTILIZATION	(X)

NASA HEADQUARTERS
WASHINGTON, D.C. 20546

25 NASA SCIENTIFIC AND TECHNICAL INFORMATION FACILITY (X)
P.O. BOX 33
COLLEGE PARK, MARYLAND 20740

1 MISSION ANALYSIS DIVISION (X)
NASA AMES RESEARCH CENTER
MOFFETT FIELD, CALIFORNIA 24035

NASA FIELD CENTERS

2	AMES RESEARCH CENTER MOFFETT FIELD, CALIFORNIA 94035	HANS M. MARK
1	GODDARD SPACE FLIGHT CENTER GREENBELT, MARYLAND 20771	MERLAND L. MOSESON CODE 620
2	JET PROPULSION LABORATORY CALIFORNIA INSTITUTE OF TECHNOLOGY 4800 OAK GROVE DRIVE PASADENA, CALIFORNIA 91103	HENRY BURLAGE, JR PROPULSION DIV. 38
2	JOHN F. KENNEDY SPACE CENTER, NASA COCOA BEACH, FLORIDA 32931	DR. KURT H. DEBUS
2	LANGLEY RESEARCH CENTER LANGLEY STATION HAMPTON, VIRGINIA 23365	ED CORTWRIGHT DIRECTOR
2	LEWIS RESEARCH CENTER 21000 BROOKPARK ROAD CLEVELAND, OHIO 44135	DIRECTOR
2	MARSHALL SPACE FLIGHT CENTER HUNTSVILLE, ALABAMA 35812	HANS G. PAUL CODE R-P+VED
2	MANNED SPACECRAFT CENTER HOUSTON, TEXAS 77058	J.G. THIBODAUX, JR. CHIEF, PROP. + POWER DIV. H. POHL

GOVERNMENT INSTALLATIONS

1	HEADQUARTERS, U.S. AIR FORCE WASHINGTON 25, D.C. 20546	COL.C.K. STAMBAUGH AFRST
1	ARNOLD ENGINEERING DEVELOPMENT CENTER ARNOLD AIR FORCE STATION TULLAHOMA, TENNESSEE 37388	DR. H.K. DOETSCH
2	AIR FORCE ROCKET PROPULSION LABORATORY RESEARCH AND TECHNOLOGY DIVISION AIR FORCE SYSTEMS COMMAND EDWARDS, CALIFORNIA 93523	RPRPD/MR. H. MAIN
1	AIR FORCE MISSILE TEST CENTER HOLLOMAN AIR FORCE BASE NEW MEXICO 45433	LIBRARY
1	AIR FORCE MISSILE TEST CENTER PATRICK AIR FORCE BASE, FLORIDA	L.J. ULLIAN
1	AERONAUTICAL SYSTEMS DIVISION AIR FORCE SYSTEMS COMMAND WRIGHT-PATTERSON AIR FORCE BASE DAYTON, OHIO 45433	D.L. SCHMIDT CODE ASRCNC-2
1	SPACE AND MISSILE SYSTEMS ORGANIZATION AIR FORCE UNIT POST OFFICE LOS ANGELES 45, CALIFORNIA 90045	COL. CLARK TECHNICAL DATA CENTER
1	DEFENSE DOCUMENTATION CENTER HEADQUARTERS CAMERON STATION, BUILDING 5 5010 DUKE STREET ALEXANDRIA, VIRGINIA 22314 ATTN- TISIA	
1	BUREAU OF NAVAL WEAPONS DEPARTMENT OF THE NAVY WASHINGTON , D. C. 20546	J. KAY RTMS-41
1	U.S. NAVAL ORDNANCE TEST STATION CHINA LAKE CALIFORNIA 93557	CODE 4562 CHIEF, MISSILE PROPULSION DIV.
1	PICATINNY ARSENAL DOVER, NEW JERSEY 07801	I. FORSTEN, CHIEF LIQUID PROPULSION LABORATORY,
1	U.S. ARMY MISSILE COMMAND REDSTONE ARSENAL ALABAMA 35809	DR. WALTER WHARTON

CPIA

1	CHEMICAL PROPULSION INFORMATION AGENCY APPLIED PHYSICS LABORATORY 8621 GEORGIA AVENUE SILVER SPRING, MARYLAND 20910	TOM REEDY

INDUSTRY CONTRACTORS

1	AEROJET-GENERAL CORPORATION P. O. BOX 296 AZUSA, CALIFORNIA 91703	W. L. ROGERS
1	AEROJET-GENERAL CORPORATION P. O. BOX 1947 TECHNICAL LIBRARY, BLDG 2015, DEPT. 2410 SACRAMENTO, CALIFORNIA 95809	R. STIFF
1	AEROJET-GENERAL CORPORATION SPACE DIVISION 9200 EAST FLAIR DR. EL MONTE, CALIFORNIA 91734	S. MACHLAWSKI
1	AEROSPACE CORPORATION 2400 EAST EL SEGUNDO BOULEVARD P. O. BOX 95085 LOS ANGELES, CALIFORNIA 90045	JOHN G. WILDER MS-2293
1	AVCO SYSTEMS DIVISION WILMINGTON, MASSACHUSETTS	HOWARD B. WINKLER
1	BEECH AIRCRAFT CORPORATION BOULDER DIVISION BOX 631 BOULDER , COLORADO	J. H. RODGERS
1	BELL AEROSYSTEMS COMPANY P.O. BOX 1 BUFFALO, NEW YORK 14240	W. M. SMITH
1	BELLCOMM 955 L-ENFANT PLAZA, S. W. WASHINGTON, D. C.	H. S. LONDON
1	BENDIX SYSTEMS DIVISION BENDIX CORPORATION 3300 PLYMOUTH ROAD ANN ARBOR, MICHIGAN 48105	JOHN M. BRUEGER

1	BOEING COMPANY P. O. BOX 3999 SEATTLE, WASHINGTON 98124	LIBRARY
1	BOEING COMPANY 1625 K STREET, N. W. WASHINGTON, D. C. 20006	LIBRARY
1	BOEING COMPANY P. O. BOX 1680 HUNTSVILLE, ALABAMA 35801	TED SNOW
1	MISSILE DIVISION CHRYSLER CORPORATION P. O. BOX 2628 DETROIT, MICHIGAN 48231	MR. JOHN GATES
1	WRIGHT AERONAUTICAL DIVISION CURTISS-WRIGHT CORPORATION WOOD-RIDGE, NEW JERSEY 07075	G. KELLEY
1	RESEARCH CENTER FAIRCHILD HILLER CORPORATION GERMANTOWN, MARYLAND	RALPH HALL
1	REPUBLIC AVIATION CORPORATION FAIRCHILD HILLER CORPORATION FARMINGDALE, LONG ISLAND, NEW YORK	LIBRARY
1	GENERAL DYNAMICS, CONVAIR DIVISION P. O. BOX 1128 SAN DIEGO, CALIFORNIA	LIBRARY
1	MISSILE AND SPACE SYSTEMS CENTER GENERAL ELECTRIC COMPANY VALLEY FORGE SPACE TECHNOLOGY CENTER P.O. BOX 8555 PHILADELPHIA, PA.	F. MEZGER F. E. SCHULTZ
1	GRUMMAN AIRCRAFT ENGINEERING CORP. BETHPAGE, LONG ISLAND NEW YORK 11714	JOSEPH GAVIN
1	HONEYWELL, INC. AEROSPACE DIV. 2600 RIDGWAY RD MINNEAPOLIS, MINN.	MR. GORDON HARMS
1	HUGHES AIRCRAFT CO. AEROSPACE GROUP CENTINELA AND TEALE STREETS CULVER CITY, CALIF. 90230	E. H. MEIER V.P.AND DIV. MGR., RESEARCH + DEV. DIV.

1	WALTER KIDDE AND COMPANY, INC. AEROSPACE OPERATIONS 567 MAIN STREET BELLEVILLE, NEW JERSEY	R. J. HANVILLE DIR. OF RESEARCH ENGR.
1	LING-TEMCO-VOUGHT CORPORATION P. O. BOX 5907 DALLAS, TEXAS, 75222	LIBRARY
1	ARTHUR D. LITTLE, INC. 20 ACORN PARK CAMBRIDGE, MASSACHUSETTS 02140	LIBRARY
1	LOCKHEED MISSILES AND SPACE CO. ATTN-TECHNICAL INFORMATION CENTER P.O. BOX 504 SUNNYVALE, CALIFORNIA 94088	J. GUILL
1	LOCKHEED PROPULSION COMPANY P. O. BOX 111 REDLANDS, CALIFORNIA 92374	LIBRARY
1	THE MARQUARDT CORPORATION 16555 SATICOY STREET VAN NUYS ,CALIF. 91409	LIBRARY
1	BALTIMORE DIVISION MARTIN MARIETTA CORPORATION BALTIMORE, MARYLAND 21203	MR. JOHN CALATHES (3214)
1	DENVER DIVISION MARTIN MARIETTA CORPORATION P. O. BOX 179 DENVER, COLORADO 80201	DR MORGANTHALER A. J. KULLAS
1	ORLANDO DIVISION MARTIN MARIETTA CORP. BOX 5837 ORLANDO, FLORIDA	J. FERM
1	MCDONNELL-DOUGLAS CORP. P. O. BOX 516 MUNICIPAL AIRPORT ST. LOUIS, MISSOURI 63166	R. A. HERZMARK
1	SPACE+INFORMATION SYSTEMS DIVISION NORTH AMERICAN ROCKWELL 12214 LAKEWOOD BOULEVARD DOWNEY, CALIFORNIA 90241	LIBRARY

1	ROCKETDYNE (LIBRARY 586-306) 6633 CANOGA AVENUE CANOGA PARK, CALIF. 91304	S. F. IACOBELLIS
1	NORTHROP SPACE LABORATORIES 3401 WEST BROADWAY HAWTHORNE, CALIFORNIA 90250	DR. WILLIAM HOWARD
1	AERONEUTRONIC CORPORATION PHILCO CORPORATION FORD ROAD NEWPORT BEACH, CALIFORNIA 92663	LIBRARY
1	ASTRO-ELECTRONICS DIVISION RADIO CORPORATION OF AMERICA PRINCETON, NEW JERSEY 08540	Y. BRILL
1	ROCKET RESEARCH YORK CENTER REDMOND, WASHINGTON 98052	F. MCCULLOUGH, JR.
1	SCIENTIFIC SERVICE BUREAU INC P. O. BOX 375 MORRISPLAINS, NEW JERSEY 07950	T. F. SEAMANS
1	STANFORD RESEARCH INSTITUTE 333 RAVENSWOOD AVENUE MENLO PARK, CALIFORNIA 94025	DR. GERALD MARKSMAN
1	SUNSTRAND AVIATION 2421 11TH STREET ROCKFORD, ILLINOIS 61101	R. W. REYNOLDS
1	TRW SYSTEMS GROUP TRW INCORPORATED ONE SPACE PARK REDONDO BEACH, CALIF. 90278	G. W. ELVERUM
1	TAPCO DIVISION 23555 EUCLID AVENUE CLEVELAND, OHIO 44117	P. T. ANGELL

1	THIOKOL CHEMICAL CORP AEROSPACE SERVICES	LIBRARY
1	THIOKOL CHEMICAL CORPORATION HUNTSVILLE DIVISION HUNTSVILLE, ALABAMA 35807	JOHN GOODLOE
1	RESEARCH LABORATORIES UNITED AIRCRAFT CORP. 400 MAIN ST. EAST HARTFORD, CONN. 06108	ERLE MARTIN
1	HAMILTON STANDARD DIVISON UNITED AIRCRAFT CORP. WINDSOR LOCKS, CONN. 06096	MR. R. HATCH
1	UNITED TECHNOLOGY CENTER 587 METHILDA AVENUE P. O. BOX 358 SUNNYVALE, CALIFORNIA 94088	DR. DAVID ALTMAN
1	FLORIDA RESEARCH AND DEVELOPMENT PRATT AND WHITNEY AIRCRAFT UNITED AIRCRAFT CORPORATION P. O. BOX 2691 WEST PALM BEACH, FLORIDA 33402	R.J. COAR
1	VICKERS, INC. BOX 302 TROY, MICHIGAN ELKTON DIVISION BRISTOL, PENNSYLVANIA	LIBRARY

UNCLASSIFIED

Security Classification

DOCUMENT CONTROL DATA - R & D

(Security classification of title, body of abstract and indexing annotation must be entered when the overall report is classified)

1. ORIGINATING ACTIVITY *(Corporate author)*

ROCKETDYNE
a division of North American Rockwell Corporation
6633 Canoga Avenue, Canoga Park, California 91304

2a. REPORT SECURITY CLASSIFICATION

UNCLASSIFIED

2b. GROUP

3. REPORT TITLE

BOUNDARY COOLED ROCKET ENGINES FOR SPACE STORABLE PROPELLANTS

4. DESCRIPTIVE NOTES *(Type of report and inclusive dates)*

Final Report, 1 April 1970 through 1 July 1971

5. AUTHOR(S) *(First name, middle initial, last name)*

R. C. Kesselring, B. L. McFarland, R. M. Knight, and R. N. Gurnitz

6. REPORT DATE

19 June 1972

7a. TOTAL NO. OF PAGES

270

7b. NO. OF REFS

13

8a. CONTRACT OR GRANT NO.

NAS7-767

b. PROJECT NO.

c.

d.

9a. ORIGINATOR'S REPORT NUMBER(S)

R-8766

9b. OTHER REPORT NO(S) *(Any other numbers that may be assigned this report)*

10. DISTRIBUTION STATEMENT

11. SUPPLEMENTARY NOTES

12. SPONSORING MILITARY ACTIVITY

13. ABSTRACT

To advance and extend the technology of boundary film/conduction cooled rocket thrust chambers to the space storable propellant combination OF_2/B_2H_6 (oxygen difluoride/diborane), a detailed evaluation of an existing analytical heat transfer model was made. Critical design parameters were identified and their importance determined. Test data reduction methods were developed to enable data obtained from short duration hot firings with a thin walled (calorimeter) chamber to be used to quantitatively evaluate the heat absorbing capability of the vapor film. Hot firings with $FLOX/B_2H_6$ were made with an existing like-doublet injector and a nickel calorimeter chamber.

DD FORM 1 NOV 65 1473

UNCLASSIFIED

Security Classification

14. KEY WORDS	LINK A ROLE	LINK A WT	LINK B ROLE	LINK B WT	LINK C ROLE	LINK C WT
Analysis and Experimentation						
Critical Design Parameters						
Test Data Evaluation Methods						
Calorimeter Hot Firings						
Fabrication Technique						